INSTITUTE OF GEOSCIENCES

Finite fault earthquake source inversions

-

Implementation and testing of a novel physics-based rupture model

Malte Metz

Cumulative dissertation

to obtain the academic degree "doctor rerum naturalium" (Dr. rer. nat.)
in the scientific discipline Geophysics/Seismology.

Submitted to the
Faculty of Mathematics and Natural Sciences
at the University of Potsdam, Germany.

Prepared at
Section 2.1 (Physics of Earthquakes and Volcanoes)
Department of Geophysics, Helmholtz Centre Potsdam -
GFZ German Research Centre for Geosciences.
&
Institute of Geosciences, University of Potsdam, Germany.

Date of disputation: 24 November 2023

Academic advisor: Prof. Dr. Torsten Dahm, University of Potsdam, Germany
Second advisor: Prof. Dr. Frank Krüger, University of Potsdam, Germany.

Reviewers:
1. Prof. Dr. Torsten Dahm
2. Prof. Martin Vallée, PhD
3. Prof. Sigurjón Jónsson, PhD

Examining committee:
1. Prof. Dr. Torsten Dahm
2. Prof. Martin Vallée, PhD
3. Prof. Dr. Jens Tronicke
4. Prof. Dr. Frank Krüger
5. Prof. Dr. Fabrice Cotton

Published online on the
Publication Server of the University of Potsdam:
https://doi.org/10.25932/publishup-61974
https://nbn-resolving.org/urn:nbn:de:kobv:517-opus4-619745

Statement of Originality

I hereby declare that this thesis is the product of my own work. All the assistance received in preparing this thesis and the sources used have been acknowledged. The work contained in this thesis has not been previously submitted for a PhD degree at any other higher education institution.

Potsdam, _____

_____

Malte Metz

Table of Contents

Abstract

Earthquake modeling is the key to a profound understanding of a rupture. Its kinematics or dynamics are derived from advanced rupture models that allow, for example, to reconstruct the direction and velocity of the rupture front or the evolving slip distribution behind the rupture front. Such models are often parameterized by a lattice of interacting sub-faults with many degrees of freedom, where, for example, the time history of the slip and rake on each sub-fault are inverted. To avoid overfitting or other numerical instabilities during a finite-fault estimation, most models are stabilized by geometric rather than physical constraints such as smoothing.

As a basis for the inversion approach of this study, we build on a new pseudo-dynamic rupture model (PDR) with only a few free parameters and a simple geometry as a physics-based solution of an earthquake rupture. The PDR derives the instantaneous slip from a given stress drop on the fault plane, with boundary conditions on the developing crack surface guaranteed at all times via a boundary element approach. As a side product, the source time function on each point on the rupture plane is not constraint and develops by itself without additional parametrization. The code was made publicly available as part of the *Pyrocko* and *Grond* Python packages. The approach was compared with conventional modeling for different earthquakes. For example, for the M_w 7.1 2016 Kumamoto, Japan, earthquake, the effects of geometric changes in the rupture surface on the slip and slip rate distributions could be reproduced by simply projecting stress vectors. For the M_w 7.5 2018 Palu, Indonesia, strike-slip earthquake, we also modelled rupture propagation using the 2D Eikonal equation and assuming a linear relationship between rupture and shear wave velocity. This allowed us to give a deeper and faster propagating rupture front and the resulting upward refraction as a new possible explanation for the apparent supershear observed at the Earth's surface.

The thesis investigates three aspects of earthquake inversion using PDR: (1) to test whether implementing a simplified rupture model with few parameters into a probabilistic Bayesian scheme without constraining geometric parameters is feasible, and whether this leads to fast and robust results that can be used for subsequent fast information systems (e.g., ground motion predictions). (2) To investigate whether combining broadband and strong-motion seismic records together with near-field ground deformation data improves the reliability of estimated rupture models in a Bayesian inversion. (3) To investigate whether a complex rupture can be represented by the inversion of multiple PDR sources and for what type of earthquakes this is recommended.

I developed the PDR inversion approach and applied the joint data inversions to two seismic sequences in different tectonic settings. Using multiple frequency bands and a multiple source inversion approach, I captured the multi-modal behaviour of the M_w 8.2 2021 South Sandwich subduction earthquake with a large, curved and slow rupturing shallow earthquake bounded by

two faster and deeper smaller events. I could cross-validate the results with other methods, i.e., P-wave energy back-projection, a clustering analysis of aftershocks and a simple tsunami forward model.

The joint analysis of ground deformation and seismic data within a multiple source inversion also shed light on an earthquake triplet, which occurred in July 2022 in SE Iran. From the inversion and aftershock relocalization, I found indications for a vertical separation between the shallower mainshocks within the sedimentary cover and deeper aftershocks at the sediment-basement interface. The vertical offset could be caused by the ductile response of the evident salt layer to stress perturbations from the mainshocks.

The applications highlight the versatility of the simple PDR in probabilistic seismic source inversion capturing features of rather different, complex earthquakes. Limitations, as the evident focus on the major slip patches of the rupture are discussed as well as differences to other finite fault modeling methods.

Zusammenfassung

Erdbebenmodelle sind der Schlüssel zu einem detaillierten Verständnis der zugrunde liegenden Bruchprozesse. Die kinematischen oder dynamischen Brucheigenschaften werden mit Hilfe von ausgedehnten Bruchmodellen bestimmt. Dadurch können Details, wie z.B. die Bruchrichtung und -geschwindigkeit oder die Verschiebungsverteilung, aufgelöst werden. Häufig sind ausgedehnte Bruchmodelle durch sehr viele freie Parameter definiert, etwa individuelle Verschiebungen und Verschiebungsrichtungen auf den diskretisierten Bruchflächenelementen. Die große Anzahl an Parametern sorgt dafür, dass Inversionsprobleme hochgradig unterbestimmt sind. Um daraus resultierende numerische Instabilitäten zu verhinden, werden diese Modelle häufig mit zusätzlichen eher geometrischen als physikalischen Annahmen stabilisiert, z.B. im Bezug auf die Rauigkeit der Verschiebung auf der Bruchfläche.

Die Basis für die Inversionsmethode in dieser Dissertaton bildet das von uns entwickelete pseudo-dynamische Bruchmodel (PDR). Die PDR basiert auf wenigen freien Parametern und einer simplen, planaren Geometrie und ergibt eine physik-gestützte Lösung für Erdbebenbrüche. Die PDR bestimmt die instantane Verschiebung basierend auf gegebenen Spannungsänderungen auf der Bruchfläche. Die Randbedingung der Spannungsänderung wird dabei zu jedem Zeitpunkt der Bruchentwicklung über eine Randelementmethode eingehalten. Als Nebenprodukt dessen kann die Herdzeitfunktion an jedem Punkt der Bruchfläche als Ergebnis des Models bestimmt werden, und muss daher nicht vorher definiert werden. Der PDR-Modellierungsansatz wurde mit anderen Modellen anhand verschiedener Erdbeben verglichen. Am Beispiel des M_w 7,1 2016 Kumamoto, Japan, Bebens konnte der Effekt einer gekrümmten Bruchfläche auf die daraus resultierenden Verschiebungsverteilung und Verschiebungsraten durch eine Projezierung der Spannungsvektoren reproduziert werden. Für das M_w 7,5 2018 Palu, Indonesien, Beben haben wir die Bruchausbreitung auf Grundlage der 2D-Eikonalgleichung und basierend auf einem angenommenen linearen Zusammenhang zwischen Bruch- und Scherwellengeschwindigkeit modelliert. Dadurch konnten wir die beobachtete Supershear-Bruchausbreitung als Ergebnis einer möglichen tiefen und daher schnelleren Bruchfront mit einer Abstrahlung an die Erdoberfläche erklären. Der PDR-Vorwärtsmodellierungs-Code wurde in den Open-Source Python Paketen *Pyrocko* und *Grond* veröffentlicht.

Meine Dissertation beleuchtet drei Aspekte der Erdbebeninversion unter Zuhilfenahme der PDR: (1) Ist eine Implementation eines simplen Bruchmodels mit wenigen Parametern in ein probabalistisches Bayesisches Inversionsprogramm möglich? Kann dies schnelle und robuste Ergebnisse für weitere Folgeanwendungen, wie Bodenbeschleunigungsvorhersagen, liefern? (2) Wie hilft die Kombination aus seismischen Breitband- und Accelerometerdaten mit Nahfelddeformationsdaten, Inversionsergebnisse mit der PDR zu verbessern? (3) Können komplexe Brüche

über einen multiplen PDR-Quellinversionsansatz aufgelöst werden und wenn ja, wann ist dies möglich?

Ich habe den PDR-Inversionsansatz entwickelt und auf zwei Erdbeben-Sequenzen in verschiedenen tektonischen Umgebungen angewandt. Mit Hilfe von verschiedenen Datensätzen in mehreren Frequenzbändern innerhalb von einfachen und multiplen Bruchflächeninversionen konnte ich das multi-modale M_w 8,2 2021 South Sandwich Erdbeben characterisieren. Dieses bestand aus einem langen, flachen, langsam brechenden Beben entlang der gekrümmten Subduktionszone, welches durch zwei kleinere, tiefere Brüche mit schnelleren Bruchgeschwindigkeiten begrenzt wurde. Die Validierung mit Ergebnissen aus einer P-Wellen Back-Projection, der Clusteranalyse von Nachbeben und einer Tsunami-Modelierung zeigten eine hohe Konsistenz mit den PDR-Resultaten.

Die Kombination von seismischen Daten und Oberflächendeformationen in einer multiplen PDR-Inversion habe ich auch zur Analyse eines Beben-Triplets vom Juni 2022 im Südosten des Irans genutzt. Die Inversionen konnten im Zusammenspiel mit relokalisierten Nachbeben einen neuen Fall von vertikaler Haupt-/Nachbebenseparation auflösen. Während die großen Hauptbeben im flachen Sediment stattfanden, sind die Nachbeben hauptsächlich entlang der tieferen Grenzfläche zwischen Sediment und kristallinem Grundgebirge aufgetreten. Eine Erklärung dafür ist das duktile Fließen einer vorhandenen Salzschicht auf der Grenzfläche, ausgelöst durch Spannungsänderungen im Zuge der Hauptbeben.

Die Anwendungen konnten die Vielseitigkeit der PDR als simples Quellmodel innerhalb von seismischen Quellinversionen zeigen. Limitierungen der Inversion, wie der augenscheinliche Fokus auf den Hauptverschiebungsbereich eines Bebens, werden in dieser Arbeit genauso diskutiert wie die Einordnung der PDR im Vergleich zu anderen ausgedehnten Quellmodellen.

1 | Introduction

This chapter introduces basic concepts and parameters of seismic source modeling and the earthquake rupture, and reflects on the currents status of seismic source modeling. The challenges related to earthquake modeling and inversion are introduced, especially when performed within a short time after the earthquake. The possible benefit and potential to include geodetic data in joint inversions, e.g., by combining seismic and satellite based continuous (e.g., GNSS) or snapshot data (e.g., InSAR) is briefly described.

How source modeling can be considered in rapid response activities is mentioned in the framework of the DFG funded EWRICA project, which I have been involved in during my doctoral studies. Within the EWRICA project also links to tsunami modeling and ground motion estimates were developed. The chapter is closed with a short outline of my research objectives and the structure of the thesis, including a description of my contribution to publications included in this cumulative dissertation.

1.1 Seismic source modeling

Large earthquakes with a magnitude equal or greater than M_w 6 activate faults or fault systems in the whole brittle crust, or even deeper within subducted lithospheric plates beneath oceanic trenches. The rupture front starts at a nucleation point (hypocentre) and then propagates rapidly in a circular, bi- or unilateral direction across the fault (Fig. 1.1). The rupture propagation speed v_r often varies between 50% and 90% of the shear wave velocity, although extremely slow or fast rupture velocities occasionally occur. Slip between the fault planes (shear dislocation) occurs immediately after the rupture front passes a point on the fault and then continues to grow until the rupture undergoes friction-controlled healing (slip pulse model, e.g., Brune, 1970, 1971; Dunham et al., 2011a, 2011b) or until the rupture front stops propagating (crack model, e.g., Sato & Hirasawa, 1973). The rupture nucleation is often associated with a strong stress anomaly (asperity) (e.g., Hicks et al., 2012; Zhao & Negishi, 1998), while the stopping of the rupture front is either related to a high-strength segment of the fault (barrier) (e.g., Aki, 1979), fault step overs (e.g., Bai & Ampuero, 2017; Wesnousky, 2006), or to the pre-existing shear stress on the fault becoming progressively lower (e.g., Weng & Ampuero, 2022).

Earthquakes can cause significant primary and secondary damage, affecting both the population and society. Primary damage to buildings and infrastructure is often linked to site effects, e.g., strong ground motion or soil liquefaction. Secondary damage may be caused by landslides,

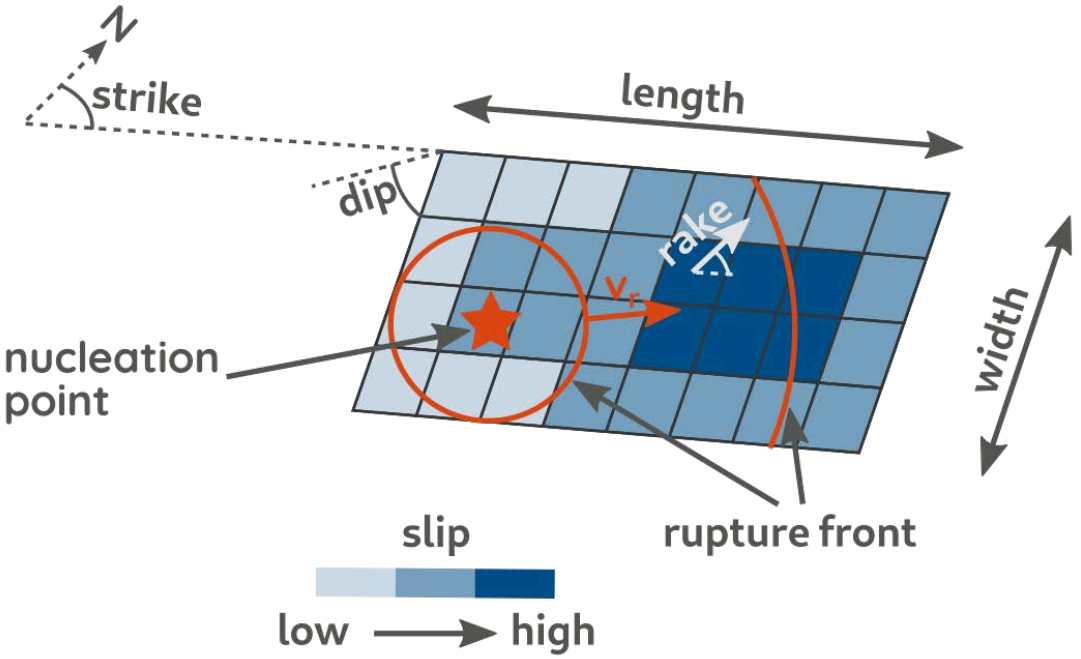

Figure 1.1: Schematic overview of common rupture parameters used to describe a kinematic rupture process. They define a kinematic rupture model with its orientation (strike, dip), its dimensions (length, width), the distributed slip along the rupture plane and the derived strength of the earthquake, and the rupture propagation pattern. The latter is controlled by the nucleation point and the rupture propagation velocity (v_r).

tsunamis or slow movements of the fault system persisting for months or years after the earthquake (post-earthquake slip, viscoelastic response). Earthquakes redistribute elastic stresses in fault systems, potentially triggering aftershocks or priming stresses for the generation of new strong earthquakes. In order to understand the earthquake rupture processes and mitigate potential damage and hazards, it is important to define and evaluate the parameters that describe the location, mechanics and rupture of the earthquake (Fig. 1.1). The source parameters and their uncertainties must be evaluated within a short time after rupture so that they can be used to assess primary and secondary hazards or be used in early warning systems, e.g. for tsunamis.

Numerous source models and rupture modeling or inversion approaches have been developed over the past decades, each of them constructed to estimate certain event parameters with specific performance requirements in mind. A rather simple but quite robust approach is the moment tensor point source model (MT). The model is established for routine source analysis (e.g., Dziewoński et al., 1981; Ekström et al., 2012, or the GEOFON data centre) and often contributes to rapid response and early warning systems. In a point source approximation the whole earthquake rupture is described by six force couples acting in a single point, the so called centroid (Gilbert, 1970). The temporal rupture process is described with a single scalar source time function. The point source approximation is sufficient to explain the radiation and strength of low-frequent seismic waves in some distance to the rupture fault segment. Choosing the MT allows to obtain very valuable first order parameters as the moment magnitude of the earthquake M_w (Hanks & Kanamori, 1979), or the possible orientation of the fault and the auxiliary plane of the earthquake, the style of faulting (normal, reverse or strike-slip) and the location of the centroid characterized by the centre of the released moment on the fault (Gilbert, 1970). Also,

information on volumetric changes (Müller, 1973) or an increased complexity of the rupture (e.g., Kuge & Lay, 1994) can be represented using isotropic or the volumetric compensated linear vector dipole (CLVD) components of the MT. The strength of this model lays in its very few parameters resolved from very low-frequent waveforms, hence being insensitive to small scale inhomogeneities of the earth structure. Thereby, inversions with this model yield rather stable results with only rough knowledge of the earths interior. Details of the rupture and their kinematic and dynamic properties can not be resolved, though.

This gap is filled with extended fault models. They additionally parametrize the nucleation and propagation of the rupture front, the dimensions and geometry of the ruptured fault segment, and the slip rate and slip distribution on the fault as a function of time and space. The various models differ in terms of the number of free parameters, the complexity and geometry of the fault and rupture process, the constraints and assumptions introduced, and the computation speed for a forward calculation or inversion for source parameters. The approaches may also handle and determine uncertainties differently. Two general approaches are usually distinguished:

1. **Kinematic rupture models:** They estimate the slip rate and slip distribution within data-driven inverse problems (e.g., Delouis et al., 2002; Dreger et al., 2005; Hartzell & Heaton, 1983; Heimann, 2011; Shimizu et al., 2020; Vasyura-Bathke et al., 2020; Zhang et al., 2014), only based on observed kinematic ground motions. No assumptions on the stress state or the frictional strength on the fault are made. Today, kinematic rupture models are often parameterized by many free parameters and therefore require constraints on the slip smoothness (e.g., Vasyura-Bathke et al., 2020) or the shape of the source time function (e.g., Tinti et al., 2005). The models are flexible and can tackle complex slip patterns but often require a predefined fault plane geometry to reduce the number of free parameters and thus the computation time of an inversion (e.g., Zhang et al., 2014).
2. **Dynamic rupture models:** These models target at the reproduction of the physics causing and governing the rupture process (e.g., Brune, 1970, 1971; Dunham et al., 2011a, 2011b; Fang & Dunham, 2013; Gabriel et al., 2013; Ruiz & Madariaga, 2011; Sato & Hirasawa, 1973; Ulrich, Vater, et al., 2019; Ulrich, Gabriel, et al., 2019). Often the stress state, frictional fault properties, the rupture geometry, its roughness, or other complexities on the fault are predefined for such models. The number of free parameters is often even larger than for kinematic modelsdespite the model by Ruiz and Madariaga, 2011. Therefore, dynamic models are rarely used for rapid response activities or implemented into probabilistic inversion schemes preventing from tracking parameter uncertainties with, e.g., bootstrapping.

Although both classes of finite fault models allow detailed insights into the slip distribution, the rupture propagation or the stress release (from dynamic modeling), they often need to be stabilized to deal with the large number of free parameters and the high non-uniqueness of the inversion (e.g., Beresnev, 2003; Mai et al., 2016). Stabilizing constraints as, e.g., on the roughness of the slip (e.g., Dreger et al., 2005; Fukuda & Johnson, 2008; Zhang et al., 2014), the source time function (e.g., Heimann, 2011; Tinti et al., 2005), the rupture propagation (e.g., Haskell, 1969), the rupture geometry (e.g., Ulrich, Vater, et al., 2019; Ulrich, Gabriel, et al., 2019), or

the mechanism reflect the a priori knowledge on the rupture processes. Stabilizing constraints improve the robustness of the inversion and lead to meaningful results (e.g. Jónsson et al., 2002), but also bear the risk of introducing unphysical constraints that may bias the solution.

The pseudo-dynamic rupture model (PDR), which is presented in my work, is different to the two approaches mentioned above. The PDR allows to independently model slip and slip rate on each sub-fault but links the slip distribution to the instantaneous geometry and stress of the ruptured fault segment, defined by the progressing rupture front. The relation between stress drop and slip is established by solving the boundary value problem for the fractured segment at discrete time steps using a numerical boundary element method (BEM). The rupture front is estimated using a simplified rupture-wave analogy. Interestingly, predefined sub-fault source time functions are not required, as the boundary value approach automatically generates them. By introducing physical constraints (boundary value problem and rupture front propagation) the number of free parameters is significantly reduced. This enables using the PDR in a probabilistic inversion to determine source parameters and the associated uncertainties.

Another potential advantage of the PDR is, when implemented in a software toolbox, that multiple types of data can be used as input for separate or joint inversions. Joint inversions of seismic broad band with continuous GNSS ground motions, static GPS measurements, or InSAR ground deformation maps have already been used in numerous studies like the characterization of induced events (e.g., Grandin et al., 2017), slow slip events (e.g., Vallée et al., 2013), earthquake sequences (e.g., Daout et al., 2020), the evaluation of moderate events (e.g., Steinberg et al., 2020; Steinberg et al., 2022), or the analysis of large earthquakes like, e.g., the M_w 7.3 1992 Landers, California, USA, earthquake (e.g., Hernandez et al., 1999), the M_w 7.5 1999 Izmit, Turkey, event (Delouis et al., 2002), the M_w 7.9 2015 Gorkha, Nepal, earthquake (e.g., Grandin et al., 2015), or the recent 2023 Türkiye, Turkey, doublet (e.g., Goldberg et al., 2023). Fault traces mapped from InSAR deformation snapshots (e.g., Mai et al., 2023) or intensity data (Goldberg et al., 2023) can also be used as a priori information pre-constraining activated faults within a pure seismic inversion.

The joint inversion allows capturing more features of an earthquake. The static ground displacement, as recorded by InSAR, help constraining the location of the rupture, the mechanism and the slip distribution (e.g., Hernandez et al., 1999). The temporal evolution of the rupture process as its source time function, the rupture origin, or the rupture propagation is resolved by the seismic data. Thereby, source modeling using static and dynamic data types may help in stabilizing the estimates and reducing the uncertainties (e.g. Delouis et al., 2002; Delouis et al., 2000; Hernandez et al., 1999).

The joint inversion gives the opportunity to combine static GPS and InSAR data sets reducing data uncertainties (e.g., Feigl et al., 2002; Jónsson et al., 2002; Pedersen et al., 2003; Sudhaus & Jónsson, 2009). With GPS being more accurate on its horizontal components and the highest sensitivity of InSAR to vertical deformations both methods are complementary (Pedersen et al., 2003). Thereby, slip distributions and fault geometries can be estimated in more detail and with less uncertainties, if appropriate data weights are chosen (e.g., Sudhaus & Jónsson, 2009).

1.2 Challenges to use extended fault models for rapid information and rapid response activities

Fitting extended rupture models in a (near-)real-time application is demanding due to the large number of free parameters fostering overfitting (Beresnev, 2003; Cesca et al., 2010) and also increasing the computation time. Therefore, finite fault estimates often reduce the tested parameter space by assuming homogeneously shaped source time functions of the sub-faults with a constant duration or rise times (Dreger et al., 2005) or by defining the rupture plane based on known faults (e.g., Diao et al., 2016; Hoechner et al., 2008) or the fault and auxiliary plane provided by a preceding MT inversion (e.g., Zhang et al., 2014). This approaches give rather accurate slip models within a short time, as shown, e.g., by Diao et al. (2016), Zhang et al. (2014), and Zheng et al. (2020).

One challenge of rapid finite fault modeling is the estimation of the source parameter uncertainties. This issue was addressed in the EWRICA project (Early-Warning and Rapid ImpaCt Assessment with real-time GNSS in the Mediterranean), I was participating in. The project provides displacement data streams derived from high rate GNSS sensors in the Mediterranean region along with broad band and accelerometric data for further applications within a joint, more probabilistic point and extended seismic source inversion approach using the probabilistic inversion tool *Grond* (Heimann et al., 2018). Models tested within the inversion were defined based on a priori data. A part of the project and my work package was the implementation and testing of the PDR as a rapid source model.

The EWRICA project also focusing on ground motion prediction using neural networks (Lehmann, Ohrnberger, et al., 2023). Their work used source ensembles with associated misfits generated from the source inversion to model, e.g., peak ground displacements.

1.2.1 Multiple source modeling

Assuming a simple rupture geometry and rupture model as the PDR with few parameters is appropriate for most applications in earthquake modeling when earthquakes release its seismic moment only/predominantly on one fault. In the case of multiple activated fault segments advanced modeling is required. Examples include multi-modal or segmented ruptures (e.g., Barka & Kadinsky-Cade, 1988; Biasi & Wesnousky, 2016; Segall & Pollard, 1980) with the M_w 7.8 2023 Pazarcik, Turkey, earthquake as a recent prominent case (e.g., Abdelmeguid et al., 2023; Mai et al., 2023; Okuwaki et al., 2023; Petersen et al., 2023). Therefore, it is interesting for my work to investigate the flexibility of the PDR and whether a combination of several PDR sources is suitable to represent a complex rupture. One advantage can be that such a combined multiple source model still requires fewer parameters than a conventional lattice approach, and could therefore also be interesting for a probabilistic inversion. The goal of a multiple source lays in the characterization of all rupture segments with major seismic moment contributions for a more complete understanding of the rupture (Steinberg et al., 2020).

Different source modeling strategies are used to analyze such complex ruptures. One solution

provided by the iterative deconvolution and stacking approach (Diao et al., 2016; Zhang et al., 2014) iteratively stacks apparent source time functions of the sub-faults. The SliP rapid finite fault inversion method (e.g., Goldberg et al., 2022; Goldberg et al., 2023; Ji et al., 2002; Koch et al., 2019) uses a wavelet transform to separate the spatial and temporal slip evolution. Both mentioned approaches require a priori information on the fault orientations and locations, the hypocentral time and location, and the magnitude of an earthquake to give fast slip estimates. Pure geodetic inversions also require a priori knowledge from seismic moment tensor inversions to constrain the fault plane orientations (e.g., Yang et al., 2023).

Another fault estimation strategy inverts for the sub-source locations and their mechanisms (e.g., Carrillo Ponce et al., 2023; Carrillo Ponce et al., 2021). The inversion is, hence, less constraint with more degrees of freedom. Therefore, such inversion approach may take longer to converge to a final solution compared to the fast source estimation appraoches mentioned above. The subevent method (e.g., Jia, Shen, et al., 2020; Jia, Wang, et al., 2020; Zhan et al., 2014) works similarly to the approach by Carrillo Ponce et al. (2023), Carrillo Ponce et al. (2021), but requires guesses on initial model parameters. This method is rather versatile and can cope with a different number or different kinds of subsources (simple point or rectangular source models).

1.3 Objectives and outline

My doctoral studies focused on the development and application of a new finite fault inversion method, based on the the pseudo-dynamic rupture model (PDR). The PDR connects the shear slip on the fault plane with the stress drop via a boundary element method. Thereby, physical estimates of the static shear dislocation are obtained on the rupture plane without further constraints. As the rupture velocity is scaling linearly with the predefined shear-wave velocity, the PDR relies on few parameters only (Chap. 2.1).

1.3.1 Objectives of my thesis

Objectives of my thesis were defined as follows:

How does the pseudo-dynamic rupture model perform compared to other known kinematic and dynamic models?

> While kinematic models aim to resolve the kinematic properties of the rupture, dynamic models obtain details on the physical causes of the rupture process, as described in Section 1.1. I want to understand, to which extent PDR modeling with its simple parameterization is comparable to results from other kinematic or dynamic models. I will refer to the model initialization and the required parameters and background information, but also compare my results e.g. from static slip or source time function modeling to known models (Chap. 2.1, but also 3 and 4).

To which extent can the usage of the pseudo-dynamic rupture model provide insights into complex rupture processes, e.g., their slip distributions, rupture speeds or rupture depths?

The question arises, if and how well we can resolve simple or complex rupture geometries and processes with the PDR. I test different approaches including seismic (broadband and accelerometric data) and geodetic inversions of single and multiple PDR sources in different tectonic regimes (Chap. 3 and 4). I analyze both the capabilities and limits of the PDR model when applied on complex earthquake ruptures..

What are gains and limits of the pseudo-dynamic rupture model when implemented in the open-source toolboxes *Pyrocko* and *Grond*?

Open-source software can contribute significantly to spreading scientific knowledge. We have decided to include the PDR into the open-source Python packages *Pyrocko* and *Grond*. I will elaborate how this affects the current value of the PDR for the scientific community in terms of reproducibility of results and further developments with respect, e.g., to multi source inversions (Chap. 3 and 4).

1.3.2 Outline of this thesis

My thesis includes a workflow from methodological developments and first tests towards a fully integrated source model, that is easy to install along with widely used seismological toolboxes and ready to use within inversions. The general outline of this dissertation is shown in Figure 1.2. In Chapter 2, the theoretical foundation of the PDR is explained and its numerical implementation in an easy-to-use software toolbox is described. Details are provided in Chapter 2.1 together with first forward modeling applications. Further refinements of the pseudo-dynamic rupture done through its' implementation within *Pyrocko* (Heimann et al., 2017) and *Grond* (Heimann et al., 2018) are presented in Chapter 2.2. Two applications of single and multi-source waveform and satellite deformation inversions in rather different tectonic environments are shown: One at the South Sandwich subduction zone in the SE Atlantic (Chap. 3) and a second one from the Arabian-Eurasian continental collision zone in SE Iran (Chap. 4).

I also want to discuss my work with respect to available models (Chap. 5) and give ideas for new and further developments based on the PDR (Chap. 6).

The cumulative dissertation comprises of three main publications, which answer my research questions (Sec. 1.3) and also highlight the workflow of the pseudo-dynamic rupture model implementation (Fig. 1.2). The first publication (Chap. 2.1) yields detailed insights into the theoretical foundation of the pseudo-dynamic rupture. It provides results from simple planar-fault and heterogeneous stress forward-modeling cases. The implemented pseudo-dynamic rupture source model is used within an inversion frame work. It allows to utilize seismic and joint seismic and

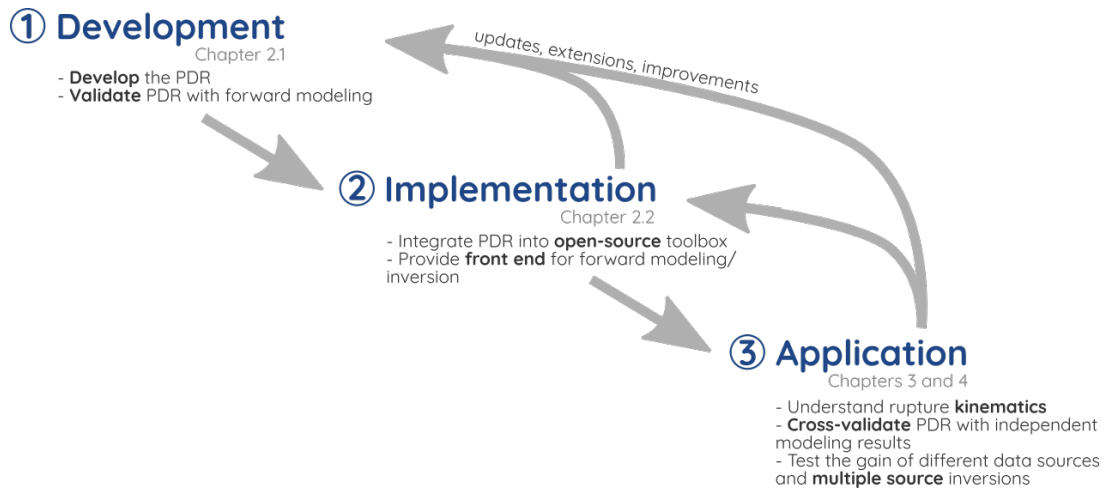

Figure 1.2: Workflow through this dissertation highlighting the different stages of the pseudo-dynamic rupture model (PDR) generation. Major targets of each step are indicated as well as the relevant chapters of my thesis.

static ground deformation. Inversion results for two earthquake sequences characterized by differing tectonic settings are presented in the Chapters 3 and 4. While Chapter 3 focuses on the complex multi-modal 2021 South Sandwich earthquake within the subduction zone, Chapter 4 resolves features of the continental collision zone of SE Iran from the 2022 seismic unrest in the Hormozghan Provence. Here, also novel multi-source inversion approaches are discussed.

1. T. Dahm, S. Heimann, **M. Metz**, M. P. Isken (2021). A self-similar dynamic rupture model based on the simplified wave-rupture analogy. Geophysical Journal International, 225 , 1586–1604. https://doi.org/10.1093/gji/ggab045

   M.M. majorly implemented the presented dynamic rupture model into the *Pyrocko* Python package and performed the forward modeling case studies of the 2015 Illapel, the 2016 Kumamoto and the 2018 Palu earthquake including their interpretation and visualization. M.M. drafted the corresponding results sections of the original manuscript.

2. **M. Metz**, F. Vera, A. Carrillo Ponce, S. Cesca, A. Babeyko, T. Dahm, J. Saul, F. Tilmann (2022). Seismic and Tsunamigenic Characteristics of a Multimodal Rupture of Rapid and Slow Stages: The Example of the Complex 12 August 2021 South Sandwich Earthquake. Journal of Geophysical Research: Solid Earth, 127 (11). https://doi.org/10.1029/2022jb024646

   M.M. developed parts of the new double pseudo-dynamic rupture inversion method (together with A.C.P.) and performed parts of the formal analysis (single and double pseudo-dynamic rupture inversion). M.M wrote the first draft of the manuscript and was responsible for the visualization of the results.

3. **M. Metz**, B. M. Asayesh, M. M. Aref, M. Jamalreyhani, P. Büyükakpınar, T. Dahm (2023). The July-December 2022 earthquake sequence in the southeastern Fars arc of Zagros mountains, Iran, Submitted to Seismica

M.M. conceptualized the study together with B.M.A. and M.M.A.. M.M. developed and implemented the new triple source inversion scheme and performed the source inversions and aftershock relocation. M.M. wrote the original draft (with contributions from B.A.M and M.J.) and was responsible for the visualization of the results.

I was involved in the preparation of four additional research papers where I could contribute with developments. Most recently, we analyzed the two 2023 Türkiye earthquakes with respect to their slip distribution and rupture propagation, but predominantly focused on aftershocks clusters in space, time and according to their mechanisms Petersen et al., 2023.

I could also use my tools for the implementation of the single force source model into the inversion software *Grond*. This was part of a study on the seismic characterization of a devastating landslide in the Himalaya by Cook et al. (2021).

A cluster analysis of earthquakes was performed on the September–December 2022 seismic unrest at the North-Atlantic Ridge (Cesca et al., 2023) which provided insights into a seismic swarm at the Mid-Atlantic Ridge with strong normal and thrust earthquakes. Within the study I used techniques as the cluster-based relocation of aftershocks which have also been included in my major publications (Trugman et al., 2023; Trugman & Shearer, 2017).

Source inversions using the PDR aim to invert for fast, reliable, and physics-based extended source models required for further analysis, e.g., tsunami forecasting or ground shaking estimation. A key process within the inversion is the calculation of synthetic waveforms. In this context I contributed to related projects. One investigated the potential of neural networks for the fast assessment of shaking parameters after an earthquake using a source ensemble (Lehmann, Ohrnberger, et al., 2023).

4. G. Petersen, P. Büyükakpınar, F. Vera, **M. Metz**, S. Cesca, K. Akbayram, J. Saul, T. Dahm (2023). The 2023 SE Türkiye seismic sequence: Rupture of a complex fault network. The Seismic Record, 3 (2), 134–143, https://doi.org/10.1785/0320230008

   M.M. was partially involved in the conceptualization of the study. M.M. performed the extended seismic source inversion and contributed to the manuscript with drafts of the finite fault methodology and its results.

5. S. Cesca, **M. Metz**, P. Büyükakpınar, T. Dahm (2023). The energetic 2022 seismic unrest related to magma intrusion at the North Mid-Atlantic Ridge, Submitted to Geophysical Research Letters

   M.M. performed the single-station template matching for event detection relocated the earthquakes. M.M. also drafted the respective methodological sections within the manuscript and contributed to the visualization of the results.

6. K. L. Cook, R. Rekapalli, M. Dietze, M. Pilz, S. Cesca, N. Purnachandra Rao, D. Srinagesh, H. Paul, **M. Metz**, P. Mandal, G. Suresh, F. Cotton, V. M. Tiwari, N. Hovius (2021). Detection and potential early warning of catastrophic flow events with regional seismic networks. Science 374, 87-92. https://doi.org/10.1126/science.abj1227

M.M. implemented the single force model into the *Grond* inversion framework. M.M. was also contributing to the review of the manuscript.

7. L. Lehmann, M. Ohrnberger, **M. Metz**, S. Heimann (2023). Accelerating low-frequency ground motion simulation for finite fault sources using neural networks. Accepted at Geophysical Journal International

   M.M. supported the developement of the physics-based waveform simulation (PWS). M.M. revised and edited the original manuscript.

2 | The self-similar fracture model - Theoretical foundations and its implementation in a software toolbox

2.1 Theory (first publication):

A self-similar dynamic rupture model based on the simplified wave-rupture analogy

T. Dahm, S. Heimann, **M. Metz**, and M. Isken (2021)

Published in Geophysical Journal International, 225(3):1586–1604
https://doi.org/10.1093/gji/ggab045

The supplementary material of this publication is available online at
https://doi.org/10.1093/gji/ggab045.

Geophysical Journal International

Geophys. J. Int. (2021) **225,** 1586–1604
Advance Access publication 2021 March 10
GJI Seismology

doi: https://doi.org/10.1093/gji/ggab045

A self-similar dynamic rupture model based on the simplified wave-rupture analogy

T. Dahm [1,2] S. Heimann,[1] M. Metz[1,2] and M.P. Isken[1,2,3]

[1] *GFZ German Research Centre for Geosciences, Physics of Earthquakes and Volcanoes,* 14473 *Potsdam, Germany. E-mail: dahm@gfz-potsdam.de*
[2] *Institute of Geosciences, University of Potsdam,* 14476 *Potsdam, Germany*
[3] *Institute for Geoscience, University of Kiel,* 24118 *Kiel, Germany*

Accepted 2021 February 1. Received 2021 January 26; in original form 2020 May 11

SUMMARY

The investigation of stresses, faults, structure and seismic hazards requires a good understanding and mapping of earthquake rupture and slip. Constraining the finite source of earthquakes from seismic and geodetic waveforms is challenging because the directional effects of the rupture itself are small and dynamic numerical solutions often include a large number of free parameters. The computational effort is large and therefore difficult to use in an exploratory forward modelling or inversion approach. Here, we use a simplified self-similar fracture model with only a few parameters, where the propagation of the fracture front is decoupled from the calculation of the slip. The approximative method is flexible and computationally efficient. We discuss the strengths and limitations of the model with real-case examples of well-studied earthquakes. These include the M_w 8.3 2015 Illapel, Chile, megathrust earthquake at the plate interface of a subduction zone and examples of continental intraplate strike-slip earthquakes like the M_w 7.1 2016 Kumamoto, Japan, multisegment variable slip event or the M_w 7.5 2018 Palu, Indonesia, supershear earthquake. Despite the simplicity of the model, a large number of observational features ranging from different rupture-front isochrones and slip distributions to directional waveform effects or high slip patches are easy to model. The temporal evolution of slip rate and rise time are derived from the incremental growth of the rupture and the stress drop without imposing other constraints. The new model is fast and implemented in the open-source Python seismology toolbox *Pyrocko*, ready to study the physics of rupture and to be used in finite source inversions.

Key words: Earthquake dynamics; Earthquake ground motions; Earthquake hazards; Earthquake source observations.

1 INTRODUCTION

Earthquake rupture, a sudden failure of rock along faults releasing internal stresses, is a complex, multifacetted process that involves a broad range of temporal and spatial scales. The study of rupture gives insights to several key parameters in seismology. It allows to discriminate the fault and auxiliary plane (e.g. Cesca *et al.* 2011a,b; Lopez-Comino & Cesca 2016) and helps to identify active faults. It can lead to estimates of stress and stress gradients on buried faults (e.g. Dahm *et al.* 2010, 2015; Lui & Huang 2019) , and possibly identify asperities and barriers where large variations of stress or strength occur (e.g. Meng *et al.* 2018). The slip and slip rate, and directional effects associated with the rupture affects ground motions generated by earthquakes (e.g. Somerville *et al.* 1997), and thus impacts the assessment of seismic hazard in a region (e.g. Rowshandel 2006) .

The rupture nucleation at the microscopic level is confined to a small volume surrounding the future nucleation point (e.g. Ohnaka 2013). It is a slow process that can take weeks or months prior to the earthquake. The co-seismic fracture itself is fast and propagates almost at the speed of elastic shear waves over long distances of the fault. Immediately after the fracture front has passed a point on the fault, the co-seismic dislocation (slip) of the two adjacent (cut) blocks is starting to grow over some time, at maximum until the rupture front has stopped everywhere to propagate. After the earthquake, post-seismic slip may still occur over the whole plane in the following weeks or months. Earthquake rupture studies aim to resolve this complex process and to simulate, or estimate, the slip on the rupture plane as a function of space and time at all scales, from microseconds to months and from a few centimetres to several hundreds of kilometres.

Simulating the radiating waves from a kinematic rupture model is straight forward. For instance, the assumed fault plane is gridded in rectangular or triangular subfaults and for each oriented subfault the slip magnitude and orientation as a function of time is

prescribed. Each subfault is considered as point source which radiates waves, by means of a Green's function approach, and the overall wave propagation towards a station is the superposition of all subfault contributions. The kinematic modelling can be turned into an inversion approach, to retrieve time-dependent slip distributions from observed waveforms and displacements. Although this is formally possible if the data cover a sufficient range of azimuth and distance, the inversion is often highly non-unique (underdetermined) and therefore interpretation and comparison is problematic (e.g. Beresnev 2003; Mai *et al.* 2016). A common approach to resolve the non-uniqueness is to minimize the length of the solution and to introduce Laplacian smoothing, slip positivity, sparsitivity and other constraints. However, unphysical constraints and a predefined geometry do impact the best models and their uncertainties. Although several Bayesian inversion approaches were recently developed to handle the uncertainties in finite fault inversion (e.g. Minson *et al.* 2013; Shimizu *et al.* 2020, Heimann *et al*. 2018), including uncertainties related to Green's function (Yagi & Fukahata 2011, Vasyura-Bathke *et al*. 2021), the effort of such methods is usually large which limits the approaches to the later detailed analysis long after the events.

Physics-based dynamic rupture models, which rely on few parameters only, are needed to allow a realistic forward modelling and to reduce the effort and non-uniqueness of the inversion. Our study develops a simplified, dynamic, semi-analytical rupture model suited for wavefield simulation and inversion. The rupture builds on the class of self-similar crack models (Kostrov 1964; Nielsen & Madariaga 2003). On one hand it is approximative as it neglects inertia and so far the details of frictional effects, and treats the rupture front growth in a simplified way. On the other hand, it is complete as the slip fulfils the boundary condition on the broken plane for every instantaneous rupture front geometry and applied stress.

A simple dynamic rupture model has first been suggested by Brune (1970, 1971). It considers the sudden application of a shear stress pulse to a circular fault, but no rupture propagation. The instantaneous shear stress drop in the fault generates a plane *SH* wave propagating with velocity v_S perpendicular to the fault plane. Brune estimated the far-field displacement of the *S* wave, ensuring that the low-frequency spectrum resembles the one of a double couple point source, and equated the amplitude spectra as a function of frequency and radius of the circular fault. The Brune's spectrum is used still today as a reference for estimating the size of an earthquake from the spectra of body waves. A more realistic circular crack rupture model was presented by Sato & Hirasawa (1973). The authors assumed that the rupture propagates from the centre to the final radius of the fault with constant velocity v_r. The slip is a function of stress drop and size of the growing circular crack. They assumed that slip has at any time the same form as that of a static crack with the size defined by the instantaneous rupture front. The model ensures that the final slip is consistent with a fracture mechanical static solution. Additional, variations of body-wave pulses in different directions to the fault and slip vector, the so-called directivity effects, are explained. Brune's amplitude spectra is reproduced for a far-distance station perpendicular to the plane, or by means of the average spectrum from all directions.

Numerical solutions to 3-D dynamic rupture problems commonly in use comprise finite difference (e.g. Madariaga *et al.* 1998), finite elements (e.g. Duan 2010), spectral elements (e.g. Kaneko *et al.* 2010) or unstructured discontinuous element methods (e.g. Tago *et al.* 2012). Such advanced modelling techniques are successfully used to study key aspects of ruptures, as for example the nucleation and arrest of induced earthquakes at reservoir level (e.g. Gallis *et al.* 2017; Buijz e *et al.* 2019). However, the exploitation of the model space with purely numerical approaches is computationally expensive. Our approach is to implement a semi-analytical, simple scheme efficient for fast simulations. We extend the simplified model by Sato & Hirasawa (1973), where we relax the assumption of a constant rupture velocity and allow for arbitrary nucleation points and shapes of the rupture front. We calculate wave radiation in a layered half-space Earth model instead of a homogeneous full space, so that realistic rupture scenarios can be simulated. The extended model needs only few parameters in addition to a point source model.

Such a simplified rupture approach allows the simple and fast simulation of scenarios that can support our understanding of the physics of rupture. We show that the self-similar rupture model can reproduce the integrated waveform and parameters which are predicted by much more complex dynamic rupture models. So the seismic moment (Aki 1966), which is a product of average slip and area of the rupture plane, is robustly predicted. The source time function (STF), and derived parameters as the corner frequency and station specific apparent rise times of the STF, reproduce observations from real earthquakes without any constraints on rise time or rupture mode. Directivity effects and changes in apparent rupture velocity as a function of distance to the nucleation point can be explained, up to the extreme of apparent super-shear ruptures. The model can explain patches of high slip, as well as the back-propagation and reflection of slip at positions where stress changes. The energy of the rupture and the fracture toughness can be estimated as a function of time, allowing for future extensions to full fracture dynamic modelling.

2 THEORY

Fig. 1 shows two end-member kinematic shear rupture models to illustrate different modes of crack growth. A so-called crack-model is realized for a circular rupture with constant rupture velocity v_r (Fig. 2a; Sato & Hirasawa 1973). The dislocation $\Delta u(r_h, t)$ (slip) is growing as long as the rupture front propagates. It is largest at the centre of the crack and has an elliptical shape towards its tips. The slip rate $\Delta \dot{u}(r_h, t)$ is non-zero at any time from the start to the stop of the rupture and everywhere on the ruptured pane. It is largest at the tip of the propagating crack and decreases towards the centre of the crack (Fig. 1a). A slip-pulse model is illustrated for a uni-directional rupture on a rectangular fault (Fig. 2b; Haskell 1964, 1966, 1969). In this model the slip rate is assumed to become zero at some distance behind the rupture front, so that the fault is at rest (heals) behind the rupture front and the slip reaches there its maximum value long before the rupture has stopped. The spatial pulse width can be defined by a constant rise time T_d times the rupture velocity. For instance, the self-healing on an infinite fault is modelled as a result of friction (e.g. Nielsen & Carlson 2000; Nielsen & Madariaga 2003).

The self-similar model developed in this paper combines both end-member rupture modes in a physical manner without imposing a frictional law and without any constraints on a rise time or healing front. We extend the concept of the self-similar circular crack of Sato & Hirasawa (1973) to arbitrary geometries of finite faults. For the modelling, we treat the rupture front estimation independent of the slip model, and base the approach on two main assumptions:

(1) the shape of the rupture front can be approximated by the solution of the Eikonal equation with rupture velocity as field parameter;

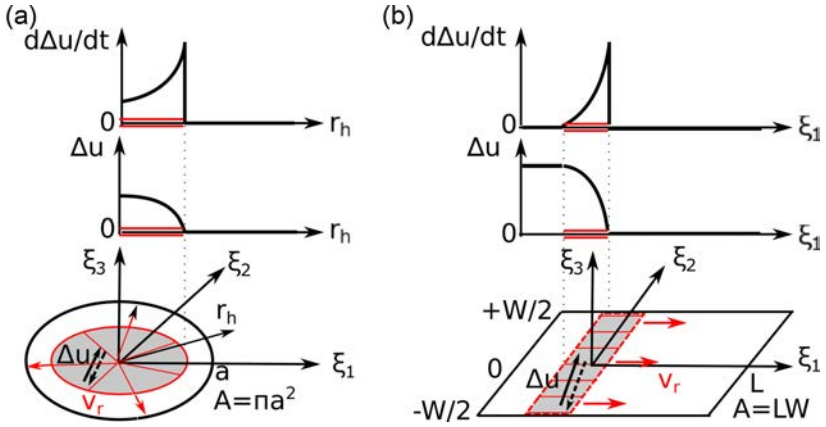

Figure 1. Sketch of two end-member kinematic shear rupture models. (a) Crack-model: circular rupture with constant rupture velocity v_r on a circular fault in the ξ_1–ξ_2 plane with radius a (Sato & Hirasawa 1973). The radial direction in the plane is r_h. The azimuth of the time-dependent dislocation Δu (slip) can have any but constant angle. The diagrams above the crack illustrate a snapshot of the slip and slip rate ($\Delta\dot{u}(t)$) as a function of r_h at the time of the reddish rupture front. (b) Slip-pulse model: uni-directional rupture in ξ_1 direction on a rectangular fault in the ξ_1–ξ_3 plane with length L and width W (e.g. Haskell 1964, 1966, 1969). The rupture front is a straight line. Slip and slip rate are plotted accordingly for a snapshot of a pulse-like rupture where only the grey band on the plane moves. The spatial centroid coordinates of both models are at $\boldsymbol{\xi} = (0, 0, 0)^T$.

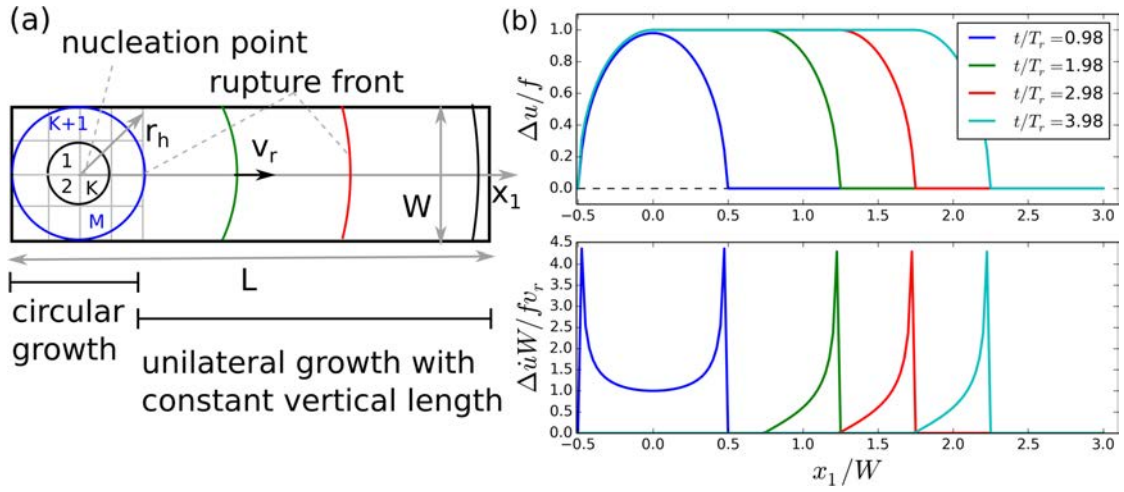

Figure 2. Illustration of the transition from crack-like growth to slip pulse growth for a vertical, rectangular crack. (a) Geometry of the rupture plane with width W and length L. The grey lines and labels indicate the gridding for numerical implementation. Instantaneous rupture front isochrones are shown by coloured lines at different times t/T_r during rupture, where $T_r = 0.5W/v_r$ and v_r is the rupture velocity. During first phase (circular growth until $r_h = W/2$) the rupture front is circular. During the second phase (unilateral growth, $r_h \gg W$) the rupture front in the centre of the crack propagates only in x_1 direction. (b) Quasi analytical solutions for the normalized dislocation Δu (slip) and slip rate $\Delta\dot{u}$. The factor f is based on the mode-II Griffith crack model and is $2(1-\nu)/\mathcal{N}$, where ν is the Poisson ratio and $\mathcal{N}$ the shear modulus. For $\nu \approx 0.45$ the factor of a circular crack equals the factor of an infinite Griffith crack—otherwise there is a small difference (not considered in the plot).

(2) the slip on the rupture plane is controlled by the instantaneous shape of the crack and the local, resolved shear stress.

As a first step, the fault orientation and the scalar moment are selected or estimated from the low-frequency content of waves in a centroid moment tensor point source inversion (e.g. Jost & Herrman 1989; Dahm & Krüger 2012, for review). The rupture front isochrones are calculated by iteratively solving the Eikonal equations of plumose lines in the rupture plane (Müller & Dahm 2000; Heimann 2010), equivalent to the solution of seismic rays in 2-D problems. Imposing the rupture velocity and shear stress on the rupture plane in advance, the self-similar crack model has only three free parameters, which are the time and 2-D location of the nucleation on the fault. For simplicity, we here set the rupture velocity proportional to the shear wave velocity in the rock (Heimann 2010).

The distribution of slip during rupture is calculated from the instantaneous size and shape of the already broken segments, which is defined by the position of the rupture front. We implement a numerical 3-D boundary element method (BEM), prescribe the stress drop ($\Delta\sigma$) and invert for dislocation (Δu). Since inertia effects on slip are neglected, and only the time-independent effect of friction is considered, the dynamic slip distribution is approximative. The BEM is fast and flexible to consider a wide range of shapes of the 3-D rupture.

Fig. 2 illustrates the concept for a rectangular rupture plane with vertical width W and length L, assuming a constant stress drop $\Delta\sigma$ on the plane and a zero stress drop behind the margins of the

plane. We use the analytical solutions of a circular and an infinite long Griffith crack (e.g. Pollard & Segall 1987) to illustrate the slip distributions on the x_1 axis in different stages of the rupture. The rupture starts at a point located at half the fault width. It is growing in the first phase in a self-similar manner with a circular rupture front at steadily increasing distance to the nucleation point in the centre. The slip in the circular growing phase is of elliptical shape with its maximum at the nucleation point (Fig. 2b). The slip rate is non-zero everywhere but largest a close distance behind the rupture front (Fig. 2b). As soon as the rupture front hits the upper and lower margin of the fault, it propagates mostly horizontal in x_1 direction (Fig. 2a). In this bi- and uni-lateral propagation phase the crack opening is approximated by the solution of a 2-D Griffith crack which is infinite in x_1 direction. Note that the maximum slip of a Griffith crack is slightly larger than the maximal slip of a circular crack, which is not considered in this example for illustration. Where the rupture front has reached its full vertical length (W) the slip does not increase with further rupture growth in x_1 direction. At this stage, the slip rate is still largest at the front of the ongoing rupture, but ceases to zero behind the front where the crack has touched the upper and lower margin of the rupture plane (Fig. 2b). In other words, a slip pulse rupture mode develops at the transition from circular to unilateral growth, without imposing any friction or other constraints. The rise time of the slip is controlled by a combination of the rupture velocity and the geometrical shape of the rupture front. Although the illustration is approximative, the example demonstrates the principle concept. The numerical implementation considers the finiteness of the plane and arbitrary rupture fronts. The following two subsections describe the details of implementation (see also flowchart in Supporting Information Fig. S1).

2.1 Rupture front simulation

The analogy of rupture processes to wave propagation is motivated by studies of rupture plane morphology, showing that curved plumose and conchoidal lines are typically orthogonal to each other (e.g. DeGraff & Aydin 1987; Helgeson & Aydin 1991; Kulander & Dean 1995; Weinberger 1999). Observation on rupture propagation and arrest on cracks, produced in plexiglas (Rummel 1987), confirm the relation of conchoidal lines representing snapshots of rupture fronts and the orthogonal plumose lines, indicating direction of rupture propagation. Detailed video analyses of the rupture development of mode I desiccation cracks in the laboratory, together with *in situ* measurements of elastic properties of the probes, could verify that the rupture front is related to a spatially variable rupture velocity on the rupture surface (Müller & Dahm 2000). Therefore, Müller & Dahm (2000) suggested to apply 2-D ray tracing methods to approximate the rupture front development in isotropic media with smoothly varying rupture velocity. The authors also pointed to important differences between seismic ray theory and rupture front development, as rupture propagation does not follow from first principles as an equation of motion. While wave velocities are material properties, the rupture velocities depend on material properties and the state of stress, pore pressure and the presence of fluids. Seismic wave and rupture fronts may both interfere and interact, but wave fronts never join as rupture fronts may do. If the strength contrast is large, the rupture front may even become discontinuous. The analogy of rupture and wave fronts is therefore only approximate in media with small strength differences, and may occasionally be even wrong. On the other hand, the analogy is suited for the purpose of defining a theoretical rupture model resembling key features of a physical rupture. It can be of benefit for efficient inversion strategies obeying only few parameters.

In order to keep the calculation of rupture fronts simple, we assume that the rupture occurs on a single plane. The orientation and size of this plane can be selected. The rupture velocity is a function of coordinates of the plane, that is, $v_r = v_r(\xi_1, \xi_2)$. For the sake of simplicity, we assume in the present study that the rupture velocity scales linearly with the shear wave velocity in the medium, where the scaling factor is taken as free parameter. The point of rupture nucleation is at (0, 0). Then, the traveltime function $T = T(\xi_1, \xi_2)$ is provided by the Eikonal equation in 2-D,

$$\left(\frac{\partial T}{\partial \xi_1}\right)^2 + \left(\frac{\partial T}{\partial \xi_2}\right)^2 = \frac{1}{v_r^2}\,. \tag{1}$$

The approach has been tested in a kinematic inversion procedure by Heimann (2010) using the fast marching level set method of Sethian (1996) to solve the Eikonal equation. Here, we reimplemented the algorithm in the *C* programming language and with bindings for Python. For reusability, we integrated it as an independent module into the open-source seismology toolbox *Pyrocko* (Heimann *et al.* 2017)[1]. The algorithm is numerically very efficient and stable. Computations are carried out on a rectangular grid, where grid spacing Δd in all dimensions is equal. A first-order finite difference scheme is sufficient in our application. Maximum errors in the calculated rupture front arrival times are on the order of $\Delta d/v_r$, so we can choose the grid spacing fine enough for any desired accuracy. The implemented tool was verified using analytical solutions and by comparison to ray tracing routine *Cake* in *Pyrocko*.

2.2 Calculation of the slip distribution

The slip is calculated sequentially using a quasi-static crack approach. In order to keep the calculation simple, we replace the physical rupture plane by a fictive planar, infinite plane. After eq. (1) has been solved for a given nucleation point, the snapshots of rupture fronts are available to define time-dependent fracture shapes (e.g. Fig. 2a). The stress drop $\Delta\sigma$ realized during rupture depends mainly on the available shear and normal stress on the fictitious rupture plane and the cohesion of friction. We assume that $\Delta\sigma$ is a fraction of the resolved shear stress on the true rupture plane with given orientation and depth. In order to keep the number of free parameter small, we suggest for future applications to estimate the shear stress from a combination of the world stress map model (Heidbach *et al.* 2018) with a simple mantle rheology, and keep the scaling factor between stress drop and shear stress as free variable. Known scaling laws between magnitude and stress drop, as given by Kanamori & Anderson (1975) and Kanamori (1994), are also used to estimate the stress drop. However, at a later stage of the implementation, or if better stress models are available, the stress drop function can be adapted by users choice. For instance, a seismicity model may be easily incorporated into the stress drop model to account for the stress release during previous major earthquakes or a coupling model to account for creeping segments on a plate boundary (e.g. Kaneko *et al.* 2010) or a rheologic model of the lithosphere. Such different models can be combined into a comprehensive stress drop model.

We employ a boundary element method (BEM) to calculate the slip distribution during rupture. The rupture plane is gridded

[1] Pyrocko module `pyrocko.eikonal_ext`

into rectangular boundary elements (Fig. 2a). Boundary values (**b**), the stress drop components in ξ_1, ξ_2 and optional ξ_3 directions (strike-parallel, dip-parallel and plane-normal), are allocated to the midpoints of the boundary elements. The dislocation vector Δu (slip) has three components in ξ_1, ξ_2 and optional ξ_3 direction (in-plane tearing, shearing and opening, respectively). Any dislocation occurring at one boundary element of the plane generates a stress drop contribution at all other boundary elements and vice versa.

Influence or Green's functions **g** are calculated between each of the boundary elements and for all possible directions and stress drop–dislocation pairs. They need to be calculated only once, when the problem is set up. The Green's functions describe the sensitivity to generate a stress drop at the midpoint of one boundary element in response to a dislocation at any other boundary element. So far, we use Green's functions for displacements and their spatial derivatives based on closed analytical expressions for dislocations on a rectangular elementary fault within a homogeneous half-space (Okada 1992). The Green's functions implemented so far do not contain elastodynamic terms. Therefore, the derived rupture scenarios are approximate and cannot be used to simulate the rupture-wave interaction. Additionally, we so far do not consider BEM Green's functions of layered media, although this could be implemented in a future release of the software.

For illustration, we map the 2-D matrix problem for the two spatial components into a 1-D vector equation (Fig. 3):

$$\begin{bmatrix} b_1 \\ b_2 \\ \vdots \\ b_K \end{bmatrix} = \begin{bmatrix} g_{11} & g_{12} & \cdots & g_{1K} \\ g_{21} & g_{22} & \cdots & g_{2K} \\ \vdots & \vdots & \ddots & \vdots \\ g_{K1} & g_{K2} & \cdots & g_{KK} \end{bmatrix} \begin{bmatrix} \Delta u_1 \\ \Delta u_2 \\ \vdots \\ \Delta u_K \end{bmatrix}, \tag{2}$$

where unknowns (Δu_j), boundary values (b_i) and Green's functions g_{ij} are only associated by indices and without spatial dependences. Note that $g_{ii} \neq 0$ (no summation convention here). K is the number of individual stress drop or dislocation components (number of boundary elements times number of directions). We use a linear least-squares inversion to obtain the dislocation response fulfilling the prescribed boundary values (Menke 1989):

$$\mathbf{\Delta u^{est}} = \left[\mathbf{g^T g}\right]^{-1} \mathbf{g^T b}. \tag{3}$$

Neither damping nor weighting is applied.

To model the dislocation field during the development of the earthquake rupture, all elements enclosed by the rupture front are determined for each increment of rupture time. They are labelled as active elements. A subset of equations from the pre-set eq. (2) is extracted for the active elements and is used in the dislocation inversion (3). Thus, for each time increment a quasi-static dislocation snapshot is obtained. A series of these snapshots between the start and stop of the rupture samples the dislocation at each grid point as a function of time.

The BEM method is implemented as a tool in the *Pyrocko* Python-toolbox for seismology (Heimann *et al.* 2017). To define boundary elements, a rectangular grid is automatically selected from the geometrical dimensions of the instantaneous rupture area and the smallest v_r. The grid size can be adjusted, but is usually much coarser than that used for the computation of the rupture front isochrones. For instance, in the examples below the number of boundary elements can be a factor of 100 smaller than the number of cells to solve the Eikonal equation, to still produce acceptable accurate solutions for the slip distribution. By comparison with analytical crack solutions, Metz (2019) studied the influence of the grid size on the precision of the solutions. Largest deviations occur close to the tip of fracture, where both the slip gradient and slip rate gradient are largest. Sparser grids increase the errors. For most typical applications, the frequencies under study are only a factor 2 or 3 larger than the corner frequency of the rupture. From the extensive numerical tests we concluded that a grid size of 50 × 20 is sufficient to model the temporal-spatial evolution of the dislocation on a 50 × 20 km sized fault plane due to a homogeneous stress drop. In terms of computational efficiency, the BEM method implementation has been optimized using *CPython* extensions and leveraging parallelization. For example, using a fault of 50 × 20 km length and a grid size of 50 × 20 boundary elements, the calculation of the Green's functions takes 1.8 s and the following estimation of 16 slip snapshots needs 4.7 s on a computer with 6 threads. So a complete forward modelling scheme using the named model parameter takes 6.5 s.

The final size of the rupture is determined by the positions where the stress drop or available shear stress becomes zero or negative, as the slip will die out within a short distance after entering such layers. Fig. 4 illustrates the concept. In a forward modelling problem the location, orientation and size of a fault plane is usually pre-defined. For instance, these regions are defined for crustal earthquakes by a superficial layer at the free surface and at depth by lower boundary of the seismogenic depth or by the temperature-controlled brittle-ductile transition. For subduction zone events a zero stress may be assigned to the volumes outside the slab. In practice, the rupture front isochrones are calculated a little into the regions of zero stress (Fig. 4) according to a defined skin thickness. The same skin thickness can be considered to define active elements in the BEM calculation of slip.

In an inversion problem, a key question is where and when to stop the rupture. While the free surface or brittle-ductile boundaries can be easily integrated in a pre-defined, rheological stress model, the lateral extent of the rupture within the seismogenic zone is constrained by the observed seismic moment M_0 of the earthquake. Here, a specific feature of the self-similar model is employed. While the time-development of rupture and slip-rate (the directivity effects) will depend on the selected nucleation point (e.g. Fig. 4), which is unknown in the inversion problem, the final slip distribution after the arrest of the rupture is independent on where the rupture nucleated. In a first exploratory run we consider rupture growth directly at the centroid location of the moment tensor solution. The calculated seismic moment steadily increases with each step-wise expansion of the rupture front. The calculation is then stopped at the position of the rupture front where the difference between calculated moment and the observed M_0 is minimal. The geometry of this particular solution explains the low-frequency radiation of observed waves and has the same numerical centroid location as the observed earthquake assuming a well-defined stress drop field (Fig. 4). Note that a small shift between numerical and observed centroid maybe considered at this stage. After the geometry of the rupture plane has been defined by this first calculation, all other possible scenarios of different hypocentres can be tested to explain the observed directivity effects by matching the observed final slip distribution (seismic moment and centroid location). Fig. 4 also illustrates that small-scale heterogeneities in rupture velocity and stress drop (barriers and asperities) can be additionally considered in the modelling geometry.

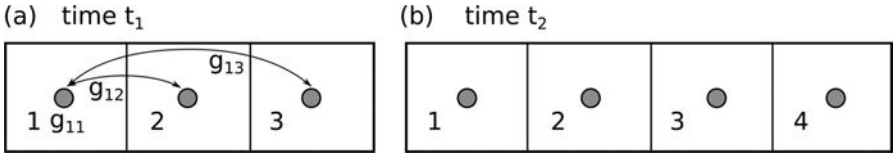

Figure 3. Illustration of the time dependent slip calculation of our model. For a time t_1 the rupture front encloses the centre points of three boundary elements. The pre-calculated Green's functions (*gij*) are then used to estimate the traction based on the slip or invert the slip from known traction boundary values. For a later time t_2 the rupture front passed also the centre of boundary element 4. Thus, the described procedure is repeated including all four boundary elements and new slip or traction distributions are obtained.

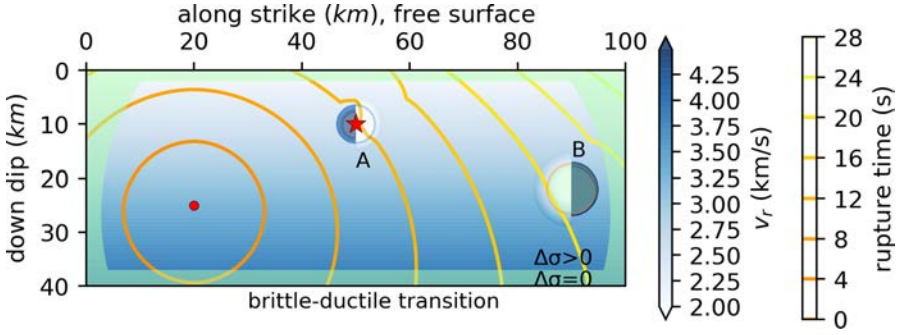

Figure 4. Setup of a fault rupture model. Given is the strike, dip and centroid location (star) of the fault. The rupture velocity (blue grid image, velocity increases with depth) is defined as a fraction of the shear wave velocity structure in the region. A background stress drop model is fixed before modelling, where the regions above 2 km below surface and below the brittle-ductile transition in 37 km depth are tapered to zero stress drop, $\Delta\sigma = 0$ (green clipped path). Two circular heterogeneities (A=asperity, B=barrier) are included as examples (colours indicate increase and decrease of rupture velocity, see Section 3.3. for more explanation). The nucleation point used for computation of rupture front isochrones (coloured contour lines) is given by the red circle.

3 APPLICATIONS AND CASE STUDIES

We demonstrate the model with two case studies of fault settings: (1) thrust faulting along an interplate subduction zone interface, and (2) the strike-slip rupture on an intracontinental, crustal subvertical fault. While the impact of the free surface, vertical and lateral variation of the rupture velocity, and stress heterogeneity on slip rate and pulse duration are illustrated, the examples demonstrate the flexibility and computational efficiency of the approach.

3.1 Subduction zone interplate earthquakes

We use the M_w 8.3 2015 Illapel, Chile, earthquake as an example of a shallow dipping earthquake rupture. In such a setting, the rupture velocity typically increases in downdip direction from very small values of less than 2 km s^{-1} at the tie of the subducting plate to more than 4.5 km s^{-1} at the lower end of the seismogenic zone. The Illapel earthquake has been studied in several papers (e.g. Fuentes *et al.* 2016; Melgar *et al.* 2016; Okuwaki *et al.* 2016; Ruiz *et al.* 2016; Tilmann *et al.* 2016; Ye *et al.* 2016; Hayes 2017; Herman *et al.* 2017; Meng *et al.* 2018). Although the high-frequency wave radiation of the Illapel 2015 earthquake indicates a complex rupture with the involvement of multiple asperities and complex rupture patterns along both dip and strike directions (e.g. Okuwaki *et al.* 2016; Ruiz *et al.* 2016; Tilmann *et al.* 2016; Meng *et al.* 2018), the low-frequency radiation is overall simpler. We basically refer to parameters reported in Tilmann *et al.* (2016), a study where continuous GNSS, broad-band seismological, teleseismic arrays and regional accelerometer data have been combined for a joint kinematic source inversion.

The megathrust earthquake ruptured a 220 km long and about 145 km wide segment of the interface between the Nazca and South America plate. The rupture nucleated downdip in a depth of about 40 km (Table 1).

The rupture velocity is 1.6 km s^{-1} in the shallow segments and increases downdip up to 2.2 km s^{-1} (see Melgar *et al.* 2016; Tilmann *et al.* 2016; Ye *et al.* 2016). If we base v_r on a shear wave velocity model combining CRUST2.0 (Bassin *et al.* 2000), AK135 (Kennett *et al.* 1995) as used by Cesca *et al.* (2016) with refined wave velocities and densities based on Contreras-Reyes *et al.* (2017) and Maksymowicz *et al.* (2015), a scaling factor of 0.6 yields a good fit to observed velocities. However, we implement an equivalent, smoothed gradient model for the rupture velocity along the slab interface, instead of first-order discontinuities as described in CRUST2.0. Uniform boundary tractions are prescribed at the fault interface, with a stress drop of 0.8 MPa (compare to Kanamori 1994). The stress drop is estimated from the background tectonic stress as, for example, given by Wortel & Cloetingh (1985). The tectonic stress tensor is rotated to obtain the shear stress on the fault plane (here 1.3 MPa). It consists of the stress drop during the earthquake and the remaining frictional strength. Using the stress drop of 0.8 MPa, which yield a good fit of the slip distribution, we estimate a frictional strength of about 0.5 MPa. The rake angle of ∼80°–90° (e.g. Tilmann *et al.* 2016) is retrieved from the projection of maximal shear stress in the rupture plane and is in agreement with the direction of the maximum horizontal stress (Heidbach *et al.* 2018). Only mode II and III rupture and no opening is assumed. Furthermore, shear stress is tapered to zero between 5 km depth and the surface, where unconsolidated sediments near the trench are present (Maksymowicz *et al.* 2015; Contreras-Reyes *et al.* 2017).

Fig. 5 shows simulation results in comparison to Tilmann *et al.* (2016). The centroid location and lateral extend of the rupture plane have been fixed following the procedure described in Fig. 4. The final static slip distribution shows a maximum slip of 5–5.5 m in the centre of the rupture along strike and in the upper half of the

Table 1. Pre-defined parameter used for the M_w 8.3 2015 Illapel earthquake. The coordinates of the anchor of the fault with normal vector **n** are defined at the surface in its midpoint. *l* and *w* give length along *x* and width along *y* of the plane; *z* refers to true depth. If more than one stress model is defined, the values overwrite the stress from the upper line. The CRUST2.0 model refers to the nomenclature given in Bassin *et al.* (2000). Earthquake parameters were defined with reference to USGS (https://earthquake.usgs.gov/earthquakes/eventpage/us20003k7a), Cesca *et al.* (2016), Fuentes *et al.* (2016), Melgar *et al.* (2016), Tilmann *et al.* (2016), Hayes (2017), and Herman *et al.* (2017).

Fault geometry and orientation		
lat/*lon*/strike/dip	length/width	**n** [*ned*]
–31.0° / –72.6° / 5° / 20°	300 km/150 km	[−0.03, 0.341, −0.94]
Nucleation		**Initial centroid**
lat/lon/*z*/*x*/*y*	M_0	lat/lon/*z*/*x*/*y*
−31.55°/–71.55°/ 38.0 km/−52.7 km/111.2 km	3.5×10^{21} Nm	−31.13°/−72.09°/ 18.1 km/−10.3 km/52.8 km
Stress model		
$\|[t_x, t_y, t_z]\| = \|\mathbf{t}\|$	range	rake [*ned*]
$\|[0.0, 0.0, 0.0]\| = 0.0$ MPa	0 km $< z \leq$ 5 km	93°, [0.03, −0.939, −0.342]
$\|[-0.04, 0.799, 0.0]\| = 0.8$ MPa	5 km $< z$	93°, [0.03, −0.939, −0.342]
Velocity model		**Boundary elements**
CRUST2.0 ID	γ	n_x/n_y
R2	0.6	35 / 20

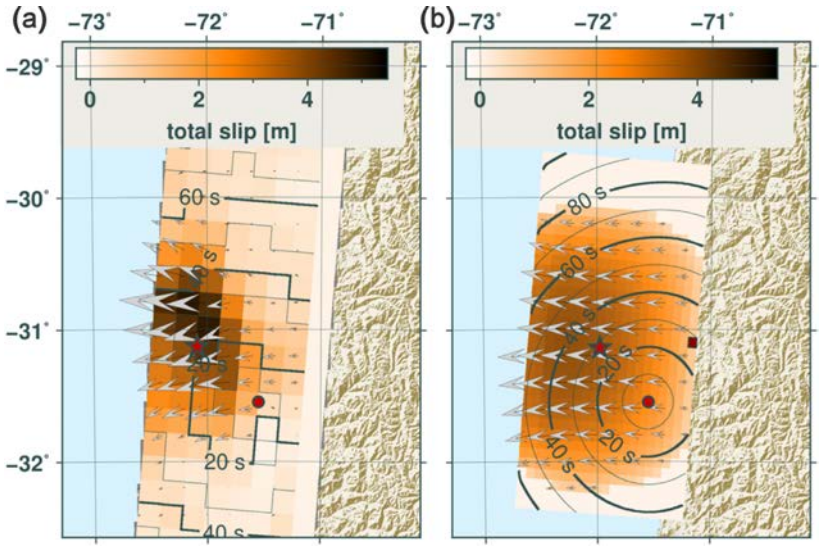

Figure 5. Comparison of the final static slip results from Tilmann *et al.* (2016) (a) (finite fault modelling using GPS) to our results (b) for the 2015 Illapel earthquake. Slip is colour-coded and contour lines indicate the rupture front arrival time. Arrows scaled by the total slip show both slip direction. The red point highlights the nucleation point, the red star the centroid given by GCMT (a) and using our self-similar rupture model (b). The red square in (b) indicates one boundary element, whose moment rate function is shown in Fig. 6(c). The main asperity is located in both cases on the upper segment of the fault plane with a maximum slip of 5–5.5 m. Also the areas of larger slip match well. Tilmann *et al.* (2016) derive a more pronounced asperity though. Their rupture front velocities are in the same range as our results obtained with the Eikonal equation.

fault up to the trench, corresponding to a depth range of 15–20 km. The estimated length, width and slip distribution is consistent with the results of Tilmann *et al.* (2016) and other studies. The modelled seismic moment of 3.284×10^{21} Nm is very similar to the $M_0 = 3.488 \times 10^{21}$ Nm estimated by Tilmann *et al.* (2016). The small misfit indicates a good accuracy considering the sparse boundary element grid and time sampling. High slip patches on a rupture plane are often interpreted as regions where elevated stress levels existed before (e.g. asperities and barriers) and led to higher slip during rupture. However, in our modelling a homogeneous stress drop model has been used, and the concentration of slip in the upper half of the centre of the fault is controlled by the shape of the fault and the free surface.

Fig. 5 also indicates the estimated direction of slip. Smooth variations of slip directions are found in the outer region of the fault, very similar to the slip variations resolved in the kinematic inversion by Tilmann *et al.* (2016). The mean slip direction is in agreement with the direction of the maximal shear stress resolved on the given plane. This is not unexpected, but demonstrates that starting from plate convergence models and the orientation of the subducting

slab can lead to a reasonable modelling of the static features of the rupture including variability of slip.

The rupture nucleation has been fixed to the hypocentre reported in Melgar *et al.* (2016) and Tilmann *et al.* (2016). A fast propagation of rupture fronts along the deeper tip of the rupture front and an upward bending of fronts towards shallower levels is indicated by the distance and curvature of the isochrones (Fig. 5b). A similar pattern, but poorly sampled, is indicated in the kinematic inversion of observed data (Fig. 5a).

It is interesting to look to predicted directivity effects and the point source equivalent STF. As we do not forward-propagate wavefields in this study, we compare moment rate functions in single points on the rupture plane, or sum them up to represent far-field STF in specific directions. For instance, the STF developed in Brune's model is calculated for a ray perpendicular to the fault. In our case, we sum 'in-phase' over all moment rate functions (MRFs) at all boundary elements to obtain the STF equivalent to the orthogonal ray. The self-similar rupture model shows a triangular shaped moment rate function, similar to the one observed in Okuwaki *et al.* (2016) and Tilmann *et al.* (2016), but with a slightly larger peak of $\sim 1 \times 10^{20}$ Nm s^{-1} (Fig. 6a). The peak of the STF retrieved by Tilmann *et al.* (2016) arrives about 5 s earlier and shows a slightly longer tail. A possible explanation can be a smaller stress drop at the northern end of the ruptured segment, so that slip on this segment would become smaller and the rupture plane would be extended in our modelling to fit M_0. For instance, Metois *et al.* (2012) developed an interseismic coupling model for the central Chilean subduction zone indicating strong segmentation along the plate interface. However, the asymmetry of the STF of the 2015 Illapel earthquake is not confirmed in every study. For instance Okuwaki *et al.* (2016) derives a symmetric STF very similar to our solution (Fig. 6a). Therefore, we do not investigate this possibility further. The far-field STF in Fig. 6(a) is the superposition of the MRFs at single boundary elements. In Figs 6(b) and (c), we plot the localized MRFs at the centroid location and at a deeper boundary element on the fault with similar rupture arrival time. The MRF at the centroid shows a slip pulse with a second peak 50 s after origin time, and a strong decay after the peak. The second peak is caused by the rupture arrival at the surface leading to larger slips and re-rupturing at the depth of the centroid. The MRF at a deeper patch on the fault is shorter in its duration and shows a stronger decay after the peak (Fig. 6c). Due to the large depth hardly any re-rupturing is recognized. The shorter duration and faster decay are explained by the large distance to the free surface and a smaller rupture front curvature at larger depth compared to the centroid location.

It is noteworthy that all the details on the MRF and STF are results from the simulation by itself, without constraining any parameter as rise time or friction. They are only controlled by the instantaneous shape of the rupture front and the interaction of boundary elements to maintain the balance of force equilibrium.

3.2 Subvertical plane intraplate earthquake

Intraplate earthquakes occur in different tectonic settings, as normal dipping faults at graben systems, low angle continental thrust faults, or on subvertical strike-slip faults where transformational strain accumulates and strike-slip earthquakes occur. We use a subvertical fault as a case study. The ruptures are often confined to a vertical width of 10 or 15 km, and the length of the rupture may have several tens to several hundreds of kilometres if the earthquakes have magnitudes above M_w 7. Rupture may involve different segments of faults with varying strike and dip. Fault segmentation and fault bending is often observed for intraplate earthquakes (and at subduction zones), and may be recognized by teleseismic data that are sensitive to changes in fault direction (e.g. Shimizu *et al.* 2020). Often, the stress drop of intraplate earthquakes is in the range of 10 MPa and large compared to interplate subduction zone events. Rupture velocity is typically small if the rupture is confined to shallow crustal depth, but some cases of fast rupture velocities above the typical crustal *S*-wave velocity (super-shear velocity) have been reported for strike-slip earthquakes with large extension. We first discuss the rupture of a shallow, medium-size strike-slip earthquake with vertical varying v_r and lateral varying $\Delta\sigma$, and then illustrate the effect of long ruptures which break parts of the upper mantle. The first case is in the style of the M_w 7.1 2016 Kumamoto, Japan, earthquake with a dip of the fault plane of 66°; the second in the style of the M_w 7.5 2018 Palu, Indonesia, event. A final example demonstrates the possibility to simulate small-scale stress and velocity heterogeneities, the so-called asperities and barriers.

The 2016 April 15 M_w 7.1 Kumamoto, Japan, earthquake ruptured a 40–55 km long and about 15–25 km wide section of the NNE trending Hinagu and NE trending Futagawa intracrustal fault zone. The study of InSAR and near fault strong motion recordings showed that the earthquake activated at least three fault segments with slightly different strike and dip angles (e.g. Asano & Iwata 2016; Kato *et al.* 2016; Kubo *et al.* 2016; Ozawa *et al.* 2016; Yarai *et al.* 2016; Moore *et al.* 2017). The slip was partitioned between these segments, with a maximum slip of 4–5 m and surface ruptures up to 2 m in the central segment (e.g. Kubo *et al.* 2016). The average stress drop of 4.5 MPa (Oth *et al.* 2017) accordingly varied with largest values up to 9 MPa at shallow depths on the central segment (Yarai *et al.* 2016) and about 1 MPa at the other segments and in the lower crust (Moore *et al.* 2017). The inferred rupture velocity is with 2.4 km s^{-1} relatively small (Asano & Iwata 2016; Yarai *et al.* 2016). Other parameters of the modelling geometry of the Kumamoto earthquake are provided in Table 2.

We use the CRUST2.0 shear wave velocity model at Kumamoto to define v_r with a factor of 0.6 v_S (Fig. 7). The seismogenic zone is defined from 0 to 18 km depth. Below the seismogenic zone, the stress drop is set to $\Delta\sigma = 0$. However, the fault model is reaching a depth of 22.8 km to investigate the slip in the underlying zone of zero stress. A free surface boundary condition has been assumed. We define three segments in the seismogenic zone from −25 to −10 km, −10 to 0 km and 0 to 25 km length, respectively, with a stress drop of $\Delta\sigma = 7.5$ MPa in the central segment and 2 MPa in the northern and southern segments (Fig. 7). The stress drop variations are quite strong, and are regarded as demonstration. They can be caused be different orientation of and/or different frictional strength on the fault segments. The nucleation point is selected at the southern upper end of the rupture plane to simulate uni-lateral rupture mode as observed for the Kumamoto earthquake. The fault segments differ in strike. We approximate these strike changes by using slightly different rakes on the centre and on both marginal segments (Table 2). Thereby the effect of a changed segment orientation in the background stress field can be assessed.

Fig. 7 shows the used velocity and stress model together with rupture front isochrones. The rupture fronts are curved in the upper crust and lag behind an almost planar rupture front propagating in the lower crust. The effect is similar to what is known from diving and refracted waves in wave-propagation problems. For the Kumamoto earthquake, the refracted rupture front is in its initial phase and does not reach the surface. However, as we

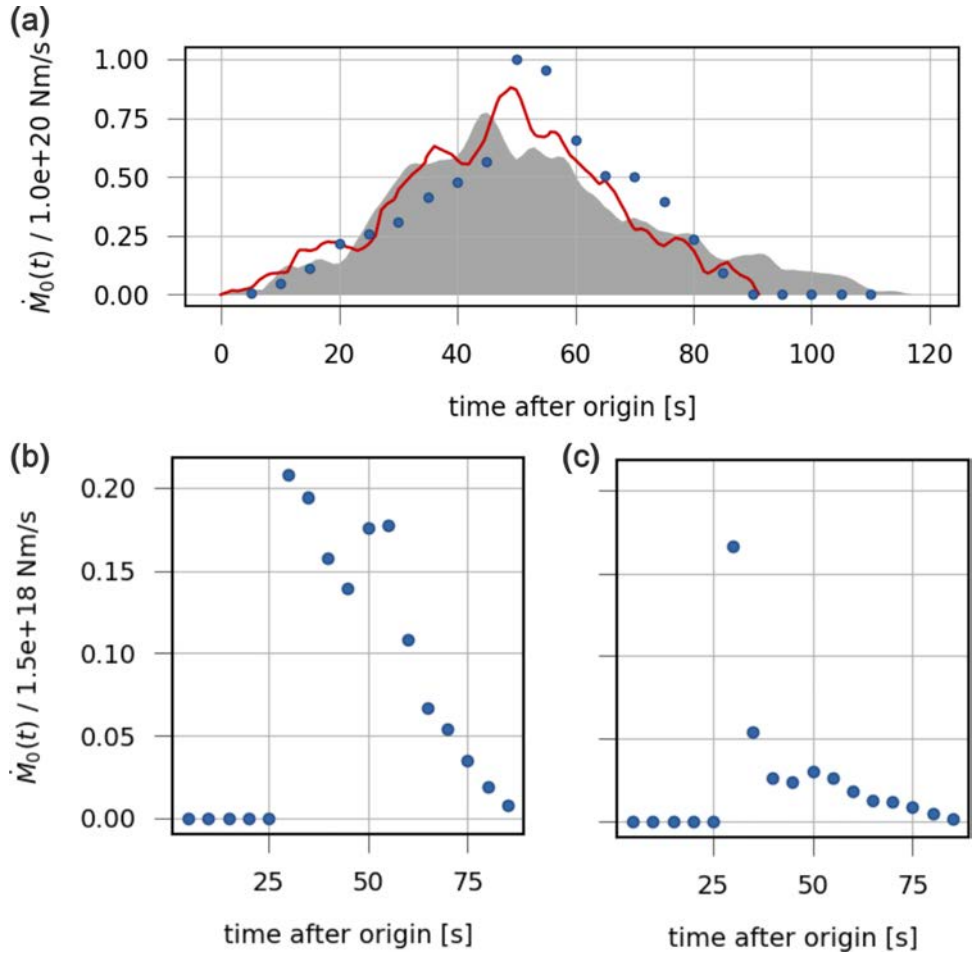

Figure 6. (a) Modelled source time function (STF) for the 2015 Illapel earthquake from Tilmann *et al.* (2016) (shaded area), from Okuwaki *et al.* (2016) (red curve) and based on our quasi-static rupture model (blue dots). The plot is normalized to the maximum modelled moment rate. (b and c) Normalized moment rate functions (MRF) for two selected boundary elements at the centroid point (b) and a boundary element at the lower edge of the rupture (c) with similar rupture arrival time (red square in Fig. 5b).

discuss later, for rupture planes of longer length the apparent horizontal rupture velocity measured at the surface may reach values close to lower crust and upper mantle shear wave velocities and can explain the observation of apparent super-shear rupture velocities.

Snapshots of the individual moment-rates of each boundary element are plotted in Fig. 8 for three times at 5, 10 and 15 s. The slip-rate (not plotted) is linearly linked with the moment rate and thus shows the same behaviour. The peak of the rate functions delineate more or less the position of the rupture front. In the first 2.5 s the rupture propagates in all directions and slip and slip rate continuously increases with spreading rupture front (crack-like growth). After the rupture has broken the full vertical width of the brittle zone at the location of the nucleation point, a transition from crack-like to pulse-like bi- and uni-lateral propagation mode is observed. The transition begins about 5 s after rupture nucleation. The shape and peak value of the moment-rate pulse do not change during the unilateral growth, with the exception when entering and leaving the central segment of high stress drop. Because of the difference in stress drop in the forward- and backward-looking segment of the rupture plane, the self-similar shearing of the fracture is distorted and the slip-rate (or moment-rate) experiences an apparent reflection, as the fault moves at positions behind the rupture front that were previously already at rest (Fig. 8). This apparent back propagation becomes more visible when we plot the colour meshed slip rate as a function of distance and time along a strike-parallel profile at medium fracture depth (Fig. 9). At a distance of $x < 25$ km, after the fracture front has entered the high stress drop region, the slip rate increases at the fracture front but also behind along the already fractured segment at $x > 25$ km where the slip pulse had already healed. The backward spreading slip rate front seems to have the same speed as v_r (Fig. 9) but a much smoother onset. The apparent backpropagation is interesting as it develops without imposing any dynamic friction. Other models have tried to explain a re-rupturing by frictional re-triggering.

Interesting is also to look to patches close to the surface and in the lower crust where we prescribed $\Delta\sigma = 0$. The interaction of the crack with the free surface leads to an increase of the slip-rate and moment-rate close to the surface. As a result, also the final slip grows asymmetrically with respect to the depth coordinate. This effect is well known from physical crack models and covered by the BEM modelling. Maybe more unexpected, Fig. 8 also shows that some slip occurs in the lower crust below the brittle zone. This tapering of crack growth into the weak zones of rock that do not carry shear

Table 2. Pre-defined parameters for the M_w 7.1 2016 Kumamoto earthquake. The coordinates of the anchor of the fault with normal vector **n** are defined at the surface in its midpoint. l and w give length along x and width along y of the plane; z refers to true depth. If more than one stress model is defined, the values overwrite the stress from the upper line. The CRUST2.0 model refers to the nomenclature given in Bassin *et al.* (2000). Earthquake parameters were defined with reference to USGS (https://earthquake.usgs.gov/earthquakes/eventpage/us20005iis), Kubo *et al.* (2016), Yarai *et al.* (2016), Asano & Iwata (2016), Yano & Matsubara (2016), Yarai *et al.* (2016), Moore *et al.* (2017), Oth *et al.* (2017), AIST (2012), Ozawa *et al.* (2016), Yagi *et al.* (2016), Kato *et al.* (2016) and Lin *et al.* (2016).

Fault geometry and orientation		
lat/lon/strike/dip	length/width	**n** [*ned*]
32.8° / 130.85° / 224° / 66°	50 km / 25 km	[0.63, −0.66, −0.41]
Nucleation		**Initial centroid**
lat/lon/z/x/y	M_0	lat/lon/z/x/y
32.75° / 130.75° / 6.4 km / 10.5 km / 7.1 km	4.5×10^{19} Nm	32.85° / 130.88° / 4.4 km /−5.5 km / 4.9 km
Stress model		
$\|[t_x, t_y, t_z]\| = \|\mathbf{t}\|$	range	rake [*ned*]
$\|[-1.76, -0.94, 0]\| = 2$ MPa $\|[-6.6, -3.53, 0]\| = 7.5$ MPa	0 km $< z \leq$ 18 km −10 km $\leq x \leq$ 0 km	180°, [0.72, 0.69, 0.0] −152°, [0.77, 0.48, 0.43]
Velocity model		**Boundary elements**
CRUST2.0 ID	γ	n_x/n_y
J1	0.6	50 / 30

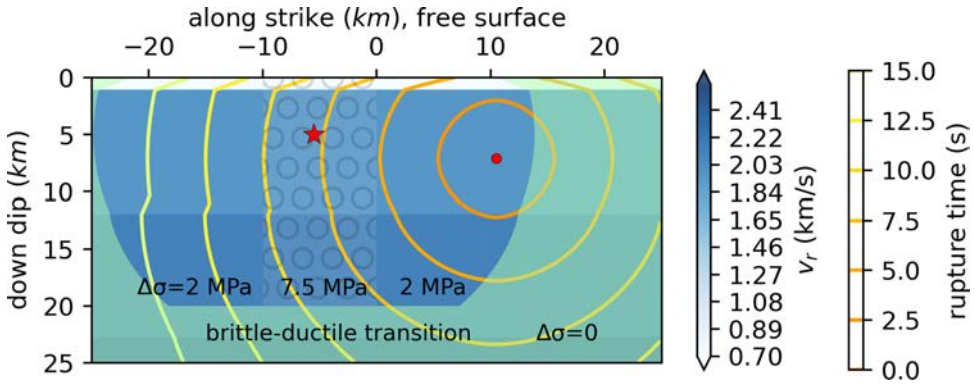

Figure 7. Geometry and model to simulate the rupture of the M_w 7.1 2016 Kumamoto, Japan, earthquake. A rupture plane of 50 × 25 km is used. The rupture velocity (blue grid), overlayed by regions of zero stress (green), is retrieved from the layer shear wave velocity model of CRUST2.0 and a factor of $\gamma = 0.6$. Rupture front isochrones are plotted for rupture nucleation point (red circle) at the southern upper end of the plane. For the stress model $\Delta\sigma = 2$ MPa is defined in down dip direction between 0 and 19.7 km . In a northern central segment of the plane of 10 km length a high stress asperity of $\Delta\sigma = 7.5$ MPa with slightly different orientation of the maximal shear (Table 2) is assumed (whitened region with circle patter). Along strike, $\Delta\sigma = 0$ (green boundary) constrains the area of non-zero slip simulation. It has been defined by simulating a rupture spreading from the centroid point (red star) until M_0 equals the moment of the point source moment tensor inversion.

stress is partly observed in nature. It is explained in our model by the self-stress created by the shearing of the planes of the fracture (e.g. Dahm 2000).

The parameters in the modelling (Table 2) were selected following the 2016 Kumamoto earthquake. We therefore compare the final slip distribution and the total duration of the rupture modelling directly with results by Kubo *et al.* (2016). The final slip distribution shows the largest slip in the shallow part of the central fault segment (Fig. 10), similar to observations. Our model slightly overestimates the near surface slip, in comparison to values given in Kubo *et al.* (2016). This indicates that the shear stress at the fault has been smaller in the uppermost layers close to the surface, a possibility we did not account for in our model. A slight change in slip direction is modelled by varying the direction of prescribed stress drop in the central segment compared to outer segments (Table 2).

We determine the rupture velocity from the linear scaling as $v_r = 0.6v_s$, which leads to velocities between 2.1 and 2.2 km s^{-1}. That is, 0.2–0.3 km s^{-1} smaller than proposed by Yarai *et al.* (2016) and Asano & Iwata (2016). Therefore, our overall duration of the rupture is with ∼ 18 s slightly larger than the one found by Kubo *et al.* (2016).

The M_w 7.5 2018 Palu (Indonesia) earthquake is a left-lateral strike-slip event that ruptured a 150–250 km long and about 30 km wide segment of the vertical Palu-Koro fault with a modelled maximum slip of 5–8 m (e.g. Fang *et al.* 2019; Song *et al.* 2019; Ulrich *et al.* 2019; Yolsal-Çevikbilen & Taymaz 2019; Okuwaki *et al.* 2020). A fast rupture front propagation of 4 to possibly more than 5 km s^{-1} was suggested by waveform modelling and back-projection of teleseismic waveforms (Bao *et al.* 2019; Fang *et al.* 2019; Socquet *et al.* 2019; Ulrich *et al.* 2019; Yolsal-Çevikbilen &

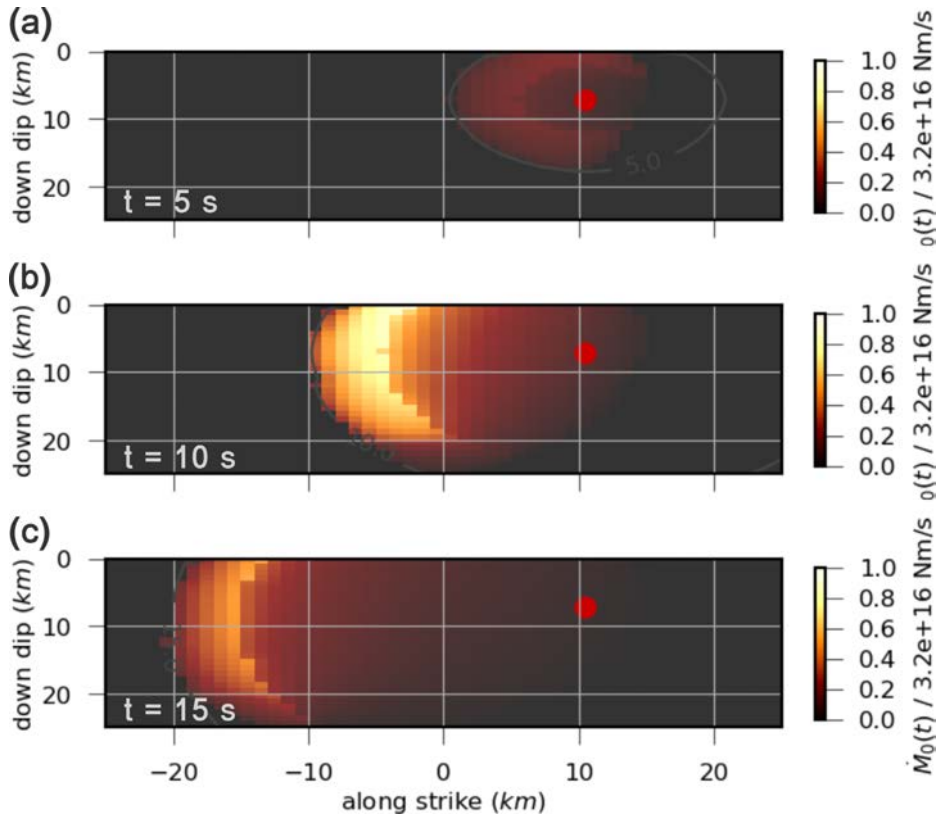

Figure 8. Snapshots of moment rate distributions for three different times: (a) $t = 5$ s, (b) $t = 10$ s and (c) $t = 15$ s. The red circle indicates the nucleation point. (a) Circular to bilateral rupture growth with major moment release close to the rupture front, with moderate moment rates. (b) Highest moment rates, as the rupture reached the high stress drop segment (compare Table 2). (c) Final stage of rupturing with lower moment rates, as the rupture front has left the high stress drop segment. The zero-stress drop in the lower crust below 18 km leads to significantly reduced moment rates in this segment.

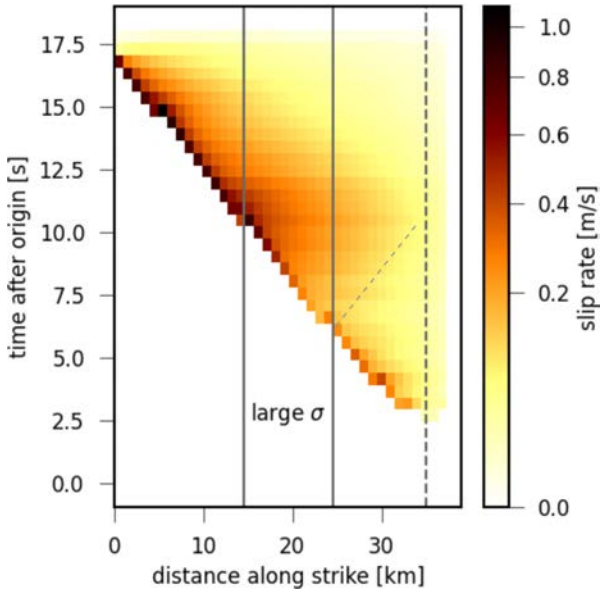

Figure 9. Colour meshed spatiotemporal evolution of the slip rate for the 2016 Kumamoto earthquake model along a profile in 10.3 km depth along strike from SW to NE. The dashed vertical line indicates the position of the focal point. The segment with high stress drop between 15 and 25 km is indicated by solid lines. The thin dashed line indicates the slowness of a back-propagating pulse reflected at the high stress segment.

Taymaz 2019; Okuwaki *et al.* 2020). We adapted the fault model to the geometry of the Palu earthquake (Table 3) to simulate an apparent super-shear rupture by using a conventional scaling factor of $v_r/v_s < 1.0$. Shear stress has been prescribed over the uppermost 20 km of the crust (following Ulrich *et al.* 2019) with a zero stress layer beneath representing the ductile part of lower crust. The location and depth of the nucleation point was subsequently varied in our modelling. Snapshots of slip rate and the final slip distribution are shown in the Supporting Information (Figs S2 and S3). We assume an enlarged rupture width of 45 km to test if rupture front refractions from the upper mantle could lead to apparent super-shear arrivals at the surface.

In Fig. 11, we compare rupture front arrival times at the boundary elements at the surface with the radiation times of high-frequency energy on the fault inferred from the backprojection of teleseismic waveforms by Bao *et al.* (2019). Similar to Bao *et al.* (2019) we assume that the location and timing of imaged radiators represent the arrival of the rupture front. The measured radiator times have a large scatter and can on average be explained using $\gamma = v_r/v_s = 0.95$, independent of the selected depth of the nucleation point between 19 and 28 *km*. The modelled arrivals times are plotted in a time-reduced scale so that sub-shear propagation ($v_r < 3.9\,\mathrm{km\,s^{-1}}$, representing the velocity between 21 and 32 km depth) is indicated by a positive slope while super-shear propagation by a negative slope. In the first 60 km the slope is negative independent of nucleation depths, while it turns into a positive slope (sub-shear arrivals) between 60 and 100 km distance. At a distance larger than 100 km from the nucleation point a shallow nucleation at a depth of 19 km continues

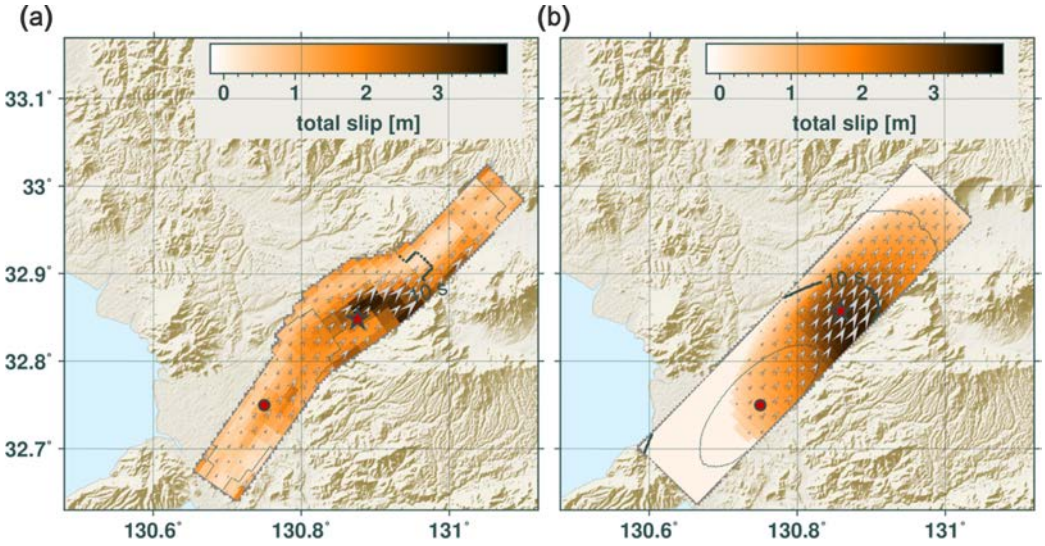

Figure 10. Static slip results from Kubo *et al.* (2016) using (a) a curved finite fault model and (b) our modelled slip distribution for the 2016 Kumamoto earthquake assuming a heterogeneous stress drop field. The slip is colour-coded and contour lines indicate the rupture front arrival in *s* after origin time. Arrows show the direction of slip. The nucleation point and centroid locations used in the respective studies are indicated by red circles and stars respectively. The overall slip distribution is similar, but we overestimate both the extension and absolute slip of the main asperity compared to Kubo *et al.* (2016).

Table 3. Pre-defined parameters for the M_w 7.5 2018 Palu earthquake. The coordinates of the anchor of the fault with normal vector **n** are defined at the surface in its midpoint. *l* and *w* give length along *x* and width along *y* of the plane; *z* refers to true depth. The CRUST1.0 model refers to the nomenclature given in Laske *et al.* (2013). Earthquake parameters were defined with reference to USGS (https://earthquake.usgs.gov/earthquakes/eventpage/us1000h3p4), GMCT, Fang *et al.* (2019), Bao *et al.* (2019), Yolsal-Çevikbilen & Taymaz (2019), Laske *et al.* (2013), Okuwaki *et al.* (2020), Ulrich *et al.* (2019) and Song *et al.* (2019).

Fault geometry and orientation		
lat/lon/strike/dip	length/width	**n** [*ned*]
-0.66° / 119.84° / 348° / 57°	150 km / 45 km	[0.17, 0.82, −0.54]
Nucleation 1		**Nucleation 2**
lat/lon/*z*/*x*/*y*		lat/lon/*z*/*x*/*y*
0.01° / 119.81° / 19 km / 73.5 km / 22.5 km		0.02° / 119.86° / 28 km / 73.5 km / 33.75 km
Stress model (normalized)		
$\|[t_x, t_y, t_z]\| = \|\mathbf{t}\|$	range	rake [*ned*]
$\|[0.97 - 0.26, 0.0]\| = 1$ MPa $\|[0.0, 0.0, 0.0]\| = 0$ MPa	0 km $\leq z \leq$ 20 km 20 km $< z$	−15°, [0.97, −0.06, 0.22] −15°, [0.97, −0.06, 0.22]
Velocity model		**Boundary elements**
CRUST1.0 tile lat/lon	γ	n_x/n_y boundary elements
-0.5°, 120°	0.95	50 / 5

the horizontal propagation with subshear velocities, while the deep nucleation at 28 km turns again into a negative slope indicating an apparent super-shear lateral propagation. We obtain a horizontal velocity of up to 4.3 km s^{-1} due to the arrival of the refracted rupture front from upper mantle depth. Backpropagation methods as the one used by Bao *et al.* (2019) have almost no vertical resolution and may falsely interpret the fast lateral propagation as super-shear, while is actually caused by the involvement of deep fault segments in rupturing.

The fast rupture of the 2018 Palu earthquake from north to south was independently deduced from the observation of Rayleigh wave Mach cones under azimuths of 134° and 220° (Bao *et al.* 2019, their Fig. 3). It is therefore interesting to simulate and illustrate the directivity of the apparent STF and of the radiated Rayleigh waves with our rupture model, which are produced without imposing any constraints on the rise time or friction. To calculate direction dependent STF we sum the moment rate function at each boundary element in the lower crust with a systematic delay of $(\mathbf{x_i} - \mathbf{x_0})\gamma/v_S$ where $\mathbf{x_i}$ and $\mathbf{x_0}$ are the coordinate vectors of the boundary element with index *i* and at the centroid location, respectively. γ is the direction cosine (unit vector) pointing from the centroid to the (far-field) station. We use $\gamma = [\pm 1, 0, 0]$, so that the shape of the full-space *S* wave pulse radiated in or against the direction of rupture is simulated, respectively. The apparent STFs for the two selected directions in Fig. 12(a) show a clear directivity pattern. The station in direction of the rupture have a short pulse, high amplitudes and a relatively short low amplitude tail. The station in opposite direction behind the propagating fracture front shows a long

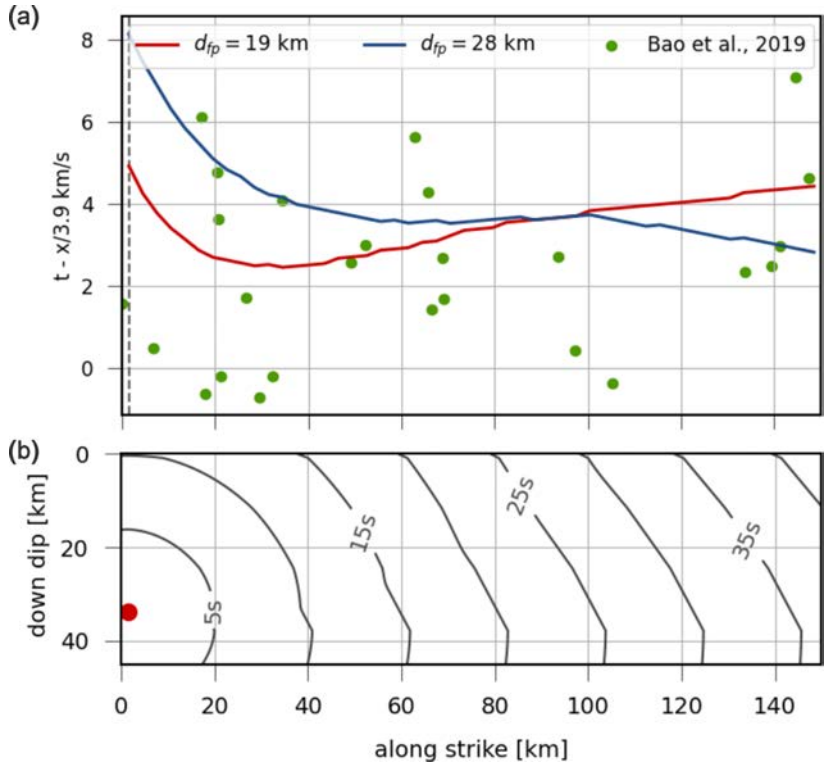

Figure 11. Illustration of the character of rupture fronts and horizontal (apparent lateral) rupture velocities as a function of the depth of the nucleation point (d_{fp}). The geometry is adapted to the 2018 Palu earthquake, where the given x coordinates along strike are measured from the rupture plane anchor point at the northern rupture tip towards south. (a) Observed (green circles, from Bao *et al.* 2019) and modelled rupture front arrivals (lines) at the surface boundary elements for a nucleation depth of 19 km (red) and 28 km (blue). Time axis has been reduced using a reduction velocity of 3.9 km s^{-1} (equivalent to rupture front velocity between 21 and 32 km depth). (b) Example of rupture front isochrones on the rupture plane for a nucleation depth of 28 km.

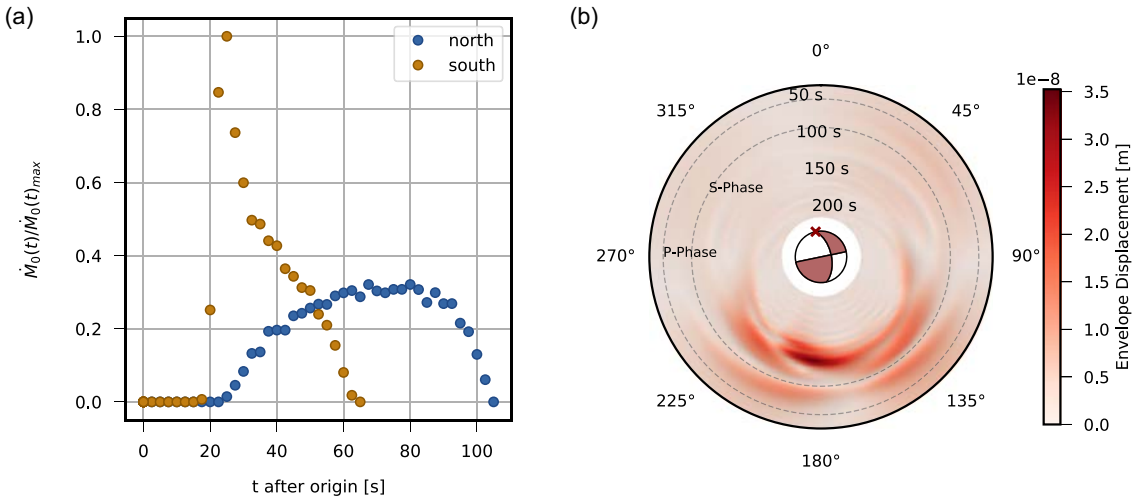

Figure 12. (a) Normalized, apparent source time function (STF) simulated in direction of the rupture front propagation (towards south, orange) and towards north (blue dots). A shorter pulse with higher amplitudes is observed for stations parallel to the fault in line with the rupture front propagation. Stations located away from the rupture front propagation show a broader (STF) with smaller amplitudes. (b) Simulated wavefield amplitudes at 400 km distance from the centroid as a function of azimuth (envelope displacement, lowpass filtered at 0.05 Hz, CRUST2.0 Green's functions, R component). Theoretical P and S arrival times are indicated by dashed lines. The red cross within the source mechanism (lower hemispherical projection) indicates the position of the nucleation point relative to the centroid at the centre of the focal solution. The strike of the rupture plane can be identified by the 350° striking time axis labels. The time increases from the outer border of the circle to the centre so that P waves are seen at a larger radius than S waves.

pulse and small amplitudes. The area under both pulses is equal. The directivity effects of the apparent STF resemble theoretical expectations.

Fig. 12(b) shows the simulation of the apparent Rayleigh wave 'Mach cones' using our subshear rupture model of the 2018 Palu earthquake. The CRUST.2 waveform Green's functions have been used together with *Pyrocko* (Heimann *et al.* 2017, 2019) to simulate synthetic displacement seismograms at a regional distance of 400 km and various azimuths. The envelopes of lowpass filtered seismograms on the radial component (R) are plotted. The simulation shows strongly enhanced *P* and Rayleigh wave amplitudes under azimuths of 135° and ∼220°, but not in opposite direction. This directivity pattern cannot be explained by the radiation pattern alone.

3.3 Rupture heterogeneity

Despite the minimalistic parametrization of the fracture, the above examples show the feasibility and flexibility of the approach to consider very different settings and earthquake scenarios. So far, we assumed a smooth, almost uniform stress drop and rupture propagation, which is well suited for the simulation of waveform effects at regional or teleseismic distances. However, the high-frequency content of near-field ground motion data often indicates that earthquake ruptures can be heterogeneous. An example for the 2015 Illapel earthquake is provided in Ruiz *et al.* (2016). Okuwaki *et al.* (2016) and Meng *et al.* (2018) used backprojection of high-frequency teleseismic body waves and showed that despite the simplicity of the low-frequency radiation, the high-frequency component of the Illapel's earthquake slip rate must have been very complex. We present two examples of how heterogeneities can be considered in our model with only a few parameters. First, for illustration, we simulate single, isolated asperities and barriers in circular form and how they can perturb planar rupture fronts and moment-rates. Asperities and barriers are described as areas on the rupture plane where stress or strength is enhanced or in general perturbed. Kerkhof (1969) studied the impact of isolated capillaries and circular, stiff inclusions on the dynamic propagation of a planar rupture front in glass. He employed a technique of ultrasonic modulation of the instantaneous, rupture front orientation at equidistant time steps, which is reflected in the resulting crack morphology (fractography). In these experiments a capillary was a circular area on the future rupture plane that was already broken, so that the stress (and the stress drop) was zero there itself. At and in front of the tip of the capillary, however, there were high stress singularities. The stiff inclusion, in contrary, created a stress singularity along its tip with opposite polarity, but with lower intensity. In Fig. 13, we plot the isochrones of the rupture fronts obtained in the laboratory experiments of Kerkhof (1969). All spatial and temporal perturbations are normalized to the diameter of the circular perturbation ($2r_0$) and the characteristic time needed to traverse the circular region. The velocity far before reaching the capillary is $\sim 150\,\mathrm{m\,s^{-1}}$. It is accelerated when approaching the capillary but retarded in the region behind the capillary until the rupture front is completely healed (Fig. 13a). Within the capillary no rupture could be tracked, as the patch is already broken. We interpret the sudden occurrence of dense 'isolines' in Fig. 13(a) after half of the capillary has been ruptured a result of frequency doubling from the nonlinear interaction of the capillary with the rupture front. The lab experiments have similarities to the 2015 Illapel earthquake, where a splitting of the high-frequency rupture front into two subfronts running along the rim of an almost circular patch, including some spots of enhanced high-frequency radiation, and their coalescence behind the 'asperity' was found (Meng *et al.* 2018). The effect of the stiff inclusion on rupture velocity shows the opposite pattern—the rupture front is strongly retarded just before reaching the circular, stiff barrier (high strength) but accelerated at both sides of the inclusion when passing the obstacle to generate a healed, undisturbed rupture front behind the heterogeneity (Fig. 13b). The 'roughness' of rupture front is overall smaller for the inclusion, because the rupture propagates within the barrier with the same of even a slightly larger velocity. The perturbation of the rupture front before entering the capillary or inclusion is clearly distinct from the well-established observation of unperturbed wave-fronts before entering structural heterogeneities. It is a clear example for the break-down of the simple linear scaling of rupture to shear wave velocity. The perturbation of v_r slightly outside the capillary or inclusion indicates that stress or stress gradient can modulate the background rupture velocity controlled by elastic modules

A stress modulation of v_r is also suggested from theoretical simulations and observations of quasi-static fracture growth in the neighbourhood of the free surface (Rivalta & Dahm 2006), or close to jumps and fringe zones in desiccation cracks (Müller & Dahm 2000), which show that the rupture front is accelerated when approaching the high stress (stress drop) region, and decelerating when leaving the high stress region or close to the high strength boundary at the fault. We use the capillary example as a model for an asperity to modulate the background rupture velocity as a function of stress around the asperity. The stress outside a penny-shaped asperity (our capillary) is described to first order by $\sigma(r > r_0) \sim \Delta\sigma\sqrt{r_0}\dfrac{1}{\sqrt{r - r_0}}$, where r_0 is the radius of the capillary and $\Delta\sigma$ is the stress drop realized on the surface of the asperity. Whether the change in stress leads to an acceleration or deceleration of rupture front depends on whether the front propagates towards or away from the high stress region. The rupture front is unperturbed if the stress gradient is perpendicular to the gradient of the rupture time (the propagation direction). The effect can be considered by the dot product between the 2-D gradient of the rupture time and stress. A linear or power-law scaling of v_r to stress can be tried to reproduce the observations in Figs 13(a) and (b). We use

$$\frac{\delta v_r}{v_r} = f\left[\hat{\nabla}|\sigma| \cdot \hat{\nabla} T\right] |\nabla\sigma|^p\,, \tag{4}$$

where f and p are determined empirically. $T(\xi_1, \xi_2)$ is the rupture time, and $\sigma(\xi_1, \xi_2)$ is the traction on the rupture plane, and $\hat{\nabla}$ is understood as unit gradient vector. The term $[\ldots]$ varies between -1 and $+1$ and accounts for the direction of the rupture front. Far from the asperity, the stress perturbation is zero, so that $\delta v_r \to 0$.

We used the expression in eq. (4) to define a perturbed rupture velocity around the circular crack asperity. f was set to 0.5, $p = 1/3$, and the maximal velocity perturbations were limited between $[0.7, 1.3]v_r$. The same model was used to simulate the inclusion, except that the polarity of the stress singularity was changed. Figs 13(c) and (d) show the simulation of rupture fronts in the same normalization as for the laboratory experiments by Kerkhof (1969). Starting conditions in the Eikonal solver were set to realize a planar rupture front propagating from left to right. The modelling exercise showed that the parameter f and p are poorly constrained in our example, but also not very critical. The largest effect is generated from setting the rupture velocity inside the asperity to zero (or a small value), so that the rupture front diffracts around the circular area and grows

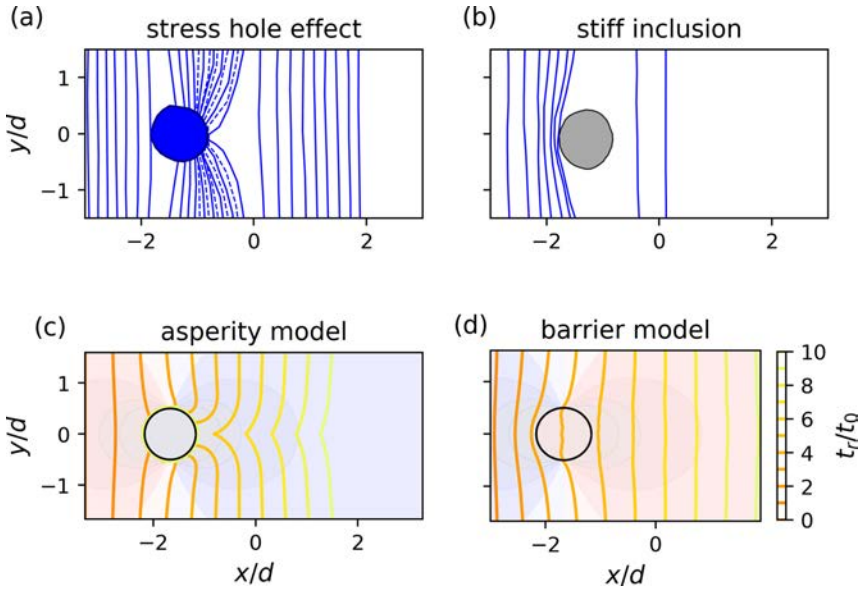

Figure 13. Observations and simulations of stress drop heterogeneities on the rupture front propagation. All features are normalized to the diameter and characteristic time of the circular heterogeneity. (a) Lab experiments in glass probe with a capillary (diameter 0.065 mm, from Kerkhof 1969) showing frozen undulations (solid lines) of the growing rupture plane at time intervals of one period of the harmonic, ultrasonic wave of 5.83 MHz. The rupture front propagated from left to right with an average velocity before reaching the capillary of 150 m s^{-1}. The dashed lines are interpreted as non-linear frequency doubling effect resulting from the interaction of the capillary with the rupture front. (b) Results from an electronmicroscop picture of rupture fronts in Opal glass (not every cycle could be measured) retarded by a spherical, stiff inclusion (CaF_2, diameter $= 3.8\ \mu m$). The harmonic ultrasonic modulation frequency was 1 MHz. The rupture propagated from left to right, the undisturbed rupture velocity is about 70 cm s^{-1} (from Kerkhof 1969). (c) Asperity case: simulated rupture front perturbation by assuming a circular, already broken region and a stress-dependent modulation of v_r according to eq. (4), indicated by coloured contours. Inside the asperity v_r was set to a small value. (d) Barrier case: modelling result using a similar velocity perturbation outside the circular region but inverted polarity. Inside the circle we used $v_r = 1.1 v_0$.

together again behind it at an acute angle. This causes roughness in slip rate, which has a stronger effect than the change of the stress drops on the asperity itself.

In Fig. 14, we compare STF and their amplitude spectra of the empirical asperity and barrier model to the spectrum of the unperturbed far-field STF. The STF of the homogeneous rupture is a smooth function in the shape of a mirrored tail fin (Fig. 14a). Its spectrum in a log–log plot resembles a typical Brune spectrum with a low-frequency plateau, corner frequency (f_c) and high-frequency attenuation with a slope of -2 (Fig. 14b). We kept the stress drop uniform in the asperity and barrier models so that the low-frequency plateau is unchanged. Because of the acceleration and deceleration of the rupture front across the obstacle, the asperity and barrier models introduce high-frequency roughness of the STF. The effect of the asperity is much larger than for the barrier Fig. 14(a) because of the stronger curvature of rupture fronts and the cusp-like merging behind the asperity. The late arrival of energy in the asperity model is associated with the slow rupture within the asperity itself. The roughness in the STF changes the amplitude spectra of the asperity and barrier in comparison to the reference spectra. Especially for the asperity model an increase in high-frequency content is seen (Fig. 14b).

The simulation of an isolated asperity or barrier is interesting for the theoretical understanding. However, more of practical interest is the complexity of slip resulting from the distributed roughness of stress drop and rupture velocity. As we show in the example below, from a technical point of view, our rupture model can easily consider such complexity. For realization of scenario earthquake near-field ground motions often stochastic slip models are assumed. In our model context, we will prescribe a stochastic variation of stress drop on the fault, implement the v_r–σ relation discussed above, and simulate slip and slip rate and if necessary the resulting seismograms at stations. Following the results of Mai & Beroza (2002), which show that slip on earthquakes often assumes a fractal distribution, we have chosen a fractal power-law approach with an exponent of -2 to define spatial perturbations of the stress drop in the range $[1, 17.8]$ MPa. Perturbations of the rupture velocity are estimated from stress drop perturbations according to (4), where in this case an exponent of $p = 1$ and a factor f was selected to map the velocity perturbations to the range between 1.1 and 3.6 km s^{-1}. Fig. 15 shows an example of the stochastic stress and velocity distribution and the amplitude spectra of simulated seismograms in direction of the rupture in a distance of 400 km and an azimuth of 33.6°. We note that the simulation of a stochastic rupture does not need additional computing power. While the stress variations alone have only a small influence on waveform complexity, the correlated effect of stress and rupture velocity clearly shows high-frequency energy above the nominal corner frequency of the source. For instance, the high-frequency ground motion often observed in near-field accelerograms (e.g. Ruiz *et al.* 2016, for Illapel) or in the backprojection of high-frequency energy in teleseismic array recordings (Okuwaki *et al.* 2016; Tilmann *et al.* 2016; Meng *et al.* 2018) may be modelled by such stochastic simulations. As the slip rate complexity is often observed at the downdip end of faults, the stress heterogeneity is possibly caused by the transition from locked to creeping fault segments.

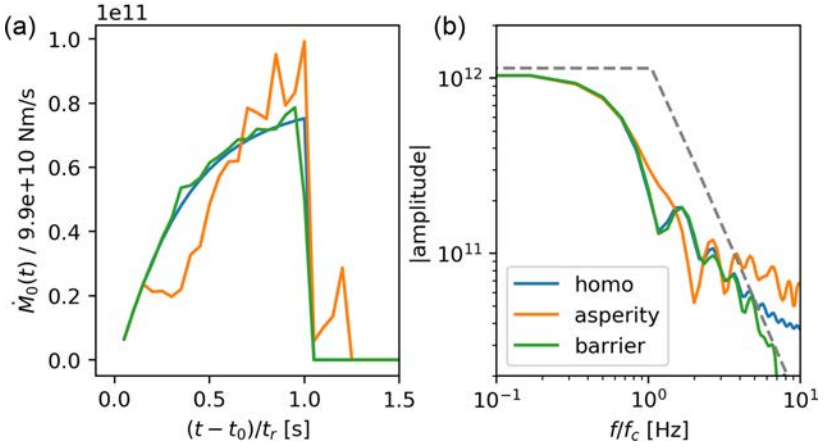

Figure 14. Full space moment rate functions (a) and the associated amplitude spectra (b) measured in the far field orthogonal to a rectangular rupture plane (20 km × 10 km). The background model (homo) had a uniform rupture velocity ($v_0 = 1\,\mathrm{km\,s^{-1}}$) and stress drop ($\Delta\sigma = 1\,\mathrm{MPa}$). Modified faults (asperity and inclusion model) consider a single, circular obstacle with a radius of 2 km. The rupture velocity has been modulated ahead of the tip of the circular region (see eq. 4), while the stress drop was kept homogeneous (see Fig. 13). For the asperity, v_r inside the asperity was set to 0.1 km s^{-1}. The time and frequency axes are normalized by the rupture duration $t_r = L/v_0 = 20\,\mathrm{s}$. The dashed line in (b) indicates the Brune spectra plateau and f^{-2} high-frequency attenuation.

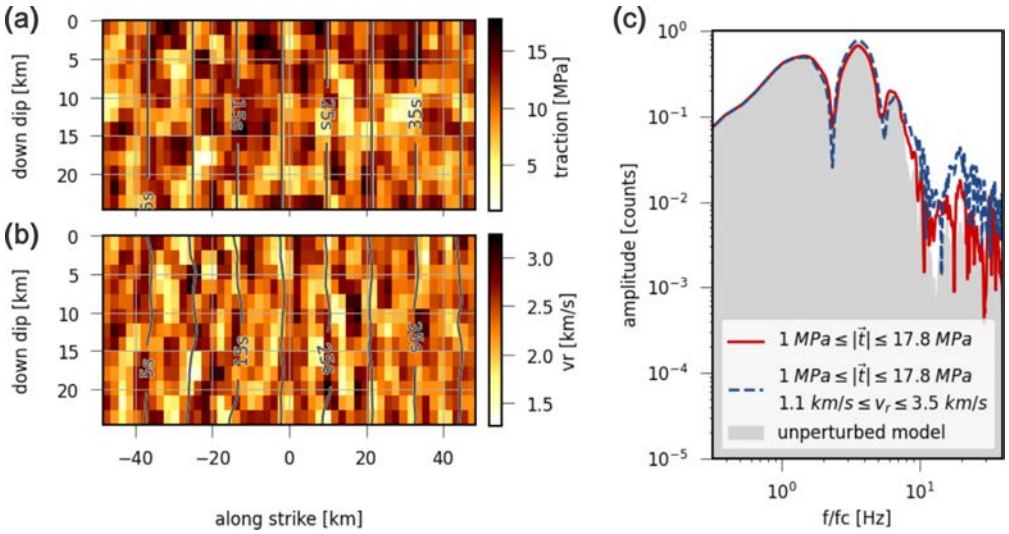

Figure 15. Simulation of stochastic rupture models of a vertical strike-slip fault, where stress drop was varied isolated (a) or strongly correlated to rupture velocity (b). For the latter, the scalar product of the traction gradient and the initial velocity vector is scaled to the given rupture velocity ranges and added onto the initial velocity field. The initial model has a homogeneous traction of 10 MPa in strike direction and a homogeneous rupture velocity field of 2.25 km s^{-1}. The range of traction and velocity variations is given in the legend. (c) Shown are the amplitude spectra of displacement records (Z component) at a station in direction of the unilatetal rupture in a distance of 400 km and an azimuth of 33.6° from the rupture top centre point. The unperturbed model spectrum is plotted as grey region. For comparison, the individual effect of a complex traction only (red line) and a complex traction correlated to rupture velocity (blue dashed line) are shown.

4 CONCLUSIONS

We implemented a self-similar fracture model for arbitrarily complex forms of the fracture front, which decouples the propagation of the fracture from the slip. The approach is computationally extremely efficient and comprises only three free parameters in addition to a point source earthquake model. At the same time it is very flexible and capable of modelling fractures and earthquake ruptures for different tectonic setting and faults in the crust and mantle. The model uses approximate relations in some parts, while exact solutions are used in other parts. For example, the propagation of the rupture front is approximated by a wave-rupture analogy, which, although not exact, is usually sufficient for the purpose of kinematic or dynamic fracture modelling. It is assumed that the rupture velocity scales to the lithospheric shear wave velocity. The instantaneous dislocation and slip on the fault is modelled exactly by means of a numerical boundary element scheme. The stress drop is given as a static input field and can be retrieved from a background stress model together with assumptions about the frictional strength at a fault with given orientation. It was found that the self-similar dynamic model explains the main low-frequency features observed during the earthquake rupture, as for example,

(1) a self-development (without external input or constraint) of circular, elliptical or rectangular ruptures with circular, bilateral or unilateral propagation at the front;
(2) a natural transition from crack-like to pulse-like rupture slip-mode in large crustal faults;

(3) the development of high slip patches close to the surface or within stress drop asperities;
(4) the penetration of slip into boundary layers of low or zero stress because of the self-stressing effect of fractures;
(5) the effect of apparent backward propagation of slip where stress drop heterogeneities exist;
(6) the development of curved and planar rupture fronts up to refracted fronts propagating with an apparent horizontal super-shear velocity;
(7) the directivity effects on waveforms including apparent Rayleigh wave Mach cones;
(8) the natural development (without controlling parameter) of a space-dependent rise time and source time function.

The method can also be used to study rupture complexity and high-frequency energy radiation if the stress field prescribed on the rupture plane is heterogeneous. We showed an example to simulate effects from isolated asperities and barriers. A second example considers a stochastic slip model where we coupled stress heterogeneity to rupture velocity perturbations. Such approaches may be interesting to study the high-frequency components of slip-rate, as e.g. observed in near-field accelerograms.

The simplified dynamic source parametrization is suited for fast numerical modelling and probabilistic inversion approaches in source seismology. For this purpose, the model has been fully integrated into an open source toolbox for seismology (*Pyrocko*, https://git.pyrocko.org/pyrocko/pyrocko) and probabilistic source inversions (*Grond*), which are directly linked to a system of static and dynamic wavefield Green's function databases. Examples of Python scripts are provided at https://pyrocko.org/docs/ under *pseudo-dynamic rupture*. The applications are therefore easy to implement and reproduce. The tools can be used for the study of earthquakes, but also for other rupture and fracture phenomena such as hydrofracking, magmatic dike intrusion or aseismic fracture growth. We would like to point out that the strengths of the simplified model lie in its simplicity and the few parameters it comprises. However, it cannot replace a complete dynamic fracture modelling, which is necessary to understand the complexity of the rupture, including the high-frequency emission of waves.

ACKNOWLEDGEMENTS

MM has been supported by the BMBF project EWRICA (03G0891A). MI thanks Dr Henriette Sudhaus and acknowledges funding by the German Research Foundation DFG through an Emmy-Noether Young-Researcher-Grant (276464525) and from the BMWi though project DEEPEN. We would like to thank two reviewers and the editor for their reviews and suggestions to improve the manuscript.

Author contributions statement: TD and SH developed the concept and theory of the self-similar rupture model. TD drafted the manuscript and initial figures and wrote a first version of the manuscript. SH coded the Eikonal solver and implemented this into the Pyrocko framework. MM, SH and MI developed a 3D BEM code and implemented this into Pyrocko GF database. MI improved the performance of the slip inversion within Pyrocko, and prepared man pages and cookbook examples. MM run basic validation and verification tests, run the final simulations and generated most of the figures. All authors contributed to writing.

REFERENCES

AIST, 2012. Active Fault Database of Japan, Research information database db095, National Institute of Advanced Industrial Science and Technology.

Aki, K., 1966. Generation and propagation of *G* waves from the Niigata earthquake of June 1964, *Bull. Earthq. Res. Inst., Univ. Tokyo,* **44,** 23–88.

Asano, K. & Iwata, T., 2016. Source rupture processes of the foreshock and mainshock in the 2016 Kumamoto earthquake sequence estimated from the kinematic waveform inversion of strong motion data, *Earth Planets Space,* **68**(147), doi:10.1186/s40623-016-0519-9.

Bao, H., Ampuero, J.P., Meng, L., Fielding, E.J., Liang, C., Milliner, C.W., Feng, T. & Huang, H., 2019. Early and persistent supershear rupture of the 2018 magnitude 7.5 Palu earthquake, *Nat. Geosci.,* **12**(3), 200–205.

Bassin, C., Laske, G. & Masters, G., 2000. The current limits of resolution for surface wave tomography in North America, *EOS, Trans. Am. geophys. Un.,* **81**(48), F897.

Beresnev, I., 2003. Uncertainties in finite-fault slip inversions: to what extend to believe? (a critical review), *Bull. seism. Soc. Am.,* **93,** 2445–2458.

Brune, J., 1970. Tectonic stress and the spectra of seismic shear waves from earthquakes, *J. geophys. Res.,* **75,** 4997–5007.

Brune, J., 1971. Correction to: "Tectonic stress and the spectra of seismic shear waves from earthquakes", *J. geophys. Res.,* **76,** 5002.

Buijze, L., Van den Bogert, P.A.J., Wassing, B.B.T. & Orlic, B., 2019. Nucleation and arrest of dynamic rupture induced by reservoir depletion, *J. geophys. Res.,* **124,** 3620–3645,

Cesca, S., Dahm, T., Juretzek, K. & Kühn, D., 2011a. Rupture process of the 7 May 2011, M_w 4.2, Ekofisk induced earthquake, *Geophys. J. Int.,* doi:10.1111/j.1365–246X.2011.05151.x.

Cesca, S., Grigoli, F., Heimann, S., Dahm, T., Kriegerowski, M., Sobiesiak, M., Tassara, C. & Olcay, M., 2016. The M_w 8.1 2014 Iquique, Chile, seismic sequence: a tale of foreshocks and aftershocks, *Geophys. J. Int.,* **204**(3), 1766–1780.

Cesca, S., Heimann, S. & Dahm, T., 2011b. Rapid directivity detection by azimuthal amplitude spectra inversion, *J. Seismol.,* **15,** 147–164.

Contreras-Reyes, E., Maksymowicz, A., Lange, D., Grevemeyer, I., Muñoz-Linford, P. & Moscoso, E., 2017. On the relationship between structure, morphology and large coseismic slip: a case study of the M_w 8.8 Maule, Chile 2010 earthquake, *Earth planet. Sci. Lett.,* **478,** 27–39.

Dahm, T., 2000. Numerical simulations of the propagation path and the arrest of fluid-filled fractures in the earth, *Geophys. J. Int.,* **141,** 623–638.

Dahm, T., Cesca, S., Hainzl, S., Braun, T. & Krger, F., 2015. Discrimination between induced, triggered, and natural earthquakes close to hydrocarbon reservoirs: a probabilistic approach based on the modeling of depletion-induced stress changes and seismological source parameters, *J. geophys. Res.,* **120**(2), 2491–2509.

Dahm, T., Hainzl, S. & Fischer, T., 2010. Bidirectional and unidirectional fracture growth during hydrofracturing: role of driving stress gradients, *Geophys. J. Int.,* **115**(18pp), doi:10.1029/2009JB006817.

Dahm, T. &Krüger, 2012. Moment tensor inversion and moment tensor interpretation, in *New Manual of Seismological Observatory Practice (NMSOP-2),* pp. 1–37, ed. Bormann, P.E., Deutsches GeoForschungsZentrum GFZ.

DeGraff, J. & Aydin, A., 1987. Surface morphology of columnar joints and its significance to mechanics and direction of joint growth, *Bull. geol. Soc. Am.,* **99,** 605–6127.

Duan, B., 2010. Role of initial stress rotation in rupture dynamics and ground motion: a case study with implications for the Wenchuan earthquake, *J. geophys. Res.,* **115,** B05301, doi:10.1029/2009JB006750.

Fang, J., Xu, C., Wen, Y., Wang, S., Xu, G., Zhao, Y. & Yi, L., 2019. The 2018 M_w 7.5 Palu earthquake: a supershear rupture event constrained by InSAR and broadband regional seismograms, *Remote Sens.,* **11**(11), 1–15.

Fuentes, M., Riquelme, S., Hayes, G., Medina, M., Melgar, D., Vargas, G., González, J. & Villalobos, A., 2016. A study of the 2015 M_w8.3 Illapel earthquake and tsunami: numerical and analytical approaches, *Pure appl. Geophys.,* **173**(6), 1847–1858.

Gallis, M., Ampuero, J., Mai, P. & Cappa, F., 2017. *Sci. Adv.,* **3,** 1–10.

Haskell, N., 1964. Total energy spectral density of elastic waves radiation from propagating faults, *Bull. Seism. Soc. Am.,* **54,** 1811–1841.

Haskell, N., 1966. Total energy and energy spectral density of elastic wave radiation from propagating faults. Part II. A statistical source model, *Bull. seism. Soc. Am.,* **56,** 125–14041.

Haskell, N., 1969. Elastic displacements in the near field of a propagating fault, *Bull. seism. Soc. Am.,* **59,** 865–908.

Hayes, G.P., 2017. The finite, kinematic rupture properties of great-sized earthquakes since 1990, *Earth planet. Sci. Lett.,* **468,** 94–100.

Heidbach, O. *et al.*, 2018. The world stress map database release 2016: crustal stress pattern across scales, *Tectonophysics,* **744,** 484–498.

Heimann, S., 2010. A robust method to estimate kinematic earthquake source parameter, *PhD thesis*, Institut für Geophysik, Universität Hamburg.

Heimann, S., Vasyura-Bathke, H., Sudhaus, H., Paul Isken, M., Kriegerowski, M., Steinberg, A. & Dahm, T., 2019. A Python framework for efficient use of pre-computed Green's functions in seismological and other physical forward and inverse source problems, *Solid Earth,* (10), 1921–1935.

Heimann, S. *et al.*, 2017. Pyrocko—an open-source seismology toolbox and library, V. 0.3, GFZ Data Services, doi:10.5880/GFZ.2.1.2017.001.

Heimann, S. *et al.*, 2018. Grond - A probabilistic earthquake source inversion framework. V. 1.0. GFZ Data Services, doi:10.5880/GFZ.2.1.2018.003.

Helgeson, D. & Aydin, A., 1991. Characteristics of joint propagation across layer interfaces in sedimentary rocks, *J. Struct. Geol.,* **13,** 897–911.

Herman, M.W., Nealy, J.L., Yeck, W.L., Barnhart, W.D., Hayes, G.P., Furlong, K.P. & Benz, H.M., 2017. Integrated geophysical characteristics of the 2015 Illapel, Chile, earthquake, *J. geophys. Res.,* **122**(6), 4691–4711.

Jamelot, A., Gailler, A., Heinrich, P., Vallage, A. & Champenois, J., 2019. Tsunami simulations of the Sulawesi M_w 7.5 event: comparison of seismic sources issued from a Tsunami warning context versus post-event finite source, *Pure appl. Geophys.,* **176,** 3351–3376.

Jost, M. & Herrman, R., 1989. A students guide to and review of moment tensors, *Seismol. Res. Lett.,* **60,** 37–57.

Kanamori, H., 1994. Mechanics of Earthquakes, *Annu. Rev. Earth planet. Sci.,* **22**(1), 207–237.

Kanamori, H. & Anderson, D.L., 1975. Theoretical basis of some empirical relations in seismology, *Bull. seism. Soc. Am.,* **65**(5), 1073–1095.

Kaneko, Y., Avouac, J. & Lapusta, N., 2010. Towards inferring earthquake patterns from geodetic observations of interseismic coupling, *Nat. Geosci.,* **3,** 363–369.

Kato, A., Nakamura, K. & Hiyama, Y., 2016. The 2016 Kumamoto earthquake sequence, *Proc. Japan Acad. B,* **92**(8), 358–371.

Kennett, B.L.N., Engdahl, E.R. & Buland, R., 1995. Constraints on seismic velocities in the Earth from traveltimes, *Geophys. J. Int.,* **122**(1), 108–124.

Kerkhof, F., 1969. *Einführung in die Bruchmechanik,* Ernst-Mach-Institut der Fraunhofer Gesellschaft.

Kostrov, B., 1964. Self-similar problems of propagation of shear cracks, *J. Appl. Math. Mech.,* **28,** 1077–1087.

Kubo, H., Suzuki, W., Aoi, S. & Sekiguchi, H., 2016. Source rupture processes of the 2016 Kumamoto, Japan, earthquakes estimated from strong-motion waveforms, *Earth Planets Space,* **68**(1), 1–13.

Kulander, B. & Dean, S., 1995. Observations on fractography with laboratory experiments for geologists, in *Fracture Topography as a Tool in Fracture Mechanics and Stress Analysis,* Vol. 92, pp. 59–82, ed. Ameen, M., Geol. Soc. Spec. Publ.

Laske, G.,Masters. G., Ma, Z. & Pasyanos, M., 2013. Update on CRUST1.0—a 1-degree global model of Earth's crust, in *EGU General Assembly 2013,* Vienna, Austria, EGU2013-2658.

Lin, A., Satsukawa, T., Wang, M., Mohammadi Asl, Z., Fueta, R. & Nakajima, F., 2016. Coseismic rupturing stopped by Aso volcano during the 2016 M_w 7.1 Kumamoto earthquake, Japan, *Science,* **354**(6314), 869–874.

Lopez-Comino, J. & Cesca, S., 2016. Source Complexity of an injection induced event: the 2016 M_w 5.1 Fairview, Oklahoma earthquake, *Geophys. Res. Lett.,* **45,** 4025–4032.

Lui, S.K. & Huang, Y., 2019. Do injection-induced earthquakes rupture away from injection wells due to fluid pressure change?, *Bull. seism. Soc. Am.,* **109,** 358–371.

Madariaga, R., Olsen, K. & Archuleta, R., 1998. Modeling dynamic rupture in a 3D earthquake fault model, *Bull. seism. Soc. Am.,* **88,** 1182–1197.

Mai, M. & Beroza, G., 2002. A spatial field model to characterize complexity in earthquake slip, *J. geophys. Res.,* **107,** doi:10.1029/2001JB000588.

Mai, M. *et al.*, 2016. The earthquake source inversion validation (SIV) project, *Seismol. Res. Lett.,* **87,** 690–708.

Maksymowicz, A., Tréhu, A.M., Contreras-Reyes, E. & Ruiz, S., 2015. Density-depth model of the continental wedge at the maximum slip segment of the Maule M_w8.8 megathrust earthquake, *Earth planet. Sci. Lett.,* **409,** 265–277.

Melgar, D. *et al.*, 2016. Slip segmentation and slow rupture to the trench during the 2015, M_w8.3 Illapel, Chile earthquake, *Geophys. Res. Lett.,* **43**(3), 961–966.

Meng, L., Baoa, H., Huanga, H., Zhanga, A., Bloorea, A. & Liub, Z., 2018. Double pincer movement: encircling rupture splitting during the 2015 M_w 8.3 Illapel earthquake, *Earth planet. Sci. Lett.,* **495,** 164–173.

Menke, W., 1989. *Geophysical Data Analysis: Discrete Inverse Theory,* revised edition, Academic Press Inc.

Metois, M., Socquet, A. & Vigny, C., 2012. Interseismic coupling, segmentation and mechanical behavior of the central Chile subduction zone, *J. geophys. Res.,* 1–16, doi:10.1029/2011JB008736.

Metz, M., 2019. A quasi-dynamic and self-consistent rupture model to simulate earthquake ruptures, *Master's thesis*, University Potsdam.

Minson, S., Simons, M. & Geck, J., 2013. Bayesian inversion for finite fault earthquake source models I—theory and algorithm, *Geophys. J. Int.,* **194,** 1701–1726.

Moore, J.D.P. *et al.*, 2017. Imaging the distribution of transient viscosity after the 2016 M_w 7.1 Kumamoto earthquake, *Science,* **356**(6334), 163–167.

Müller, G. & Dahm, T., 2000. Fracture morphology of tensile cracks and rupture velocity, *J. geophys. Res.,* **105,** 723–738.

Nielsen, S. & Carlson, J., 2000. Rupture pulse characterization: self-healing, self-similar, expanding solutions in a continuum model of fault dynamics, *Bull. seism. Soc. Am.,* **90,** 1480–1497.

Nielsen, S. & Madariaga, R., 2003. On the self-healing fracture mode, *Bull. seism. Soc. Am.,* **93,** 2375–2388.

Ohnaka, M., 2013. *The Physics of Rock Failure and Earthquakes,* Cambridge Univ. Press.

Okada, Y., 1992. Internal deformation due to shear and tensile faults in a half-space, *Bull. seism. Soc. Am.,* **82,** 1018–1040.

Okuwaki, R., Hirano, S., Yagi, Y. & Shimizu, K., 2020. Inchworm-like source evolution through a geometrically complex fault fueled persistent supershear rupture during the 2018 Palu Indonesia earthquake, *Earth planet. Sci. Lett.,* **547,** doi:10.1016/j.epsl.2020.116449.

Okuwaki, R., Yagi, Y., Arangui, A., Juan Gonzalez, J. & Gonzalez, G., 2016. Rupture process during the 2015 Illapel, Chile earthquake: zigzag-along-dip rupture episodes, *Pure appl. Geophys.,* **173,** 1011–1020.

Oth, A., Miyake, H. & Bindi, D., 2017. On the relation of earthquake stress drop and ground motion variability, *J. geophys. Res.,* **122**(7), 5474–5492.

Ozawa, T., Fujita, E. & Ueda, H., 2016. Crustal deformation associated with the 2016 Kumamoto earthquake and its effect on the magma chamber of Aso volcano, in *Japan Geoscience Union Meeting,* Chiba, Japan, MIS34-P42.

Pollard, D. & Segall, P., 1987. Theoretical displacements and stresses near fractures in rock: with application to faults, joints, veins, dikes, and solution surfaces, in *Fracture Mechanics of Rocks,* pp. 277–347, ed. Atkinson, B., Academic Press INC.

Rivalta, E. & Dahm, T., 2006. Acceleration of buoyancy-driven fractures and magmatic dikes beneath the free surface, *Geophys. J. Int.,* **166,** 1424–1439.

Rowshandel, B., 2006. Incorporating source rupture characteristics into ground-motion hazard analysis models, *Seismol. Res. Lett.,* **77**(6), 708–722.

Ruiz, S. *et al.*, 2016. The seismic sequence of the 16 September 2015 M_w 8.3 Illapel, Chile, earthquake, *Seismol. Res. Lett.,* **87,** 789–799.

Rummel, F., 1987. Fracture mechanics approach to hydraulic fracturing stress measurements, in *Fracture Mechanics of Rocks,* pp. 217–239, ed. Atkinson, B., Academic Press INC.

Sato, T. & Hirasawa, T., 1973. Body wave spectra from propagating shear cracks, *J. Phys. Earth,* **21,** 415–431.

Sethian, J., 1996. A fast marching level set method for monochromatic advancing fronts, *Proc. Natl. Acad. Sci. USA,* **93,** 1591–1595.

Shimizu, K., Yagi, Y., Okuwaki, R. & Fukahata, Y., 2020. Development of an inversion method to extract information on fault geometry from teleseismic data, *Geophys. J. Int.,* **220,** 1055–1065.

Socquet, A., Hollingsworth, J., Pathier, E. & Bouchon, M., 2019. Evidence of supershear during the 2018 magnitude 7.5 Palu earthquake from space geodesy, *Nat. Geosci.,* **12,** 192–199.

Somerville, P., Smith, N., Graves, R.W. & Abrahamson, N.A., 1997. Modification of empirical strong ground motion attenuation relations to include the amplitude and duration effects of rupture directivity, *Seismol. Res. Lett.,* **68,** 199–222.

Song, X., Zhang, Y., Shan, X., Liu, Y., Gong, W. & Qu, C., 2019. Geodetic observations of the 2018 M_w 7.5 Sulawesi earthquake and its implications for the kinematics of the Palu fault, *Geophys. Res. Lett.,* **46**(8), 4212–4220.

Tago, J., Cruz-Atienza, V., Virieux, J., Etienne, V. & Sanches-Sesma, F., 2012. A 3D hp-adaptive discontinuous Galerkin method for modeling earthquake dynamics, *J. geophys. Res.,* **117,** doi:10.1029/2012JB009313.

Tilmann, F. *et al.*, 2016. The 2015 Illapel earthquake , central Chile , a type case for a characteristic earthquake? *Geophys. Res. Lett.,* **43,** 1–26.

Ulrich, T. *et al.*, 2019. Coupled, physics-based modeling reveals earthquake displacements are critical to the 2018 Palu, Sulawesi tsunami, *Pure appl. Geophys.,* **176,** 4069–4109.

Vasyura-Bathke, H., Dettmer, J., Dutta, R., Mai, P.M. & Jónsson, S., 2021. Accounting for theory errors with empirical Bayesian noise models in nonlinear centroid moment tensor estimation, doi:10.1093/gji/ggab034, 0956-540X.

Weinberger, R., 1999. Initiation and growth of cracks during dessication of stratified muddy sediments, *J. Struct. Geol.,* **21,** 3381–3396.

Wortel, M. & Cloetingh, S., 1985. Accretion and lateral variations in tectonic structure along the Peru–Chile trench, *Tectonophysics,* **112**(1), 443–462.

Yagi, Y. & Fukahata, J., 2011. Introduction of uncertainty of Greens function into waveform inversion for seismic source processes, *Geophys. J. Int.,* **186,** doi:10.1111/j.1365–246X.2011.05043.x.

Yagi, Y., Okuwaki, R., Enescu, B., Kasahara, A., Miyakawa, A. & Otsubo, M., 2016. Rupture process of the 2016 Kumamoto earthquake in relation to the thermal structure around Aso volcano, *Earth Planets Space,* **68**(118), doi:10.1186/s40623-016-0492-3.

Yano, T. & Matsubara, M., 2016. The significance of seismicity after the 2016 Kumamoto earthquake sequence, in *Japan Geoscience Union Meeting,* Chiba, Japan, MIS34-P05.

Yarai, H. *et al.*, 2016. Crustal deformation of the 2016 Kumamoto earthquake, in *Japan Geoscience Union Meeting,* Chiba, Japan, MIS34-03.

Ye, L., Lay, T., Kanamori, H. & Koper, K.D., 2016. Rapidly estimated seismic source parameters for the 16 September 2015 Illapel, Chile M_w 8.3 earthquake, *Pure appl. Geophys.,* **173**(2), 321–332.

Yolsal-Çevikbilen, S. & Taymaz, T., 2019. Source characteristics of the 28 September 2018 M_w 7.5 Palu–Sulawesi, Indonesia (SE Asia) earthquake based on inversion of teleseismic bodywaves, *Pure appl. Geophys.,* **176**(10), 4111–4126.

SUPPORTING INFORMATION

Supplementary data are available at *GJI* online.

Figure S1. Flowchart illustrating the input and output, the parametrization and the computation of the pseudo-dynamic rupture model.

Figure S2. Comparison of moment rate snapshots for the 2018 Palu earthquake assuming (a) a shallow (19 km) and (b) a deep (28 km) nucleation point depth (see Table 3).

Figure S3. Final static slip results from the inversion in Jamelot *et al.* (2019) (a) and our forward modelling results (b) for the 2018 Palu earthquake. Slip is colour-coded and contour lines indicate the rupture front arrival time (in panel b for our model). The red point indicates the nucleation point used in our model.

Please note: Oxford University Press is not responsible for the content or functionality of any supporting materials supplied by the authors. Any queries (other than missing material) should be directed to the corresponding author for the paper.

2.2 Numerical implementation of the PDR in a Python toolbox for seismology

In order to use the PDR model for source inversion, it was implemented in the existing Python toolbox *Pyrocko* (Heimann et al., 2017), and also in the Bayesian bootstrap optimization tool *Grond* (Heimann et al., 2018). This allows for easy and flexible use of the PDR in an inversion together with waveform data, or a combination of seismic waveform attributes and geodetic data as continuous GNSS or LOS InSAR. This section highlights the different aspects of the numerical implementation of the PDR in *Grond*.

Further details on the use of the PDR source model are given in the *Pyrocko* online documentation: https://pyrocko.org/docs/current/topics/pseudo-dynamic-rupture.html or https://pyrocko.org/docs/current/library/examples/index.html.

2.2.1 Forward modeling of the PDR

The *Pyrocko* Python library (Heimann et al., 2017), which is a widely used and well maintained seismological toolbox, hosts the PDR. *Pyrocko* yields, besides, e.g., utilities for plotting and seismic data handling, a module for synthetic waveform calculation from pre-calculated Green's Functions based on various seismic source definitions (Heimann et al., 2019). We adopted the PDR as a source model for *Pyrocko*, a first step towards the implementation of the PDR into the inversion tool *Grond* (Heimann et al., 2018).

Discretization of the PDR

Waveform forward modeling within *Pyrocko* (Heimann et al., 2019) requires a discretization of the PDR into individual moment tensor point sources distributed along the rupture plane. The goal is to generate synthetic waveforms, which include all kinematic and static rupture effects, e.g., the rupture propagation with the maximum precision possible. Therefore, we defined a discretization scheme for the extended rupture model that reduces aliasing effects caused by large point source spacing (adopted from Heimann, 2011):

$$\Delta x = min\left(l_{patch}, w_{patch}, \Delta x_{gf}, \Delta depth_{gf}\right) \tag{2.1}$$

$$\Delta l = \frac{l_{patch}}{\lceil l_{patch}/\Delta x \rceil + 1} \tag{2.2}$$

$$\Delta w = \frac{w_{patch}}{\lceil w_{patch}/\Delta x \rceil + 1}. \tag{2.3}$$

The maximum point source spacing Δx is defined by the minimum of the dimensions of a sub-fault patch l_{patch}, w_{patch} or the lateral (Δx_{gf}) and vertical ($\Delta depth_{gf}$) grid node spacing of the used Green's Function store. A sufficient number of point sources is used to cover all details of small rupture planes. Using the same sampling as the Green's functions store grid

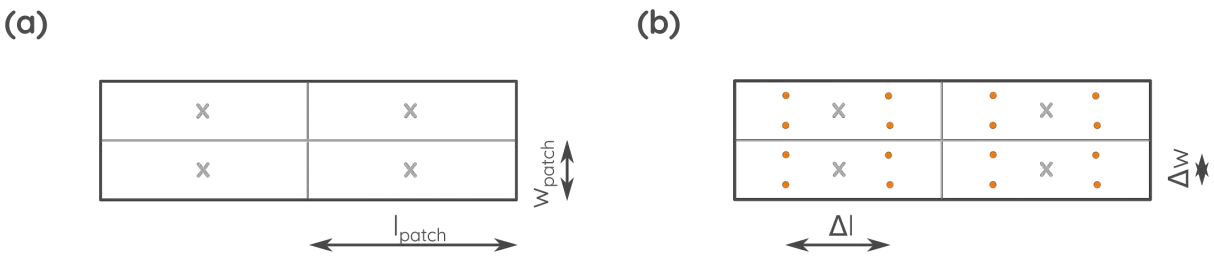

Figure 2.1: Discretization of the rupture plane and sub-faults into point sources. (a) shows the initial setup with a fault consisting of four sub-faults with the respective center marked as grey crosses. (b) indicates the retrieved regularly gridded point source locations (orange dots).

node spacing prevents from aliasing from to coarse sampling.
The calculation of the point source spacing along strike (Δl) or in down-dip direction (Δw) increases the number of point sources per sub-fault to four or more. This results in a better resolution and a reduced risk of aliasing. It also assures an even spacing of point sources along the rupture plane (Fig. 2.1).
The contribution of each point source to the moment release of a sub-fault scales inversely proportional with the number of point sources within each sub-fault (Heimann, 2011).

Definition of subsurface models used with the PDR

Within *Grond*, the PDR model requires two subsurface velocity models (elastic property models). The first one is needed to calculate synthetic seismograms. It is usually defined when selecting (or calculating) a database of pre-computed Green's functions. A description is given in Heimann et al. (2019). As a relatively new option, Green's functions for continuous GNSS and InSAR static displacements can also be considered. They also rely on the same layered velocity model as the synthetic seismic traces.

We decided to base also the subsurface model used in the BEM model to construct dislocations (instantaneous slip) to the velocity information provided in the seismic Green's function database. However, the BEM implemented in PDR today still uses a homogeneous half-space and cannot consider layered Earth models. As a compromise, we calculate average velocities depending on the position of the source.

Our implementation makes use of the analytical equations of Okada (1992) provided for an elastic and homogeneous half-space. This equations are used to calculate the linear coefficients linking stress drop and slip on the sub-faults (Chap. 2.1). Thereby, we can model effects as higher near-surface slips (Metz, 2019). The elastic constants used within Okada (1992) are extracted from a layered ground model. We decided to average them along the rupture plane in order to obtain one valid pair of Lamés parameter. Thereby, elastic constants always mimic the ground in the depth of the rupture (Fig. 2.2).
Both the rupture front and wave propagation are still controlled by the layered medium (Heimann et al., 2018; Heimann et al., 2019, and Chap. 2.1)

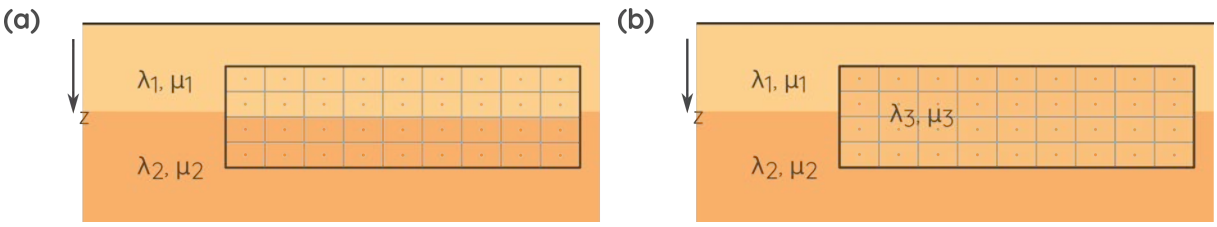

Figure 2.2: Idealized implementation of the homogeneous half-space as required by Okada (1992) for the calculation of the coefficients. Different colors indicate two layers of the original ground model, which are characterized by different elastic constants λ and μ. (a) shows the initial setup with the sub-fault elastic parameters being assigned based on the ground model and the sub-fault center depth. (b) shows the final result with constant, averaged elastic constants along the whole rupture plane.

Activation scheme of the discretized PDR

When used within an inversion, PDR modeling and especially the calculation of the coeffcients linking slip and stress drop can be computationally expensive. This effect increases with a higher number of sub-faults. Reducing the number of sub-faults and, hence, the resolution of the PDR increases the calculation speed. It also effects the activation time of the discretized point sources and thereby influences, e.g., modeled synthetic waveforms. We allow for two modes within the implemented PDR source model (Fig. 2.3)

- **rough:** All point sources within one sub-fault are jointly activated, when the rupture front passes the center of the sub-fault. This mode is in line with the developments explained within Chapter 2.1, but results in modeling a spiky moment release function, if the number of sub-faults is to low compared to the dimension of the rupture (Fig. 2.4a).
- **smooth:** Each point source within one sub-fault is activated independently, when the rupture front passes its location. Mimicing the rupture propagation in more detail compared to the rough mode yields a smoother moment release function over time (Fig. 2.4b).

It is worth to mention, that the choice of any activation scheme does not affect static parameters as the final slip distribution or the moment release of the PDR.

2.2.2 Inversion

The PDR has been implemented into *Grond*, a bootstrap based bayesian optimization tool for inversions of seismic and/or ground deformation data (Heimann et al., 2018). *Grond* estimates best and mean models and provides information on parameter uncertainties, trade offs and the quality of the inversion within a well maintained and broadly used environment. Adaptive weighting schemes allow for a simple use of seismic and/or static deformation data. This section aims to explain the settings made within the PDR inversion setup and provides more details of the multiple source inversion implementation, which is used within the Chapters 3 and 4. A schematic overview of the PDR inversion in *Grond* with its specific options is provided in Figure 2.5.

Chapter 2.1 defines PDR earthquake modeling as a multi-step process:

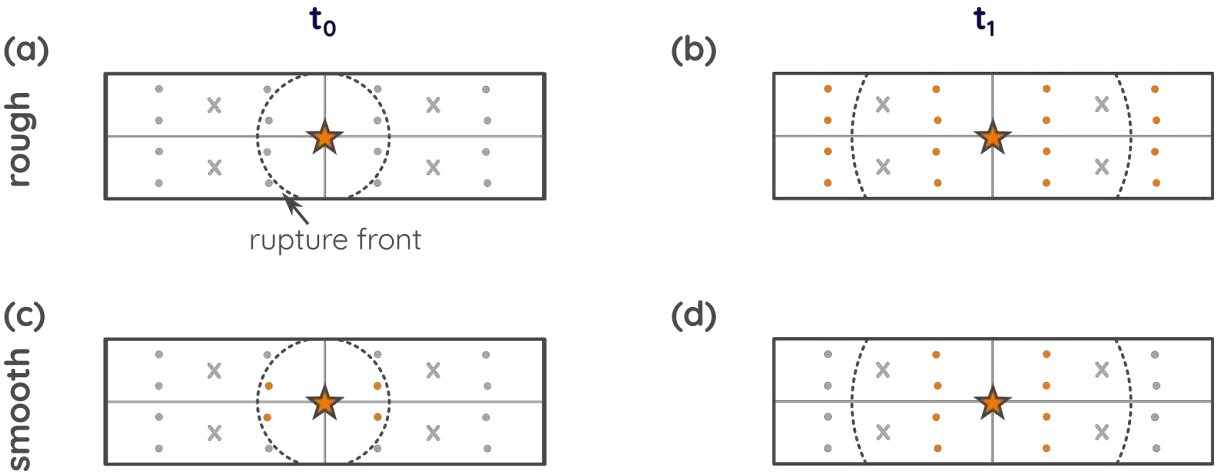

Figure 2.3: Rough (a, b), and smooth, (c, d) activation of the point sources discretizing the PDR rupture plane shown for two discrete times t_0 and t_1. The rough mode activates all point sources (orange dots) of a sub-fault at the time t_1, when the rupture front passes the sub-fault center (grey cross). Contrary, the smooth mode activates each individual point source, when the rupture front passes its location.

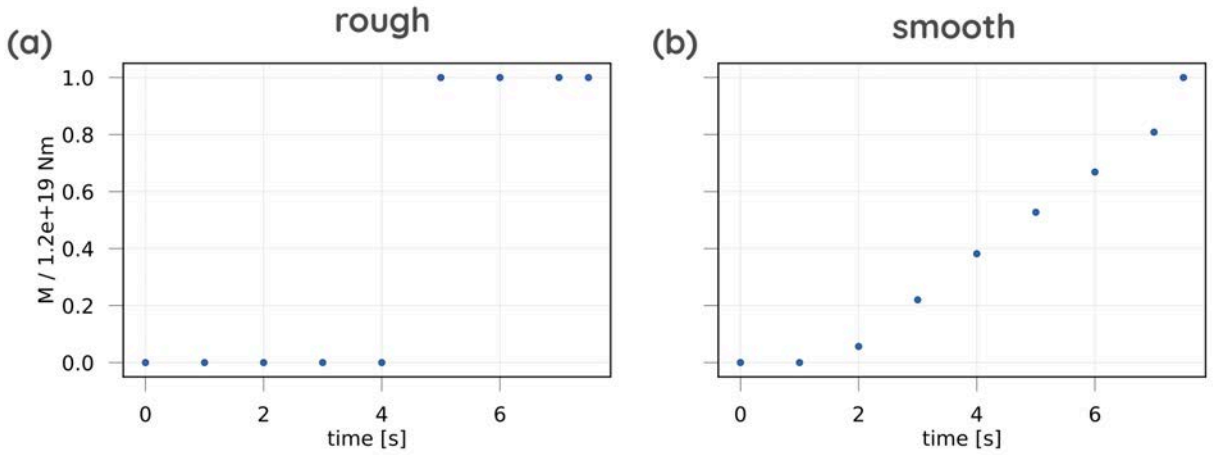

Figure 2.4: Moment release function of a simple one-sub-fault PDR with a rough (a), and smooth (b) activation of the point sources discretizing the PDR rupture plane. The cumulative final moment is the same for both cases.

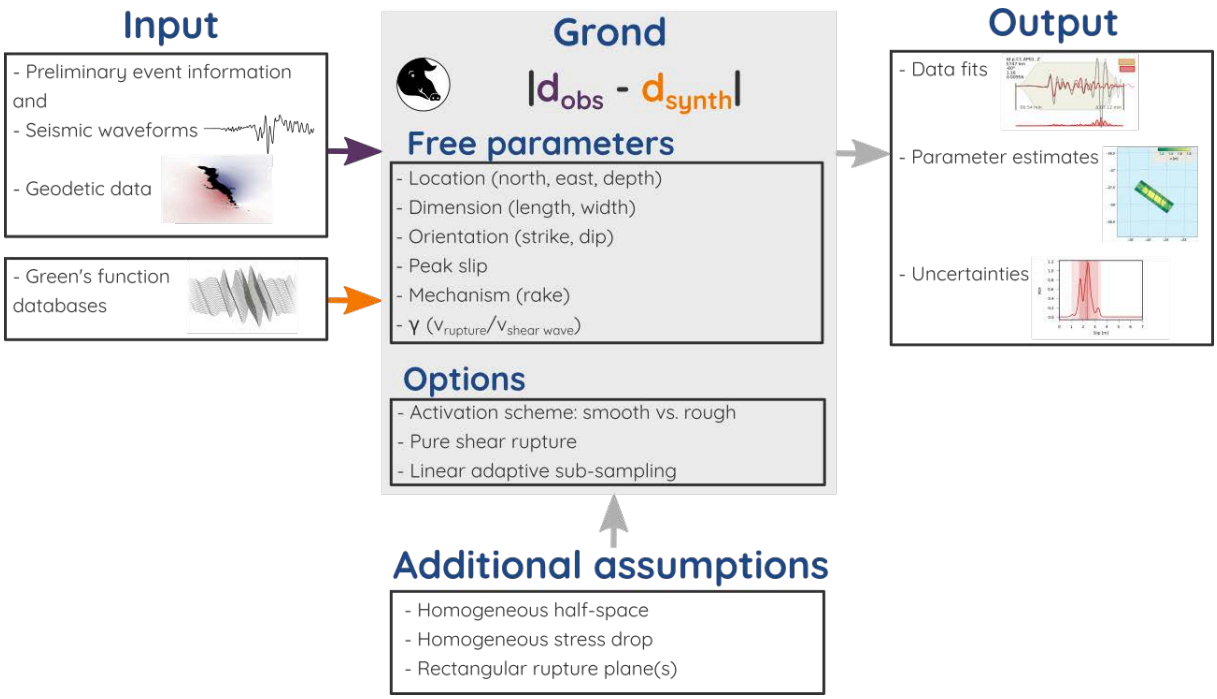

Figure 2.5: Schematic overview of the PDR inversion implemented in the development branch `dyn_rupt` of *Grond* with the required input data (left), assumptions made for a more performant inversion (bottom), the optimized parameters and specific options within the *Grond* inversion and an exemplary list of outputs (right) (modified after https://data.pyrocko.org/presentations/pyrocko-workshop-dgg-2021/, last accessed 06 June 2023).

1. Definition of rupture plane dimensions and orientation,
2. Definition of the stress drop distribution along the plane,
3. Estimation of the activated sub-faults and the resulting final, static slip using a known centroid location and moment release (e.g., from MT inversion),
4. Estimate of the quasi-dynamic rupture evolution based on a known nucleation point.

This procedure requires a profound knowledge on the centroid location and magnitude, the fault orientation and the stress state. We estimate these parameters during the PDR inversion, instead of using a priori knowledge. Therefore, different steps were made to enhance the PDR performance within the *Grond* inversion frame work. These steps include the definition of the stress drop, the estimation of the rupture dimensions and defining the linear adaptive sub-sampling scheme.

At the time of writing this thesis, the PDR is available as a part of the development branch `dyn_rupt` of *Grond* and will be added to the `main` branch in near future.

Assumption of homogeneous stress drop and peak slip

Opposing the forward modeling examples shown in Chapter 2.1 we are using a homogeneous stress drop along the rupture plane in the PDR inversions with *Grond* (Fig. 2.6). This simplification reduces the number of parameters within the inversion significantly. Instead of independent stress drops and rakes for each sub-fault we only invert for two scalar values for rake and stress drop. Normal stress is assumed to be constant and zero (see Chap. 2.2.2). The simplified approach

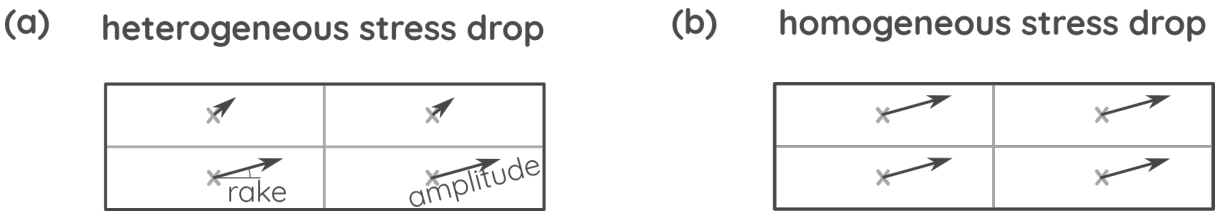

Figure 2.6: Comparison of the stress drop distribution according to Chapter 2.1 (a) and the implementation within *Grond* (b). Arrows show the amplitude and direction of the stress drop defined by the rake. Rakes and amplitudes in (a) are variable and can be defined based on a priori knowledge on the stress state. In (b) all rakes and amplitudes are constant to reduce the number of free parameters within the inversion.

provides the user with the opportunity to exploit the linear relation between stress-drop, moment release and the dislocation. Thereby, *Grond* inverts for the peak slip as a measure comparable with other studies and models instead of the stress drop.

Assumption of a pure shear rupture

The linear coefficients between stress drop and dislocation need to be calculated for each PDR source model (Sec. 2.2.1). Depending on the number of sub-faults, this can be computationally expensive. To speed up the inversion, we can assume a shear rupture with no significant fraction of opening within *Grond*. This allows to neglect the opening along the fault and, hence, to reduce the number of required coefficients. This option is implemented into *Grond* as the `pure_shear` switch.

Assumption of a rectangular rupture plane

The procedure defined in Chapter 2.1 requires to calculate the time-dependent moment contributions of each discretized point source twice; once to estimate the rupture extends with curved edges based on a known centroid location and once for waveform generation within the kinematic modeling. Our implementation within *Grond* assumes the planar fault to be also rectangular. Thereby, we can reduce the number of moment rate modeling runs required and, hence, increase the speed of the inversion. Contrary to Chapter 2.1, this setup neglects curved rupture edges.

Linear adaptive sub-sampling

A PDR source model with denser sub-fault spacing can resolve the slip distribution in more detail compared to one with a coarse sub-fault grid. However, such dense model will suffer from decreased computation speeds compared to a coarser one because of the increased size of the required coefficient matrix (Sec. 2.2.1 and 2.2.1).

The linear adaptive sub-sampling of the PDR within *Grond* allows to use both speed and resolution advantages of the coarse and finer model, respectively (Fig. 2.7). The sampling refines the number of sub-faults through the inversion between a given lower and upper limit. At first, coarse models are used fitting majorly the low-frequent part of the waveform to constrain centroid location, magnitude and the mechanism and orientation of the rupture. Later, models with a

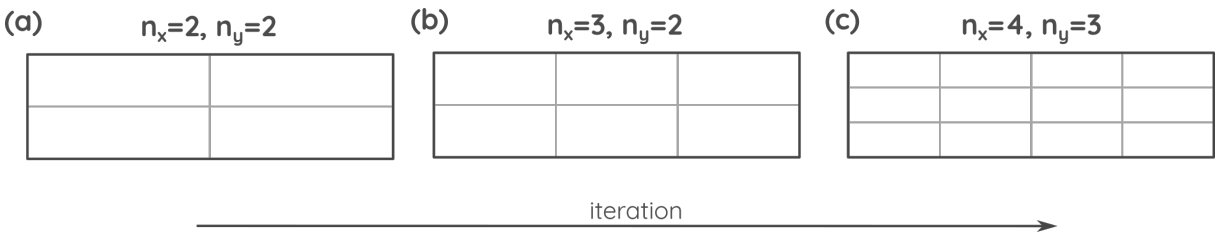

Figure 2.7: Exemplary for linear adaptive sub-sampling of the number of sub-faults through a *Grond* inversion. It starts with a coarse sub-fault grid (a), which will be refined (b) through the inversion depending on the iteration until the given maximum number of sub-faults (c).

higher number of sub-faults allow to capture details within the higher-frequency waveforms as generated by the rupture propagation or the slip distribution.

Multiple source inversion

Complex rupture processes along curved faults or when containing several subevents can not be modelled as a single seismic source because of their increased complexity. I discuss double and triple PDR modeling techniques within the Chapters 3 and 4. The double DC and double PDR source inversion methods in Chapter 3 rely on a development by Carrillo Ponce et al. (2023), Carrillo Ponce et al. (2021). The double source inversions rely on a relative weighting scheme between the sub-sources. This weighting scheme gives the distance, depth- and time-shift of each sub-source from the common centroid location based on the relative moment contribution of each sub-source to the joint moment release. Other parameters like the rupture orientation are independent for each sub-source allowing to capture complex rupture processes, e.g., along a curved fault plane.

The triple DC and triple PDR inversion schemes are designed to capture several distinct rupture processes well separated in seismic signals, but with overlapping contributions within the satellite deformation data (Chap. 4). Opposing to the double source implementation, all sub-sources are solely defined by independent parameters. Thereby, each event is treated independently with respect to the fit of the seismic data. The fit to the satellite deformation data is always characterized by the summed static displacements of all sub-sources, though.

3 | Second publication

Seismic and Tsunamigenic Characteristics of a Multimodal Rupture of Rapid and Slow Stages: The Example of the Complex 12 August 2021 South Sandwich Earthquake

M. Metz, F. Vera, A. Carrillo Ponce, S. Cesca, T. Dahm, J. Saul, and F. Tilmann (2022)

Published in Journal of Geophysical Research: Solid Earth, 127, e2022JB024646
https://doi.org/10.1029/2022JB024646

The appendix and supplementary material of this publication is available online at https://doi.org/10.1029/2022JB024646.

JGR Solid Earth

RESEARCH ARTICLE
10.1029/2022JB024646

Seismic and Tsunamigenic Characteristics of a Multimodal Rupture of Rapid and Slow Stages: The Example of the Complex 12 August 2021 South Sandwich Earthquake

M. Metz[1,2], F. Vera[1,3], A. Carrillo Ponce[1,2], S. Cesca[1], A. Babeyko[1], T. Dahm[1,2], J. Saul[1], and F. Tilmann[1,3]

[1]GFZ German Research Centre for Geosciences, Potsdam, Germany, [2]Institute of Geosciences, University of Potsdam, Potsdam, Germany, [3]Institute of Geological Sciences, Freie Universität Berlin, Berlin, Germany

Key Points:

- A combination of multiple approaches, inversion setups, and frequency ranges deciphered the complex earthquake of 2021 South Sandwich
- The rupture consisted of four subevents with the largest occurring as a shallow slow rupture parallel to the South Sandwich Trench
- Forward modeling proves that the large, shallow thrust subevent caused the recorded tsunami

Correspondence to:
M. Metz,
mmetz@uni-potsdam.de

Citation:
Metz, M., Vera, F., Carrillo Ponce, A., Cesca, S., Babeyko, A., Dahm, T., et al. (2022). Seismic and tsunamigenic characteristics of a multimodal rupture of rapid and slow stages: The example of the complex 12 August 2021 South Sandwich earthquake. *Journal of Geophysical Research: Solid Earth*, *127*, e2022JB024646. https://doi.org/10.1029/2022JB024646

Received 26 APR 2022
Accepted 5 OCT 2022

Author Contributions:
Conceptualization: S. Cesca, T. Dahm, F. Tilmann
Data curation: J. Saul
Formal analysis: M. Metz, F. Vera, A. Carrillo Ponce, S. Cesca, A. Babeyko
Software: M. Metz, A. Carrillo Ponce
Supervision: T. Dahm, F. Tilmann
Visualization: M. Metz, F. Vera, A. Babeyko
Writing – original draft: M. Metz, F. Vera, A. Carrillo Ponce, S. Cesca, A. Babeyko
Writing – review & editing: T. Dahm, J. Saul, F. Tilmann

Abstract On 12 August 2021, a >220 s lasting complex earthquake with M_w > 8.2 hit the South Sandwich Trench. Due to its remote location and short interevent times, reported earthquake parameters varied significantly between different international agencies. We studied the complex rupture by combining different seismic source characterization techniques sensitive to different frequency ranges based on teleseismic broadband recordings from 0.001 to 2 Hz, including point and finite fault inversions and the back-projection of high-frequency signals. We also determined moment tensor solutions for 88 aftershocks. The rupture initiated simultaneously with a rupture equivalent to a M_w 7.6 thrust earthquake in the deep part of the seismogenic zone in the central subduction interface and a shallow megathrust rupture, which propagated unilaterally to the south with a very slow rupture velocity of 1.2 km/s and varying strike following the curvature of the trench. The slow rupture covered nearly two-thirds of the entire subduction zone length, and with M_w 8.2 released the bulk of the total moment of the whole earthquake. Tsunami modeling indicates the inferred shallow rupture can explain the tsunami records. The southern segment of the shallow rupture overlaps with another activation of the deeper part of the megathrust equivalent to M_w 7.6. The aftershock distribution confirms the extent and curvature of the rupture. Some mechanisms are consistent with the mainshocks, but many indicate also activation of secondary faults. Rupture velocities and radiated frequencies varied strongly between different stages of the rupture, which might explain the variability of published source parameters.

Plain Language Summary The earthquake of 12 August 2021 along the deep-sea trench of the South Sandwich Islands in the South Atlantic reached a magnitude of 8.2 and triggered a tsunami. The automatic earthquake parameter determination of different agencies showed very different results shortly after the earthquake and partially underestimated the tsunami potential of the earthquake. A possible reason was the complex rupture process and that the tsunami was generated by a long and shallow slow slip rupture sandwiched between more conventional fast slip subevents at its northern and southern ends. In addition, the fault surface, which extended over 450 km, was highly curved striking 150°–220°. We investigated the different components of the seismic wavefields in different frequency ranges and with different methods. The analysis shows how even complex earthquakes can be deciphered by combining analyzing methods. The comparison with aftershocks and the triggered tsunami waves confirms our model that explains the South Sandwich rupture by four subevents in the plate boundary along the curved deep-sea trench. Here, the depth, rupture velocities, and slip on each segment of the rupture vary considerably. The method can also be applied to other megathrust earthquakes and help to further improve tsunami warnings in the future.

1. Introduction

The Sandwich plate (SW) is located in the Scotia Sea in the southern Atlantic at the junction of the Antarctic (AN), Scotia (SC), and South America (SA) plates (Figure 1). It is confined by the East Scotia Spreading Ridge (ESR) to the west, strike-slip segments to the north and the south, and the westward subduction of the SA plate with a rate of 62–72 mm/yr at the South Sandwich Trench (SST) to the east (e.g., Beniest & Schellart, 2020; Larter et al., 2003; Thomas et al., 2003).

Effects of mantle inflow, the adjacent strike-slip systems, and the slab bending result in a complex stress field, which causes a change in dominant focal mechanisms from trench-perpendicular compressive in the central segment of the SST to oblique strike-slip and reverse mechanisms with variable strikes within 100–200 km of the

Journal of Geophysical Research: Solid Earth 10.1029/2022JB024646

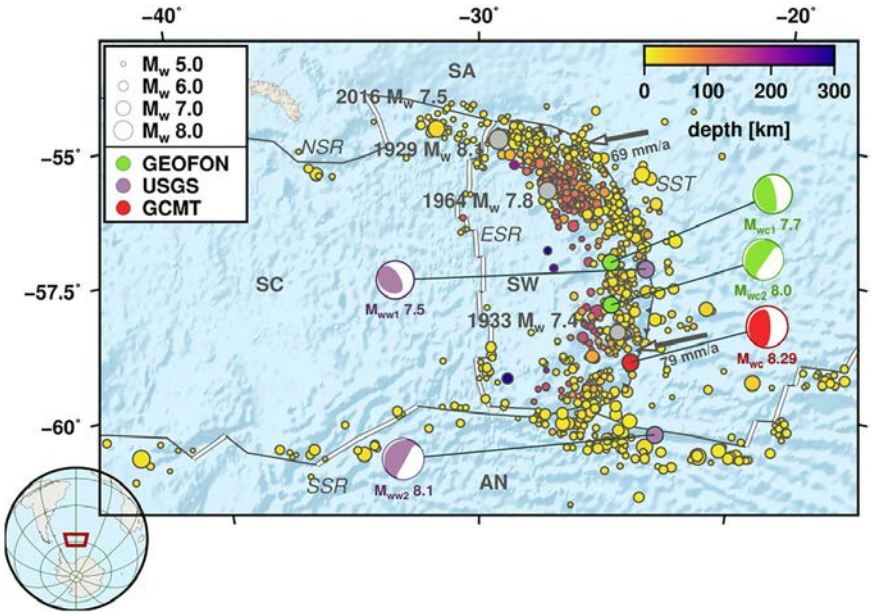

Figure 1. Seismicity and moment tensor (MT) solutions of the 12 August 2021 earthquakes are plotted together with bathymetry and outlines of the Sandwich plate (SW) in between the Scotia (SC), South America (SA), and Antarctic (AN) plates. Plate boundary labels indicate: NSR, North Scotia Ridge; SSR, South Scotia Ridge; SST, South Sandwich Trench; ESR, East Scotia Spreading Ridge (from Bird (2003); except that the SST was manually adjusted according to the location of the deformation front in bathymetry (minimum in EW profiles) between 58°S and 60.6°S as its location is rather uncertain according to Thomas et al. (2003), and the SST in Bird's plate model did not match bathymetry). Pre-event seismicity is plotted by circles (1,013 earthquakes, $M_w > 5.0$, 1976—11 August 2021, from GCMT; depth color-coded). Deviatoric MT solutions from different agencies for two main shocks of the 12 August sequence are plotted in lower hemispherical projections (see legend for color coding and Table 1). Labels M_{wc} indicate centroid MTs, M_{ww} the W-phase MT, and numbers 1 and 2 the first or second events, respectively. Note that the final GCMT solution is only a single long period MT solution representing the whole rupture.

northern and southern edges of the SST (e.g., Abe, 1972, 1981, 1982; Forsyth, 1975; Giner-Robles et al., 2009; Leat et al., 2004; Purcaru & Berckhemer, 1982).

Only few large earthquakes with $M_w \geq 7.5$ have been reported for the region before 1975: the shallow extensional M_w 8.1 1929 event close to the northern tip of the SST, the large shallow M_w 7.4–7.5 1933 earthquake of unknown mechanism type and the deep extensional M_w 7.8 1964 earthquake in the subducted slab (e.g., Abe, 1972, 1981; Bondár et al., 2015; Forsyth, 1975; Okal & Hartnady, 2009; Wilson, 1940). In addition to these, Global CMT (further GCMT) reports an M_w 7.5 thrust event at the northern edge of the SST in 2016 (Figure 1).

After over 90 years since the last great South Sandwich earthquake with $M_w \geq 8$, a complex earthquake hit the eastern margin of the SW on 12 August 2021 (Figure 1) with short interevent times between reported subevents. The seismic records were complex and indicated a complex rupture process. For instance, the teleseismic body and Rayleigh waves at the broadband station BFO have a very different appearance at high and low frequencies in comparison to an aftershock with similar mechanism and location (Figure 2). Strong low frequency waves appear much more extended and with different patterns, suggesting that different subevents possibly ruptured after the first earthquake generating more complex coda waves, causing major difficulties in the semiautomatic earthquake analysis (Hubbard, 2021). This may explain the unusual variety of focal mechanism solutions and magnitude estimates between different agencies as USGS, GEOFON, and GCMT (Table 1). GCMT first reported the doublet as two separate earthquakes with M_w 8.3 and 7.9 for the first and second events, respectively (see e.g., Jia et al., 2022, for the originally distributed GCMT estimates), but later switched to a single long duration (300 s) earthquake with M_w 8.3. The solutions of USGS and GEOFON assume an earthquake doublet with magnitudes of M_w 7.5–7.7 for the first and M_w 8.0–8.2 for the second subevent. Global catalog depths range from very shallow (i.e., ≤20 km for GEOFON and GCMT) to depths of 35–50 km (USGS CMT). Proposed focal mechanisms agree on a thrust mechanism with one very shallow dipping plane (average dip 17°), as expected for plate interface events. The strike direction varies significantly both between the two subevents and for the same subevent

Journal of Geophysical Research: Solid Earth 10.1029/2022JB024646

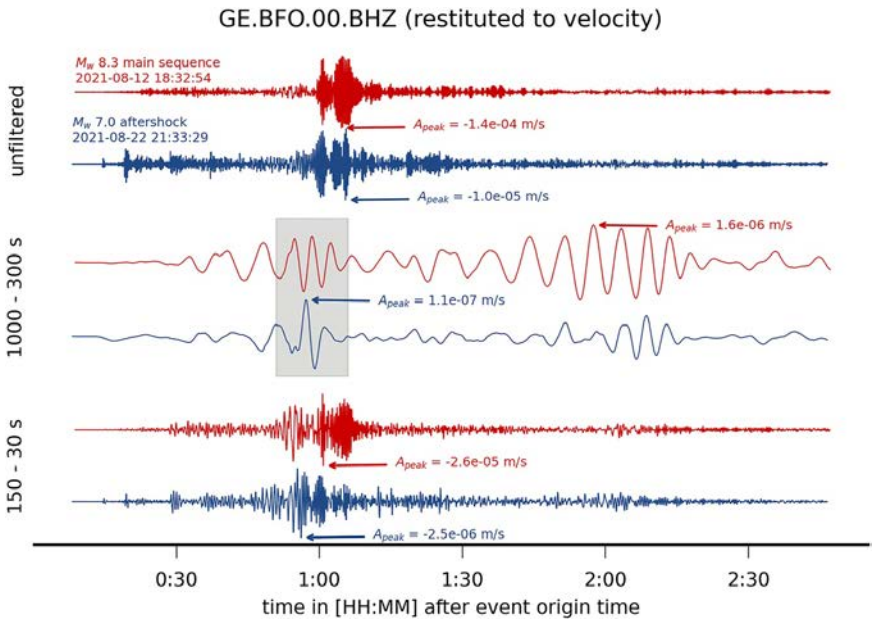

Figure 2. Comparison of vertical broad band waveforms of the main shock sequence (red) and an aftershock (blue) recorded at station GE.BFO.00 in 12,150 or 12,420 km epicentral distance from the main and the aftershock origin, respectively. Velocity traces were restituted (top) and additionally filtered in very low (middle) and intermediate frequency range (bottom). Time is given relative to the epicentral time of the earthquakes given in the top left. The gray box highlights the Rg surface wave phase. Each trace is normalized to its maximum absolute amplitude (value and time indicated by A_{peak} for each trace).

between different agencies though. The earthquake caused a tsunami with amplitudes ranging from 10 to 64 cm, e.g., recorded at tide gauges at King Edward Point on South Georgia Island, Stanley on the Falkland Islands and Antarctica Base Prat on the South Shetland Islands (Flanders Marine Institute (VLIZ), Intergovernmental Oceanographic Commission (IOC), 2021). Due to the absence of any tsunami early warning system for the Atlantic coasts of Africa and South America, no tsunami information was released for these regions, and an information statement was issued only for the Caribbean and North American shore lines by PTWC (https://tsunami.gov/events/PHEB/2021/08/12/21224001/2/WECA43/WECA43.txt, last visited 29 March 2022).

A multiple event inversion combining centroid moment tensors (MTs) and a simplified extended rupture model applied to the complex rupture (Jia et al., 2022) yielded a total of five subevents, where the dominant subevent indicated very shallow and very slow southward rupture propagation with a rupture velocity of ≈1 km/s. Their

Table 1
Selected Standard Centroid Moment Tensor (MT) and W-Phase Inversion Results Published From Different Agencies for 12 August 2021 South Sandwich Earthquakes

Agency	Method	Periods	Time	Lat, lon	Depth (km)	M_w	Dip (°)	Duration
Single event								
GCMT	C + W	450-50 s	18:35:25	−59.48°, −24.34°	20	8.29	14	300 s
Event 1								
GEOFON	E	600-40 s	18:32:50	−57.64°, −25.33°	13	7.70	11	—
USGS	W	500-150 s	18:33:31	−57.70°, −25.19°	51	7.50	26	29 s
Event 2								
GEOFON	E + W	600-40 s	18:35:22	−58.42°, −25.21°	11	7.98	12	—
USGS	W	1,000-200 s	18:36:56	−60.81°, −23.16°	36	8.13	11	133 s

Note. Origin times reported by USGS are 18:32:52 and 18:35:17 for the first and second events, respectively. GEOFON does not report centroid times or locations, and origin times and location are reported in this table.

Inversion methods: E—epicentral MT inversion (body and surface waves); W—W-phase MT inversion; C + W—joint body, surface, and W-phase centroid MT inversion; E + W—joint body, surface, and W-phase MT inversion at the epicenter.

Journal of Geophysical Research: Solid Earth 10.1029/2022JB024646

results thus indicate a typical tsunami earthquake behavior (as explained by Bilek and Lay (2018)) with a tsunamigenic slow rupturing event in the shallow conditionally stable domain of a subduction megathrust.

The 12 August 2021 rupture represents the largest moment release along the SST in the instrumental period. The simultaneous occurrence of fast and slow rupture modes as stated by Jia et al. (2022) is rarely observed so clearly, but led to an increased complexity of the rupture process of the earthquake. This complexity makes it challenging to reconstruct the rupture processes and estimate its tsunamigenic potential from standard seismological analysis approaches, even more so as no near field GNSS observations are available.

With this study we aim to resolve the static properties and kinematic processes of both the fast and slow ruptures from seismic source inversion and back-projection. We use Bayesian inversion techniques for both MTs and extended seismic source inversion. That allows to quantify also the uncertainties of our solutions for both derived rupture mechanisms but also the location. Furthermore, we explore the implications of the rupture model for tsunami excitation by forward modeling and comparing to the observed tide gauge records from several island stations and the coast of South America. The rupture characterization is complemented by an analysis of the locations and mechanisms of the largest aftershocks.

In the following we will refer to the different stages of the complex rupture as subevents of the earthquake.

2. MT Inversions of the Main Shocks and the Aftershocks

Individual centroid MT inversions have been performed using the Grond software (Heimann et al., 2018) for the two main shocks (as indicated by GEOFON) and 88 aftershocks recorded until end of August 2021. In this approach, the MT components (full for the main shocks and deviatoric for the aftershocks), the centroid location, time, and duration are estimated from waveform records, mostly Rayleigh and Love waves, assuming a simple half sinusoidal source time function. The inversion uses a particle swarm method paired with bootstrapping to estimate nonlinear uncertainties for all parameters. Each inversion fitted displacement waveforms in the time domain. All observed waveforms were visually inspected and noisy, saturated, clipped, or incomplete traces were removed. Filter and taper applied within the inversion used cosine tapers in frequency and time domain. Frequency ranges given in the following confine the flat part of the cosine taper. Further information on the tapers is given in Appendix A and Tables A1 and C1.

For estimation of the MT source parameters for the two main shocks as referenced by GEOFON (referred to as CMT inversions of subevents A and D), bandpass-filtered (0.01–0.03 Hz) teleseismic records (2,500–10,000 km epicentral distance) at 64 stations with good coverage in azimuth and distance were fitted on the vertical and transverse components.

In addition, we carried out a very low frequency inversion of the W-phase signals (referred to as CMT inversion of subevent B) from 0.001 to 0.01 Hz on the vertical and radial components with the aim to constrain the total magnitude of the event (following Kanamori and Rivera (2008) and Duputel et al. (2012)). Due to the very long period nature of the W-phase, we expect to characterize the whole complex earthquake. A second full-waveform low frequency (0.001–0.01 Hz) inversion considering longer time windows (referred to as CMT inversion of subevent C) was performed to capture all characteristics of the rupture. For all inversions, the AK135 Earth model from Kennett et al. (1995) was assumed.

The same inversion method was applied to 88 out of the 202 globally recorded aftershocks with $M_w \geq 5.0$, but with different parameters. Here, waveforms from 200 to 2,500 km epicentral distance were used to ensure good signal-to-noise ratios and exclude saturated data. For the 114 excluded events, high seismic noise levels or waveform overlap with stronger events prevented robust MT inversion. Bandpass-filtered (0.02–0.04 Hz for best signal-to-noise ratios) full waveforms were fitted on the vertical, transverse, and radial components. The obtained MT solutions and those for five additional earthquakes from the GEOFON MT catalog were clustered (Cesca, 2020) based on the similarity of their focal mechanisms, using the Kagan angle (Kagan, 1991) as metric. Clusters are recognized if there are at least two other earthquakes with mutual Kagan angles $\leq 30°$. Further details and waveform fits can be found in Appendix A and B.

Journal of Geophysical Research: Solid Earth 10.1029/2022JB024646

3. Finite Fault Dynamics From Self-Similar Dynamic Extended Rupture Model

The self-similar dynamic rupture model (or pseudo dynamic rupture model—PDR) utilizes a flexible 3D boundary element method to invert for the instantaneous slip caused by a prescribed stress drop on each activated patch of an extended rupture, defined by the area behind the rupture front (Dahm et al., 2021; Metz, 2019). As a first-order approximation, the rupture speed scales linearly with the *S* wave velocity extracted from the layered AK135 Earth model (Kennett et al., 1995). With a prescribed rupture speed model, the rupture front at each time step is approximated using the 2D Eikonal equation.

We integrated the PDR into the Bayesian inversion scheme of Grond (Heimann et al., 2018) as a source option. In our realization, the PDR assumes a planar fault, a constant stress drop, and constant rake along the whole plane, which reduces the number of free parameters within the inversion significantly compared to individual rakes and stress drops on each subfault. Due to this simplified scheme, we expect the PDR inversions to focus on the major slip patches.

We do not fix the orientation of the fault, the slip direction (governed by the rake) nor centroid and origin location prior to the inversion, but leave them as parameters in the inversion. Thereby, 13 free parameters are estimated: length, width, strike, and dip of the fault plane; origin time and location, both absolute and relative to the fault plane; and rake angle, stress drop, and the scaling coefficient v_r/v_s between the rupture speed v_r and the *S* wave velocity v_s. Any deviation between the *S* wave velocity of the used Ground model and the true shear wave velocity will also result in a change of the scaling coefficient. Slower *S* wave velocities as often observed in megathrusts (e.g., Miller et al., 2021) will cause a decrease of the scaling coefficient. Hence, any interpretation will be done on the absolute rupture velocity instead of the scaling coefficient. Note that the seismic moment is calculated using the inverted slip, area of the rupture plane, and the mean shear modulus of the depth section covered by the PDR rupture plane.

We decided not to preconstrain the location of the rupture using a known slab geometry. That allows to access also the location uncertainty in a fully Bayesian manner. In a first approach, we apply the PDR inversion independently to subevents A and D by a careful selection of time windows (example in Figure 4), considering that between 4,000 and 10,000 km epicentral distances the high-frequency *P* waves of subevent D arrive significantly earlier than the high-frequency *S* waves of event A, thus avoiding wave interference. We use displacement seismograms on vertical and transverse components, bandpass filtered between 0.01 and 0.05 Hz.

Although such a time separation approach is possible for the smaller subevents A and D, it is suboptimal to analyze the slow rupture processes of subevents B and C in between, because a constructive and destructive superposition of radiated low frequency waves cannot be considered. Therefore, the PDR inversion of subevents B and C was formulated as a joint inversion. Very low frequency vertical and radial displacement records (0.001–0.01 Hz) were used including the W-phase signal as well as the *S* wave and surface waves. The two PDR models have independent parameters allowing also independent fault plane orientations and subevent magnitudes. The new simultaneous Bayesian inversion scheme for source doublets parametrizes the time, distance, and azimuth between the two subevents and is described in more detail in Carrillo Ponce et al. (2021). Detailed inversion reports and waveform fits can be found in Appendix C.

4. Teleseismic Back-Projection

We used a multiarray back-projection method (Vera et al., 2021) of vertical very short-period *P* waves (0.5–2.0 Hz) recorded at several arrays in Chile, the Caribbean, Australia, and South Africa. Each array was weighted individually based on its azimuthal distribution, i.e., proportionally to the sum of the two half-angles measured between the azimuths of target and neighboring arrays (see example in Figure D2a). Combining semblance and energy radiated maps, we are able to characterize the spatial and temporal rupture evolution with associated relative strength of each short-period energy emission above 0.5 Hz.

P waves were extracted using arrival times from the IASP91 velocity model (Kennett & Engdahl, 1991). Theoretical arrival times have been additionally calibrated using static station corrections following the aftershock calibration method (Palo et al., 2014) to correct for earth heterogeneities and their effect on the arrival times (e.g., Ishii et al., 2007; Meng et al., 2016; Palo et al., 2014). Station corrections are derived as the average residuals of eight aftershocks with thrust mechanisms assumed to rupture the same fault as the mainshocks (Table D1).

Journal of Geophysical Research: Solid Earth 10.1029/2022JB024646

Compared to the standard practice of calibrating station corrections based on the catalog hypocenter, this makes the absolute positioning of the rupture track less susceptible to mislocation of any single event.

More details on the teleseismic back-projection are presented in Appendix D.

5. Tsunami Simulation

The South Sandwich rupture has triggered a tsunami that was recorded at a number of tide gauge stations located at various azimuths and distances around the epicenter. We employ these observations to provide an independent first-order check for our source model. In particular, we would like to check if tsunami arrival times and amplitudes (which are essentially far-field proxis for the position, orientation, and average magnitude of the tsunamigenic slip) are roughly consistent with tide gauge observations. We cannot expect perfect match because of the limitations due to the numerical model and accuracy of the bathymetry (see also comprehensive discussion in Romano et al. (2016)).

We do this first-order validation by simulating tsunami propagation in long wave approximation using the in-house code easyWave, which implements the leap-frog finite difference numerical scheme at a staggered grid according to the TSUNAMI-F1 algorithm by Goto et al. (1997). The initial conditions are set according to the vertical seafloor displacement. This offset was calculated over a 600 × 600 km grid centered at the joint centroid location of the PDR results of the subevents B and C (Figure 6), using the PsGrn/PsCmp code by Wang et al. (2006), the flat earth approximation and assuming elastic structure as in the AK135 Earth model (Kennett et al., 1995). The tsunami source trigger is assumed to be instantaneous. Despite the relatively long rupture time of ≈220 s, this assumption is still valid since the rupture velocity is at least 5–6 times faster than the tsunami propagation in the source area. Given these initial conditions, tsunami propagation was simulated on a SRTM30 Plus (Becker et al., 2009) bathymetric grid downsampled to a 1 arc min resolution. As this resolution is too coarse to simulate wave evolution in the vicinity of coastal tide gauges, we used the commonly accepted technique, and recorded simulated waveforms at offshore positions in deep water (at least 50-m depth) with the subsequent tsunami height projection onto the nearest coast estimated with the coastal amplification factor (Glimsdal et al., 2019; Kamigaichi, 2015). In particular, for tide gauges located at coasts with shallowing bathymetry—stations "imbt" and "stan"—we used Green's law (Kamigaichi, 2015), whereas for the stations located in wall-like conditions—"kepo1," "mais," and "prat3"—we used factor 2 which corresponds to the perfect reflection at a vertical wall as derived from linear wave theory. Offshore waveforms were additionally time-shifted according to the calculated offshore-to-onshore tsunami propagation time assuming linear near-shore bathymetry shallowing (Romano et al., 2016).

6. Results and Discussion

The 2021 South Sandwich earthquake is characterized by complex rupture processes on the central and southern segments of the South Sandwich subduction zone. The earthquake is bounded by two M_w 7.5–7.6 thrust subevents (A and D) in the north and south of a shallow rupture plane (Table 2 and Figure 3). Both subevents A and D radiated seismic energy in frequencies as expected from standard scaling relations (e.g., Brune, 1970) and are characterized by mean rupture velocities of 1.5–2.1 km/s scaling linearly with the *S* wave velocity by a factor of 0.40–0.49. Both A and D occurred as thrust events at the plate boundary of SW and SA plate on trench parallel striking rupture planes with respective centroid depths of 18 ± 5 or 31 ± 4 km. In between both high-frequency subevents, a very shallow segment (top edge depth of 10 ± 4 km) of the plate boundary ruptured over a length of >450 km with a curved plane striking subparallel to the curvature of the plate boundary (subevents B and C) as retrieved from inversion of very low frequency seismograms. A maximum shear slip of 5.8 ± 2.2 m, a total moment release of $2.24 \cdot 10^{21}$ Nm, and v_r/v_s ratios of 0.33 and 0.37 (for both subevents B and C, respectively) were obtained, implying a mean rupture velocity in the range of 1.2–1.5 km/s. Both shallow depth and significant coseismic slip indicate tsunamigenic potential of this phase of the rupture. We will now describe the results of the various inversions in more detail. Probability density functions and complete lists of parameter uncertainties derived from the Bayesian inversions are provided in the Appendix.

The individual PDR inversions of the two high-frequency subevents A and D yield two thrust events (dip 20°) with strikes parallel to the plate boundary. Subevent D occurred 240 km SSW of subevent A about 200 s later, corresponding to a gap of ≈100 s between the end of rupture A and onset of rupture D (Tables 2 and C2 and Figure 3). The first subevent A is shallower compared to D with top edge depths of 10 versus 23 km and has a larger along-strike extent of 150 versus 58 km but a smaller maximum slip of 2.3 versus 3.1 m. The moderately

Journal of Geophysical Research: Solid Earth 10.1029/2022JB024646

Table 2
Major Results for the Individual Subevents and From Different Approaches

Subevent	A	B		C		D	All
Method	PDR	CMT	PDR	CMT	PDR	PDR	BP[a]
Period range (s)	100-20	1,000-100		1,000-100		100-20	2-0.5
Geometry							
Length (km)	150 ± 32	—	270 ± 56	—	178 ± 48	58 ± 11	462
Width (km)	42 ± 7	—	34 ± 10	—	49 ± 14	48 ± 8	—
Strike	147° ± 16°	199° ± 23°	172° ± 8°	196° ± 21°	218° ± 9°	219° ± 9°	—
Dip	21° ± 5°	43° ± 16°	29° ± 13°	45° ± 10°	39° ± 9°	20° ± 2°	—
Rake	80° ± 11°	86° ± 34°	96° ± 16°	64° ± 36°	111° ± 13°	128° ± 8°	—
Distance (km)[b]	243 (A–D)	216 (B–C)	202 ± 71	—	—	—	—
Azimuth[b]	199° (A–D)	183° (B–C)	184° ± 14°	—	—	—	—
Centroid depth (km)	18 ± 5	32 ± 19	18 ± 4	16 ± 6	25 ± 4	31 ± 4	—
Kinematics							
Origin time	18:32:54 ± 2 s	18:32:44 ± 19 s		18:35:15 ± 13 s		18:36:01 ± 2 s	—
Centroid time	18:33:35	18:35:09 ± 12 s 18:33:55	18:36:09 ± 2 s	18:35:53	—	18:36:17	
v_{rup} (km/s)	1.5		1.2		1.5	2.1	1.2
Duration (s)	81	385 ± 21	163	123 ± 4	78	24	300
Magnitude							
Max. slip (m)	2.3 ± 0.5	—	5.8 ± 2.2	—	5.0 ± 1.7	3.1 ± 0.5	—
M_w	7.57	8.14 ± 0.05	8.02	7.91 ± 0.03	7.98	7.61	—
$\sum M_w$	7.79 (A + D)	8.25 (B + C)	8.20	—	—	—	—

[a]Back-projection. [b]Given with respect to centroid location.

lower slip and shallower rupture in less rigid material finally makes the moment magnitude of A, M_w 7.57, a little smaller than that of D, M_w 7.61, in spite of the much larger rupture area of the former event. The origin of A at the northern segment of its fault plane leads to bilateral rupture with higher moment release for a duration of 60 s prior to pure unilateral propagation towards south (Figures 3a, 3c, and 3d). The later subevent D lasted only 24 s and is characterized by mostly down dip and southward rupture propagation. Our inferred rupture propagation of A and D fits well with the results from back-projection of high-frequency body waves (Figures 3c and 3d), which also indicate southward rupture propagation. The location and timing of subevent D fits well with the area outlined by the largest high-frequency energy emissions, although back-projection results indicate a larger extent of this zone. They do also show later emissions than the PDR results would suggest and could image the stopping of the rupture characterized by a strong rupture velocity decrease (Madariaga, 1977; Tilmann et al., 2016). A small patch of emitters at 58°S is colocated with the southern termination of the subevent A plane. CMT inversions (Appendix A) also confirm most of the PDR inversion results. Magnitudes are smaller, though, with M_w 7.31 and 7.40 for A and D, respectively and a shorter duration of 21 s estimated for A. The centroid depth extracted from the CMT inversion for A fitting first arriving *P* and *S* wave signals only is significantly deeper than obtained using the PDR with 40 ± 6 km compared to 18 ± 5 km. The PDR inversion fitted signals succeeding the first arrivals of *P* and *S* waves. These signals are likely emitted by the shallower segment of the megathrust, which ruptured simultaneously with the subevent A (Figure 3d). Mechanisms, locations, and times of A and D are consistent with subevents E1, E2, E4, and E5 by Jia et al. (2022). Our inversion of subevent A as an extended rupture reproduces E1 and E2 with similar location, slightly longer duration and also larger magnitude (M_w 7.6 compared to cumulative M_w 7.4), as it fits a longer part of the first rupture signal. While E4 and E5 match in time, mechanism, and location of our subevent D, they show a larger moment release (cumulative M_w 7.9 versus 7.6).

Journal of Geophysical Research: Solid Earth 10.1029/2022JB024646

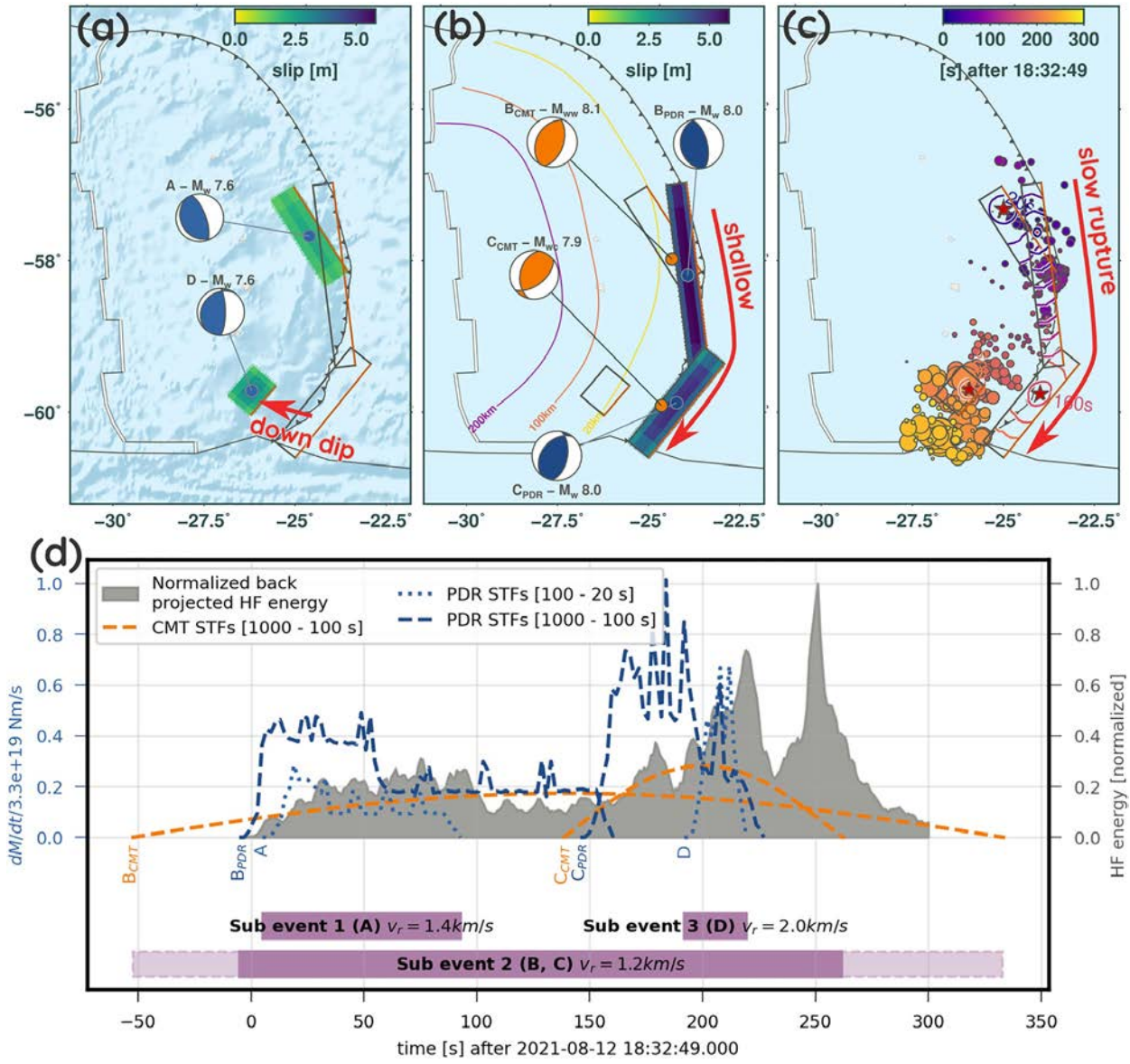

Figure 3. Results of the multifrequency analysis including key interpretations (red arrows). (a) Final static slip maps and associated centroid moment tensors (MTs) retrieved from the body wave inversions (0.01–0.05 Hz) for subevents A and D using the pseudo dynamic rupture (PDR). (b) The results for the very low frequency CMT and PDR inversions of subevents B and C. Rectangular outlines in (a), (b) show the location of the PDR solutions for subevents B, C or A, D, respectively (visualizes spatial relationships between the overlapping rupture planes). (c) The kinematics of the rupture. Contours indicated rupture propagation derived from PDR with respective subevent origins as red stars. Dots show high-frequency energy emitters (0.5–2 Hz, size scales with energy release) from back-projection. (d) Comparison of the normalized, radiated high-frequency energy back-projected to the moment rate source time functions (STF) retrieved from waveform inversions in different frequency ranges and with different approaches. The time reference is the origin time of the first subevent in the GEOFON catalog.

The static and kinematic parameters of the shallow and slow rupturing subevent B were derived from a CMT inversion of the W-phase at 0.001–0.01 Hz, and for subevent C from full waveform CMT (i.e., including surface waves) and PDR (using a joint inversion of two rupture planes), using the same frequency range. The individual CMT point-source inversions yield similar thrust mechanisms striking 196°–199° and dipping ≈45°, but with an increased oblique component for subevent C compared to B (CMT inversions of subevents B and C in Table 2 and Figure 3). The CMT moment magnitude M_w of C, which predominantly fitted the surface waves (Figures 4, A11, and A12) is estimated with 7.91 ± 0.03 compared to 8.14 ± 0.05 for subevent B. C ruptured later and with a shorter duration (123 ± 4 s versus 385± 21 s for C and B, respectively). Both centroids are located close to the trench with C 216 km further south and significantly shallower (16 ± 6 km) compared to B (32 ± 19-km depth).

Journal of Geophysical Research: Solid Earth 10.1029/2022JB024646

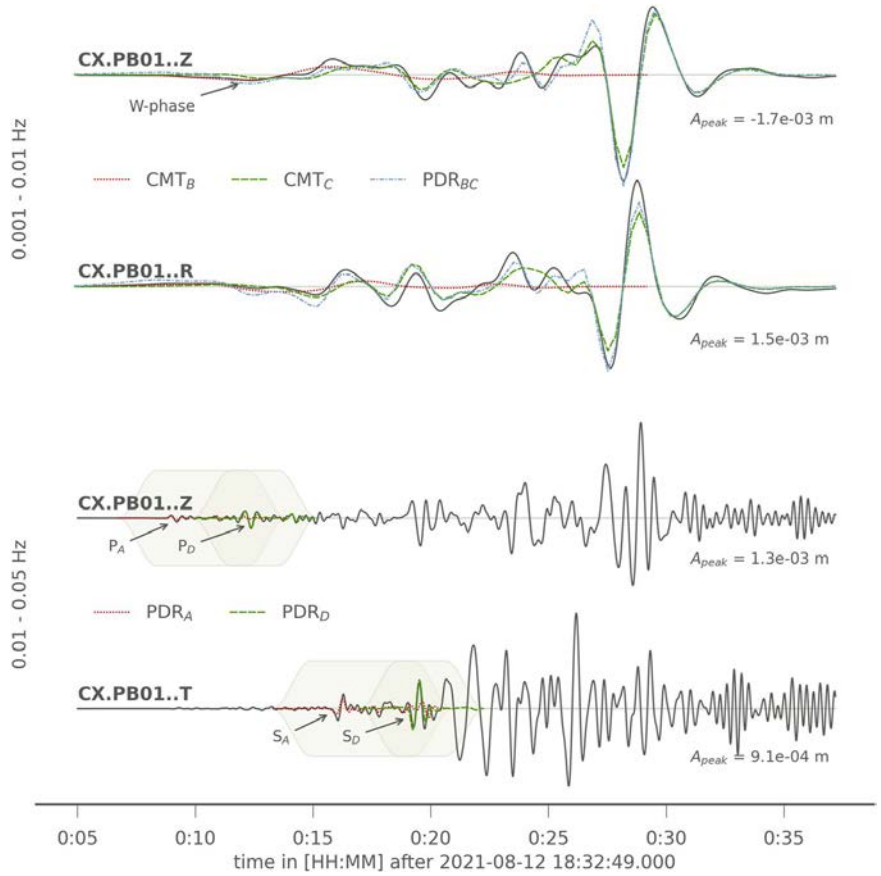

Figure 4. Waveform fits of the vertical and horizontal components for the seismic station CX.PB01.00 (distance: ≈5,500 km, azimuth: ≈300°). Fits for the pseudo dynamic rupture (PDR) and CMT inversions of subevents B and C are shown in the top rows, for the high-frequent (0.01–0.05 Hz) PDR inversions of subevents A and D in the bottom rows (Table 2). Dark lines show the filtered, observed displacement traces, colored lines the filtered, and tapered synthetic signals of the best model within each inversion given in the legend. Synthetic traces are only drawn for the time windows defined within each inversion. Peak amplitudes of each observed, filtered trace are used for normalization and are given as A_{peak}. Major phases (P, S, and W-phase) are annotated. Exemplary shape and position of the applied cosine tapers are shown as shaded areas indicating the chosen time windows within the inversion for fits of subevents A and D.

The centroid locations of each plane retrieved from joint inversion of two extended PDR planes fit well with the CMT solutions but with a shallower depth for subevent B of 18 ± 4 km indicating robust spatial resolution. Each plane strikes subparallel to the plate boundary with respective dips of 30°–40° for B and C. Rakes of 96° ± 16° and 111° ± 13° indicate pure thrust for B and oblique thrust for C. Maximum slip of 5.8 ± 2.2 or 5.0 ± 1.7 m with subevent moment magnitudes M_w of 8.02 and 7.98 (cumulative M_w 8.2) were obtained for B and C, respectively. B and C jointly ruptured a 450 km long and 34–49 ± 14-km wide shallow segment of the plate boundary. The rupture started on the northern segment close to the origin of subevent A in time (18:32:44 ± 19 s for B compared to 18:32:54 ± 2 s for A) and space (uncertainties in Figures C1 and C2). The rupture propagated first bilaterally and later unilaterally towards the south with slow mean rupture velocities of initially 1.2 km/s during event B, and then 1.5 km/s during event C (Figure 3c). Rupture velocities at the top edges of the rupture were close to 1.1/1.3 km/s for B and C, respectively. The higher speed of C leads to a shorter duration (78 s versus 163 s) and a higher peak moment rate compared to B (Figure 3d).

Both CMT and PDR estimate a similar cumulative M_w 8.2–8.25 with a long duration of at least 225 s, covering the central and southern shallow segment of the plate boundary with a joint centroid location close to the GCMT solution and with similar mechanism and magnitude (Tables 1 and C3). As fitting only the very long period W-phase, the CMT inversion of subevent B is unable to capture the nucleation phase accurately but instead characterizes the whole complex rupture process. That is indicated by the negative start of the CMT B source time function as well as by its long duration covering the whole rupture process (Figure 3d). The rotated focal mecha-

Journal of Geophysical Research: Solid Earth 10.1029/2022JB024646

nism of the W-phase based CMT solution, which has a significant NE-striking component, compared to the PDR B solution supports this interpretation (Figures 3b and 3d). The joint PDR inversion aims to fit the superposition of both W-phases and surface wave waveforms (Figures 4 and C10–C13). In the full-waveform inversion, we inevitably also fit signals emitted from subevents A and D. That leads to a partial overlap in time with subevents A and D and space with the subevent A (Figure 3). The spatial gap between the derived best rupture planes of C and D could be caused by the focus on major slip patches of our PDR inversion setup. As shown in Figure C3, we also obtain a larger location uncertainty for rupture plane C, which is linked to the high number of parameters to be resolved in the double PDR inversion. This may explain the unexpected location of the best rupture plane for C partially to the East of the SST. Nevertheless, our results including uncertainties (Figure C3 and Table C3) are consistent with the known slab location and geometry (e.g., Hayes et al., 2018).

We find a strong agreement with the results of Jia et al. (2022) from both their W-phase and multievent inversions. The CMT W-phase inversion (subevent B) yields a comparable cumulative duration, magnitude, thrust mechanism, and centroid location, but with a steeper dip of the preferred nodal plane (43° ± 16° versus 14°), which could be caused by larger time windows and a broader frequency band used in our case. The PDR mechanisms, magnitudes, and centroid locations of B and C coincide well with the subevents E3, E4, and E5. Again our preferred results show larger dips (30°–45°), but with large uncertainties of 9°–16° (Tables A2, C2, and C3). They could be an effect of the curved path of the rupture along the slab, as a strong trade-off between the orientations of nodal planes of the CMT solutions suggest.

Back-projected high-frequency seismic energy emitters are located mainly to the west and hence down dip of the shallow high slip patch as defined by rupture plane C. This has been observed at different megathrust earthquakes as the 2010 Maule (e.g., Kiser & Ishii, 2012; Koper et al., 2012), 2011 Tohoku (e.g., Duan, 2012; Ide et al., 2011; Lay, 2018; Lee et al., 2011; Simons et al., 2011; Suzuki et al., 2011; Wang & Mori, 2011) or 2015 Illapel earthquake (e.g., Tilmann et al., 2016). This characteristic of megathrust events is assumed to be associated with both longer rupture duration in shallow depth and heterogeneous friction or structural features on the shallow plate interface causing only moderate energy emissions along the shallow rupture (Bilek et al., 2004; Lay et al., 2012). We recognize these moderate to low energy emissions colocated with the inverted rupture planes of the subevents A, B, and partially C. Their emission times and the retrieved rupture velocity (1.2 km/s) fit well the inverted rupture propagations and velocities of A, B, and C (Figure 3c). With back-projection, such slow rupturing stages (1.0 km/s $\leq v_{rup} \leq$ 1.5 km/s) have been observed in the case of the 2011 Tohoku earthquake (e.g., Meng et al., 2011; Wang & Mori, 2011). The strong spatial and temporal coherency between the obtained rupture front propagation from low frequent finite fault inversions and the high-frequent back-projection have been observed in lab experiments by Marty et al. (2019).

The spatial extent of the aftershocks from 56°S to 60.5°S confirms the inferred rupture length from the PDR inversions (Figure 5). Locations are rather diverse with accumulations down dip from the inferred shallow high slip rupture planes of subevents B and C. These aftershocks are colocated with the major back-projected high-frequency energy emitters, as also observed e.g., at the 2010 Maule earthquake (Palo et al., 2014).

The aftershocks show heterogeneous focal mechanisms; we find eight clusters consisting of 61 events in total, with 31 unclustered events. The largest cluster 0 indicates oblique thrust faulting with moderate dips, and additionally a number of unclustered events show thrust mechanisms. The location of most of these events is close to the plate interface, and strikes are broadly subparallel to the strike directions of the closest trench segments, but dips are mostly too steep to be consistent with a plate interface origin (profiles A–A′, B–B′, C–C′). Only very few events have both hypocenters and focal mechanism dips consistent with a plate interface origin, and they tend to be the deepest, westernmost thrust events in the aftershock sequence, e.g., the two large unclustered events in the NW of profile C (profile distance ∼40 km), and maybe the deep cluster 0 event in profile B. However, the dips of subevents B and C of the main shock also are steeper than the expected interplate dip, such that events of cluster 0 and some of the unclustered thrust events can probably be considered to have occurred on the same fault as the main shock.

Multiple clusters with predominant normal faulting are found (1, 3, 5, and 7), which occur in very different tectonic settings: Along the SSR (cluster 1 with large strike-slip component), along the SW-SA plate boundary and within the subducted SA plate (profiles A–A′, B–B′, C–C′). A few of these events occur on the outer rise, especially in the south (cluster 7 in C–C′ and also cluster 4 in B–B′, which is oblique between strike-slip and normal faulting). Strong normal faulting events in the outer rise are often observed after large shallow subduction zone ruptures (Bilek & Lay, 2018). The occurrence of this type of events adjacent to subevents B and C along the plate boundary thus lends support to their interpretation as slip along the very shallow megathrust.

Journal of Geophysical Research: Solid Earth 10.1029/2022JB024646

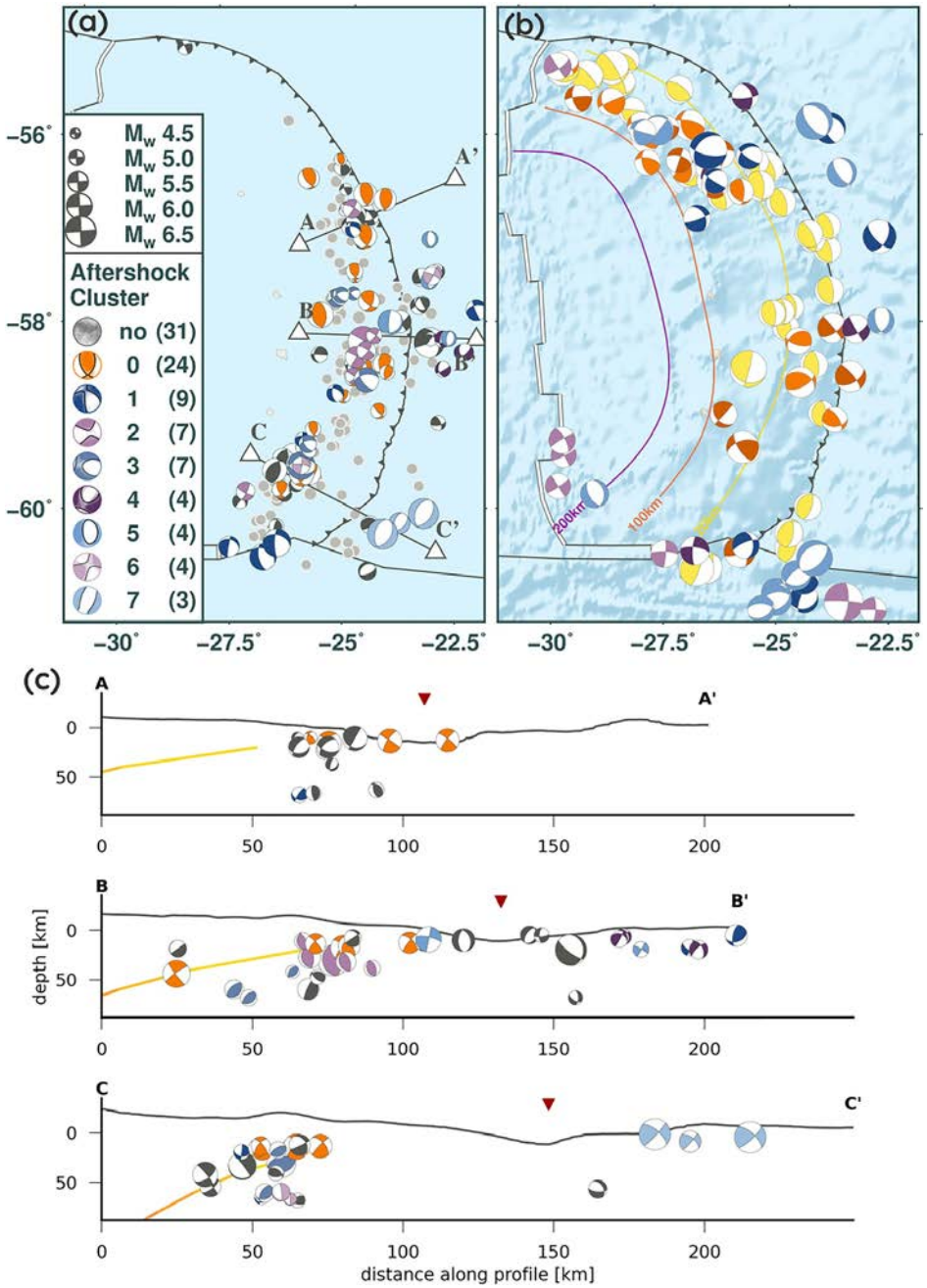

Figure 5. Aftershock centroid locations and mechanisms are shown as map (a) and cross-sectional view along three profiles A − A′, B − B′, and C − C′ (c). (b) gives pre-event source mechanisms of GCMT solutions ($M_w > 6$—locations of all $M_w > 5$ events are shown in Figure 1). Focal mechanisms are scaled with magnitude. Their colors indicate cluster families (see legend in (a), where fuzzy moment tensors (MTs) of each cluster are shown, with the representative nodal plane indicated by dark line). Gray dots in (a) show aftershocks from 12 to 31 August 2021 taken from a joint USGS and GCMT catalog. The SLAB2.0 slab interface (Hayes et al., 2018) is indicated by iso-depth lines in (b) and is shown as a colored line along each profile in (c). Gray lines show the bathymetry (ETOPO1 with vertical exaggeration factor of 6). The red triangle indicates the position of the trench defined by bathymetry.

Strike-slip clusters are found with the events mostly elongated along a SW-striking lineament of events in the downgoing plate (clusters 2 and 6). Multiple clusters with diverse dominant mechanisms near the adjacent plate boundaries (SSR) indicate complex reactivation of secondary faults. The complex patterns in the central segment (profile B–B′) are already evident on events recorded prior to the 2021 main shock (Figure 5b) indicating diverse faulting on unknown faults.

Journal of Geophysical Research: Solid Earth 10.1029/2022JB024646

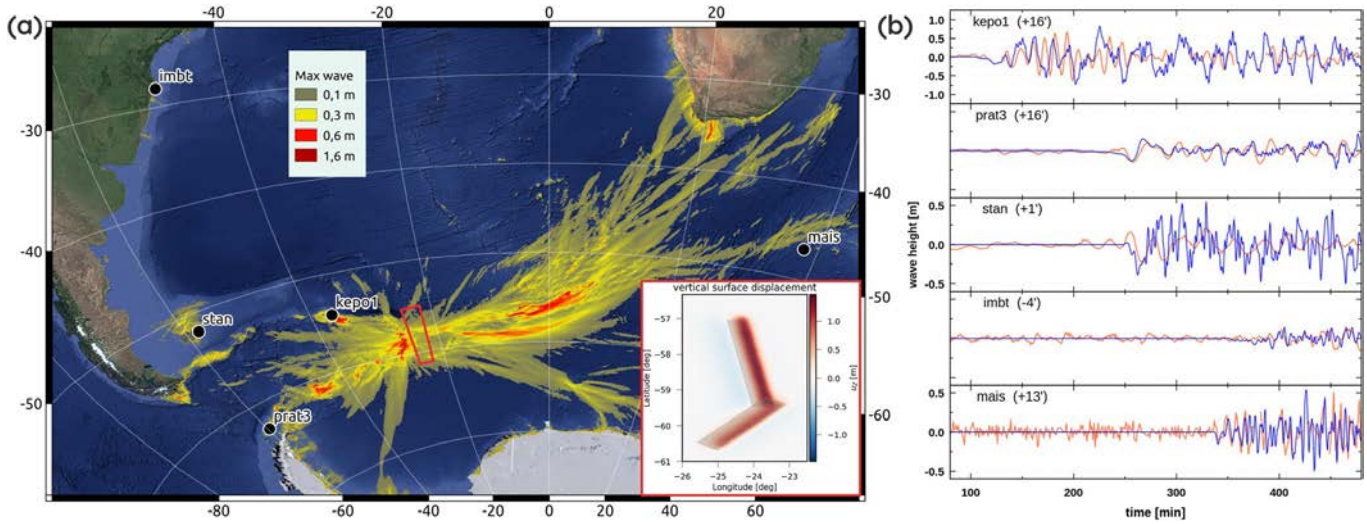

Figure 6. Forward tsunami modeling with initial conditions corresponding to the vertical seafloor displacement as predicted by the PDR model results for subevents B and C. Tsunami triggering is assumed as instantaneous vertical displacement of the seafloor at the joint centroid time of 18:34:46. (a) Maximum tsunami wave heights (values < 0.1 m clipped). Also shown are positions of tide gauges. The insert indicates initial conditions for tsunami modeling located within the red box on the map. (b) Modeled (blue) versus observed (red) mareograms at the tide gauges sorted by distance to the epicenter. Values in brackets indicate additional time shifts in (min) applied for the optimal fit (see Romano et al., 2016). Note that all data except "kepo1" are plotted in the same scale.

We compared our focal mechanisms to available solutions from GCMT for 16 aftershocks giving a median Kagan angle of ≈38° (see also Figure B1). Eleven of the compared events have an acceptable Kagan angle below 45°. Locations changed by 32 ± 6 km with an average depth difference of −10 ± 11 km. Deviations in location and focal mechanism might be caused by our choice of an oceanic ground model and also different station setups used within our inversions compared to GCMT.

The tsunami forward modeling results confirm the tsunamigenic character of the subevents B and C: Simulated tsunami wave heights at tide gauge positions at different azimuths and distances around the epicenter are generally consistent with observations (Figure 6) with poorer fit for the Stanley tide gauge in the Falklands (station "stan"). We note that the tsunami observations were not used for the source inversion, i.e., tsunami simulations present a fully independent check of our best source model (here the joint PDR models of subevents B and C).

The polarities of the first onset and the shapes and amplitudes of the first oscillation of modeled and observed tsunami waves show good agreement. The increasing differences at later times are expected and arise due to the simplifying assumptions in the forward modeling as these are strongly affected by local resonances and reflections. Resolving these effects would require high-resolution coastal bathymetry and thus cannot be reproduced with the global bathymetry data set used in our modeling.

The geographical pattern of wave propagation (Figure 6a) shows the largest wave heights to the East and West of the SST, as expected from the rupture geometry and mechanism, with maximum wave heights up to >1 m along the South Sandwich Islands and South Georgia. It is in good agreement with findings reported by Roger et al. (2022) which also show the wave guiding effect of the shallower rift systems of the SA-AN and Africa-AN plates with enhanced wave heights there. Less significant local highs in wave heights are predicted in further directions, e.g., along a South East striking trajectory as a result of the complex ground displacement pattern.

Slowing down of rupture velocities in the shallower parts of the plate boundary have been observed worldwide e.g., the 2010 Maule, Chile earthquake (e.g., Kiser & Ishii, 2012; Koper et al., 2012), the 2011 Tohoku, Japan earthquake (e.g., Duan, 2012; Ide et al., 2011; Lay, 2018; Lee et al., 2011; Simons et al., 2011; Suzuki et al., 2011; Wang & Mori, 2011) or the 2015 Illapel, Chile earthquake (Tilmann et al., 2016), and often been associated with a combination of small shear wave velocities and enhanced fluid pore pressures (e.g., Song et al., 2009). Enhanced fluid pore pressure is also postulated to control the occurrence of slow slip events in subduction zones (e.g., Audet et al., 2009; Kato et al., 2010; Kodaira et al., 2004), as an extreme example of slow earthquake rupture.

Journal of Geophysical Research: Solid Earth 10.1029/2022JB024646

Recent laboratory studies on frictional rupture under varying fluid overpressure support such an explanation (Passelegue et al., 2020). Experiments could reproduce the full range of observed rupture velocities on the same interfaces, only controlled by the initial effective stress which defines the available shear stress and fracture energy at the onset of slip. Large initial shear stress, meaning small fluid pore pressure, seemed to promote fast rupture velocities and fast slip rates, while high pore pressures lead to slow rupture velocities.

7. Conclusions

Our analysis of the 2021 South Sandwich earthquake elucidated the complex interaction of smaller subevents with a large and shallow slow rupturing subevent within one earthquake along the curved slab interface using multiple independent techniques. We could link different stages of the complex earthquake to the different results obtained by international agencies, which shows the strong method dependency of their results when applied to such a complex rupture. Finally, we were able to link the recorded tsunami to the slow rupturing event. The comparison with known large tsunamigenic thrust events as the 2010 Maule, 2011 Tohoku, or 2015 Illapel earthquakes revealed strong similarities in the static and dynamic rupture properties as well as in distribution of back-projected energy and aftershocks.

This earthquake highlights the necessity of a more comprehensive analysis of seismic signals for tsunami early warning, especially where no near field GNSS stations are available to constrain the rupture.

Appendix A: Main Shock MT Inversion

MTs are the mathematical representation of a seismic source based on generalized force couples, and the centroid MT method relates those force couples with the ground motion generated by them as long as a point-source characterization is well suited for the evaluated problem. The centroid MT inversion returns the centroid location and time, duration, and the six independent MT components of the source, which encode the scalar moment and focal mechanism of the event.

A1. Centroid and W-Phase MT Inversion of the Doublet

In order to characterize the South Sandwich 12 August 2021 earthquake, we apply a centroid MT inversion for each subevent individually by inverting them using different distance-dependent time windows (Table A1).

Table A1
Chosen Dynamic Time Windows for the Inversions

Inversion	A_{CMT}	B_{CMT}	C_{CMT}	D_{CMT}
P wave time window relative to t_P				
t_{min} (s)	−220 (100)	—	—	−130 (100)
t_{max} (s)	+70 (100)	—	—	+160 (100)
S wave time window relative to t_S				
t_{min} (s)	−220 (100)	—	—	−130 (100)
t_{max} (s)	+70 (100)	—	—	+160 (100)
W-Phase time window relative to t_P				
t_{min} (s)	—	−1,000 (1,000)	—	—
t_{max} (s)	—	+1,100 (1,000)	—	—
Full-waveform inversion time window relative to t_S				
t_{min} (s)	—	—	−1,000 (1,000)	—
t_{max} (s)	—	—	$v_{surf}(2.0)$[a] + 1,000 (1,000)	—

Note. Corner times of the used cosine taper are defined as t_{min}, $t_{min} + t_{taper}$, $t_{max} - t_{taper}$, t_{max} with respect to the inverted event centroid time (format: <time> (taper)).
t_P—*P* wave arrival time using AK135.
t_S—*S* wave arrival time using AK135.
[a]$v_{surf}(XX)$ indicating surface wave arrival with velocity of *XX* km/s.

Journal of Geophysical Research: Solid Earth 10.1029/2022JB024646

Conflict of Interest

The authors declare no conflicts of interest relevant to this study.

Data Availability Statement

All data used in this study are openly available from the below sources.

Seismic broadband recordings for the main shock and the aftershocks were downloaded from the Incorporated Research Institutions for Seismology (IRIS) Data Management Center (https://ds.iris.edu/wilbert3/find_event, last accessed November 2021) and the GEOFON program of the GFZ German Research Centre for Geosciences using data from the GEVN partner networks (last accessed November 2021). A detailed overview on the used networks is given in the supplement. Event information were downloaded from Global CMT (Dziewoński et al., 1981; Ekström et al., 2012), USGS (U.S. Geological Survey (USGS), 2020), and the GEOFON program of the GFZ German Research Centre for Geosciences using data from the GEVN partner networks. Tide gauge data were provided by Flanders Marine Institute (VLIZ), Intergovernmental Oceanographic Commission (IOC) (2021). Bathymetric data from NOAA National Geophysical Data Center (2009) were used for the plots.

The used software included Pyrocko (Heimann et al., 2019), Grond (Heimann et al., 2018), GMT 5.4 (Wessel et al., 2013), and Seiscloud (Cesca, 2020) for the seismological studies and plots. Green's functions used within Grond were calculated using QSSP, PsGrn, PsCmp, and Pyrocko (Heimann et al., 2017; Wang et al., 2006, 2017). Tsunami modeling was done using easyWave (https://www.gfz-potsdam.de/en/software/tsunami-wave-propagations-easywave).

Acknowledgments
Malte Metz was supported by the BMBF project EWRICA (03G0891B), Angela Carrillo Ponce and Felipe Vera received funds by the National Agency for Research and Development (ANID)/Scholarship Program: Doctorado BECAS CHILE 2019-72200544 (ACP) and 2017-72180166 (FV). Open Access funding enabled and organized by Projekt DEAL.

References

Abe, K. (1972). Focal process of the South Sandwich Islands Earthquake of May 26, 1964. *Physics of the Earth and Planetary Interiors*, *5*, 110–122. https://doi.org/10.1016/0031-9201(72)90080-5

Abe, K. (1981). Magnitudes of large shallow earthquakes from 1904 to 1980. *Physics of the Earth and Planetary Interiors*, *27*(1), 72–92. https://doi.org/10.1016/0031-9201(81)90088-1

Abe, K. (1982). Magnitude, seismic moment and apparent stress for major deep earthquakes. *Journal of Physics of the Earth*, *30*, 321–330. https://doi.org/10.4294/jpe1952.30.321

Albuquerque Seismological Laboratory (ASL)/USGS. (1988). *Global Seismograph Network-IRIS/USGS*. International Federation of Digital Seismograph Networks. https://doi.org/10.7914/SN/IU

Albuquerque Seismological Laboratory (ASL)/USGS. (1993). *Global Telemetered Seismograph Network (USAF/USGS)*. International Federation of Digital Seismograph Networks. https://doi.org/10.7914/SN/GT

Albuquerque Seismological Laboratory (ASL)/USGS. (2006). *Caribbean USGS Network*. International Federation of Digital Seismograph Networks. https://doi.org/10.7914/SN/CU

Alfred Wegener Institute for Polar and Marine Research (AWI). (1993). AW-AWI Network Antarctica. *Deutsches GeoForschungsZentrum GFZ*. https://doi.org/10.14470/NJ617293

Audet, P., Bostock, M., Christensen, N., & Peacock, S. (2009). Seismic evidence for overpressured subducted oceanic crust and megathrust fault sealing. *Nature*, *457*, 76–78. https://doi.org/10.1038/nature07650

Australian National University (Anu, Australia). (2011). *Australian Seismometers in Schools*. International Federation of Digital Seismograph Networks. https://doi.org/10.7914/SN/S1

Becker, J. J., Sandwell, D. T., Smith, W. H. F., Braud, J., Binder, B., Depner, J., et al. (2009). Global bathymetry and elevation data at 30 arc seconds resolution: Srtm30_plus. *Marine Geodesy*, *32*, 355–371. https://doi.org/10.1080/01490410903297766

Beniest, A., & Schellart, W. P. (2020). A geological map of the Scotia Sea area constrained by bathymetry, geological data, geophysical data and seismic tomography models from the deep mantle. *Earth-Science Reviews*, *210*, 103391. https://doi.org/10.1016/j.earscirev.2020.103391

Bilek, S. L., & Lay, T. (2018). Subduction zone megathrust earthquakes. *Geosphere*, *14*(4), 1468–1500. https://doi.org/10.1130/GES01608.1

Bilek, S. L., Lay, T., & Ruff, L. J. (2004). Radiated seismic energy and earthquake source duration variations from teleseismic source time functions for shallow subduction zone thrust earthquakes. *Journal of Geophysical Research*, *109*, B09308. https://doi.org/10.1029/2004JB003039

Bird, P. (2003). An updated digital model of plate boundaries. *Geochemistry, Geophysics, Geosystems*, *4*(3), 1027. https://doi.org/10.1029/2001GC000252

Bondár, I., Engdahl, E. R., Villaseñor, A., Harris, J., & Storchak, D. (2015). ISC-GEM: Global Instrumental Earthquake Catalogue (1900-2009), II. Location and seismicity patterns. *Physics of the Earth and Planetary Interiors*, *239*, 2–13. https://doi.org/10.1016/j.pepi.2014.06.002

Brune, J. N. (1970). Tectonic stress and the spectra, of seismic shear waves from earthquakes. *Journal of Geophysical Research*, *75*(26), 4997–5009. https://doi.org/10.1029/JB075i026p04997

Carrillo Ponce, A., Dahm, T., Cesca, S., Tilmann, F., Babeyko, A., & Heimann, S. (2021). Bayesian multiple rupture plane inversion to assess rupture complexity: Application to the 2018 Mw 7.9 Alaska earthquake. In *EGU General Assembly 2021*. https://doi.org/10.5194/egusphere-egu21-1583

Cesca, S. (2020). Seiscloud, a tool for density-based seismicity clustering and visualization. *Journal of Seismology*, *24*, 443–457. https://doi.org/10.1007/s10950-020-09921-8

Cesca, S., Sugan, M., Rudzinski, L., Vajedian, S., Niemz, P., Plank, S., et al. (2022). Massive earthquake swarm driven by magmatic intrusion at the Bransfield Strait, Antarctica. *Communications Earth & Environment*, *3*, 89. https://doi.org/10.1038/s43247-022-00418-5

CONICET (OSCO). (2017). Observatorio Sismológico CIGEOBIO CONICET (OSCO). Retrieved from http://sismo.conicet.gov.ar

Journal of Geophysical Research: Solid Earth 10.1029/2022JB024646

Dahm, T., Heimann, S., Metz, M., & Isken, M. P. (2021). A self-similar dynamic rupture model based on the simplified wave-rupture analogy. *Geophysical Journal International*, *225*, 1586–1604. https://doi.org/10.1093/gji/ggab045

Department of Geological Survey of Botswana. (2001). Botswana Seismological Network (BSN).

Duan, B. (2012). Dynamic rupture of the 2011 mw 9.0 Tohoku-Oki earthquake: Roles of a possible subducting seamount. *Journal of Geophysical Research*, *117*, B05311. https://doi.org/10.1029/2011JB009124

Duputel, Z., Rivera, L., Kanamori, H., & Hayes, G. (2012). W phase source inversion for moderate to large earthquakes (1990–2010). *Geophysical Journal International*, *189*(2), 1125–1147. https://doi.org/10.1111/j.1365-246X.2012.05419.x

Dziewoński, A. M., Chou, T.-A., & Woodhouse, J. H. (1981). Determination of earthquake source parameters from waveform data for studies of global and regional seismicity. *Journal of Geophysical Research*, *86*(B4), 2825–2852. https://doi.org/10.1029/JB086iB04p02825

Ekström, G., Nettles, M., & Dziewoński, A. M. (2012). The global CMT project 2004–2010: Centroid-moment tensors for 13,017 earthquakes. *Physics of the Earth and Planetary Interiors*, *200*(201), 1–9. https://doi.org/10.1016/j.pepi.2012.04.002

Flanders Marine Institute (VLIZ), Intergovernmental Oceanographic Commission (IOC). (2021). Sea level station monitoring facility Retrieved from http://www.ioc-sealevelmonitoring.org

Forsyth, D. W. (1975). Fault Plane solutions and tectonics of the South Atlantic and Scotia Sea. *Journal of Geophysical Research*, *80*(11), 1429–1443. https://doi.org/10.1029/JB080i011p01429

GEOFON Data Centre. (1993). GEOFON Seismic Network. Deutsches GeoForschungsZentrum GFZ. Retrieved from http://geofon.gfz-potsdam.de/doi/network/GE

Geoscience Australia (GA). (1994). Australian National Seismograph Network (ANSN).

GEUS Geological Survey of Denmark and Greenland. (1976). Danish Seismological Network.

GFZ German Research Centre For Geosciences, & Institut Des Sciences De L'Univers-Centre National De La Recherche CNRS-INSU. (2006). IPOC Seismic Network. Integrated Plate boundary Observatory Chile-IPOC. https://doi.org/10.14470/pk615318

Giner-Robles, J. L., Pérez-López, R., Rodríguez-Pascua, M. A., Martínez-Díaz, J. J., & González-Casado, J. M. (2009). *Present-day strain field on the south American slab underneath the Sandwich plate (southern Atlantic ocean): A kinematic model* (Vol. 328, pp. 155–167). Geological Society Special Publication. https://doi.org/10.1144/SP328.6

Glanville, H. (2021). *Muswellbrook (Mus)* [Dataset]. International Federation of Digital Seismograph Networks. https://doi.org/10.7914/SN/YW_2021

Glimsdal, S., Løvholt, F., Harbitz, C., Romano, F., Lorito, S., Orefice, S., et al. (2019). A new approximate method for quantifying tsunami maximum inundation height probability. *Pure and Applied Geophysics*, *176*, 3227–3246. https://doi.org/10.1007/s00024-019-02091-w

Goto, C., Ogawa, Y., Shuto, N., & Imamura, F. (1997). *IUGG/IOC time project, numerical method of tsunami simulation with the leap-frog scheme* (Vol. 35). IOC Manuals and Guides.

Hayes, G. P., Moore, G. L., Portner, D. E., Hearne, M., Flamme, H., Furtney, M., & Smoczyk, G. M. (2018). Slab2, a comprehensive subduction zone geometry model. *Science*, *362*(6410), 58–61. https://doi.org/10.1126/science.aat4723

Heimann, S., Isken, M., Kühn, D., Sudhaus, H., Steinberg, A., Vasyura-Bathke, H., et al. (2018). Grond—A probabilistic earthquake source inversion framework. *GFZ Data Services*. https://doi.org/10.5880/GFZ.2.1.2018.003

Heimann, S., Kriegerowski, M., Isken, M., Cesca, S., Daout, S., Grigoli, F., et al. (2017). *Pyrocko—An open-source seismology toolbox and library*. GFZ Data Services. Retrieved from http://dataservices.gfz-potsdam.de/panmetaworks/showshort.php?id=escidoc:2144891

Heimann, S., Vasyura-Bathke, H., Sudhaus, H., Paul Isken, M., Kriegerowski, M., Steinberg, A., & Dahm, T. (2019). A Python framework for efficient use of pre-computed Green's functions in seismological and other physical forward and inverse source problems. *Solid Earth*, *10*(6), 1921–1935. https://doi.org/10.5194/se-10-1921-2019

Hubbard, J. (2021). Mixed earthquake signals in the South Sandwich Islands. https://doi.org/10.32858/temblor.202

Ide, S., Baltay, A., & Beroza, G. C. (2011). Shallow dynamic overshoot and energetic deep rupture in the 2011 Mw 9.0 Tohoku-Oki earthquake. *Science*, *332*(6036), 1426–1429. https://doi.org/10.1126/science.1207020

INGEOMINAS-Servicio Geologico Colombiano (SGC Colombia). (1993). *Red Sismologica Nacional de Colombia*. International Federation of Digital Seismograph Networks. Retrieved from https://www.fdsn.org/networks/detail/CM/

Institut de physique du globe de Paris (IPGP). (2008). *GNSS, seismic broadband and strong motion permanent networks in West Indies*. Université de Paris: Institut de physique du globe de Paris (IPGP). https://doi.org/10.18715/ANTILLES.WI

Institut de physique du globe de Paris (IPGP), & École et Observatoire des Sciences de la Terre de Strasbourg (EOST). (1982). *GEOSCOPE, French Global Network of broad band seismic stations*. Université de Paris: Institut de physique du globe de Paris (IPGP). https://doi.org/10.18715/GEOSCOPE.G

Institute of Geological and Nuclear Sciences Ltd (GNS New Zealand). (1988). New Zealand National Seismograph Network. Retrieved from http://info.geonet.org.nz/display/equip/New+Zealand+National+Seismograph+Network

Instituto Geofisico Escuela Politecnica Nacional (IG-EPN Ecuador). (2002). Ecuador Seismic Network.

Instituto Nicaraguense de Estudios Territoriales (INETER). (1975). Nicaraguan Seismic Network. International Federation of Digital Seismograph Networks. Retrieved from https://www.fdsn.org/networks/detail/NU/

Ishii, M., Shearer, P. M., Houston, H., & Vidale, J. E. (2007). Teleseismic P wave imaging of the 26 December 2004 Sumatra-Andaman and 28 March 2005 Sumatra earthquake ruptures using the Hi-net array. *Journal of Geophysical Research*, *112*, B11307. https://doi.org/10.1029/2006JB004700

Istituto Nazionale di Oceanografia e di Geofisica Sperimentale. (1992). *Antarctic Seismographic Argentinean Italian Network-OGS*. International Federation of Digital Seismograph Network. https://doi.org/10.7914/SN/AI

Jia, Z., Zhan, Z., & Kanamori, H. (2022). The 2021 South Sandwich Island Mw 8.2 earthquake: A slow event sandwiched between regular ruptures. *Geophysical Research Letters*, *49*, e2021GL097104. https://doi.org/10.1029/2021GL097104

Kagan, Y. Y. (1991). 3-D rotation of double-couple earthquake sources. *Geophysical Journal International*, *106*(3), 709–716. https://doi.org/10.1111/j.1365-246X.1991.tb06343.x

Kamigaichi, O. (2015). Tsunami forecasting and warning. In R. Meyers (Ed.), *Extreme environmental events*. Springer. https://doi.org/10.1007/978-1-4419-7695-6

Kanamori, H., & Rivera, L. (2008). Source inversion of W phase: Speeding up seismic tsunami warning. *Geophysical Journal International*, *175*(1), 222–238. https://doi.org/10.1111/j.1365-246X.2008.03887.x

Kato, A., Iidaka, T., Ikuta, R., Yoshida, Y., Katsuma, K., Iwasaki, T., et al. (2010). Variations of fluid pressure within the subducting oceanic crust and slow earthquakes. *Geophysical Research Letters*, *37*, L14310. https://doi.org/10.1029/2010GL043723

Kennett, B., & Engdahl, E. (1991). Traveltimes for global earthquake location and phase identification. *Geophysical Journal International*, *105*(2), 429–465. https://doi.org/10.1111/j.1365-246x.1991.tb06724.x

Journal of Geophysical Research: Solid Earth 10.1029/2022JB024646

Kennett, B., Engdahl, E., & Buland, R. (1995). Constraints on seismic velocities in the Earth from traveltimes. *Geophysical Journal International*, *122*(1), 108–124. https://doi.org/10.1111/j.1365-246X.1995.tb03540.x

Kiser, E., & Ishii, M. (2012). Combining seismic arrays to image the high-frequency characteristics of large earthquakes. *Geophysical Journal International*, *188*(3), 1117–1128. https://doi.org/10.1111/j.1365-246X.2011.05299.x

Kodaira, S., Iidaka, T., Kato, A., Park, J.-O., Iwasaki, T., & Kaneda, Y. (2004). High pore fluid pressure may cause silent slip in the Nankai Trough. *Science*, *304*. https://doi.org/10.1126/science.1096535

Koper, K. D., Hutko, A. R., Lay, T., & Sufri, O. (2012). Imaging short-period seismic radiation from the 27 February 2010 Chile (mw 8.8) earthquake by back-projection of p, pp, and pkikp waves. *Journal of Geophysical Research*, *117*, B02308. https://doi.org/10.1029/2011JB008576

Larter, R. D., Vanneste, L. E., Morris, P., & Smythe, D. K. (2003). *Structure and tectonic evolution of the South Sandwich arc* (Vol. 219, pp. 255–284). Geological Society Special Publication. https://doi.org/10.1144/gsl.sp.2003.219.01.13

Lay, T. (2018). A review of the rupture characteristics of the 2011 Tohoku-Oki mw 9.1 earthquake. *Tectonophysics*, *733*, 4–36. https://doi.org/10.1016/j.tecto.2017.09.022

Lay, T., Kanamori, H., Ammon, C. J., Koper, K. D., Hutko, A. R., Ye, L., et al. (2012). Depth-varying rupture properties of subduction zone megathrust faults. *Journal of Geophysical Research*, *117*, B04311. https://doi.org/10.1029/2011JB009133

Leat, P. T., Pearce, J. A., Barker, P. F., Millar, I. L., Barry, T. L., & Larter, R. D. (2004). Magma genesis and mantle flow at a subducting slab edge: The South Sandwich arc-basin system. *Earth and Planetary Science Letters*, *227*(1–2), 17–35. https://doi.org/10.1016/j.epsl.2004.08.016

Lee, S.-J., Huang, B.-S., Ando, M., Chiu, H.-C., & Wang, J.-H. (2011). Evidence of large scale repeating slip during the 2011 Tohoku-Oki earthquake. *Geophysical Research Letters*, *38*, L19306. https://doi.org/10.1029/2011GL049580

Madariaga, R. (1977). High-frequency radiation from crack (stress drop) models of earthquake faulting. *Geophysical Journal International*, *51*(3), 625–651. https://doi.org/10.1111/j.1365-246X.1977.tb04211.x

Marty, S., Passelègue, F. X., Aubry, J., Bhat, H. S., Schubnel, A., & Madariaga, R. (2019). Origin of high-frequency radiation during laboratory earthquakes. *Geophysical Research Letters*, *46*, 3755–3763. https://doi.org/10.1029/2018GL080519

Meng, L., Inbal, A., & Ampuero, J. P. (2011). A window into the complexity of the dynamic rupture of the 2011 mw 9 Tohoku-Oki earthquake. *Geophysical Research Letters*, *38*, L00G07. https://doi.org/10.1029/2011GL048118

Meng, L., Zhang, A., & Yagi, Y. (2016). Improving back projection imaging with a novel physics-based aftershock calibration approach: A case study of the 2015 Gorkha earthquake. *Geophysical Research Letters*, *43*, 628–636. https://doi.org/10.1002/2015GL067034

Metz, M. (2019). *A quasi-dynamic and self-consistent rupture model to simulate earthquake ruptures (Master Thesis)*. Universität Potsdam. https://doi.org/10.25932/publishup-47310

Miller, P. K., Saffer, D. M., Abers, G. A., Shillington, D. J., Bécel, A., Li, J., & Bate, C. (2021). P- and S-wave velocities of exhumed metasediments from the Alaskan subduction zone: Implications for the in situ conditions along the megathrust. *Geophysical Research Letters*, *48*, e2021GL094511. https://doi.org/10.1029/2021GL094511

Neidell, N. S., & Taner, M. T. (1971). Semblance and other coherency measures for multichannel data. *Geophysics*, *36*(3), 482–497. https://doi.org/10.1190/1.1440186

NOAA National Geophysical Data Center. (2009). *ETOPO1 1 arc-minute global relief model*. NOAA National Centers for Environmental Information. https://doi.org/10.7289/V5C8276M

Observatório Nacional, Rio de Janeiro. (2011). *Rede Sismográfica do Sul e do Sudeste*. International Federation of Digital Seismograph Networks. https://doi.org/10.7914/SN/ON

Observatorio San Calixto (OSC Bolivia). (1913). *Bolvian Seismic Network*. International Federation of Digital Seismograph Networks. https://doi.org/10.7914/SN/BV

Okal, E. A., & Hartnady, C. J. (2009). The South Sandwich Islands earthquake of 27 June 1929: Seismological study and inference on tsunami risk for the South Atlantic. *South African Journal of Geology*, *112*(3–4), 359–370. https://doi.org/10.2113/gssajg.112.3-4.359

Palo, M., Tilmann, F., Krueger, F., Ehlert, L., & Lange, D. (2014). High-frequency seismic radiation from Maule earthquake (Mw 8.8, 2010 February 27) inferred from high-resolution backprojection analysis. *Geophysical Journal International*, *199*(2), 1058–1077. https://doi.org/10.1093/gji/ggu311

Passelegue, F., Almakari, M., Dublanchet, P., Barras, F., Fortin, J., & Violay, M. (2020). Initial effective stress controls the nature of earthquakes. *Nature Communications*, *11*, 5132. https://doi.org/10.1038/s41467-020-18937-0

Penn State University. (2004). *AfricaArray*. International Federation of Digital Seismograph Networks. https://doi.org/10.7914/SN/AF

Purcaru, G., & Berckhemer, H. (1982). Quantitative relations of seismic source parameters and a classification of earthquakes. *Tectonophysics*, *84*(1), 57–128. https://doi.org/10.1016/0040-1951(82)90154-8

Roger, J., Hebert, H., Jamelot, A., Gusman, A., Power, W., & Hubbard, J. (2022). *The south sandwich circum-Antarctic tsunami of August 12, 2021: Widespread propagation using oceanic ridges*. In EGU General Assembly 2022. https://doi.org/10.5194/egusphere-egu22-904

Romano, F., Piatanesi, A., Lorito, S., Tolomei, C., Atzori, S., & Murphy, S. (2016). Optimal time alignment of tide-gauge tsunami waveforms in nonlinear inversions: Application to the 2015 Illapel (Chile) earthquake. *Geophysical Research Letters*, *43*, 226–311. https://doi.org/10.1002/2016GL071310

Rössler, D., Krueger, F., Ohrnberger, M., & Ehlert, L. (2010). Rapid characterisation of large earthquakes by multiple seismic broadband arrays. *Natural Hazards and Earth System Sciences*, *10*(4), 923–932.

Scripps Institution of Oceanography. (1986). *Global Seismograph Network-IRIS/IDA*. International Federation of Digital Seismograph Networks. https://doi.org/10.7914/SN/II

Simons, M., Minson, S. E., Sladen, A., Ortega, F., Jiang, J., Owen, S. E., et al. (2011). The 2011 magnitude 9.0 Tohoku-Oki earthquake: Mosaicking the megathrust from seconds to centuries. *Science*, *332*(6036), 1421–1425. https://doi.org/10.1126/science.1206731

Song, T.-R. A., Helmberger, D., Brudzinski, M., Clayton, R., Davis, P., Perez-Campos, X., & Singh, S. (2009). Subducting slab ultra-slow velocity layer coinciding with silent earthquakes in Southern Mexico. *Science*, *324*, 502–506. https://doi.org/10.1126/science.1167595

Suzuki, W., Aoi, S., Sekiguchi, H., & Kunugi, T. (2011). Rupture process of the 2011 Tohoku-Oki mega-thrust earthquake (m9.0) inverted from strong-motion data. *Geophysical Research Letters*, *38*, L00G16. https://doi.org/10.1029/2011GL049136

Thomas, C., Livermore, R., & Pollitz, F. (2003). Motion of the Scotia Sea plates. *Geophysical Journal International*, *155*(3), 789–804. https://doi.org/10.1111/j.1365-246X.2003.02069.x

Tilmann, F., Zhang, Y., Moreno, M., Saul, J., Eckelmann, F., Palo, M., et al. (2016). The 2015 Illapel earthquake, central Chile, a type case for a characteristic earthquake? *Geophysical Research Letters*, *43*, 574–583. https://doi.org/10.1002/2015GL066963

Universidad de Chile. (2012). Red Sismologica Nacional. International Federation of Digital Seismograph Networks. Retrieved from https://www.fdsn.org/networks/detail/C1/

Universidad de Chile, Dept de Geofisica (DGF UChile Chile). (1991). Chilean National Seismic Network.

Universidad Nacional de San Juan (Unsjargentina). (1958). West Central Argentina Network.

Journal of Geophysical Research: Solid Earth 10.1029/2022JB024646

Universidade de Sao Paulo (USP). (1988). Brazilian Lithospheric Seismic Project (BLSP).

U.S. Geological Survey (USGS). (2020). Earthquake lists, maps, and statistics. Retrieved from https://www.usgs.gov/natural-hazards/earthquake-hazards/lists-maps-and-statistics

Vera, F., Tilmann, F., & Saul, J. (2021). A decade of short-period earthquake rupture histories from multi-array back-projection. *Earth and Space Science Open Archive*. https://doi.org/10.1002/essoar.10508660.1

Wang, D., & Mori, J. (2011). Rupture process of the 2011 off the Pacific coast of Tohoku earthquake (mw 9.0) as imaged with back-projection of teleseismic p-waves. *Earth, Planets and Space*, *63*, 17. https://doi.org/10.5047/eps.2011.05.029

Wang, R., Heimann, S., Zhang, Y., Wang, H., & Dahm, T. (2017). Complete synthetic seismograms based on a spherical self-gravitating Earth model with an atmosphere-ocean-mantle-core structure. *Geophysical Journal International*, *210*(3), 1739–1764. https://doi.org/10.1093/gji/ggx259

Wang, R., Lorenzo-Martin, F., & Roth, F. (2006). PsGrn/PsCmp—A new code for calculating co- and post-seismic deformation, geoid and gravity changes based on the viscoelastic-gravitational dislocation theory. *Computers & Geosciences*, *32*, 527–541. https://doi.org/10.1016/j.cageo.2005.08.006

Wessel, P., Smith, W. H., Scharroo, R., Luis, J., & Wobbe, F. (2013). Generic mapping tools: Improved version released. *Eos, Transactions American Geophysical Union*, *94*, 409–410. https://doi.org/10.1002/2013EO450001

Wilson, J. T. (1940). The love waves of the South Atlantic earthquake of August 28, 1933. *Bulletin of the Seismological Society of America*, *30*(3), 273–301. https://doi.org/10.1785/bssa0300030273

4 | Third publication

The July-December 2022 earthquake sequence in the southeastern Fars arc of Zagros mountains, Iran

M. Metz, B. M. Asayesh, M. M. Aref, M. Jamalreyhani, P. Büyükakpınar, and T. Dahm
(2023)

Submitted to Seismica

Non-peer reviewed manuscript submitted to SEISMICA

The July-December 2022 earthquake sequence in the southeastern Fars arc of Zagros mountains, Iran

Malte Metz * [1,2], **Behnam Maleki Asayesh** [1,2], **Mohammad Mohseni Aref** [2], **Mohammadreza Jamalreyhani** [3], **Pınar Büyükakpınar** [1,2], **Torsten Dahm** [1,2]

[1]GFZ German Research Centre for Geosciences, Potsdam, Germany, [2]Institute of Geosciences, University of Potsdam, Potsdam, Germany, [3]Institute of Geophysics, University of Tehran, Tehran, Iran

Author contributions: *Conceptualization*: Malte Metz, Behnam Maleki Asayesh, Mohammad Mohseni Aref, Mohammadreza Jamalreyhani. *Methodology*: Malte Metz. *Software*: Malte Metz. *Formal Analysis*: Malte Metz. *Data curation*: Mohammad Mohseni Aref, Mohammadreza Jamalreyhani, Pınar Büyükakpınar. *Writing - Original draft*: Malte Metz, Behnam Maleki Asayesh, Mohammad Mohseni Aref, Mohammadreza Jamalreyhani. *Writing - Review & Editing*: Malte Metz, Behnam Maleki Asayesh, Mohammadreza Jamalreyhani, Pınar Büyükakpınar, Torsten Dahm. *Visualization*: Malte Metz, Behnam Maleki Asayesh. *Supervision*: Pınar Büyükakpınar, Torsten Dahm.

Abstract Within two hours on 01 July 2022, three earthquakes of M_w 5.8–6.0 hit the SE Fars Arc, Iran. In the following months, the region, characterized by the collision of the Iranian and the Arabian plate, thrust faulting, and salt diapirism, was struck by more than 120 aftershocks of mL 3.1–5.2, of which two of the largest events occurred within one minute on 23 July 2022 in spatial vicinity to each other. We analyzed both the large mainshocks and aftershocks using different techniques, such as the inversion of seismic and satellite deformation data in a joint process, and aftershock relocation. Our results indicate the activation of thrust faults within the lower sedimentary cover of the region along with high aftershock activity at significantly larger depth, supporting the model of a crustal strain decoupling during the collision in the Fars Arc. We resolved a magnitude difference of $>$0.2 magnitude units between seismic and joint seismic and satellite deformation inversions probably caused by afterslip, thereby allowing to bridge between results from international agencies and earlier studies. We also find evidence for an event doublet and triplet activating the same or adjacent faults within the sedimentary cover and the basement

Non-technical summary On 01 July 2022, three moderate earthquakes with magnitudes of 5.8–6.0 occurred in the Zagros mountain range in the Hormozghan province, SE Iran. Their close occurrence in space and time impedes the analysis of such events. Using seismic and satellite deformation data within well-proven and newly developed earthquake parameter estimation tools, we found evidence for south-dipping thrust events within the shallow sedimentary layer. The relocation of more than 120 aftershocks with local magnitudes 3.1-–5.2 revealed a strong spatial concentration in larger depths of 10–15 km beneath the mainshocks. This result is consistent with the

*Corresponding author: mmetz@gfz-potsdam.de

scenario of shallow-depth mainshocks followed by separated, deeper aftershock sequences, as already observed at the western edge of the Hormuz Strait.

1 Introduction

The north-south convergence of ~2–3 cm yr^{-1} between the Arabian and Eurasian plates has led to active faulting and folding, volcanic activities, mountainous terrain, and variable crustal thickness in the Iranian Plateau (IP) (e.g., Stoecklin, 1968; Vernant et al., 2004; Viltres et al., 2022). This convergence gave rise to the 1,800 km long and 200-300 km wide Zagros continental collision zone in the southwestern part of the IP, which accommodates approximately one-third to one-half of the plate motion (e.g., Vernant et al., 2004; Masson et al., 2005). The Zagros mountain range, which is one of the seismically most active regions in the Alpine-Himalayan orogenic belt, is subdivided into three major tectonostratigraphic domains from SW to NE, (1) the Mesopotamia-Persian Gulf Foreland Basin, (2) the Zagros Fold-Thrust Belt (ZFTB), and (3) High Zagros Zone (HZZ). The Simply Folded Belt (SFB) or Zagros Foreland Folded Belt (ZFFB) as a subdomain of ZFTB, is the topographically lower-elevation part of the range where most of the active deformation in the Zagros is concentrated (e.g., Falcon, 1974; Hessami et al., 2001; Talebian and Jackson, 2004; Alavi, 2007; Oveisi et al., 2009). The SFB itself is laterally subdivided into four physiographic provinces from NW to SE, namely the Kirkuk Embayment, the Lurestan Arc, the Dezful Embayment, and the Fars Arc (Fig. 1a) (e.g., Stoecklin, 1968; Alavi, 2007; Nissen et al., 2011). The collision zone in the foreland involves 10–15 km thick sections of sedimentary rocks, including extended layers of evaporites and salt decoupling the deformation in the sedimentary strata from the Arabian continental basement (e.g., Stoecklin, 1968). This exceptional setting has resulted in one of the world's most productive oil and gas basins (Jamalreyhani et al., 2021).

Multiple earthquakes and doublets are triggered and subsequential mainshocks of comparable size rupturing the same or adjacent faults within a short time (e.g., Lay and Kanamori, 1980; Ammon et al., 2008). The occurrence of doublets is explained by heterogeneous stress on pre-existing faults with geometrical complexities (e.g., steps, bends) and stress transfers from the first to the second event of the doublet (e.g., Xu and Schwartz, 1993; Jia et al., 2020; Zhang et al., 2021; Taymaz et al., 2022; Astiz et al., 1988). Doublets have been observed in different tectonic settings, as (1) within subduction zones (Lay and Kanamori, 1980; Xu and Schwartz, 1993; Ammon et al., 2008; Lay, 2015; Ye et al., 2013, 2016; Jia et al., 2020), (2) in collision zones (e.g., Thapa et al., 2018), (3) transform fault systems (e.g., Zhang et al., 2021; Sokos et al., 2015; Dal Zilio and Ampuero, 2023) or (4) on normal faults in sedimentary basins (e.g., Cesca et al., 2013).

The central IP and its bounding tectonic structure were hit by several doublets or multiple earthquakes during the last decade, as the NW Iranian 2012 Ahar-Varzagan and 2020 Qotur-Ravian doublets (Ansari, 2016; Ghods et al., 2015; Donner et al., 2015; Momeni and Tatar, 2018; Taymaz et al., 2022) or the December 2017 Hojedk triplet in SE Iran (e.g., Freund, 1970; Walker and Jackson, 2002; Savidge et al., 2019; Asayesh et al., 2020) (Fig. 1a). The occurrence of doublets in the ZFTB is associated with the complex thrust and fold belts in the Zagros mountains with a highly deformed and sliding sedimentary and evaporitic cover with massive syncline and anticline structures (Roustaei et al., 2010). More recently, ZFTB hosted doublets in Southern Iran, the so-called 2021 Fin doublet (Fathian et al., 2022; Rezapour and

Jamalreyhani, 2022), and the 2022 Charak events. These events drew the attention of scientists to the region to better understand the physical mechanism of earthquake doublets, which is crucial for hazard and risk assessment.

Our study area is located in the Fars Arc (FA), which is the ∼700 km-long segment situated in the East of the SFB with a high-rate seismicity zone in Zagros (Fig. 1b) (e.g., Karasözen et al., 2019). FA is bounded by the Kazerun Fault in the West and the Bandar Abbas syntaxis in the East and works as the transition zone to the Makran accretionary to the East (Edey et al., 2020) (Fig. 1b). The seismicity of the FA is dominated by shallow thrust events on steep dipping (30°-60°) blind faults in the sedimentary cover or the underlying crystalline basement (e.g., Jahani et al., 2009; Nissen et al., 2011). Tatar et al. (2004) revealed 10 mm yr^{-1} present-day shortening, with NNE-SSW trending at the center of the FA. Surface shortening is here accommodated by several symmetric W-E to NW-SE trending anticlines and synclines with amplitudes within the scale of kilometers and wavelengths of ∼10-–20 km (e.g., Edey et al., 2020). The relationship between buried seismic faults and surface anticlines in the FA is still debated (Walker et al., 2005). Several surface diapirs, which indicate the presence of the Precambrian-Cambrian Hormuz salt layer between the basement and sedimentary cover, are also observed in the FA (Jahani et al., 2009). The occurrence of anthropogenic earthquakes has been reported in this collision zone recently (Jamalreyhani et al., 2021, >[and references therein).

Recently, on 14 November 2021, the Fin area in the FA was struck by an earthquake doublet (M_w 6.2 and M_w 6.3) (Nemati, 2022; Fathian et al., 2022; Rezapour and Jamalreyhani, 2022) co-located with an earlier sequence of earthquakes (M_w 4.9–5.7) on 25 March 2006 (Roustaei et al., 2010) (Fig. 1c, 2). Furthermore, the area experienced many significant single events in 2021, including the 16 March NW Lenge earthquake (M_w 5.9), the 15 June Charak earthquake (M_w 5.5), the 21 June Mogham earthquake (M_w 5.2), and the 25 June Charak second earthquake (M_w 5.6). Some, such as the 2005 Qeshm and the 2006 Fin earthquakes, ruptured the lower sedimentary and were accompanied by aftershocks in significantly greater depth (Nissen et al., 2010, 2011, 2014). This vertical separation of main- and aftershocks might be driven by the mainshock, causing stress changes within the deeper and harder Hormuz layer. As a result of the stress perturbation, the Hormuz salt may flow, leading to a breakup of intercalated, harder, non-evaporitic sediments and surrounding rocks.

Within this tectonic frame, three earthquake sequences stroke the Hormozgan Province, characterized by M_w 5.3–6.1 earthquakes and a series of aftershocks. They occurred on 01 July 2022 (3 earthquakes of M_w 5.7–6.1), further sequence A, on 23 July 2022 (2 earthquakes of M_w 5.3–5.6), further sequence B, and on 30 November 2022 (1 earthquake of M_w 5.6), further sequence C (Fig. 1c, 2, Tab. 1). All sequences hit the same region SW from the Fin doublet, W from the 2005–2009 seismic sequence on the Island of Qeshm and close to the mapped Zagros Foredeep Fault (ZFF) and Mountain Front Fault (MFF). Reported fault mechanisms from different agencies for the earthquakes mainly indicate pure thrust faulting with striking ENE–WSW to ESE–WNW and N-S shortening. Reported locations scatter primarily along the eastern termination of the ZFF. The only exception is earthquake B2 located ∼25 km to the N along the MFF with a strong oblique component. Using satellite geodesy Yang et al. (2023) suggests that two south-dipping thrust faults were activated during the mainshocks A1 and A3 striking ESE with dip angles of 65°and 33°, a peak slip of ∼1.1 m and ∼1.3 m and a geodetic moment release equivalent to M_w 6.22 and M_w 6.23, respectively.

Analysis of earthquake doublets or sequences with interevent times smaller than the travel time of surface waves to a station is challenging, as time windows and stations need to be carefully selected to avoid overlay of seismic sig-

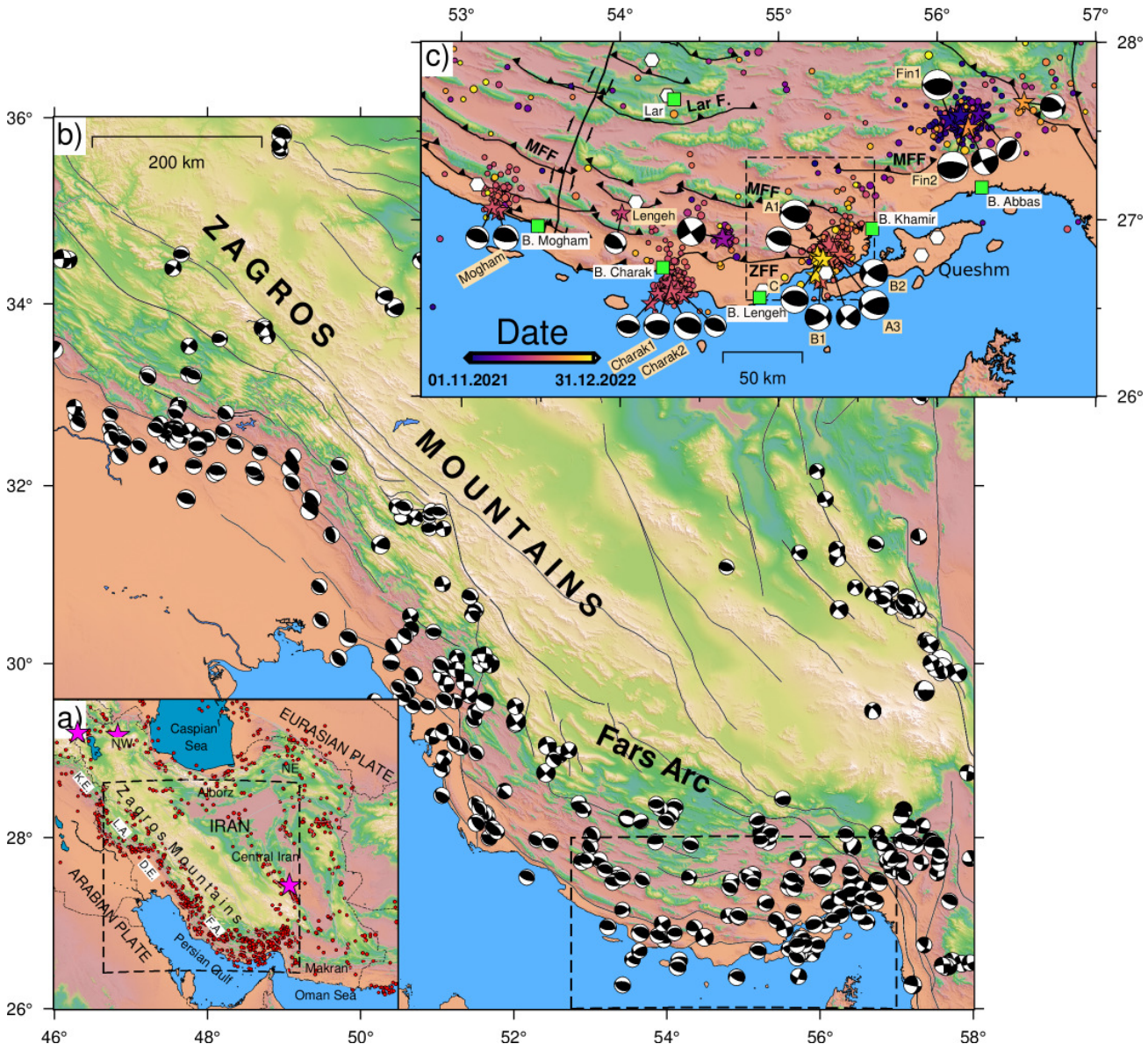

Figure 1 a) The Iranian plateau and its seismotectonic settings. Red circles are M $>$ 5.0 earthquakes from 1900 to 2022 from the USGS catalog. The magenta stars show the location of the 2012 Ahar-Varzagan doublet, the 2020 Qotur-Ravian doublet, and the 2017 Hojedk triplet. The Fars arc (F.A.), Dezful embayment (D.E.), Lurestan arc (L.A.), and the Kirkuk embayment (K.E.) from SE to NW are four tectonostratigraphic domains of the most active part of the Zagros (the Simply Folded Belt). b) SE part of the Zagros Mountains at the leading edge of the Arabia-Eurasia collision zone and focal mechanism of moderate and large events ($M_w >= 5$) from the gCMT catalog until October 2021. Black lines show major mapped active faults. c) A zoom-in of the Hormozghan area. The white hexagons show the historical events (Ambraseys and Melville, 2005) and colored circles demonstrate the seismicity from November 2021 until December 2022 from Iranian Seismological Center (IRSC) catalog. Colored stars depict 33 events with M $>$ 4.5 during this period. For 20 of them, gCMT reported focal mechanisms (black beach balls). The dashed rectangle depicts the location of Fig. 2.

nals (e.g., Jia et al., 2022; Metz et al., 2022). The joint inversion of multiple sources using seismograms and near-field data, e.g., static displacements derived from InSAR (Steinberg et al., 2020, 2022), can help to constrain the geometry of individual earthquake sources. The direct inversion of doublet sources can further resolve the onset and propagation of the ruptures (e.g., Metz et al., 2022). The back projection of the radiated high-frequency energy helps to unravel the rupture processes (e.g., Daout et al., 2020; Steinberg et al., 2022; Metz et al., 2022). Furthermore, the analysis of aftershocks might help in constraining the fault systems activated during the doublets (e.g., Ammon et al.,

Table 1 Selected standard centroid moment tensor inversion results published by different agencies for 01 July 2022, 23 July 2022 and 30 November 2022 earthquakes. Centroid times are given.

ID	Agency	Time	Lat, Lon	Depth	M_w	Strike, Dip, Rake
Sequence A: 01 July 2022						
A1	gCMT	21:32:08	26.68°, 55.18°	12 km	6.1	113°, 52°, 110° 282°, 42°, 66°
	GEOFON	21:32:08	26.89°, 55.23°	10 km	6.0	103°, 52°, 98° 271°, 39°, 80°
	USGS	21:32:08	26.942°, 55.227°	10 km	6.0	95°, 51°, 83° 286°, 39°, 98°
A2	GEOFON	23:24:13	26.85°, 55.29°	10 km	5.9	-, -, - -, -, -
	USGS	23:24:14	26.920°, 55.219°	10 km	5.7	96°, 47°, 100° 262°, 47°, 80°
A3	gCMT	23:25:15	26.69°, 55.13°	12 km	6.1	121°, 45°, 138° 245°, 62°, 54°
	GEOFON	23:25:15	26.82°, 55.33°	10 km	6.0	110°, 22°, 118° 261°, 71°, 79°
	USGS	23:25:15	26.887°, 55.285°	10 km	6.0	94°, 34°, 96° 267°, 56°, 86°
Sequence B: 23 July 2022						
B1	gCMT	16:07:56	26.65°, 55.52°	12 km	5.5	56°, 59°, 34° 307°, 62°, 144°
	GEOFON	16:07:49	26.75°, 55.28°	10 km	5.3	82°, 33°, 108° 240°, 59°, 79°
	USGS	16:07:48	26.880°, 55.210°	10 km	5.3	126°, 35°, 133° 258°, 65°, 65°
B2	gCMT	16:09:08	26.73°, 55.22°	12 km	5.6	128°, 65°, 148° 233°, 61°, 29°
	GEOFON	16:09:08	26.98°, 55.52°	10 km	5.5	120°, 48°, 140° 240°, 61°, 50°
	USGS	16:09:07	27.002°, 55.366°	10 km	5.4	121°, 58°, 150° 228°, 64°, 36°
Sequence C: 30 November 2022						
C1	gCMT	15:17:43	26.69°, 55.21°	12 km	5.6	107°, 54°, 101° 270°, 40°, 77°
	GEOFON	15:17:43	26.83°, 55.29°	10 km	5.6	101°, 68°, 91° 278°, 22°, 28°
	USGS	15:17:41	26.887°, 55.239°	5 km	5.6	94°, 65°, 86° 285°, 26°, 99°

Agencies:
gCMT - Global CMT (Dziewoński et al., 1981; Ekström et al., 2012)
GEOFON - GEOFON program using data from the GEVN partner networks (Quinteros et al., 2021)
USGS - USGS National Earthquake Information Center, PDE

2008; Ghods et al., 2015; Donner et al., 2015; He et al., 2018; Metz et al., 2022).

In this regard, we analyzed the processes leading to earthquake doublets in Southern Iran. We use a combination of InSAR, local, regional, and teleseismic data within new joint inversion schemes for multiple sources and locations

of known aftershocks to gain deeper insights into the source mechanism and rupture kinematics. Our analysis complements studies focusing on satellite deformation data (e.g., Yang et al., 2023) by resolving temporal aspects and rupture parameters and constraining the position of the activated fault system from aftershocks.

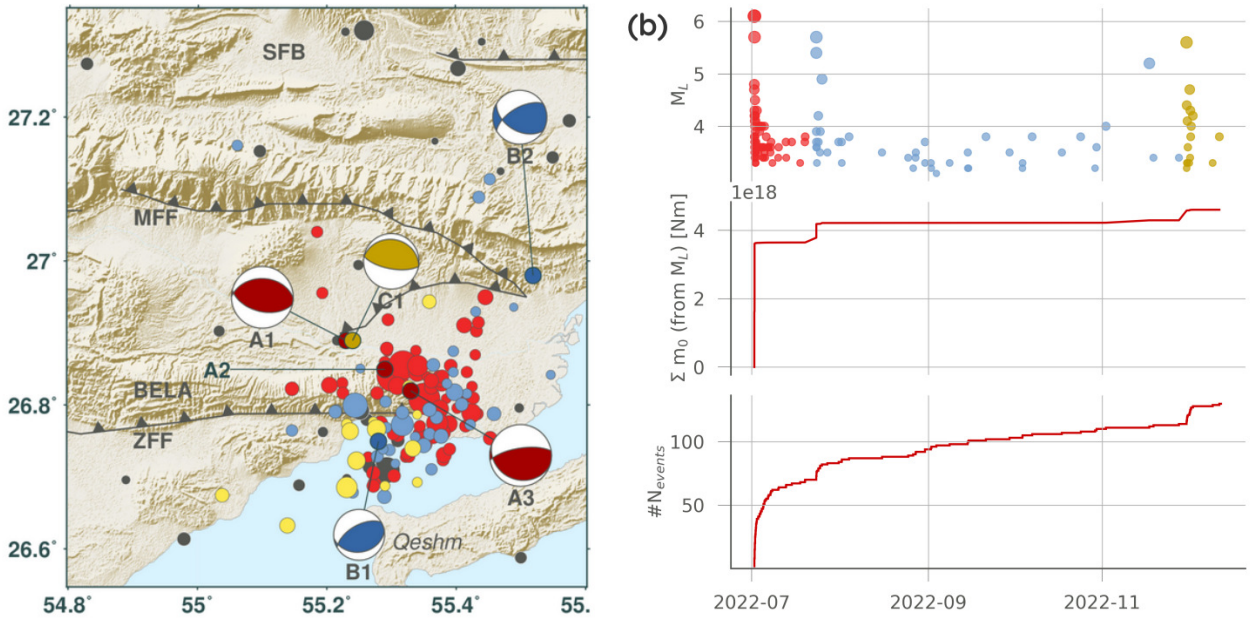

Figure 2 Seismicity from IRSC in Southern Iran before 01 July 2022 (grey dots) and after (colored dots), including GEOFON MT solutions (or location for A2) for the mainshocks (a). Colors of the dots and MTs indicate the time after 1 July (red), after 22 July (blue), or after 30 November (yellow), respectively. (b) shows the temporal seismicity evolution (ML, cumulative moment, and the number of events) using the IRSC catalog with the same color coding as in (a). Major tectonic/seismic features highlighted/annotated in (a) are the Mountain Front Fault (MFF), the Zagros Foredeep Fault (ZFF), the Simply Folded Belt (SFB), and the Bandar-e-Lengeh anticline (BELA).

2 Materials and methods

2.1 InSAR Data preprocessing

Interferometric Synthetic Aperture Radar (InSAR) surface displacement measurements play a crucial role in constraining earthquake locations, particularly in finite fault inversions (e.g., Ide, 2007; Steinberg et al., 2020). For our multisource inversion approaches, we use Sentinel-1 interferograms. The unwrapped and geocoded interferograms were obtained from an ascending orbit (track 130, 22 June 2022, to 4 July 2022) and a descending orbit (track 166, 25 June 2022, to 7 July 2022), each with a 12-day temporal baseline, along with essential metadata and coherence data via the COMET-LiCSAR web portal. The Generic Atmospheric Correction Online Service (GACOS) offers tropospheric delay products (Yu et al., 2017, 2018b,a) aimed at reducing tropospheric noise in interferograms. However, due to the negative impact of GACOS-based corrections on unwrapped interferograms, we opted to employ a linear method that leverages the correlation between phase and elevation for stratified tropospheric noise correction (Doin et al., 2015).

We processed InSAR time series for ascending track 130 and descending tracks 166 using the open-source Miami InSAR Time-series software in Python (MintPy) (**?**) and the Hybrid Pluggable Processing Pipeline (HyP3) service (Hogenson et al., 2016). HyP3 is a cloud-native infrastructure that offers a generic processing platform for SAR data, including interferometric processing. It streamlines the generation of interferograms, coherence maps, and unwrapped phase products by automating the necessary processing steps. The HyP3 service facilitated our processing

of Sentinel-1 data, enabling consistent and efficient generation of interferometric products. The results demonstrated similar deformation patterns for both ascending and descending tracks, providing consistency and confidence in our findings.

Corrected displacement maps are post-processed using the software toolbox Kite (Isken et al., 2017) (Fig.3). Post-processing includes an empirical variance-covariance estimation of the data error as an input for data weighting within the later inversion (Sudhaus and Jónsson, 2009) and irregular quadtree subsampling (Jónsson et al., 2002) (Fig.7).

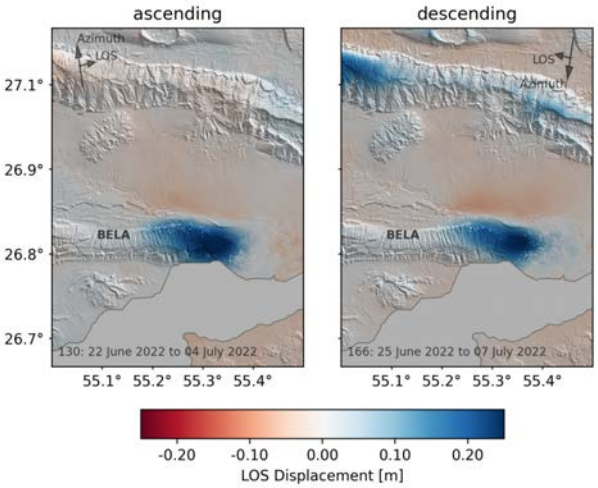

Figure 3 Ground deformation derived from satellite data from ascending (left) and descending tracks of Sentinel 1. Track ID and acquiring dates are shown in the bottom left. The line of sight (LOS) and satellite track (azimuth) directions are indicated by arrows. The displayed deformation is used as input for the joint inversions.

2.2 Bayesian moment tensor (MT) inversion of the mainshocks

We performed moment tensor (MT) point source inversions on both the individual mainshocks and also jointly on the whole sequence A using the Bayesian inversion software Grond (Heimann et al., 2018). Utilizing a particle swarm method combined with bootstrapping, Grond estimates non-linear uncertainties of all inversion parameters. We fit the MT components (full and deviatoric for the individual source inversions and double couple (DC) for the joint inversion), centroid location, time, and duration based on waveform and ground displacement fits. Individual earthquake inversions used teleseismic and regional body waves signals, recorded at 18 teleseismic and seven regional stations with an epicentral distance of ∼230 - 10,000 km with carefully selected time windows to ensure less overlap between the signals emitted by subsequent earthquakes. Due to inaccessible regional data, all inversions for C1 used only the teleseismic dataset. Before inversion, data were visually inspected, and all noisy, incomplete, or corrupted signals were removed. All waveforms have been fitted as bandpass-filtered displacements (0.015–0.06 Hz for A1 and A3, 0.02–0.06 Hz for A2, B1, B2, and C1) in time domain on the vertical and transverse components. Lower frequency limits were chosen to suppress low-frequent noise. Relatively low upper-frequency limits diminish high-frequent site effects and reduce the effect of structural inhomogeneities not captured within our ground model on the data fit. Synthetic waveforms were generated based on Green's functions calculated with QSEIS (Wang, 1999) using the AK135 global and a regional velocity model (Karasözen et al., 2019; Jamalreyhani et al., 2021).

A joint inversion scheme described as the double DC or double single force source by Carrillo Ponce et al. (2021)

was adapted and then used for the earthquakes of sequence A. The original approach allows for simultaneous source estimates via parameterizing the temporal and spatial distance between subevents with the focus on single, but complex earthquakes. It subsequently enables the use of seismic records characterized by overlapping signals of different subevents. Furthermore, ground displacements recorded by InSAR with their coarse temporal resolution can be fitted to the superposed synthetic ground displacements of all inverted subevents. The mentioned inversion scheme was enhanced for simultaneous inversions of three earthquakes as required for a complete assessment of sequence A. These inversions used seismic and satellite deformation data within separate and joint runs. Satellite deformation data were fitted to synthetic ground displacements calculated with PSGRN and PSCMP (Wang et al., 2003; Wang, 2005; Wang et al., 2006) using the regional velocity model by Karasözen et al. (2019); Jamalreyhani et al. (2021). An interpretation of the triple source inversion must be done with care as more free parameters within the inversion may also lead to overfitting or the fitting of noise signals. The double source setup could not be applied to sequence B due to high noise levels on the satellite deformation.

Throughout this article, we will always refer to the mean model and the standard deviations derived from the inversions.

2.3 Bayesian inversion of the finite faults

Extended rupture characteristics have been estimated using the pseudo-dynamic rupture (PDR) (Metz, 2019; Dahm et al., 2021). This extended rupture model depends on a flexible boundary element method based on Okada (1992) to iteratively estimate the instantaneous dislocation on the fault from a prescribed stress drop behind a moving rupture front. The rupture front propagation is estimated there using the 2D Eikonal equation and the rupture velocity linearly scaling with the shear wave velocity of the regional velocity model by Karasözen et al. (2019); Jamalreyhani et al. (2021). The further parameterization was chosen as in Metz et al. (2022) aiming 13 parameters to fit per fault: the top edge location, the rupture orientation, length and width of the rupture plane, the maximum shear slip, the rake, the relative origin coordinates, the origin time, and the scaling factor between the rupture and shear wave velocity.

The inversion settings are the same as for the MT inversions using individual and joint inversion approaches. Due to the lack of regional data for C1 and noisy satellite deformation records for sequence B, we performed PDR inversions only on the earthquakes of sequence A.

2.4 Relocation of aftershocks

Earthquake relocation is vital to improve the spatial resolution of seismic sequences. We used the GrowClust3D.jl relocation method (Trugman and Shearer, 2017; Trugman et al., 2023), which implements a cluster-based relocation scheme based on relative time shifts between P and S-wave arrivals of events with similar waveforms. The method initially requires a high waveform similarity among the different events and clustered initial locations.

Time shifts are converted into distance and azimuths using pre-calculated travel times based on a 1D velocity model; the required ray tracing was performed using the same regional ground model as for the inversions (Karasözen et al., 2019; Jamalreyhani et al., 2021). Due to limitations in waveform data access, we adopted the scheme to handle picked Pg, Pn, Sg, and Sn arrivals derived from the IRSC catalog. Required relative time shifts for two events were obtained by subtracting absolute arrival times for matching stations.

This approach allows getting a first-order relocation of the catalog with the limitations caused by the arrival time picks provided only to the tenth of a second and the lack of quality control parameters as the cross-correlation coefficient. In total, 120 aftershocks of all three sequences A, B, and C with M_L larger 3.0 from 01 July 2022 until 12 December 2022 were relocated (Fig. 2).

3 Results

In the following we will summarize our findings. Due to indications for dominant southward dipping thrusting (Yang et al., 2023) we will discuss our point source results emphasizing the south-dipping nodal planes.

The analysis of seismic data yields robust MT solutions for seven events M_w larger 5.3 from 01 July 2022 to 30 November 2022 (Fig. 4a,b, S1–S6, Tab. 2, S1, S2). All indicate rupture on E-W striking planes (88 - 118°) with one focal plane dipping with 37–68°towards the South. Dips vary from shallow 37–39°(A3, B1) to more than 60°(A1, B2, C1). While events A1, A2, and C1 show rather pure thrust (rake of 80–100°), events A3 (rake of 120°) and especially B1 and B2 (rake of 132–142°) indicate oblique faulting. The magnitudes of the events range from 5.27 for event B1 to 6.01 for event A3 with the highest magnitudes observed for sequence A (M_w 5.73–6.01). All centroids of sequence A are located close to each other beneath or slightly to the North of the Bandar-e-Lengeh anticline (BELA) in depths of 6.8–8.0 km. B1 and B2 occurred in larger depths of 10.4–11.5 km, with B1 being co-located with sequence A and B2 shifted by 10 km towards the North. The later event C1 shows a strong location migration towards the West by ≈ 20 km. Its centroid lays beneath the BELA at a shallow depth of 5.4 km.

Independent finite fault solutions obtained from seismic data for sequence A yield preferred orientations of the fault plane but with minimal misfit differences compared to the inversions for the auxiliary nodal plane (Fig. 4, S7–S9, Tab. 2, S4). Preferred fault planes strike towards West (260°) and dip towards North by 28°for A2 or strike East (102–107°) with a southward dip of 41–61°. Rakes of 85–115°indicate pure thrust faulting with a slight oblique component for A3. Source plane extends range from 9.5 ± 2.3 km $\times$ 3.4 ± 1.5 km in length and width for A3 up to 19.3 ± 3.0 km $\times$ 8.1 ± 1.3 km for A2. Resolved top edge depths are similar through all events of sequence A ranging from 3.1 ± 0.7 km for A1 to 4.1 ± 0.6 km for A3 (Tab. S4). Significant uncertainties indicate a poor resolution of the rupture origin location and hence the rupture propagation. However, all events of sequence A yield prevailing westward motion along the respective fault planes. Centroids derived from the PDR are similar to the MT solutions in location, magnitude, and orientation. Inferred centroid depths are slightly smaller, with 5.2–6.2 km. Also, the magnitude estimate for event A2 deviates from the MT solutions with M_w 5.87 compared to 5.73 ± 0.03. Inverted tractions range from 0.6 MPa for A2 to 2.7 MPa for A1 and 18.2 MPa for A3.

Modeled waveforms show a high fit in amplitude and phase for both CMT and PDR inversions (Fig. 6 top row, S1–S9). PDR fits of the mean model of A1 indicate an overestimation of the amplitude at the displayed station GE.SANI. Fits for the later event A2 are characterized by a slight amplitude deficit of the modeled compared to the observed waveforms for both PDR and CMT solutions.

For sequence A, joint inversions were carried out using seismic and satellite deformation data within a triple source inversion scheme. The triple source inversion accounts for the limited temporal resolution of satellite deformation data, which only measures the overlapping effect of the three sources. The triple DC point source inversion

fits the seismic, and the satellite deformation data and yields results in agreement with our previous seismic inversions (Fig. 5a,b, 6, 7a,b, S10, Tab. 2, S3). All mechanisms indicate thrust faulting along an E-W striking plane. The MT for A3 shows a significantly smaller oblique proportion and a much larger dip towards the South (78°) of one of its nodal planes compared to the similarly oriented plane of the pure seismic inversion (39°). The moment release indicates the highest magnitude for A1 with M_w 6.27, about 0.3 magnitude units larger than the results from the pure seismic inversion. Synthetic waveforms (Fig. 6, S10) show significantly larger amplitudes compared to the observed and the synthetic traces from the pure seismic inversion (Fig. S1), suggesting that the satellite deformation data forces the seismic moment of A1 to have larger values. On the other hand, magnitude estimates for A2 and the corresponding waveform fits are similar to the observed traces. Finally, A3 is characterized by underestimating the waveform amplitude and the magnitude compared to observed traces and the seismic modeling. The locations of the centroid double couple MTs are generally well resolved with the largest errors for A2 (max. 4.1 km horizontal and 2.7 vertical error - Tab. S3). The depth of A3 is significantly larger than estimated from seismic data (7.9 km).

The joint inversion of three PDR finite fault planes yields stable estimates, especially for A1, with more significant uncertainties for A2 and A3. All events are characterized as E-W striking thrust earthquakes with south dipping source planes (Fig. 5c,d, 6, 7, S11, Tab. 2, S5). Fault orientations are mainly in agreement with results from the other inversion approaches. Contrary to the single PDR inversion, the joint inversion favors a south-dipping fault plane for A2. We also obtain a larger oblique component but with larger uncertainties (rake of 134 $\pm$ 22°) for A3 compared to point source and single finite fault inversions. The estimated seismic moment from the mean model centroid yields A1 as the largest event with M_w 6.42 and a maximum shear dislocation of 2.26 $\pm$ 0.37 m, while A2 and A3 released a moment equivalent to M_w 5.91 (slip of 0.39 $\pm$ 0.20 m) and M_w 5.98 (slip of 0.50 $\pm$ 0.24 m). For A1 and A2, both magnitudes and maximum dislocations are overestimated compared to all other inversion approaches with the largest magnitude and slip increases for A1 of more than 0.4 magnitude units and ~1.4 m, respectively, compared to the single point source or PDR seismic inversions. Waveform fits (Fig. 6, S11) indicate good phase retrieval, especially for A1 and A2. Slight phase shifts are observable for some records of A3. Similarly to the triple DC inversion, we obtain an amplitude overestimation for A1, which is even more prominent. Waveform amplitudes for A2 and A3 generally fit well. Satellite deformation data shows a high correlation in the estimated deformation pattern with larger residuals of $\sim$ 10 cm. The ascending track fit is characterized by an underestimation of the maximum deformation measured at the BELA. In contrast, the descending track shows larger residuals along the NE boundary of the BELA (Fig. 7c,d). The centroid location and depth of A1 beneath the northern edge of the BELA are in good agreement with solutions from the other inversion approaches. Centroids of A2 and A3 are co-located south of the BELA beneath the Tangeh Khoran, indicating a shift of $\sim$ 10 $\pm$ 8–9 km towards the South compared to the other inversion results (Tab. S5). The respective depths are in the range of 10.1–11.1 km, which is up to 6 km larger than the results from our other inversion approaches. Derived stress drop values show different results compared to the independent event inversions with 2.6 MPa for A2, 2.7 MPa for A3 and 7.4 MPa for A1.

120 aftershocks of the IRSC catalog occurring 01 July 2022 and 12 December 2022 have been relocated with average vertical (depth) and horizontal location shifts and uncertainties of 0.41$\pm$0.39 km and 0.67$\pm$0.82 km, respectively (Fig. 8, S12, Tab. S6). The simultaneous optimization of the origin times yields an average shift of 0.1 $\pm$ 0.1 s. The majority

of events are located in depths of 10–15 km scattering within a $\sim 10 \times 10$ km wide area around 26.8°lat, 55.35°lon. They are characterized by minor location errors (Fig. S12). Larger errors in the relocation of up to 3 km horizontally and 2 km in depth are observed for the few events located towards the North and SW of the major aftershock area. The location of most aftershocks fits well with inversion results from both MT and PDR inversions, except the MT solution of C1. The westward location shift of C1 compared to sequences A and B (Fig. 4) is not reflected in the relocated aftershocks. We also do not resolve any scattering of aftershocks along preferred planes.

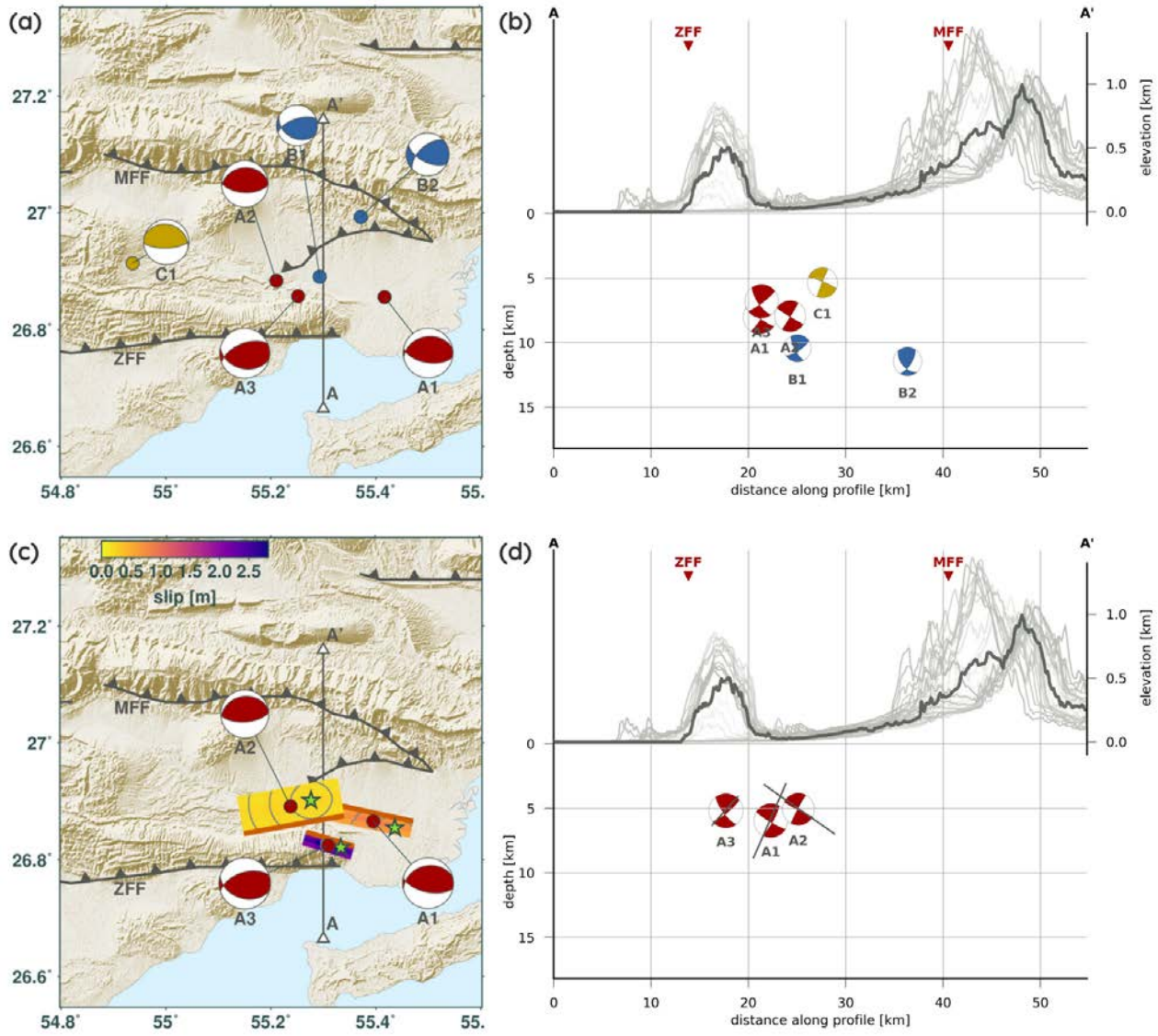

Figure 4 Results of seismic inversions with centroids from full MT inversions as map (a) and along the profile (b). PDR inversion results using seismic data are shown as map (c) and profile (d) with their centroids (dots), rupture plane locations, final slip, rupture origin (green star) and rupture propagation contour lines (every 2 s, grey lines in (c)). Grey lines in (d) indicate the PDR rupture plane locations and orientations through their respective centroids.

4 Discussion and Interpretation

The analyzed earthquakes between 01 July 2022 and 12 December 2022 highlight the interaction of large, shallow thrust earthquakes in the sedimentary layer with smaller aftershocks in the upper basement or deeper sedimentary cover (Fig. 9), which is a peculiarity of the continent-continent collision in the Zagros Mountains. (see e.g., Nissen

Table 2 Centroid locations and orientations derived from MT and PDR inversions using both seismic and a joint seismic and InSAR dataset. The ensemble mean solution is given. Full set of resolved parameters including uncertainties are given in Tables S1–S5.

ID	Method	Time	Lat, Lon	Depth	M_w	max. Slip	Strike, Dip, Rake
Sequence A: 01 July 2022							
A1	MTs	21:32:08.7	26.856°, 55.417°	8.0 km	5.97	-	100°, 58°, 101°
							260°, 33°, 83°
	MTj	21:32:06.3	26.835°, 55.340°	8.3 km	6.27	-	94°, 66°, 79°
							299°, 26°, 113°
	PDRs	21:32:08.8	26.861°, 55.390°	6.2 km	5.96	0.82 m	102°, 61°, 102°
	PDRj	21:32:09.4	26.851°, 55.292°	8.2 km	6.42	2.26 m	98°, 67°, 87°
A2	MTs	23:24:14.8	26.884°, 55.210°	7.9 km	5.73	-	93°, 59°, 95°
							264°, 32°, 83°
	MTj	23:24:15.7	26.826°, 55.153°	11.9 km	5.78	-	85°, 65°, 94°
							256°, 25°, 82°
	PDRs	23:24:14.6	26.896°, 55.234°	5.2 km	5.87	0.24 m	260°, 28°, 85°
	PDRj	23:24:11.6	26.748°, 55.301°	11.1 km	5.91	0.39 m	102°, 59°, 86°
A3	MTs	23:25:14:3	26.858°, 55.252°	6.8 km	6.01	-	104°, 39°, 120°
							248°, 57°, 69°
	MTj	23:25:15.5	26.858°, 55.270°	6.1 km	5.93	-	92°, 78°, 95°
							251°, 13°, 69°
	PDRs	23:25:14.5	26.838°, 55.272°	5.6 km	5.98	2.83 m	107°, 41°, 115°
	PDRj	23:25:20.9	26.756°, 55.226°	10.1 km	5.98	0.50 m	106°, 48°, 134°
Sequence B: 23 July 2022							
B1	MTs	16:07:47.6	26.891°, 55.293°	10.4 km	5.27	-	118°, 37°, 132°
							250°, 64°, 64°
B2	MTs	16:09:07.8	26.993°, 55.372°	11.5 km	5.42	-	116°, 60°, 142°
							227°, 58°, 36°
Sequence C: 30 November 2022							
C1	MTs	15:17:46.9	26.914°, 54.936°	5.4 km	5.63	-	88°, 68°, 83°
							286°, 23°, 107°

Methods:

MTs - Full moment tensor inversion from seismic data.

MTj - Joint inversion of triple DC sources from seismic and InSAR data.

PDRs - PDR inversion from seismic data.

PDRj - Joint inversion of triple PDR sources from seismic and InSAR data.

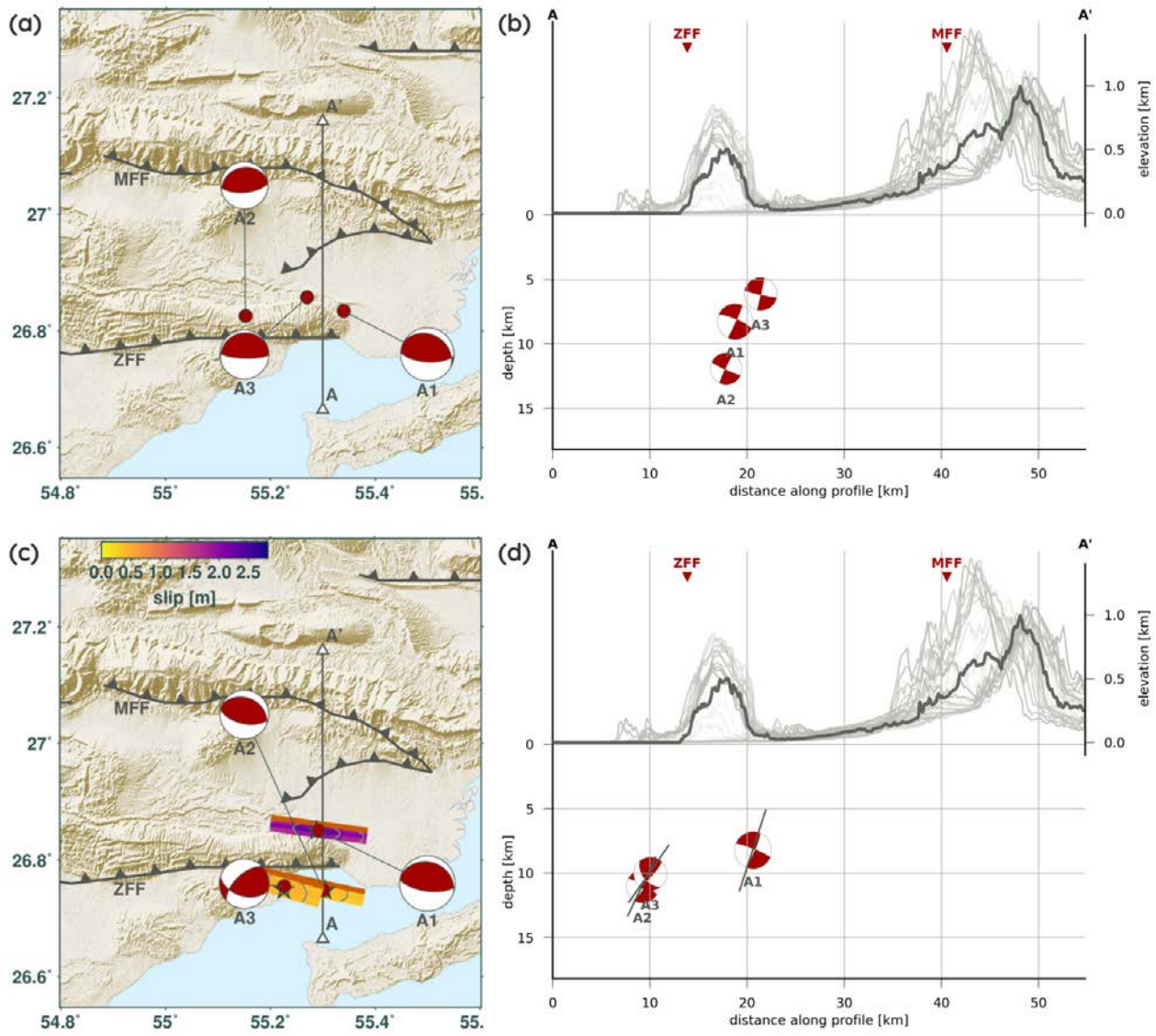

Figure 5 Results of joint seismic and satellite deformation data inversions with centroids from joint 3 DC inversion as map (a) and along the profile (b). Joint PDR inversion results using seismic and satellite deformation data are shown as map (c) and profile (d) with their centroids (dots), rupture plane locations, final slip, rupture origin (green star) and rupture propagation contour lines (every 2 s, grey lines in (c)). Grey lines in (d) indicate the PDR rupture plane locations and orientations through their respective centroids.

et al., 2011, 2014). Using different inversion approaches, we can also resolve significant differences in the earthquake parameter estimates due to uncaptured tectonic processes or uncertainties in the used ground models. In the following, we will discuss our results related to regional tectonics, the effect of the incorporated satellite deformation data and its seismological implications, and the quality of the newly developed triple source inversion scheme.

4.1 Mainshock mechanisms and location

The earthquakes in Zagros generally have low to strong magnitudes up to M_w 7.3 and commonly occur on blind faults (Barnhart et al., 2013; Karasözen et al., 2019; Asayesh et al., 2022; Jamalreyhani et al., 2022; Nissen et al., 2019), often in depths between 8 and 14 km (e.g., Ni and Barazangi, 1986; Baker et al., 1993; Hessami et al., 2001; Talebian and Jackson, 2004; Jamalreyhani et al., 2021; Nissen et al., 2019). Rupture includes the sedimentary layer, called a "competent group", which spans from ≈ 4–8.5 km in the SE Fars Arc (FA) which is decoupled from the crystalline

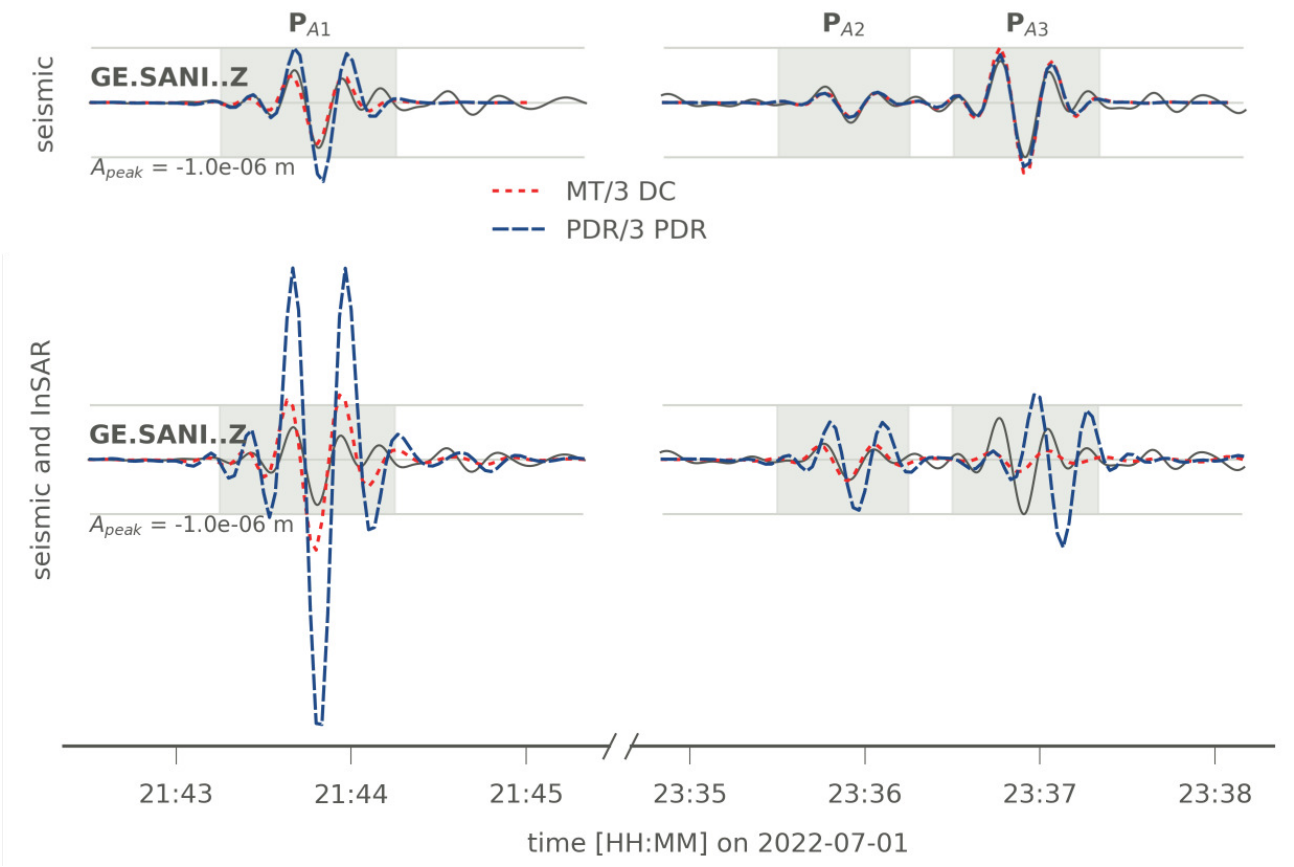

Figure 6 P-wave fits for sequence A (left A1, right A2 and A3) displayed on the vertical displacement records of station GE.SANI (distance $\approx 8,215$ km, azimuth $\approx 119°$) for seismic (top row) and joint inversions (bottom row). Observed, restituted and filtered records are given in black, fitted traces in colored lines. Horizontal grey lines indicate the peak amplitude of the observed records with the value given as A_{peak}. Grey background with the top labels indicate the major P-wave signal of the different events.

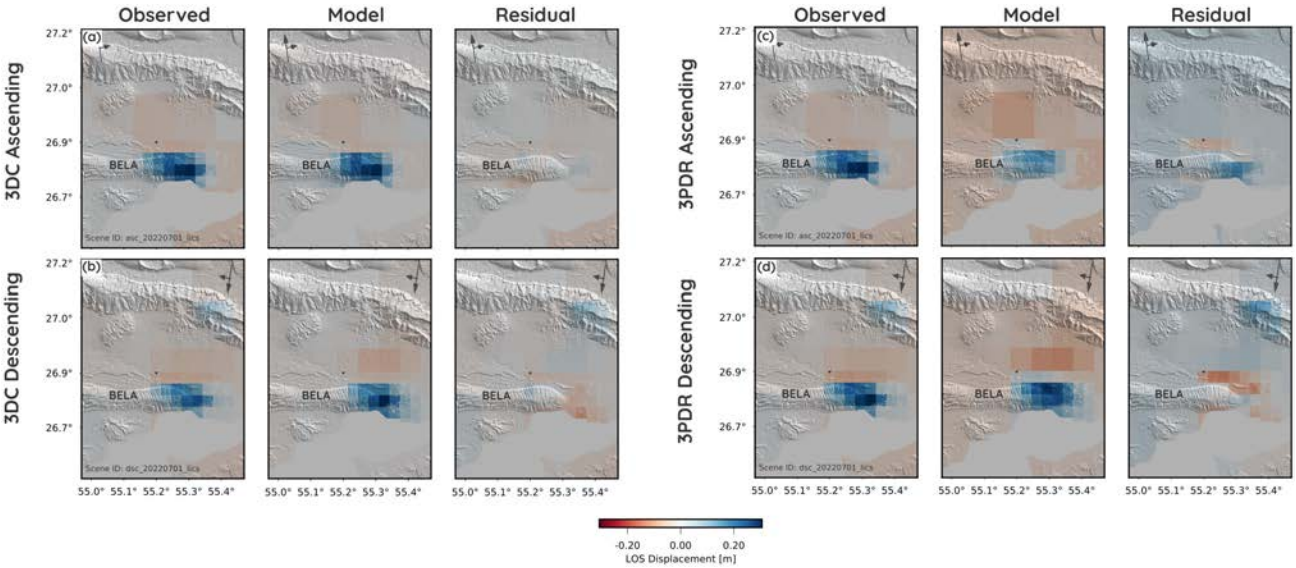

Figure 7 InSAR fits for joint 3DC (ascending - a, descending - b) and 3PDR (ascending - c, descending - d) inversions with quadtree subsampled observed data (1st column), the mean model fit (2nd column) and the corresponding residual (3rd column).

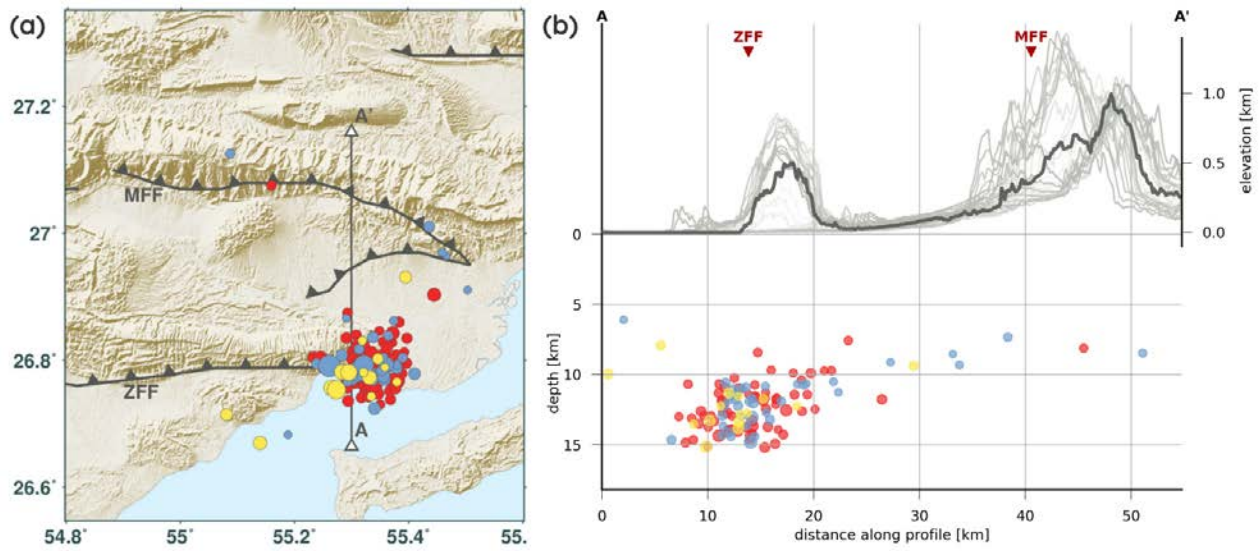

Figure 8 Map (a) and profile (b) of the IRSC catalog after relocation between 01 July 2022 and 12 December 2022. Mainshocks of sequences A, B and C are excluded. Colors indicate the time after sequence A (red), B (blue) or C (yellow). Points scale with reported local magnitude.

basement by the Hormuz Salt Formation at about 8–10 km (Nissen et al., 2011), a formation intercalated with stronger non-evaporitic layers. The earthquakes A1, A3, and C1 occur between 5 and 8 km depth (Fig. 4, 5), which indicates they ruptured only in the competent group. Also Roustaei et al. (2010); Nissen et al. (2010, 2011); Barnhart et al. (2013); Elliott et al. (2015) have found most $M_w > 5$ events in the shallow sedimentary layer between $\sim$ 5–10 km. The later earthquake doublets B1 and B2 (and possibly also A2), occurred at a larger depth between 10.5 and 11.5 km, indicating a possible stress transfer from the shallow primary events A1 and A3 into depth activating the deeper sedimentary Hormuz layer, interface between sediments and basement and/or faults within the crystalline basement. This stress transfer and activation significantly deeper strata is also evident from the aftershock depth range of 10–15 km below the Bandar-e-Lengeh anticline (BELA), which fits well with earlier estimates of aftershock depths e.g. for the 2005 Qeshm or 2006 Fin earthquakes (e.g., Talebian and Jackson, 2004; Tatar et al., 2004; Nissen et al., 2011; Yaminifard et al., 2012). The scenario of a shallow mainshock followed by a separated, deeper aftershock sequence has been observed and described by Nissen et al. (2011) and Yaminifard et al. (2012) for the 2005 Qeshm earthquake. The pattern may indicate that characteristic earthquakes in the competent group of the sedimentary cover are controlled by a combination of stress and forces from the horizontal collision and buoyant salt movements, while the crystalline basement of the crust is moving as a decoupled, rigid body beneath the ZFFB. Aftershocks can be induced in the basement if Coulomb stress changes occur. However, the crustal shortening in this layer is either accommodated by ductile deformation or further to the north beneath the HZZ, where the crust is thickest. In addition to thrust faulting and shortening, transverse strike-slip faults play a role in the evolution of Zagros. For instance, Talebian and Jackson (2004) emphasized the importance of strike-slip faults in the basement of the southeastern-most Zagros, which has also been revealed by Yaminifard et al. (2012) studying aftershocks of the 2005 Qeshm Island event.

Sequence A is dominated by the two largest thrust events of M_w ~6.0 (A1 and A3). Satellite radar data (InSAR) show largest deformations on the BELA and minor deformation towards North (Fig. 3, 7). (Yang et al., 2023) have derived two southward dipping rupture planes with angles of 33–65°from the deformation pattern. Despite the steeply

dipping planes, no surface ruptures were observed. This is, however, common for thrust events in Zagros mountains (e.g., Berberian, 1995; Regard et al., 2004; Yamini-Fard et al., 2007; Edey et al., 2020). From our joint seismic and InSAR inversion, we find a southward dipping plane of 48 $\pm$ 13°(Triple PDR) or 78 $\pm$ 2°(Triple DC) (Tab. 2, S3) for the second large event of sequence A (A3). However, Yang et al. (2023) interpret A3 as a possible southward dipping but low angle, shallow splay fault of A1 with a dip of about 33°. The results of our single PDR seismic inversions yield similar dip angles as the triple PDR inversion between 41°and 48°on the southward dipping plane, supporting better the results by USGS, gCMT, and GEOFON. Prevailing dips for thrust events are up to 60°(Jahani et al., 2009; Nissen et al., 2011). The steep dip estimate of 78°from the triple DC inversion is well above this range. It could be a result of our triple source inversion setup with many free parameters, allowing for overfitting of small amplitude satellite deformation data (Fig. 7). The poor waveform fits from the triple DC inversion for A3 compared to the single MT inversion support the interpretation of overfitting satellite deformation data at the expense of the waveform data fit (Fig. 6, S3, S10).

Event A2 is characterized by rather good waveform fits (Fig. 6) and comparable solutions through all applied techniques and inversion setups. However, the joint inversions yield a significantly larger centroid depth of 11.1–11.9 vs. 5.2–7.9 km. The larger depth would imply that A2 ruptured within the upper basement, lower sediments or along their interface. The low-angle northward dipping rupture plane, resolved from PDR inversions, fits well with the latter interpretation of a low-angle detachment earthquake along the interface (Nissen et al., 2011) (Fig. 9 left column). Resolved dips of more than 20°make this scenario unlikely. Instead of a steeply northward dipping fault plane, the ZFF could also be of listrical shape propagating into the sediment-basement interface as indicated by Jahani et al. (2009) (Fig. 9 center column). Such fault shape could accommodate events with intermediate north dipping focal planes as observed. A rupture of listric or ramp-flat faults within the basement, as suggested for the 2017 M_w 7.3 Sarpol-e Zahab earthquake (e.g., Fathian et al., 2021; Guo et al., 2022; Zhao et al., 2023) is unlikely in our case. A centroid depth at the top level of the basement and no observable spatial clustering of aftershocks along listric lineaments in the basement, prohibits such interpretation. We favor the interpretation of Yang et al. (2023), though assuming A2 as a foreshock to A3 on the thrust fault plane of A1 or A3 (Fig. 9 right column). The shallow centroid depths from seismic inversions and the similar focal plane orientations support this hypothesis. Coulomb failure stress changes caused by A1 or A2 on the fault plane of A3 calculated by Yang et al. (2023) also strengthen this interpretation.

Our finite fault inversions with slip estimates for the two largest events of 0.82 $\pm$ 0.25 m (single PDR) or 2.26 $\pm$ 0.37 m (triple PDR) for A1 and 2.82 $\pm$ 0.88 m (single PDR) or 0.50 $\pm$ 0.24 m (triple PDR) for A3 support findings on different recent earthquakes in the FA (e.g., for 2005 Qeshm, 2006 Fin, 2008 Qeshm or 2013 Khaki-Shonbe earthquakes) that coseismic slip is mainly accommodated within the competent group (Lohman and Barnhart, 2010; Elliott et al., 2015; Nissen et al., 2007, 2010; Roustaei et al., 2010; Jamalreyhani et al., 2021). Our slip estimates are significantly larger than results from Yang et al. (2023), who estimate peak slips of up $\sim$ 1.25 m. From seismic data, we also estimate different locations for the high slip patch of A1 compared to Yang et al. (2023). It is shifted further to the East with respect to their results. The joint finite fault inversion yields swapped locations of A1 and A3 compared to Yang et al. (2023). While they resolve A1 to the west of A3, we obtain the opposite results. This could be caused by the limited

temporal resolution in the study of Yang et al. (2023) as based only on satellite deformation data. Besides the slip, first-order estimates of the rupture kinematics are obtained from finite fault inversions. Although shipping with larger uncertainties (Tab. S4), single PDR inversion solutions indicate dominant westward rupture propagation. This indicates, that the earlier A1 ruptured into the region of A2 and A3 (Fig. 4, 5).

We have obtained rather variable stress drops for sequence A ranging from 0.6 MPa to 18.2 MPa, which are in agreement with static stress drops retrieved for earthquakes by Kanamori (1994). The different tractions retrieved from single fault plane estimates and the joint triple PDR are the result of variability in the resolved fault dimensions, maximum dislocations and depths between independent and joint finite fault inversions.

4.2 Vertical separation of aftershocks

Relocated aftershocks are spatially concentrated around the eastern tip of the BELA and scatter mainly in a depth of 10–15 km, which implies aftershock activity is either in the upper crystalline basement (Talebian and Jackson, 2004; Tatar et al., 2004; Nissen et al., 2011) or deeper sediments (Jahani et al., 2009; Nissen et al., 2014). We also see a vertical separation of the aftershocks from the mainshock in the SFB, which fits well with observations by Nissen et al. (2010, 2011, 2014) for the 2005 Qeshm and 2006 Fin earthquakes. While mainshocks rupture the middle-lower sedimentary cover, aftershocks occur in the basement or the deeper sediments within the Hormuz formation. Hence our aftershock locations also indicate a relatively shallow top boundary of this aftershock region at $\approx$ 10 km depth compared to findings of Nissen et al. (2014). The co-location of the mainshocks and aftershocks, despite C1, could highlight Coulomb stress changes, or dynamic stress transfer from the mainshocks into the deeper and harder Hormuz formation (Nissen et al., 2010, 2014). The salt may flow as a response to the stress changes causing aftershocks within the formation and its surroundings. The substantial location shift between C1 and its aftershocks could be due to location uncertainties and poor spatial resolution of our seismic inversion caused by the lack of regional seismic or ground deformation data. Nevertheless, as derived from travel time picks without quality constraints, our relocations are only valid as a first-order approximation of the aftershock locations. As we used the same ground model for relocation as for the inversions, uncertainties and structural inconsistencies between the model and the actual underground structure might have also caused a bias within the relocation.

4.3 Implications from joint data and multisource inversion

The newly implemented triple source inversion scheme has proven its usability for complex rupture inversions using multiple satellite deformation and seismic data. We resolved major features of deformation and seismic data, especially when using the triple DC source model. However, additional free parameters in the triple source inversion scheme have also affected the results, as increased centroid depths for A2 and partially A3, larger uncertainties and the large waveform fit residuals, especially for A3. Different weighting schemes for the relative misfit contribution of surface deformation data fits compared to waveform fits were employed to reduce such effects but did not fully solve this issue.

Comparing results from single source seismic and combined source joint seismic and satellite data inversions, we obtain a significant increase in the cumulative moment release with the latter inversion approach (Fig. 4, 5). Our seismic inversions for sequence A yield a cumulative moment release equivalent to M_w 6.24–6.26, similar to

results from GEOFON (M_w 6.29) or USGS with M_w 6.25. Meanwhile, our joint inversion approaches give M_w 6.39–6.52. These values confirm results from Yang et al. (2023), who have obtained a cumulative moment release equivalent to M_w of 6.43. This 60–70% increase in modeled moment release derived from the triple DC inversion could be caused by a significant afterslip resolved in the satellite deformation data with their broad temporal coverage but not in the seismic data. Observations of afterslip within Zagros reveal a rather large relative contribution to the ground deformation (Zhao et al., 2023) and can yield significant overestimation of the magnitude in the range of 0.1 to >0.2 magnitude units (Weston et al., 2012). This behavior might be caused by the complex tectonics of the Zagros, e.g., its' salt diapirism (Yang et al., 2023). Another reason for the magnitude differences could be our choice of the ground model. It is specific to the Zagros region (Karasözen et al., 2019; Jamalreyhani et al., 2021). Nevertheless, underground structure variations, as evident from, e.g., Nissen et al. (2011); Jahani et al. (2009); Jamalreyhani et al. (2021) along the Zagros, can not be fully resolved due to the lack of local tomographies. The choice of a rather low-frequency range for waveform fitting reduces such structural effects, though. Nevertheless, local studies, e.g., a tomography using the aftershocks of the sequence combined with seismic profiles, could enhance the knowledge and shed light on this issue. The significant moment release overestimation with an increase of 145–165% from the triple PDR inversion is likely to be also influenced by our inversion setup with many free parameters as the larger uncertainties and misfits suggest (Fig. 7, 6, S11, Tab. 2, S5).

We have resolved a sequence of three earthquakes close in time and space with similar focal mechanisms (sequence A). As likely rupturing the adjacent patches of the same faults or adjacent splay faults (Yang et al., 2023) it can be characterized as an event triplet according to the definition of Lay and Kanamori (1980); Ammon et al. (2008). It highlights a region of large tectonic complexity with overthrusting, opposed dipping splay faults, and the effect of the Hormuz salt formation limiting rupture propagation (Nissen et al., 2011). Also, sequence B might be a doublet with its short interevent time and similar mechanisms. We can not resolve if both ruptured on one common fault, though (Fig. 4a,b, 9). Here, a more detailed investigation of stress transfers could help to understand this part of the sequence better. Our observations of an event doublet and triplet fit well with recent observations of two other doublets (November 2021 Fin and June 2022 Charak - e.g., Nemati, 2022; Fathian et al., 2022; Rezapour and Jamalreyhani, 2022) highlighting the tectonic complexity of the SE Fars arc.

5 Conclusions

The 2022 earthquake sequence in SE Iran has revealed a rather complex interaction of larger shallow thrust faults within the sedimentary cover with deeper, smaller events at the interface to and within the crystalline basement. The sequence was initiated with two M_w ~6.0 thrust events on 01 July 2022 within the lower sediments at depths of 4–9 km, likely occurring on a south-dipping splay fault to the Zagros Foredeep Fault beneath the Bandar-e-Lengeh anticline. One smaller M_w 5.7–5.8 event rupturing one minute before the second large event highlights either an early activation of deeper strata or might also have been co-located on the main shock faults. The event triplet caused high aftershock activity within the deeper sediments or upper crystalline basement characterized by depths of 10–15 km beneath the Bandar-e-Lengeh anticline with several larger thrust events. It provides a new case of observable vertical separation of the main- and aftershocks in SE Iran and may be caused by a complex stress state within the

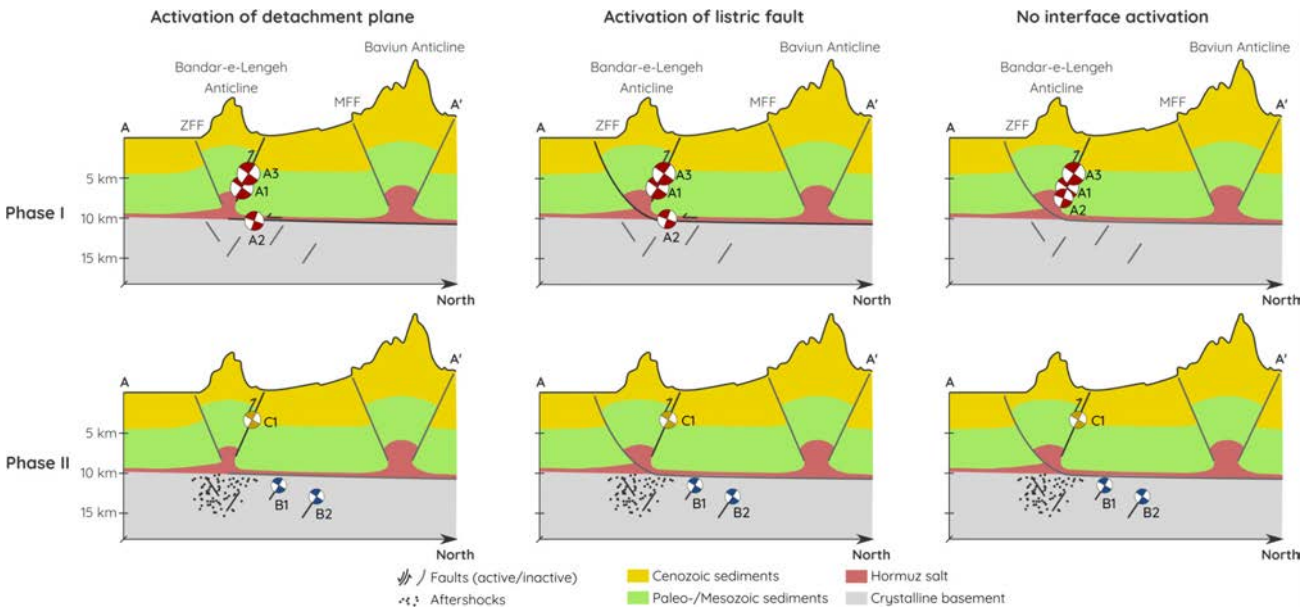

Figure 9 Interpretation of the tectonic processes during the July-December 2022 sequence. Phase I (top row) indicates the rupture processes on the 01 July 2022 while phase II (bottom row) resolves the later events. Moment tensors do not show correct rotations but shall illustrate general trends in location and mechanism. We show three interpretation possibilities using an activation of the detachment plane (left), a listric fault cutting through the sediments (center) or a rupture independent of the sediment to basement interface (right).

deeper sediments and the crystalline basement beneath. Magnitude overestimations when utilizing satellite ground deformation data also indicate a significant afterslip activity due to salt diapirism. The comprehensive analysis of main- and aftershocks using available seismic and ground deformation data has embedded the July–December 2022 sequence into the complex tectonics in the SE Fars arc with frequent occurrence of event doublets over the past year. The lack of regional and local seismic records and the rather uncertain ground models limited the accuracy of our results. This issue highlights the need for further detailed tectonic studies in the region and better data accessibility to understand better the geophysical processes and their potential risk within the SE Fars arc.

Conflict of competing interests

The authors declare that the research was conducted in the absence of any commercial or financial relationships that could be construed as a potential conflict of interest.

Contributions of the authors

MM, BMA, MMA, and MJ were involved in the general conceptualization of the study. MM developed and implemented the triple source inversion scheme and performed analysis of the main- and aftershocks. PB performed the focal depth estimation based on teleseismic body wave phases. BAM, MJ, and PB provided the IRSC seismic data and catalog. MMA performed pre-processing of the satellite deformation data and performed subsequent tests on satellite imagery.

MM wrote the original draft with major contributions of BAM and MJ within the introduction and discussion, and of PB within the methods section. MMA provided the methodological overview on satellite data preparation. Images within the draft were generated by MM, BAM, and PB. (Fig. 1). MM, BAM, MJ, PB, and TD provided substantial

feedback to the draft through their reviews.

TD, and PB have supervised and guided this study.

Acknowledgments

Malte Metz was supported by the BMBF project EWRICA (03G0891B). Behman Maleki Asayesh was funded by the DFG - Research Training Group “NatRiskChange" and Pınar Büyükakpınar is funded by project 407141557 of the Deutsche Forschungsgemeinschaft (DFG, German Research Foundation).

We would like to thank Simone Cesca, Sebastian Hainzl, Sebastian Heimann and Henriette Sudhaus for feedback and guidance on different parts of our study and continuous support. We are also grateful for the helpful comments of Daniel Trugman on the use of the GrowClust3D.jl algorithm.

Data and Resources

Our references source mechanisms were derived from the GEOFON program of the GFZ German Research Centre for Geosciences using data from the GEVN partner networks, global CMT (e.g., Dziewoński et al., 1981; Ekström et al., 2012) and USGS.

The aftershock catalog, body wave travel time picks and regional waveforms were downloaded from the Iranian Seismological Center (IRSC) available at http://irsc.ut.ac.ir/.

Furthermore we used teleseismic waveform data from the following seismic networks: AK (Alaska Earthquake Center, Univ. of Alaska Fairbanks, 1987), DK (GEUS Geological Survey of Denmark and Greenland, 1976), G (Institut de physique du globe de Paris (IPGP) and École et Observatoire des Sciences de la Terre de Strasbourg (EOST), 1982), GE (GEOFON Data Centre, 1993), GT (Albuquerque Seismological Laboratory (ASL)/USGS, 1993), II (Scripps Institution of Oceanography, 1986), IC (Albuquerque Seismological Laboratory (ASL)/USGS, 1992), IN (India Meteorological Department, 2000), IU (Albuquerque Seismological Laboratory (ASL)/USGS, 1988), QZ (LTD Seismological Experience and Methodology Expedition of the Committee of Science of the Ministry of Education and Science of the Republic of Kazakhstan, 2003), RM (Regional Integrated Multi-Hazard Early Warning System (RIMES Thailand), 2008) and WM (San Fernando Royal Naval Observatory (ROA), Universidad Complutense De Madrid (UCM), Helmholtz-Zentrum Potsdam Deutsches GeoForschungsZentrum (GFZ), Universidade De Évora (UEVORA, Portugal) and Institute Scientifique Of Rabat (ISRABAT, Morocco), 1996).

Satellite deformation data was downloaded from LiCSAR. LiCSAR contains modified Copernicus Sentinel data 2022 analysed by the Centre for the Observation and Modelling of Earthquakes, Volcanoes and Tectonics (COMET). LiCSAR uses JASMIN, the UK’s collaborative data analysis environment (http://jasmin.ac.uk). LiCSAR products can be accessed through the COMET-LiCSAR-portal website at https://comet.nerc.ac.uk/COMET-LiCS-portal/.

Besides the mentioned software we used GMT5.4 for map plotting (Wessel et al., 2013) and their GSHHG dataset for shore lines (e.g., Wessel and Smith, 1996). Topographic data provided by SRTM (Becker et al., 2009) was used for our map and profile plots. Faults plotted were obtained from Hessami et al. (2003). For InSAR processing we used the the Hybrid Pluggable Processing Pipeline (HyP3) platform (Hogenson et al., 2016), while MintPy was utilized a robust solution for InSAR time series analysis and unwrapping error correction (Yunjun et al., 2022). Furthermore

473 kite was used for satellite deformation data preprocessing (Isken et al., 2017).

References

Alaska Earthquake Center, Univ. of Alaska Fairbanks. Alaska Regional Network, 1987.

Alavi, M. Structures of the Zagros fold-thrust belt in Iran. *American Journal of science*, 307(9):1064–1095, 2007. doi: 0.2475/09.2007.02.

Albuquerque Seismological Laboratory (ASL)/USGS. Global Seismograph Network - IRIS/USGS, 1988.

Albuquerque Seismological Laboratory (ASL)/USGS. New China Digital Seismograph Network, 1992.

Albuquerque Seismological Laboratory (ASL)/USGS. Global Telemetered Seismograph Network (USAF/USGS), 1993.

Ambraseys, N. and Melville, C. *A History of Persian Earthquakes*. Cambridge Earth Science Series. Cambridge University Press, 2005.

Ammon, C. J., Kanamori, H., and Lay, T. A great earthquake doublet and seismic stress transfer cycle in the central Kuril islands. *Nature*, 451(7178):561–565, 2008. doi: 10.1038/nature06521.

Ansari, S. Co-seismic stress transfer and magnitude-frequency distribution due to the 2012 Varzaqan-Ahar earthquake doublets (Mw 6.5 and 6.4), NW Iran. *Journal of Asian Earth Sciences*, 132:129–137, 2016. doi: 10.1016/j.jseaes.2016.10.006.

Asayesh, B. M., Zarei, S., and Zafarani, H. Effects of imparted Coulomb stress changes in the seismicity and cluster of the December 2017 Hojedk (SE Iran) triplet. *International Journal of Earth Sciences*, 109:2307–2323, 2020. doi: 10.1007/s00531-020-01901-0.

Asayesh, B. M., Zafarani, H., Hainzl, S., and Sharma, S. Effects of large aftershocks on spatial aftershock forecasts during the 2017–2019 western Iran sequence. *Geophysical Journal International*, 232(1):147–161, 2022. doi: 10.1093/gji/ggac333.

Astiz, L., Lay, T., and Kanamori, H. Large intermediate-depth earthquakes and the subduction process. *Physics of the Earth and Planetary Interiors*, 53(1-2):80–166, 1988. doi: 10.1016/0031-9201(88)90138-0.

Baker, C., Jackson, J., and Priestley, K. Earthquakes on the Kazerun Line in the Zagros Mountains of Iran: strike-slip faulting within a fold-and-thrust belt. *Geophysical Journal International*, 115(1):41–61, 1993. doi: 10.1111/j.1365-246X.1993.tb05587.x.

Barnhart, W. D., Lohman, R. B., and Mellors, R. J. Active accommodation of plate convergence in Southern Iran: Earthquake locations, triggered aseismic slip, and regional strain rates. *Journal of Geophysical Research: Solid Earth*, 118(10):5699–5711, 2013. doi: 10.1002/j-grb.50380.

Becker, J. J., Sandwell, D. T., Smith, W. H. F., Braud, J., Binder, B., Depner, J., Fabre, D., Factor, J., Ingalls, S., H Kim, S-and Ladner, R., Marks, K., Nelson, S., Pharaoh, A., Trimmer, R., Von Rosenberg, J., Wallace, G., and Weatherall, P. Global Bathymetry and Elevation Data at 30 Arc Seconds Resolution: SRTM30_PLUS. *Marine Geodesy*, 32:355–371, 2009. doi: 10.1080/01490410903297766.

Berberian, M. Master "blind" thrust faults hidden under the Zagros folds: active basement tectonics and surface morphotectonics. *Tectonophysics*, 241(3-4):193–224, 1995. doi: 10.1016/0040-1951(94)00185-C.

Carrillo Ponce, A., Dahm, T., Cesca, S., Tilmann, F., Babeyko, A., and Heimann, S. Bayesian multiple rupture plane inversion to assess rupture complexity: application to the 2018 Mw 7.9 Alaska earthquake. In *EGU General Assembly 2021, Online, 19–30 Apr 2021*, number EGU2021-1583, 2021. doi: 10.5194/egusphere-egu21-1583.

Cesca, S., Braun, T., Maccaferri, F., Passarelli, L., Rivalta, E., and Dahm, T. Source modelling of the M5–6 Emilia-Romagna, Italy, earthquakes (2012 May 20–29). *Geophysical Journal International*, 193(3):1658–1672, 03 2013. doi: 10.1093/gji/ggt069.

Dahm, T., Heimann, S., Metz, M., and Isken, M. P. A self-similar dynamic rupture model based on the simplified wave-rupture analogy. *Geophysical Journal International*, 225:1586–1604, 2021. doi: 10.1093/gji/ggab045.

Dal Zilio, L. and Ampuero, J. P. Earthquake doublet in Turkey and Syria. *Commun Earth Environ*, 4:73, 2023. doi: 10.1038/s43247-023-00747-z.

Daout, S., Steinberg, A., Isken, M. P., Heimann, S., and Sudhaus, H. Illuminating the spatio-temporal evolution of the 2008–2009

511 qaidam earthquake sequence with the joint use of insar time series and teleseismic data. *Remote Sensing*, 12(17):1–23, 2020.
512 doi: 10.3390/rs12172850.

513 Doin, M.-P., Lasserre, C., Peltzer, G., Cavalie, O., and Doubre, C. Corrections of stratified tropospheric delays in SAR interferometry: Valida-
514 tion with global atmospheric models. *Remote Sensing of Environment*, 160:155–170, 2015. doi: 10.1016/j.jappgeo.2009.03.010.

515 Donner, S., Ghods, A., Krüger, F., Rößler, D., Landgraf, A., and Ballato, P. The Ahar-Varzeghan earthquake doublet (Mw 6.4 and 6.2) of 11
516 August 2012: Regional seismic moment tensors and a seismotectonic interpretation. *Bulletin of the Seismological Society of America*, 105
517 (2):791–807, 2015. doi: 10.1785/0120140042.

518 Dziewoński, A. M., Chou, T.-A., and Woodhouse, J. H. Determination of earthquake source parameters from waveform data for studies of
519 global and regional seismicity. *Journal of Geophysical Research*, 86(B4):2825–2852, 1981.

520 Edey, A., Allen, M. B., and Nilfouroushan, F. Kinematic Variation Within the Fars Arc, Eastern Zagros, and the Development of Fold-and-Thrust
521 Belt Curvature. *Tectonics*, 39, 2020. doi: https://doi.org/10.1029/2019TC005941.

522 Ekström, G., Nettles, M., and Dziewoński, A. M. The global CMT project 2004-2010: Centroid-moment tensors for 13,017 earthquakes. *Physics
523 of the Earth and Planetary Interiors*, 200-201:1–9, 2012. doi: 10.1016/j.pepi.2012.04.002.

524 Elliott, J., Bergman, E., Copley, A., Ghods, A., Nissen, E., Oveisi, B., Tatar, M., Walters, R., and Yamini-Fard, F. The 2013 Mw 6.2 Khaki-Shonbe
525 (Iran) Earthquake: Insights into seismic and aseismic shortening of the Zagros sedimentary cover. *Earth and Space Science*, 2(11):435–
526 471, 2015. doi: 10.1002/2015EA000098.

527 Falcon, N. L. Southern Iran: Zagros Mountains. *Geological Society, London, Special Publications*, 4(1):199–211, 1974.
528 doi: 10.1144/GSL.SP.2005.004.01.11.

529 Fathian, A., Atzori, S., Nazari, H., Reicherter, K., Salvi, S., Svigkas, N., Tatar, M., Tolomei, C., and Yaminifard, F. Complex co- and postseismic
530 faulting of the 2017–2018 seismic sequence in western Iran revealed by InSAR and seismic data. *Remote Sensing of Environment*, 253
531 (December), 2021. doi: 10.1016/j.rse.2020.112224.

532 Fathian, A., Atzori, S., Svigkas, N., Tolomei, C., Shugar, D. H., and Reicherter, K. Source Characteristics of the Fin Doublet Earthquake of
533 14 November 2021 (Mw 6.2 and Mw 6.3) Utilizing InSAR Data. In *IGARSS 2022 - 2022 IEEE International Geoscience and Remote Sensing
534 Symposium*, pages 2119–2122, 2022. doi: 10.1109/IGARSS46834.2022.9883591.

535 Freund, R. Rotation of strike slip faults in Sistan, southeast Iran. *The Journal of Geology*, 78(2):188–200, 1970. doi: 10.1086/627500.

536 GEOFON Data Centre. GEOFON Seismic Network, 1993. http://geofon.gfz-potsdam.de/doi/network/GE.

537 GEUS Geological Survey of Denmark and Greenland. Danish Seismological Network, 1976. https://www.fdsn.org/networks/detail/DK/.

538 Ghods, A., Shabanian, E., Bergman, E., Faridi, M., Donner, S., Mortezanejad, G., and Aziz-Zanjani, A. The Varzaghan-Ahar, Iran, Earthquake
539 Doublet (Mw 6.4, 6.2): Implications for the geodynamics of northwest Iran. *Geophysical Journal International*, 203(1):522–540, 2015.
540 doi: 10.1093/gji/ggv306.

541 Guo, Z., Motagh, M., Hu, J. C., Xu, G., Haghighi, M. H., Bahroudi, A., Fathian, A., and Li, S. Depth-Varying Friction on a Ramp-Flat Fault
542 Illuminated by 3-Year InSAR Observations Following the 2017 Mw 7.3 Sarpol-e Zahab Earthquake. *Journal of Geophysical Research: Solid
543 Earth*, 127(12), 2022. doi: 10.1029/2022JB025148.

544 He, P., Ding, K., and Xu, C. The 2016 Mw 6.7 Aketao earthquake in Muji range, northern Pamir: Rupture on a strike-slip fault constrained
545 by Sentinel-1 radar interferometry and GPS. *International Journal of Applied Earth Observation and Geoinformation*, 73:99–106, 2018.
546 doi: https://doi.org/10.1016/j.jag.2018.06.001.

547 Heimann, S., Isken, M., Kühn, D., Sudhaus, H., Steinberg, A., Vasyura-Bathke, H., Daout, S., Cesca, S., and Dahm, T. Grond - A probabilistic
548 earthquake source inversion framework, 2018.

549 Hessami, K., Koyi, H. A., Talbot, C. J., Tabasi, H., and Shabanian, E. Progressive unconformities within an evolving foreland fold–thrust belt,
550 Zagros Mountains. *Journal of the Geological Society*, 158(6):969–981, 2001. doi: 10.1144/0016-764901-007.

551 Hessami, K., Jamali, F., and Tabassi, H. Major active faults of Iran. *IIEES, Tehran*, 2003.

552 Hogenson, K., Kristenson, H., Kennedy, J., Johnston, A., Rine, J., Logan, T. A., Zhu, J., Williams, F., Herrmann, J., and Smale, J. Hybrid
553 Pluggable Processing Pipeline (HyP3): A Cloud-Native Infrastructure for Generic Processing of SAR Data. In *In Proceedings of the 2016*
554 *AGU Fall Meeting, San Francisco, CA, USA, 12–16 December 2016*, 2016.

555 Ide, S. Bayesian multiple rupture plane inversion to assess rupture complexity: application to the 2018 Mw 7.9 Alaska earthquake. In
556 Kanamori, H., editor, *Slip inversion in Earthquake Seismology*, volume 4, pages 193–224. Elsevier, 2007. doi: 10.1016/B978-044452748-
557 6/00068-7.

558 India Meteorological Department. National Seismic Network of India , 2000.

559 Institut de physique du globe de Paris (IPGP) and École et Observatoire des Sciences de la Terre de Strasbourg (EOST). GEOSCOPE, French
560 Global Network of broad band seismic stations, 1982. http://geoscope.ipgp.fr/networks/detail/G/.

561 Isken, M., Sudhaus, H., Heimann, S., Steinberg, A., Daout, S., and Vasyura-Bathke, H. Kite - Software for Rapid Earthquake Source Optimi-
562 sation from InSAR Surface Displacement, 2017.

563 Jahani, S., Callot, J. P., Letouzey, J., and De Lamotte, D. F. The eastern termination of the Zagros Fold-and-Thrust Belt, Iran: Structures,
564 evolution, and relationships between salt plugs, folding, and faulting. *Tectonics*, 28(6), 2009. doi: 10.1029/2008TC002418.

565 Jamalreyhani, M., Pousse-Beltran, L., Büyükakpınar, P., Cesca, S., Nissen, E., Ghods, A., López-Comino, J. Á., Rezapour, M., and Najafi, M.
566 The 2019–2020 Khalili (Iran) Earthquake Sequence—Anthropogenic Seismicity in the Zagros Simply Folded Belt? *Journal of Geophysical*
567 *Research: Solid Earth*, 126(12):1–19, 2021. doi: 10.1029/2021JB022797.

568 Jamalreyhani, M., Rezapour, M., Cesca, S., Dahm, T., Heimann, S., Sudhaus, H., and Isken, M. P. Insight into the 2017–2019 Lurestan arc
569 seismic sequence (Zagros, Iran); complex earthquake interaction in the basement and sediments. *Geophysical Journal International*,
570 230:114–130, 2022. doi: https://doi.org/10.1093/gji/ggac057.

571 Jia, Z., Shen, Z., Zhan, Z., Li, C., Peng, Z., and Gurnis, M. The 2018 Fiji Mw 8.2 and 7.9 deep earthquakes: One doublet in two slabs. *Earth*
572 *and Planetary Science Letters*, 531:115997, 2020. doi: https://doi.org/10.1016/j.epsl.2019.115997.

573 Jia, Z., Zhan, Z., and Kanamori, H. The 2021 South Sandwich Island Mw 8.2 earthquake: a slow event sandwiched between regular ruptures.
574 *Geophys. Res. Lett.*, 49:1–8, 2022. doi: 10.1029/2021GL097104.

575 Jónsson, S., Zebker, H., Segall, P., and Amelung, F. Fault slip distribution of the 1999 Mw 7.1 Hector Mine, California, earthquake,
576 estimated from satellite radar and GPS measurements. *Bulletin of the Seismological Society of America*, 92(4):1377–1389, 2002.
577 doi: 10.1785/0120000922.

578 Kanamori, H. Mechanics of Earthquakes. *Annual Review of Earth and Planetary Sciences*, 22(1):207–237, 1994. doi: 10.1146/an-
579 nurev.earth.22.1.207.

580 Karasözen, E., Nissen, E., Bergman, E. A., and Ghods, A. Seismotectonics of the Zagros (Iran) From Orogen-Wide, Calibrated Earthquake
581 Relocations. *Journal of Geophysical Research: Solid Earth*, 124(8):9109–9129, 2019. doi: 10.1029/2019JB017336.

582 Lay, T. The surge of great earthquakes from 2004 to 2014. *Earth and Planetary Science Letters*, 409:133–146, 2015.
583 doi: 10.1016/j.epsl.2014.10.047.

584 Lay, T. and Kanamori, H. Earthquake Doublets in the Solomon Islands. *Physics ofthe Earth and Planetary Interiors*, 21:283–304, 1980.

585 Lohman, R. B. and Barnhart, W. D. Evaluation of earthquake triggering during the 2005–2008 earthquake sequence on Qeshm Island, Iran.
586 *Journal of Geophysical Research*, 115, 2010. doi: https://doi.org/10.1029/2010JB007710.

LTD Seismological Experience and Methodology Expedition of the Committee of Science of the Ministry of Education and Science of the Republic of Kazakhstan. Seismic network of the Seismological Experience and Methodology Expedition CS MES RK, 2003.

Masson, F., Chéry, J., Hatzfeld, D., Martinod, J., Vernant, P., Tavakoli, F., and Ghafory-Ashtiani, M. Seismic versus aseismic deformation in Iran inferred from earthquakes and geodetic data. *Geophysical Journal International*, 160(1):217–226, 2005. doi: 10.1111/j.1365-246X.2004.02465.x.

Metz, M. A quasi-dynamic and self-consistent rupture model to simulate earthquake ruptures. masterthesis, Universität Potsdam, 2019.

Metz, M., Vera, F., Carrillo Ponce, A., Cesca, S., Babeyko, A., Dahm, T., Saul, J., and Tilmann, F. Seismic and Tsunamigenic Characteristics of a Multimodal Rupture of Rapid and Slow Stages: The Example of the Complex 12 August 2021 South Sandwich Earthquake. *Journal of Geophysical Research: Solid Earth*, 127(11), 2022. doi: 10.1029/2022jb024646.

Momeni, S. and Tatar, M. Mainshocks/aftershocks study of the August 2012 earthquake doublet on Ahar-Varzaghan complex fault system (NW Iran). *Physics of the Earth and Planetary Interiors*, 283:67–81, 2018. doi: https://doi.org/10.1016/j.pepi.2018.08.001.

Nemati, M. The November 2021 Fin (SE Zagros , Iran) doublet earthquakes of reverse faults in a transpressional tectonic regime. Technical report, Shahid Bahonar University of Kerman, 2022.

Ni, J. and Barazangi, M. Seismotectonics of the Zagros continental collision zone and a comparison with the Himalayas. *Journal of Geophysical Research: Solid Earth*, 91(B8):8205–8218, 1986. doi: 10.1029/JB091iB08p08205.

Nissen, E., Ghorashi, M., Jackson, J., Parsons, B., and Talebian, M. The 2005 Qeshm Island earthquake (Iran) - A link between buried reverse faulting and surface folding in the Zagros Simply Folded Belt? *Geophysical Journal International*, 171(1):326–338, 2007. doi: 10.1111/j.1365-246X.2007.03514.x.

Nissen, E., Yamini-Fard, F., Tatar, M., Gholamzadeh, A., Bergman, E., Elliott, J. R., Jackson, J. A., and Parsons, B. The vertical separation of mainshock rupture and microseismicity at Qeshm island in the Zagros fold-and-thrust belt, Iran. *Earth and Planetary Science Letters*, 296(3-4):181–194, 2010. doi: 10.1016/j.epsl.2010.04.049.

Nissen, E., Tatar, M., Jackson, J. A., and Allen, M. B. New views on earthquake faulting in the Zagros fold-and-thrust belt of Iran. *Geophysical Journal International*, 186(3):928–944, 2011. doi: 10.1111/j.1365-246X.2011.05119.x.

Nissen, E., Jackson, J., Jahani, S., and Tatar, M. Zagros "phantom earthquakes" reassessed - The interplay of seismicity and deep salt flow in the Simply Folded Belt? *Journal of Geophysical Research: Solid Earth*, 119(4):3561–3583, 2014. doi: 10.1002/2013JB010796.

Nissen, E., Ghods, A., Karasözen, E., Elliott, J. R., Barnhart, W. D., Bergman, E. A., Hayes, G. P., Jamal-Reyhani, M., Nemati, M., Tan, F., Abdulnaby, W., Benz, H. M., Shahvar, M. P., Talebian, M., and Chen, L. The 12 November 2017 M w 7.3 Ezgeleh-Sarpolzahab (Iran) Earthquake and Active Tectonics of the Lurestan Arc. *Journal of Geophysical Research: Solid Earth*, 124(2):2124–2152, 2019. doi: 10.1029/2018JB016221.

Okada, Y. Gravity and potential changes due to shear and tensile faults in a half-space. *Journal of Geophysical Research*, 82(2):1018–1040, 1992. doi: 10.1029/92JB00178.

Oveisi, B., Lavé, J., Van Der Beek, P., Carcaillet, J., Benedetti, L., and Aubourg, C. Thick-and thin-skinned deformation rates in the central Zagros simple folded zone (Iran) indicated by displacement of geomorphic surfaces. *Geophysical Journal International*, 176(2):627–654, 2009.

Quinteros, J., Strollo, A., Evans, P. L., Hanka, W., Heinloo, A., Hemmleb, S., Hillmann, L., Jaeckel, K., Kind, R., Saul, J., Zieke, T., and Tilmann, F. The GEOFON Program in 2020. *Seismological Research Letters*, 92(3):1610–1622, 02 2021. doi: 10.1785/0220200415.

Regard, V., Bellier, O., Thomas, J.-C., Abbassi, M., Mercier, J., Shabanian, E., Feghhi, K., and Soleymani, S. Accommodation of Arabia-Eurasia convergence in the Zagros-Makran transfer zone, SE Iran: A transition between collision and subduction through a young deforming

system. *Tectonics*, 23(4), 2004.

Regional Integrated Multi-Hazard Early Warning System (RIMES Thailand). Regional Integrated Multi-Hazard Early Warning System, 2008.

Rezapour, M. and Jamalreyhani, M. R. Source fault analyses from InSAR data and aftershocks for the Fin doublet earthquakes on 14 November 2021 in Hormozgan province, South Iran. *Earth and Space Physics*, 2022. doi: https://doi.org/10.22059/jesphys.2022.337959.1007399.

Roustaei, M., Nissen, E., Abbassi, M., Gholamzadeh, A., Ghorashi, M., Tatar, M., Yamini-Fard, F., Bergman, E., Jackson, J., and Parsons, B. The 2006 March 25 Fin earthquakes (Iran) - insights into the vertical extents of faulting in the Zagros Simply Folded Belt. *Geophysical Journal International*, 181(3):1275–1291, 2010. doi: 10.1111/j.1365-246X.2010.04601.x.

San Fernando Royal Naval Observatory (ROA), Universidad Complutense De Madrid (UCM), Helmholtz-Zentrum Potsdam Deutsches GeoForschungsZentrum (GFZ), Universidade De Évora (UEVORA, Portugal) and Institute Scientifique Of Rabat (ISRABAT, Morocco). The Western Mediterranean BB seismic Network, 1996.

Savidge, E., Nissen, E., Nemati, M., Karasözen, E., Hollingsworth, J., Talebian, M., Bergman, E., Ghods, A., Ghorashi, M., Kosari, E., et al. The December 2017 Hojedk (Iran) earthquake triplet—sequential rupture of shallow reverse faults in a strike-slip restraining bend. *Geophysical Journal International*, 217(2):909–925, 2019. doi: 10.1093/gji/ggz053.

Scripps Institution of Oceanography. Global Seismograph Network - IRIS/IDA, 1986.

Sokos, E., Kiratzi, A., Gallovič, F., Zahradník, J., Serpetsidaki, A., Plicka, V., Janský, J., Kostelecký, J., and Tselentis, G. A. Rupture process of the 2014 Cephalonia, Greece, earthquake doublet (Mw6) as inferred from regional and local seismic data. *Tectonophysics*, 656:131–141, 2015. doi: 10.1016/j.tecto.2015.06.013.

Steinberg, A., Sudhaus, H., Heimann, S., and Krüger, F. Sensitivity of InSAR and teleseismic observations to earthquake rupture segmentation. *Geophysical Journal International*, 223(2):875–907, 2020. doi: 10.1093/gji/ggaa351.

Steinberg, A., Sudhaus, H., and Krüger, F. Using teleseismic backprojection and InSAR to obtain segmentation information for large earthquakes: a case study of the 2016 Mw 6.6 Muji earthquake. *Geophysical Journal International*, 2022.

Stoecklin, J. Structural history and tectonics of Iran: a review. *AAPG bulletin*, 52(7):1229–1258, 1968. doi: 10.1306/5D25C4A5-16C1-11D7-8645000102C1865D.

Sudhaus, H. and Jónsson, S. Improved source modelling through combined use of InSAR and GPS under consideration of correlated data errors: Application to the June 2000 Kleifarvatn earthquake, Iceland. *Geophysical Journal International*, 176(2):389–404, 2009. doi: 10.1111/j.1365-246X.2008.03989.x.

Talebian, M. and Jackson, J. A reappraisal of earthquake focal mechanisms and active shortening in the Zagros mountains of Iran. *Geophysical Journal International*, 156(3):506–526, 2004. doi: 10.1111/j.1365-246X.2004.02092.x.

Tatar, M., Hatzfeld, D., and Ghafory-Ashtiany, M. Tectonics of the Central Zagros (Iran) deduced from microearthquake seismicity. *Geophysical Journal International*, 156(2):255–266, 2004. doi: 10.1111/j.1365-246X.2003.02145.x.

Taymaz, T., Ganas, A., Berberian, M., Eken, T., Irmak, T. S., Kapetanidis, V., Yolsal-Çevikbilen, S., Erman, C., Keleş, D., Esmaeili, C., Tsironi, V., and Özkan, B. The 23 February 2020 Qotur-Ravian earthquake doublet at the Iranian-Turkish border: Seismological and InSAR evidence for escape tectonics. *Tectonophysics*, 838:229482, 2022. doi: https://doi.org/10.1016/j.tecto.2022.229482.

Thapa, D. R., Tao, X., Fan, F., and Tao, Z. Aftershock analysis of the 2015 Gorkha-Dolakha (Central Nepal) earthquake doublet. *Heliyon*, 4(7): e00678, 2018. doi: 10.1016/j.heliyon.2018.e00678.

Trugman, D. T. and Shearer, P. M. GrowClust: A Hierarchical clustering algorithm for relative earthquake relocation, with application to the Spanish Springs and Sheldon, Nevada, earthquake sequences. *Seismological Research Letters*, 88(2):379–391, 2017. doi: 10.1785/0220160188.

Trugman, D. T., Chamberlain, C. J., Savvaidis, A., and Lomax, A. GrowClust3D.jl: A Julia Package for the Relative Relocation of Earthquake Hypocenters Using 3D Velocity Models. *Seismological Research Letters*, 94(1):443–456, 2023. doi: 10.1785/0220220193.

Vernant, P., Nilforoushan, F., Hatzfeld, D., Abbassi, M., Vigny, C., Masson, F., Nankali, H., Martinod, J., Ashtiani, A., Bayer, R., et al. Present-day crustal deformation and plate kinematics in the Middle East constrained by GPS measurements in Iran and northern Oman. *Geophysical Journal International*, 157(1):381–398, 2004. doi: 10.1111/j.1365-246X.2004.02222.x.

Viltres, R., Jónsson, S., Alothman, A., Liu, S., Masson, F., Doubre, C., Reilinger, R., Viltres, R., Jónsson, S., Alothman, A., Liu, S., and Leroy, S. Present-day motion of the Arabian plate. *Tetonics*, 41(3), 2022. doi: 10.1029/2021TC007013.

Walker, R. and Jackson, J. Offset and evolution of the Gowk fault, SE Iran: a major intra-continental strike-slip system. *Journal of structural Geology*, 24(11):1677–1698, 2002. doi: 10.1016/S0191-8141(01)00170-5.

Walker, R. T., Andalibi, M. J., Gheitanchi, M. R., Jackson, J. A., Karegar, S., and Priestley, K. Seismological and field observations from the 1990 November 6 Furg (Hormozgan) earthquake: A rare case of surface rupture in the Zagros mountains of Iran. *Geophysical Journal International*, 163(2):567–579, 2005. doi: 10.1111/j.1365-246X.2005.02731.x.

Wang, R. A simple orthonormalization method for stable and efficient computation of Green's functions. *Bulletin of the Seismological Society of America*, 89:733–741, 1999. doi: 10.1785/BSSA0890030733.

Wang, R. The dislocation theory: a consistent way for including the gravity effect in (visco)elastic plane-earth models. *Geophysical Journal International*, 161:191–196, 2005. doi: 10.1111/j.1365-246X.2005.02614.x.

Wang, R., Lorenzo-Martín, F., and Roth, F. Computation of deformation induced by earthquakes in a multi-layered elastic crust - FORTRAN programs EDGRN/EDCMP. *Computer and Geosciences*, 29:195–207, 2003. doi: 10.1016/S0098-3004(02)00111-5.

Wang, R., Lorenzo-Martín, F., and Roth, F. PSGRN/PSCMP - a new code for calculating co- and post-seismic deformation, geoid and gravity changes based on the viscoelastic-gravitational dislocation theory. *Computer and Geosciences*, 32:527–541, 2006. doi: 10.1016/j.cageo.2005.08.006.

Wessel, P. and Smith, W. H. F. A global, self-consistent, hierarchical, high-resolution shoreline database. *Journal of Geophysical Research*, 101:8741–8743, 1996. doi: 10.1029/96JB00104.

Wessel, P., Smith, W. H., Scharroo, R., Luis, J., and Wobbe, F. Generic mapping tools: Improved version released. *Eos*, 94(45):409–410, 2013. doi: 10.1002/2013EO450001.

Weston, J., Ferreira, A. M., and Funning, G. J. Systematic comparisons of earthquake source models determined using InSAR and seismic data. *Tectonophysics*, 532-535:61–81, 2012. doi: 10.1016/j.tecto.2012.02.001.

Xu, Z. and Schwartz, S. Y. Large earthquake doublets and fault plane heterogeneity in the northern Solomon Islands subduction zone. *Pure and Applied Geophysics PAGEOPH*, 140(2):365–390, 1993. doi: 10.1007/BF00879412.

Yamini-Fard, F., Hatzfeld, D., Farahbod, A., Paul, A., and Mokhtari, M. The diffuse transition between the Zagros continental collision and the Makran oceanic subduction (Iran): microearthquake seismicity and crustal structure. *Geophysical Journal International*, 170(1):182–194, 2007. doi: 10.1111/j.1365-246X.2006.03232.x.

Yaminifard, F., Tatar, M., Hessami, K., Gholamzadeh, A., and Bergman, E. Aftershock analysis of the 2005 November 27 (Mw 5.8) Qeshm Island earthquake (Zagros-Iran): Triggering of strike-slip faults at the basement. *Journal of Geodynamics*, 61:138–147, 2012. doi: 10.1016/j.jog.2012.04.005.

Yang, Y.-h., Li, X., Hu, J.-c., Song, J., Zhao, J., and Yassaghi, A. The 2022 Hormozgan Doublet Earthquake : Two Blind Thrusts-Related Folding in Zagros Fold-And-Thrust Belt , Southeast Iran. *Geophysical Research Letters*, 50, 2023. doi: 10.1029/2022GL101902.

Ye, L., Lay, T., Kanamori, H., and Koper, K. D. Energy Release of the 2013 Mw 8.3 Sea of Okhotsk Earthquake and Deep Slab Stress Hetero-

geneity. *Science*, 341(September):1380–1384, 2013. doi: 10.1126/science.1242032.

Ye, L., Lay, T., Kanamori, H., Zhan, Z., and Duputel, Z. Diverse rupture processes in the 2015 Peru deep earthquake doublet. *Science Advances*, 2(6):1989–1990, 2016. doi: 10.1126/sciadv.1600581.

Yu, C., Penna, N. T., and Li, Z. Generation of real-time mode high-resolution water vapor fields from GPS observations. *Journal of Geophysical Research: Atmospheres*, 122:2008–2025, 2017. doi: 10.1002/2016JD025753.

Yu, C., Li, Z., and Penna, N. T. Interferometric synthetic aperture radar atmospheric correction using a GPS-based iterative tropospheric decomposition model. *Remote Sensing of Environment*, 204:109–121, 2018a. doi: 10.1016/j.rse.2017.10.038.

Yu, C., Li, Z., Penna, N. T., and Crippa, P. Generic Atmospheric Correction Model for Interferometric Synthetic Aperture Radar Observations. *Journal of Geophysical Research: Solid Earth*, 123:9202–9222, 2018b. doi: 10.1029/2017JB015305.

Yunjun, Z., Fattahi, H., and Amelung, F. Small baseline InSAR time series analysis: Unwrapping error correction and noise reduction. *Remote Sens.*, 14(336), 2022. doi: 10.1016/j.cageo.2019.104331.

Zhang, X., Feng, W., Li, D., Yin, F., and Yi, L. Diverse rupture processes of the 2014 Kangding, China, earthquake doublet (MW 6.0 and 5.7) and driving mechanisms of aftershocks. *Tectonophysics*, 820:229118, 2021. doi: https://doi.org/10.1016/j.tecto.2021.229118.

Zhao, X., Xu, C., Wen, Y., He, K., and Yang, J. Early post-seismic deformation of the 2017 Mw 7.3 Darbandikhan, Iran/Iraq Earthquake on a flat-ramp-flat fault. *Tectonophysics*, 853:229809, 2023. doi: 10.1016/j.tecto.2023.229809.

4.1 Supporting information

Seismica

Supporting Information for

The July-December 2022 earthquake sequence in the southeastern Fars arc of Zagros mountains, Iran

Metz, M.[1,2], Asayesh, B. M.[1,2], Aref, M. M.[1], Jamalreyhani, M.[2,3], Büyükpinar, P.[2], Dahm, T[1,2]

Institute of Geosciences, University of Potsdam, Potsdam, Germany; GFZ German Research Centre for Geosciences, Potsdam, Germany; Institute of Geophysics, University of Tehran, Tehran, Iran

Contents of this file

Additional Supporting Information (Files uploaded separately)

File Table_S1.pdf: Full MT solutions for the seven earthquakes A1-A3, B1, B2 and C1 derived from seismic data.

File Table_S2.pdf: Deviatoric MT solutions for the seven earthquakes A1-A3, B1, B2 and C1 derived from seismic data.

File Table_S4.pdf: Results for individual finite fault inversions using seismic data.

File Table_S5.pdf: Finite fault solutions for the earthquakes A1-A3 from a joint 3 PDR inversion using seismic and InSAR data.

File Table_S7.pdf: Aftershocks of the IRSC catalog including uncertainties after relocation using the GrowClust3D.jl algorithm.

Introduction

We provide waveform fits obtained from the different full CMT and PDR finite fault inversions shown and discussed in the main text (Fig. S1–S11). They highlight the number of records available and their fit with respect to the different inversion approaches and the different earthquakes. Complementing that mean model parameters and their standard deviations are provided for deviatoric MT inversions (file Table_S1), full MT inversions (file Table_S2) and joint 3 double couple source inversion of sequence A (Tab.S3).
Both single source PDR solutions (file Table_S4) as well as the joint 3 PDR inversion results (file Table_S5) are given as well. In this regard we also yield PDR solutions for the less preferred nodal plane (file Table_S4).

Complementing on the mainshock inversions focal depth estimations based on teleseismic P-wave depth phases are shown (Fig. S12–S17). A map of the used arrays is given in Figure S18. Both, used seismic arrays, and the focal depth estimates, are summarized in Table S6.

Besides there is also some more detailed information on the aftershock relocation. In this regard we have displayed uncertainties of the relocated catalog (Fig. S19). The supplemental file Table_S7 provides the relocated catalog along with all uncertainties.

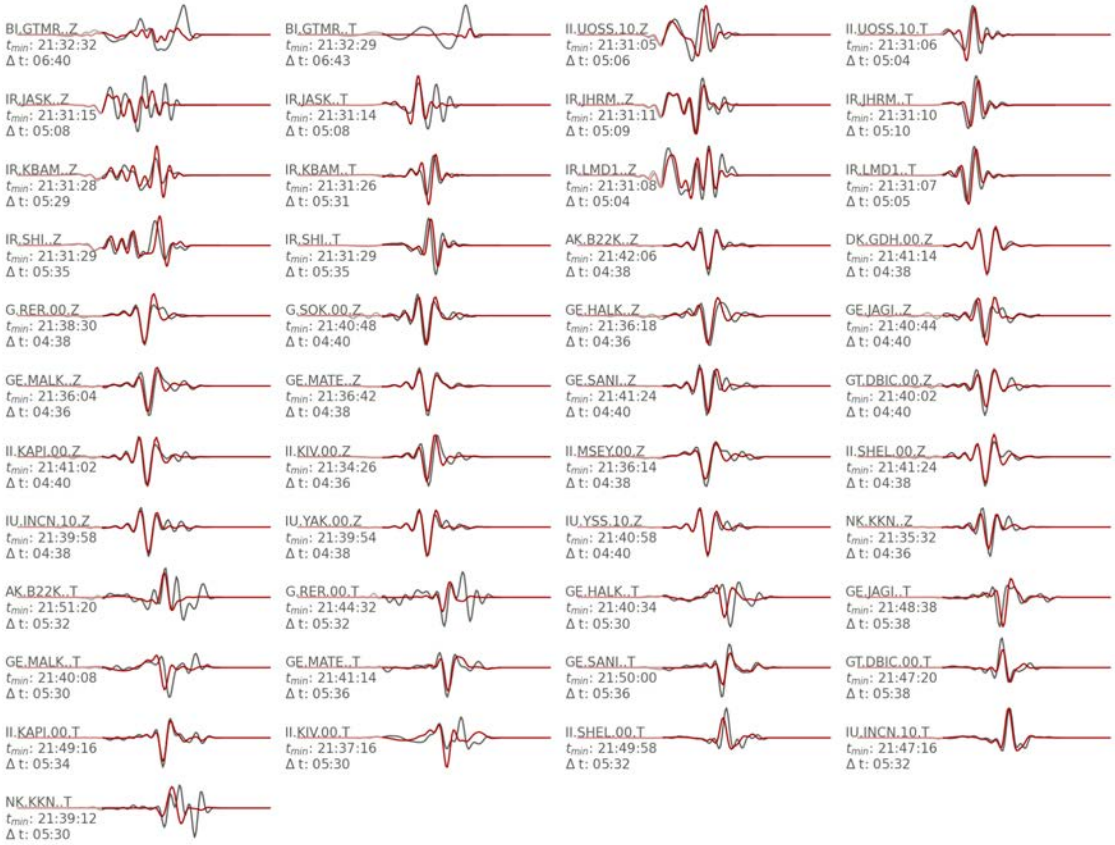

Figure S1. Waveform fits of the mean model (red) and observed data (black) from full MT inversion of earthquake A1. Channel information, start time of each trace and length of the given traces are given left of each trace.

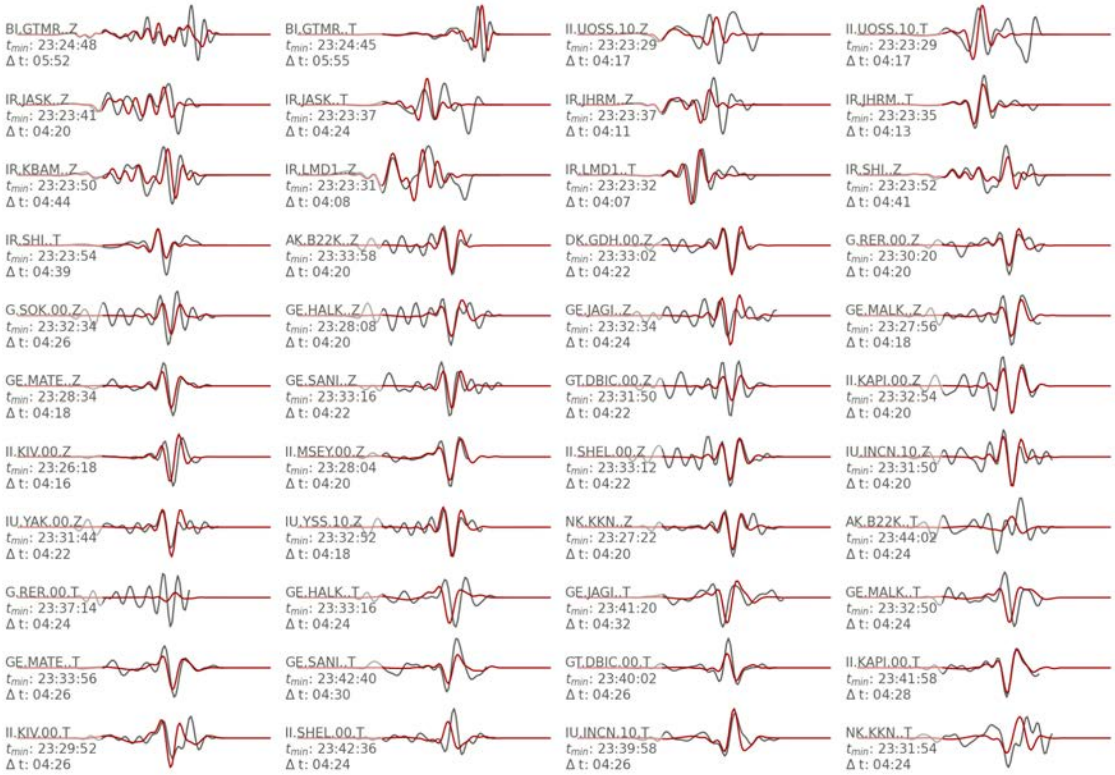

Figure S2. Waveform fits of the mean model (red) and observed data (black) from full MT inversion of earthquake A2. Channel information, start time of each trace and length of the given traces are given left of each trace.

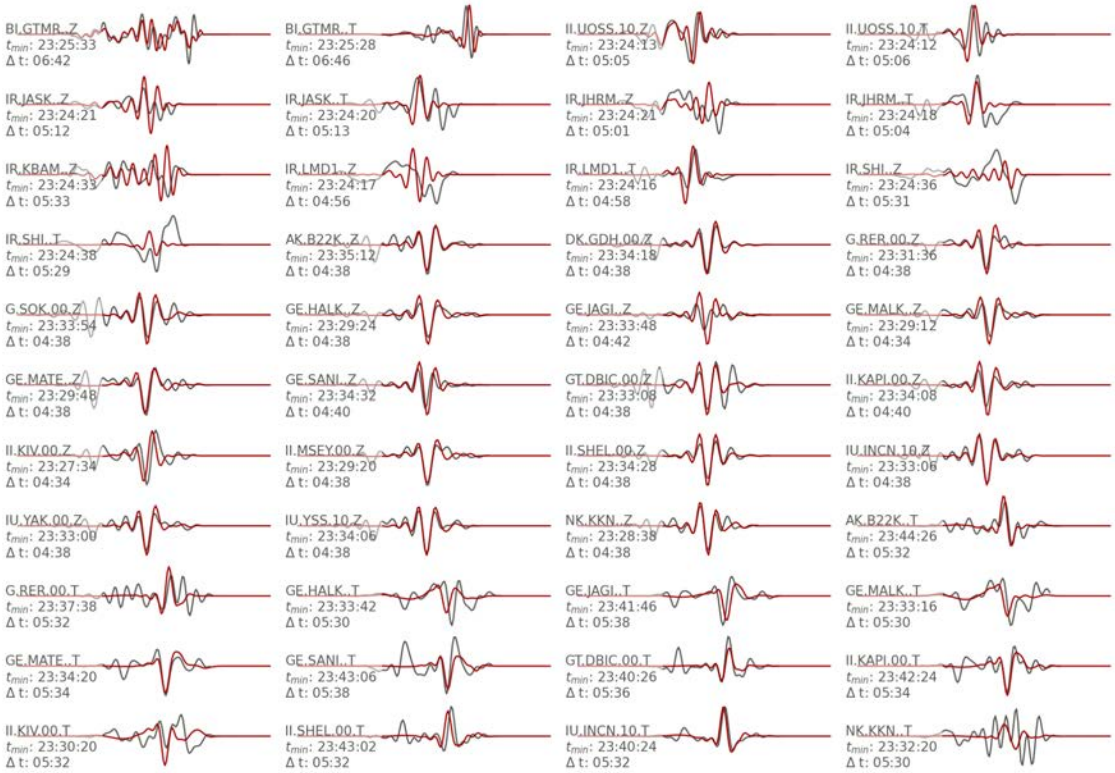

Figure S3. Waveform fits of the mean model (red) and observed data (black) from full MT inversion of earthquake A3. Channel information, start time of each trace and length of the given traces are given left of each trace.

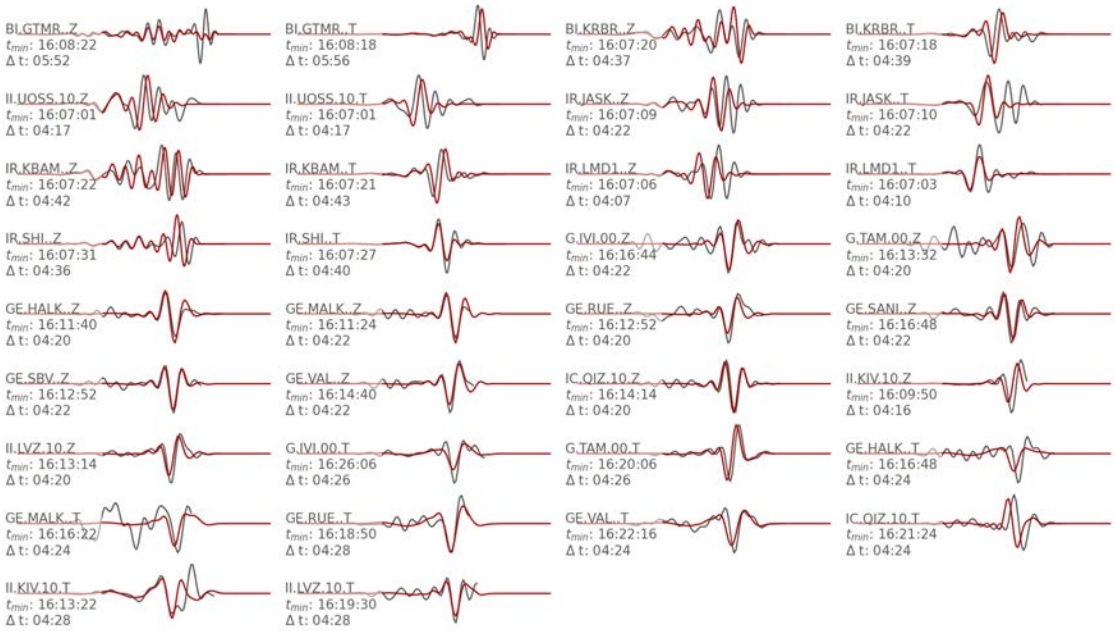

Figure S4. Waveform fits of the mean model (red) and observed data (black) from full MT inversion of earthquake B1. Channel information, start time of each trace and length of the given traces are given left of each trace.

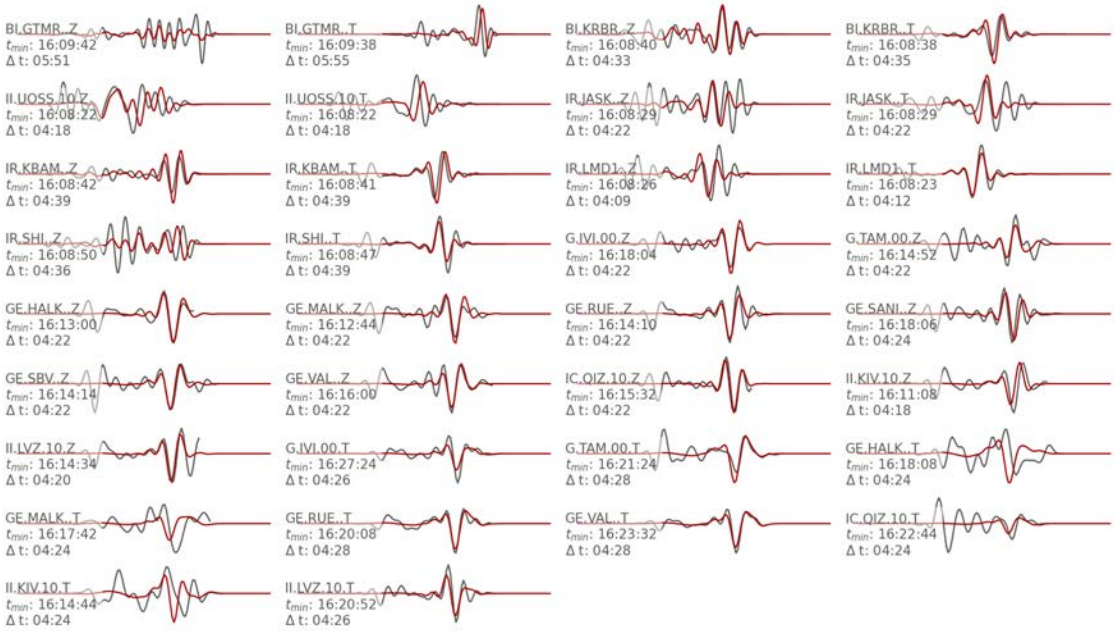

Figure S5. Waveform fits of the mean model (red) and observed data (black) from full MT inversion of earthquake B2. Channel information, start time of each trace and length of the given traces are given left of each trace.

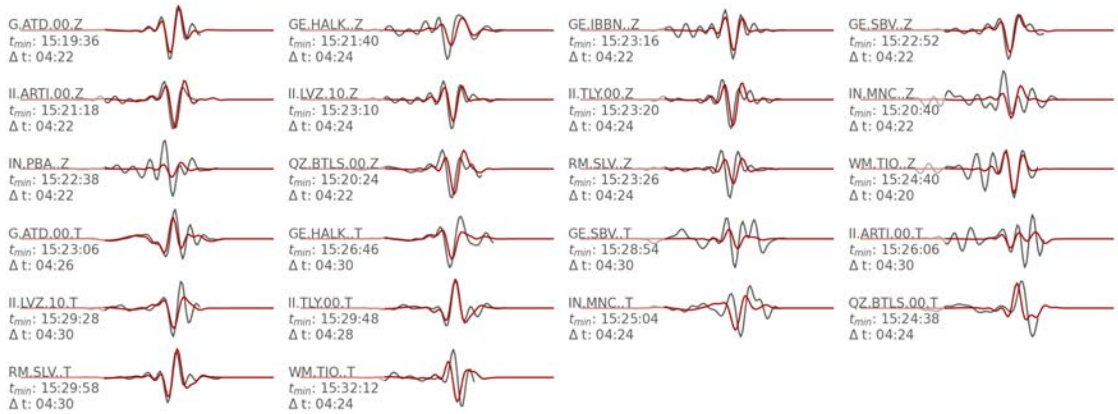

Figure S6. Waveform fits of the mean model (red) and observed data (black) from full MT inversion of earthquake C1. Channel information, start time of each trace and length of the given traces are given left of each trace.

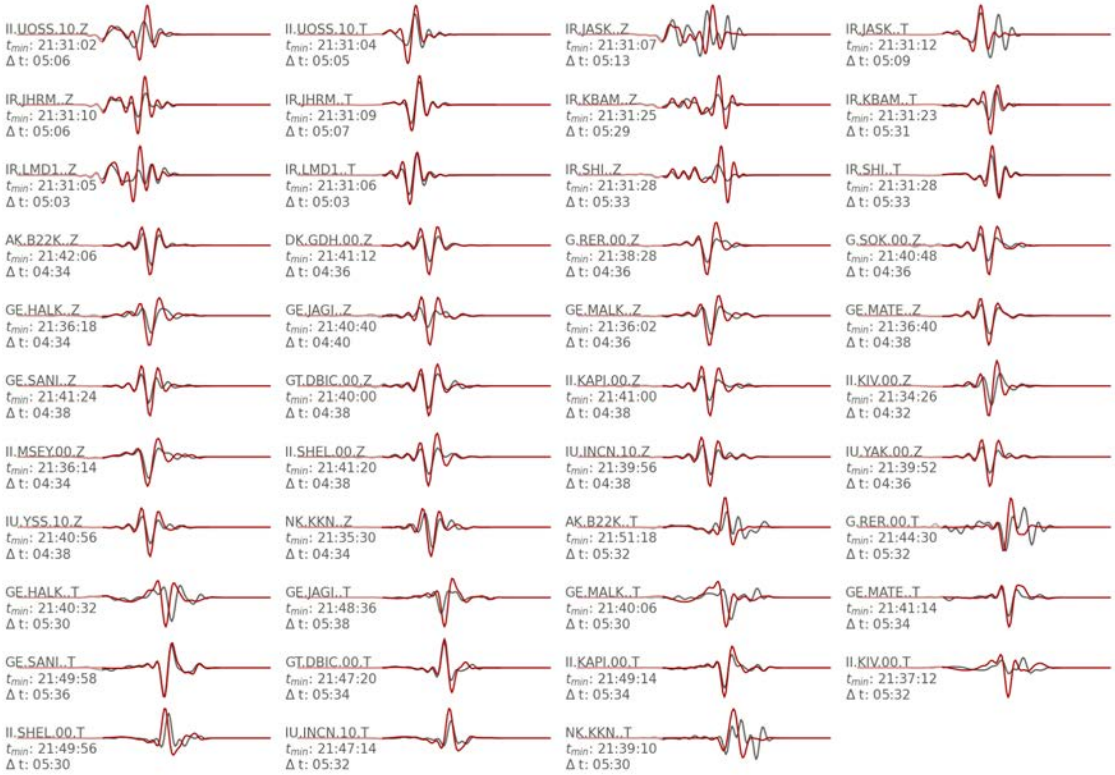

Figure S7. Waveform fits of the mean model (red) and observed data (black) from PDR inversion of earthquake A1. Channel information, start time of each trace and length of the given traces are given left of each trace.

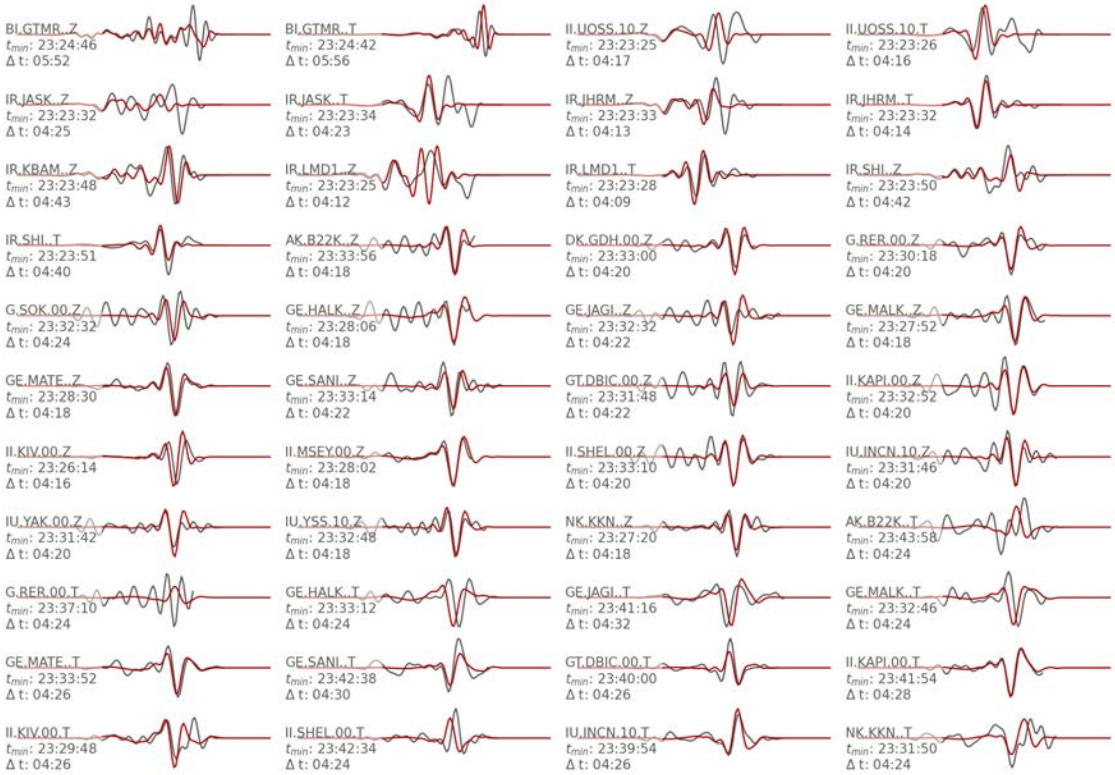

Figure S8. Waveform fits of the mean model (red) and observed data (black) from PDR inversion of earthquake A2. Channel information, start time of each trace and length of the given traces are given left of each trace.

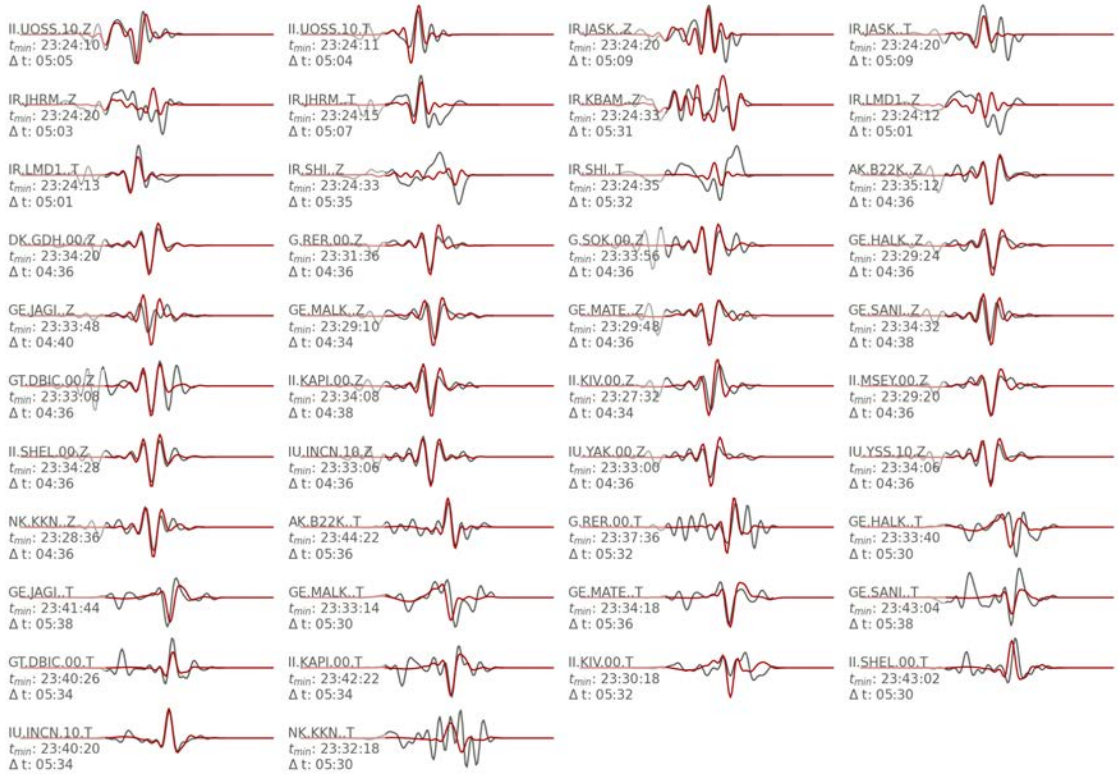

Figure S9. Waveform fits of the mean model (red) and observed data (black) from PDR inversion of earthquake A3. Channel information, start time of each trace and length of the given traces are given left of each trace.

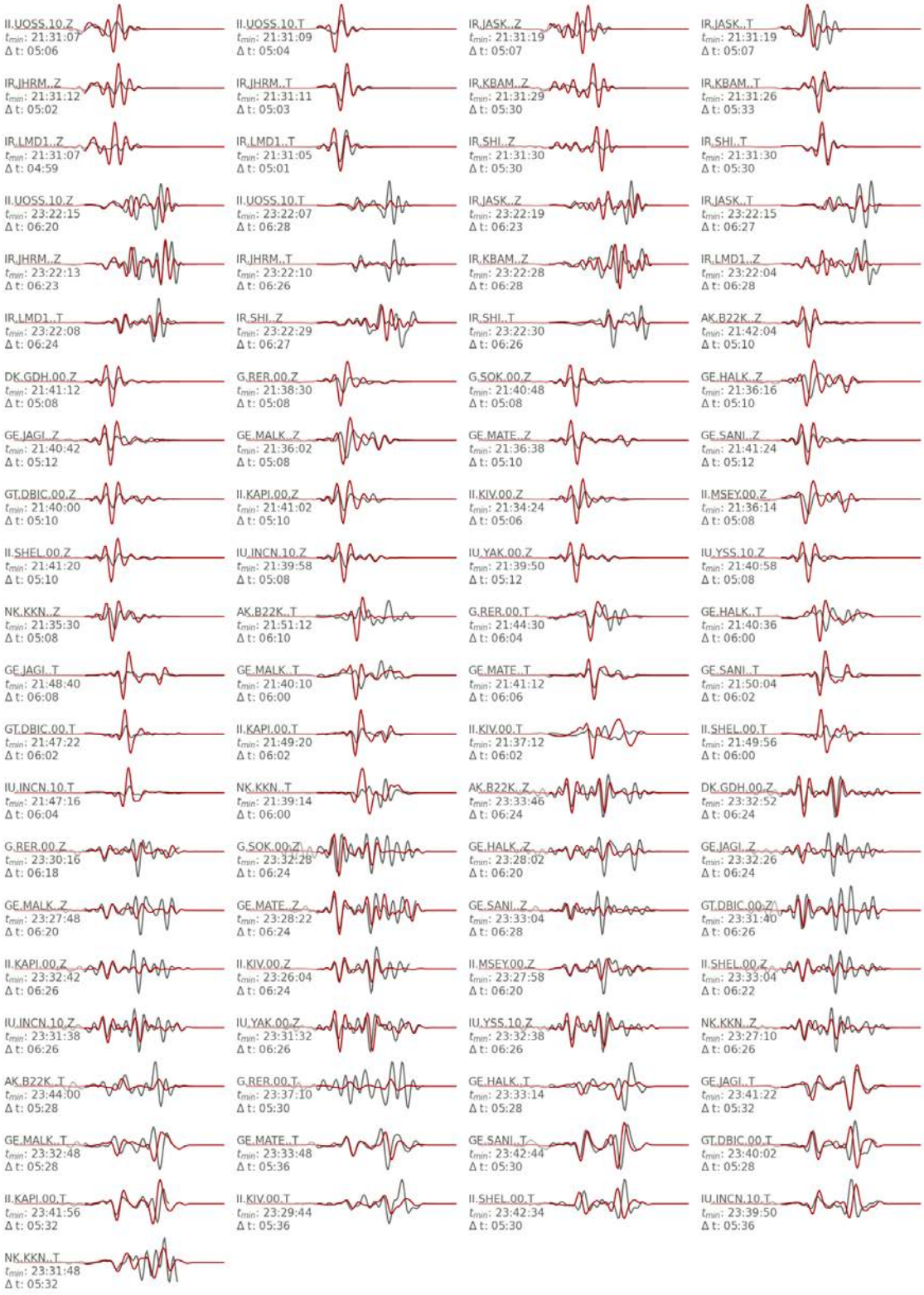

Figure S10. Waveform fits of the mean model (red) and observed data (black) from joint 3 double dc inversion of earthquakes A1, A2 and A3 using seismic and satellite deformation data. Channel information, start time of each trace and length of the given traces are given left of each trace.

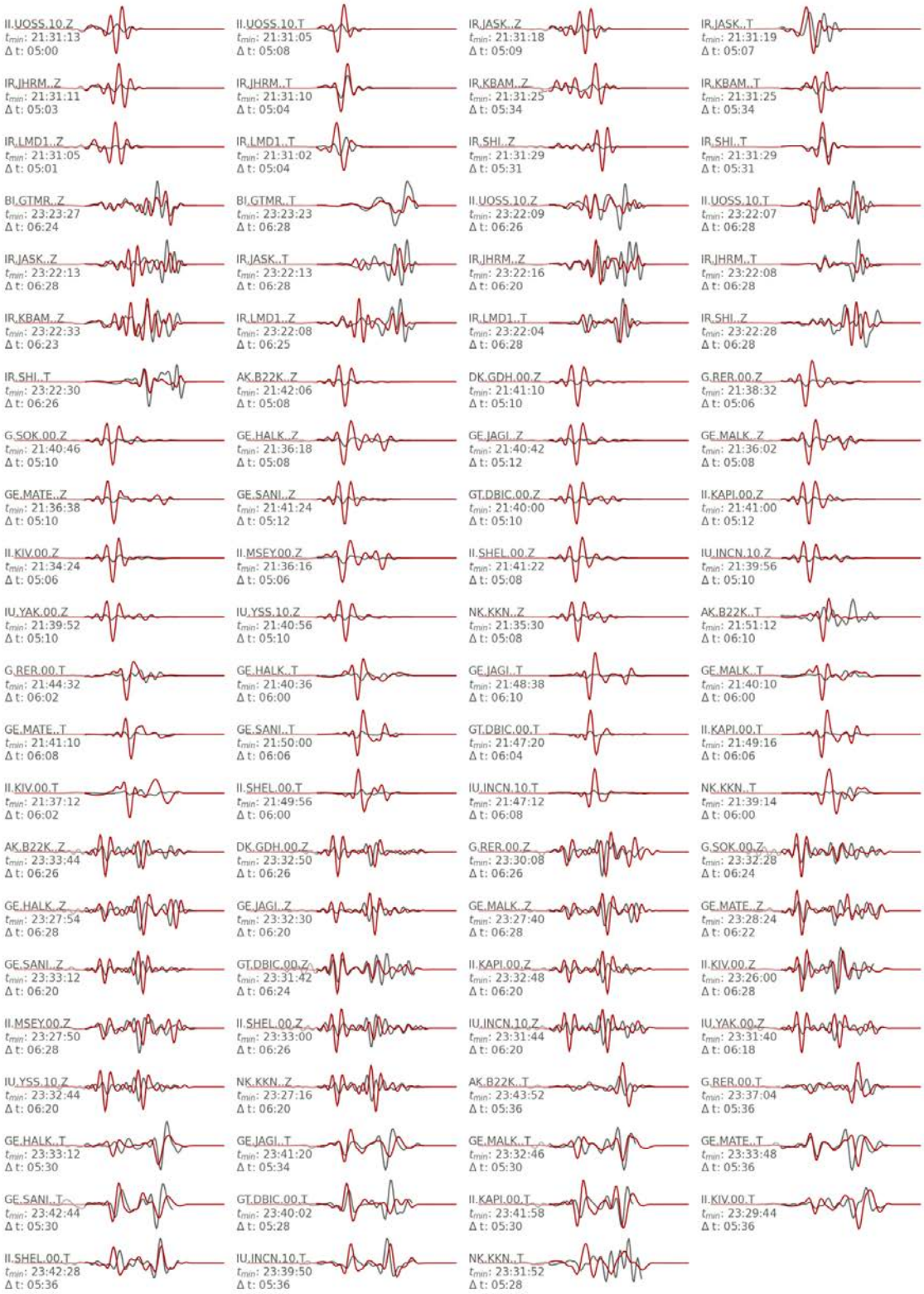

Figure S11. Waveform fits of the mean model (red) and observed data (black) from joint 3 PDR inversion of earthquakes A1, A2 and A3 using seismic and satellite deformation data. Channel information, start time of each trace and length of the given traces are given left of each trace.

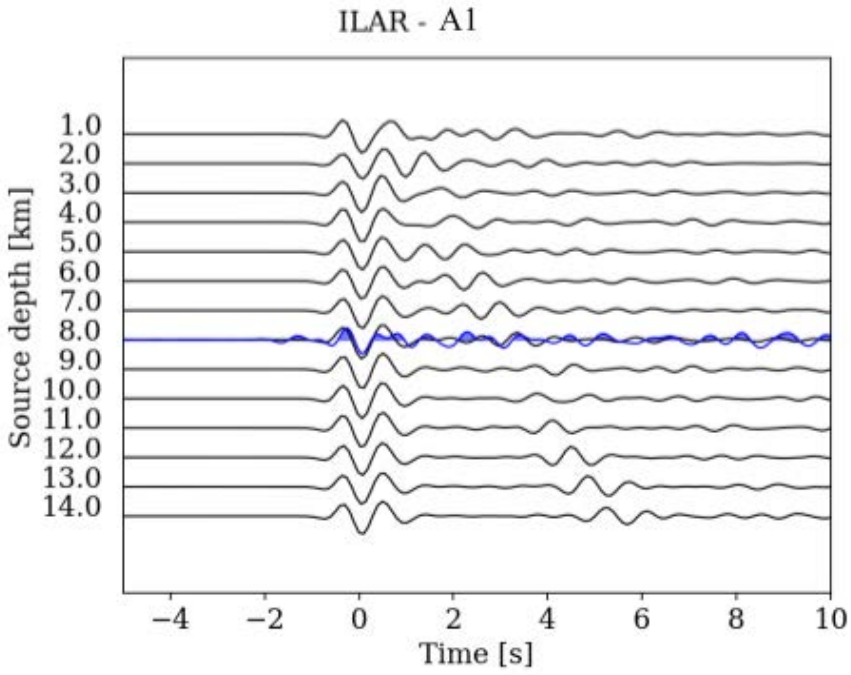

Figure S12. Best focal depth estimate for A1 derived from the stacked vertical trace of the ILAR network. Black lines show synthetic traces modelled for a source in the given depths along a path to the array centre. The blue line, shown at the preferred focal point depth, indicates the observed stacked trace of the network.

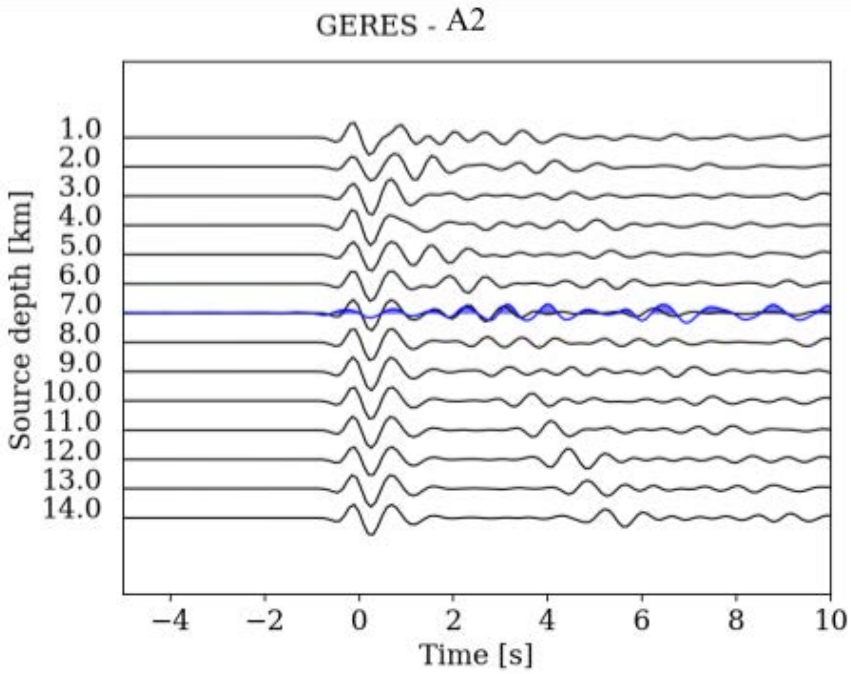

Figure S13. Best focal depth estimate for A2 derived from the stacked vertical trace of the GERES network. Black lines show synthetic traces modelled for a source in the given depths along a path to the array centre. The blue line, shown at the preferred focal point depth, indicates the observed stacked trace of the network.

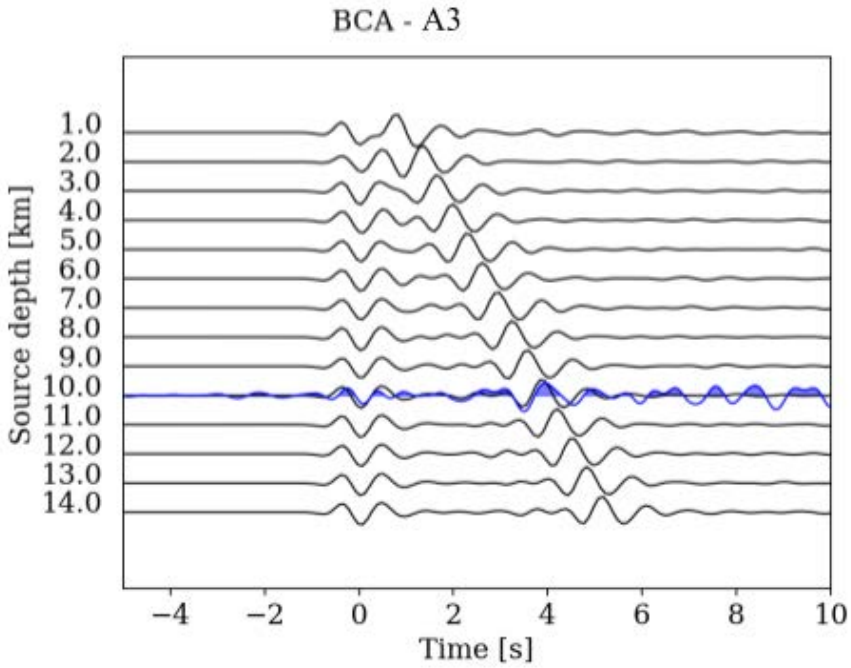

Figure S14. Best focal depth estimate for A3 derived from the stacked vertical trace of the BCA network. Black lines show synthetic traces modelled for a source in the given depths along a path to the array centre. The blue line, shown at the preferred focal point depth, indicates the observed stacked trace of the network.

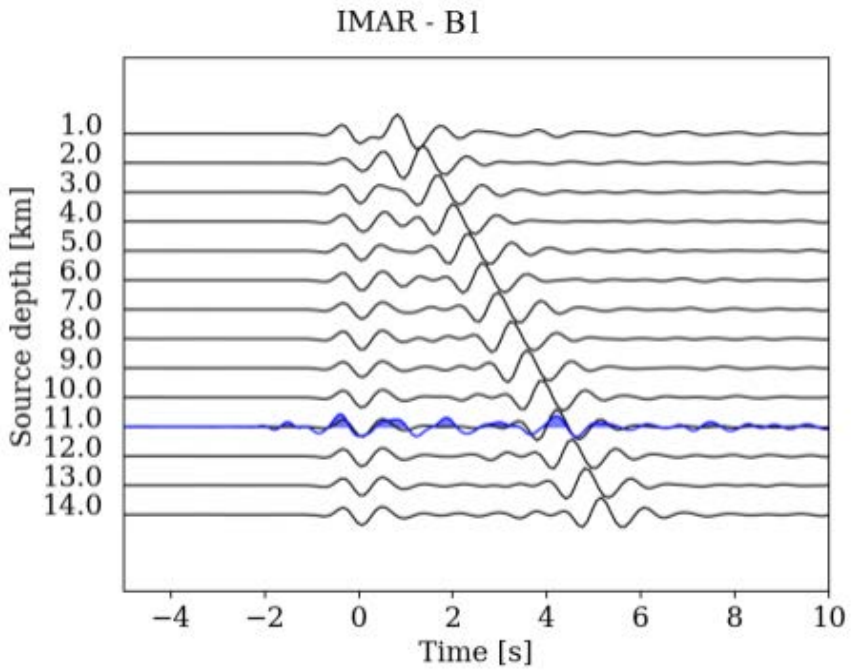

Figure S15. Best focal depth estimate for B1 derived from the stacked vertical trace of the IMAR network. Black lines show synthetic traces modelled for a source in the given depths along a path to the array centre. The blue line, shown at the preferred focal point depth, indicates the observed stacked trace of the network.

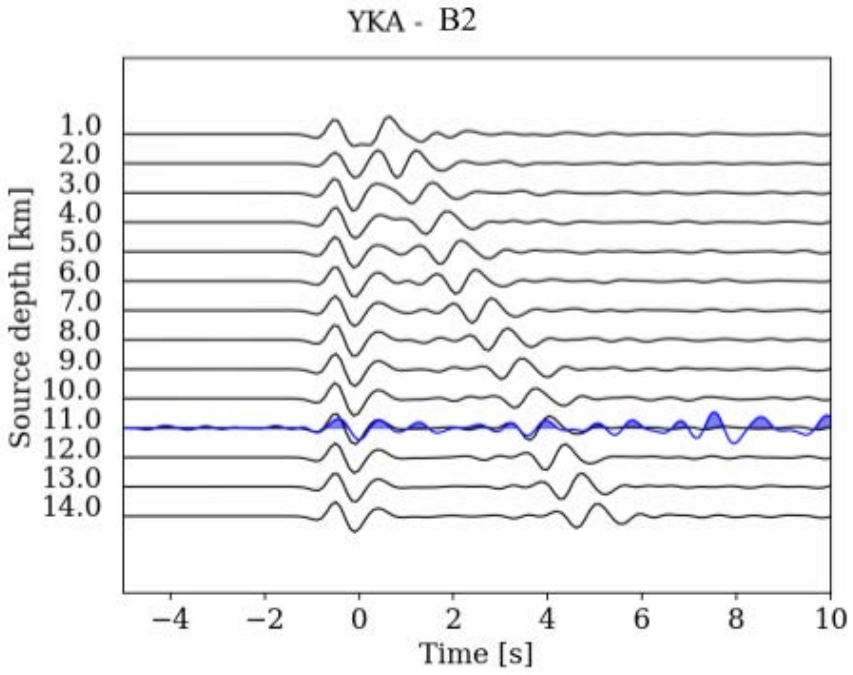

Figure S16. Best focal depth estimate for B2 derived from the stacked vertical trace of the YKA network. Black lines show synthetic traces modelled for a source in the given depths along a path to the array centre. The blue line, shown at the preferred focal point depth, indicates the observed stacked trace of the network.

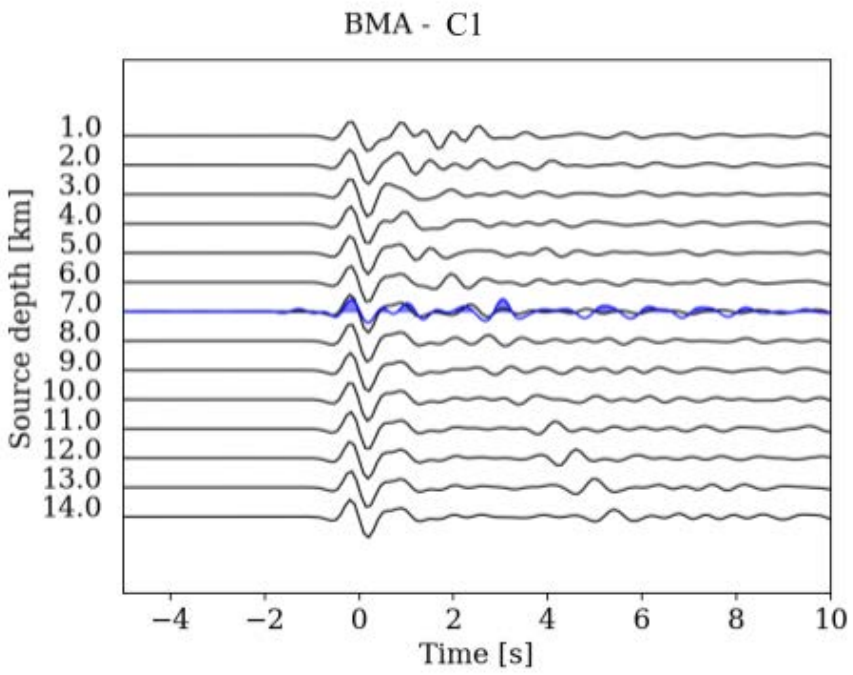

Figure S17. Best focal depth estimate for C1 derived from the stacked vertical trace of the BMA network. Black lines show synthetic traces modelled for a source in the given depths along a path to the array centre. The blue line, shown at the preferred focal point depth, indicates the observed stacked trace of the network.

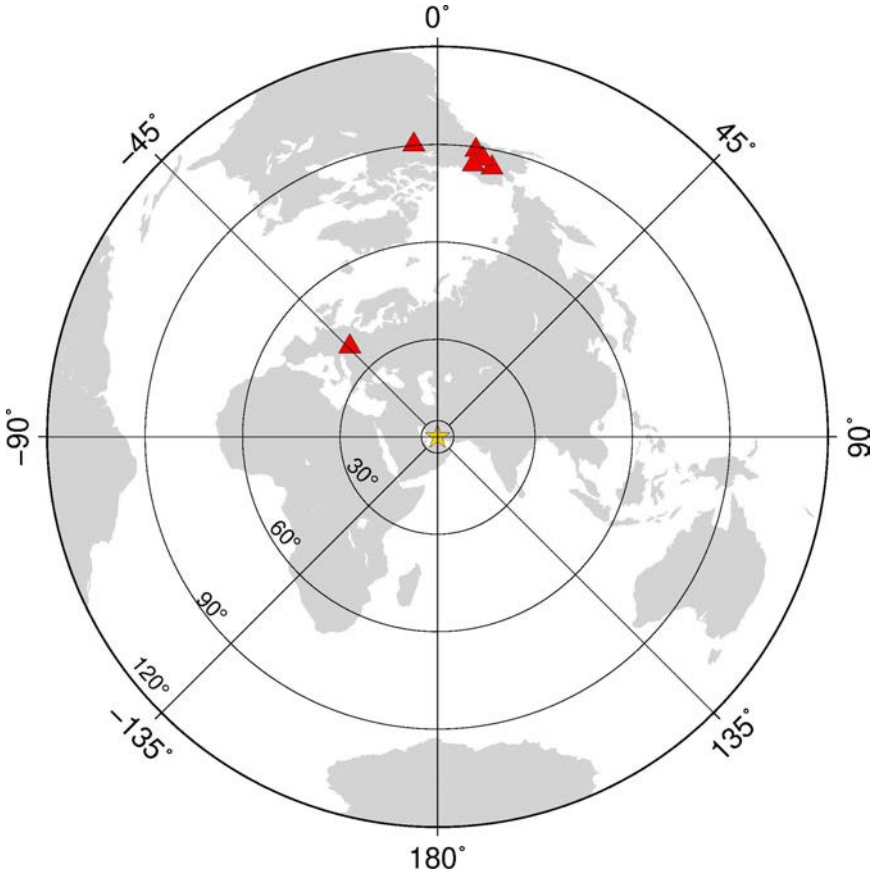

Figure S18. Network locations (red triangles) used within the abedeto focal depth estimation tool are shown with respect to the earthquake locations (yellow star). Further information on the networks is given in Table S6.

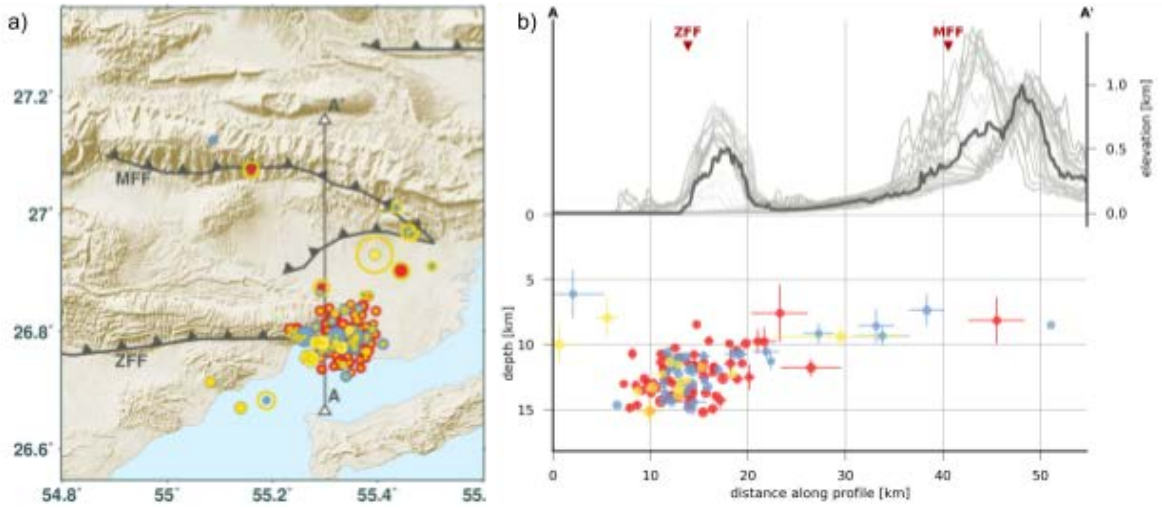

Figure S19. Relocated aftershock distribution (a) on map view and (b) along the profile shown in (a). Horizontal location uncertainties in (a) are indicated by yellow circles. Horizontal and vertical location uncertainties in (b) are shown as horizontal and vertical bars.

Table S1: Deviatoric moment tensor solutions for the mainshocks derived from seismic data inversion. Standard deviations are given in the same units as values if not denoted separately. Standard deviation values are indicated by *_std* as part of their parameter name. *rmij* indicates relative moment tensor components. Absolute moment contributions can be derived from them combined with the magnitude.

Table S2: Full moment tensor solutions for the mainshocks derived from seismic data inversion. Standard deviations are given in the same units as values if not denoted separately. Standard deviation values are indicated by *_std* as part of their parameter name. *rmij* indicates relative moment tensor components. Absolute moment contributions can be derived from them combined with the magnitude.

Event ID	A1	A2	A3
date	2022-07-01	2022-07-01	2022-07-01
time	21:32:06.27	23:24:15.71	23:25:15.51
time_std [s]	6.2	2.6	4.4
lat [deg]	26.8345	26.8262	26.8582
north_shift_std [km]	0.3	4.1	0.2
lon [deg]	55.3401	55.1525	55.2701
east_shift_std [km]	0.38	5.1	0.29
strike [deg]	93.9	85	92
strike_std	4.4	19	3.8
dip [deg]	66.1	65	77.6
dip_std	2.7	11	1.6
rake [deg]	79.2	94	94.8
rake_std	7.1	22	4.6
depth [km]	8.27	11.9	6.13
depth_std	0.17	2.7	0.19
mw	6.27	5.78	5.928
mw_std	0.018	0.11	0.028
misfit	0.5446307		

Table S3: Double couple (DC) moment tensor solutions for the mainshocks of sequence A derived from a joint 3 DC source inversion using seismic and satellite deformation data. Standard deviations are given in the same units as values if not denoted separately. Standard deviation values are indicated by *_std* as part of their parameter name. *rmij* indicates relative moment tensor components. Absolute moment contributions can be derived from them combined with the magnitude.

Table S4: PDR finite fault solutions for the mainshocks derived from seismic data inversions. Less preferred solutions inverting for the auxiliary nodal planes are shown in dark grey columns. Standard deviations are given in the same units as values if not denoted separately. Standard deviation values are indicated by *_std* as part of their parameter name. *Gamma* indicates the ratio between rupture and shear wave velocity. *Depth* refers to the depth of the top edge of the resolved rupture plane. The location given with *Lat* and *Lon* resolves the top edge centre location.

Table S5: PDR finite fault solutions for the mainshocks derived from a joint 3 PDR inversion using seismic and satellite deformation data. Standard deviations are given in the same units as values if not denoted separately. Standard deviation values are indicated by *_std* as part of their parameter name. *Gamma* indicates the ratio between rupture and shear wave velocity. *Depth* refers to the depth of the top edge of the resolved rupture plane. The location given with *Lat* and *Lon* resolves the top edge centre location.

Event ID	ArrayCode	Array Center Lat [deg]	Array Center Lon [deg]	Focal depth [km]
A1	ILAR	64.77045	-146.87907	8.0
A2	GERES	48.83591	13.70060	8.0
A3	BCA	63.06266	-141.78724	10.0
B1	IMAR	65.98615	-153.75525	11.0
B2	YKA	62.49937	-114.67831	11.0
C1	BMA	67.42937	-144.55291	7.0

Table S6: Information on used arrays and retrieved focal depth for the six mainshocks using the abedeto tool. Array codes and centre coordinates are given.

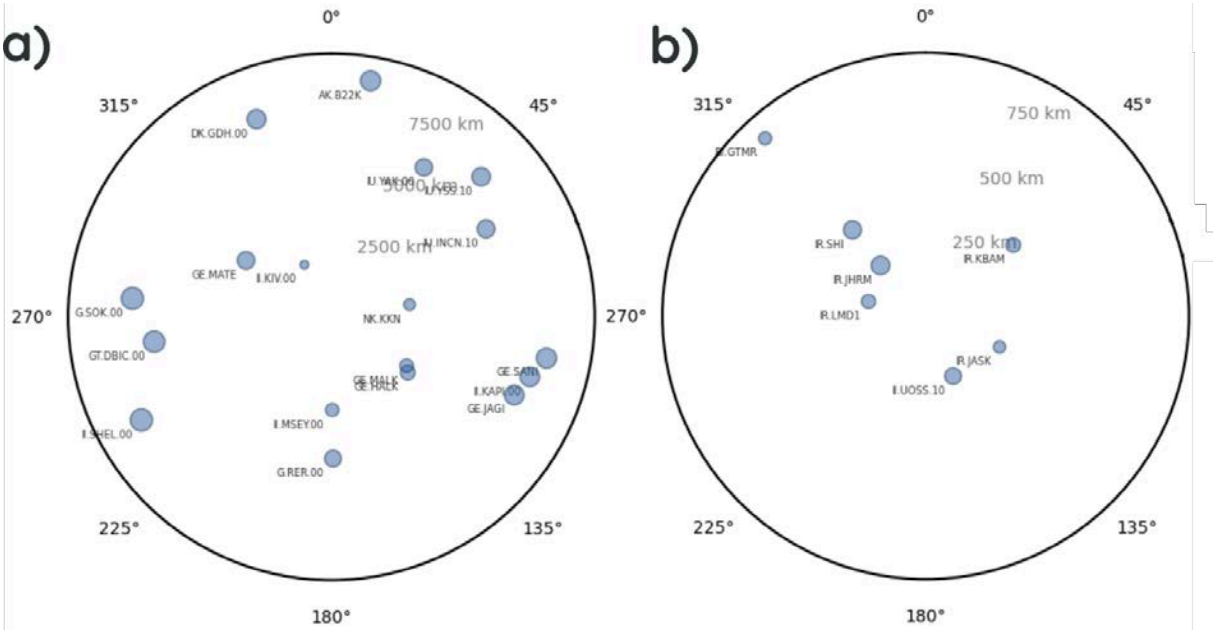

Figure 4.1: Exemplary station distribution for the 3PDR inversion runs indicating the azimuth and the distance of the (a) distant regional and teleseismic and (b) local and close regional stations.

5 | Discussion

This chapter reflects on the objectives defined in Chapter 1.3 using the major findings from the thesis. A comparison to other approaches is given in Section 5.1. PDR modeling results for complex rupture processes are discussed in Section 5.2. Finally, in Section 5.3, I will give a brief overview on the gains and limits of the current numerical implementation of the PDR.

5.1 Comparison of the PDR with other dynamic and kinematic rupture models

The PDR is able to resolve static and kinematic properties of an earthquake including the released seismic moment, the slip pattern and slip rate distribution, the orientation and location of the fault plane, and the rupture propagation using stress forward modeling (Chap. 2.1) or a slip inversion (Chap. 3, 4, Petersen et al., 2023). In this section, I want to discuss the PDR, its parametrization and its results compared to kinematic and dynamic models.

5.1.1 The performance of the PDR compared to dynamic rupture models

Here, I discuss the PDR setup and both results from synthetic forward modeling and inversions in comparison with other dynamic models.

Most importantly, static dislocations obtained from the PDR satisfy the preset physical boundary conditions, so the prescribed stress drop field. Assuming a known static dislocation, the PDR can estimate stress drop fields from simple forward modeling, as shown in Chapter 2.1 for the M_w 8.3 2015 Illapel, Chile, and M_w 7.3 2016 Kumamoto, Japan, earthquakes. The modelled tractions fit well with given literature values (e.g., Kanamori, 1994; Kanamori & Anderson, 1975). Such assumptions are also required for other dynamic models (e.g., Ulrich, Vater, et al., 2019; Ulrich, Gabriel, et al., 2019).

We have shown that a heterogeneous stress field along the planar PDR fault plane can be used to model effects of reduced frictional strength or a change of the fault plane orientation within a given background stress field (Chap. 2.1). These effects were observed for the M_w 7.3 2016 Kumamoto, Japan, earthquake (Yu et al., 2019) and have also been derived in other cases, as, e.g., for the M_w 7.8 2016 Kaikoura, New Zealand, earthquake (e.g., Ulrich, Vater, et al., 2019).

Brune (1970, 1971) provided a simple dynamic model estimating the shear slip rate and the resulting dislocation on a rupture as well as the emitted amplitude spectrum of a source based on the shear stress. As shown in Chapter 2.1 and in Metz (2019), the PDR model can explain a slip pulse rupture mode (e.g., Haskell, 1969) without defining friction or rupture healing with highest slip rates following shortly after the rupture front. Synthetic far-field spectra modeled with the PDR show a strong coherency with the classical Brune spectra for source time functions, with a low-frequency plateau and a ω^{-2} decay at high frequencies. I could also show, that the PDR is able to reproduce rupture kinematics of a crack-like shear rupture (Sato & Hirasawa, 1973) or the opening of a pressurised crack (see Chap. 2.1 and Metz (2019)).

Dynamic rupture models, as for instance realized with the software package SeiSol (Dumbser & Käser, 2006; Pelties et al., 2014; Uphoff et al., 2017), are able to simulate complex rupture processes. They can reveal the activation of multi-segmented ruptures as the Kaikoura earthquake (e.g., Ulrich, Gabriel, et al., 2019) and yield physical explanations for supershear such as reduced fault strength and an highly overstressed nucleation patch (e.g., Abdelmeguid et al., 2023; Ulrich, Vater, et al., 2019). With the rupture velocity not being pre-defined in SeiSol, supershear is predicted as outcome of the simulation. This is different in the PDR model, where the rupture front propagation problem has been separated from the problem to estimate slip. In order to calculate rupture front isochrones the PDR needs a pre-defined rupture velocity model. Reducing the effort we have so far assumed a linear scaling of the rupture velocity with the shear wave velocity in the layered Earth model. A scaling coefficient has been introduced either as a free parameter in the inversion (Chap. 3, 4, and Petersen et al., 2023), or it is simply preset if the resolution is poor (Chap. 2.1).

We cannot exclude the possibility that supershear is caused by a special combination of prestress and the geological and physical properties on the fault. However, forward modeling with the PDR for the M_w 7.5 2018 Palu, Indonesia, earthquake suggest that supershear may also be caused by an upwards refraction of the rupture front from depth where the rupture velocity is larger (Chap. 2.1). Such an apparent supershear rupture velocity is possibly difficult to distinguish from an intrinsic supershear speed. For the 2023 Türkiye earthquake, we do not find evidences for supershear rupture speed (Petersen et al., 2023) opposing assumptions made in the dynamic modeling by ,e.g., Abdelmeguid et al., 2023. Based on teleseismic broad band and near-field strong motion records, our PDR inversion resolves a rupture propagation to shear wave velocity ratio of 0.7±0.07. Derived rupture speeds are well below supershear (2.6±0.4 km/s), as also obtained from high-frequency multi-array back-projection (average rupture speed of 1.8 km/s). The back projection gives a maximum rupture speed of 3.4 km/s, which is close to the crustal shear wave velocity reported by CRUST2.0 (3.5 km/s).

Frictional settings are crucial within dynamic models (e.g. Dunham et al., 2011a, 2011b; Fang & Dunham, 2013). They define the resistance of the fault against slip. The PDR does not take any friction into account, neither dynamic nor static. Thereby, we neither model locked fault areas, where friction prevents any slip, nor can we model self-healing (e.g., Dunham et al., 2011a, 2011b; Fang & Dunham, 2013). PDR forward modeling tests reveal slip pulses, which, however, never heal to a slip rate of exactly zero even if the amplitudes are very small (compare modeling for the Kumamoto earthquake in Chap. 2.1). The shape of the slip pulses modeled

with the PDR is controlled by the rupture front geometry. The geometrical aspects of rupture front propagation, in combination with a heterogeneous stress field, can even generate secondary effects as the backward propagation of slip into already ruptured areas.

The PDR does neither include secondary dynamic effects like dynamic strengthening and weakening (e.g., Beeler et al., 2008; Di Toro et al., 2004; Dunham et al., 2011a; Noda et al., 2009; Perfettini & Ampuero, 2008; Tsutsumi & Shimamoto, 1997; Tullis & Goldsby, 2003, 2003) nor off-fault energy dissipation as discussed by Gabriel et al. (2013). Hence, effects like contact melting (Hirose & Shimamoto, 2005; Tsutsumi & Shimamoto, 1997) or tixotrophic behaviour of hydrated layer of amorphous silica - the formation of a friction-reducing silica gel at the fault plane interface (Di Toro et al., 2004; Tullis & Goldsby, 2003) can not be reproduced with the PDR.

Neglecting frictional parameters, dynamic strengthening or weakening, energy dissipation or topography reduces the resolved dynamics, when using the PDR. Therefore, the simplicity results in a much faster forward modeling compared to high level dynamic models as SeisSol. While a modeling of a rupture scenario of the Kaikoura earthquake took 2 h on a supercomputer with 3000 cores (Ulrich, Vater, et al., 2019), a PDR inversion with 100,000 tested scenarios can be performed within 2 days on a 4 core computer with 64 GB RAM. A single scenario is simulated within few seconds. The PDR source model therefore opens the possibility performing a probabilistic inversion using a bootstrap or Bayesian search approach, as I have shown in the Chapters 3, 4 and also in Petersen et al. (2023).

Within the latter, we could resolve the major slip segment rupturing during the first of the two 2023 Türkiye earthquakes and the rupture propagation along the segment from a PDR inversion. This region is co-located with the region of highest slip-rates, as obtained from dynamic modeling by Abdelmeguid et al. (2023). Our inversion does also resolve the time difference between the rupture origin on the Narli fault and the start of the rupture on the main strand of the Eastern Anatolian Fault Zone, indicating comparable resolution on essential kinematic parameters.

5.1.2 Similarities and differences of the PDR compared to kinematic rupture models

Kinematic source models resolve the slip-distribution and also the rupture front propagation along an extended rupture plane. Kinematic models are often described as a highly under-determined inversion problem, because they typically involve a large number of sub-faults where each of them allows for varying the dislocations for each time step, the arrival times of the rupture front, and the sub-fault source time function shapes and durations (e.g., Beresnev, 2003; Cesca et al., 2010). Therefore, kinematic models are often stabilized with additional constraints on the slip distribution, the rupture speed or the source time function.

The PDR does not require any smoothing of slip. Instead, the static slip always fulfills the boundary conditions of the given stress drop. A regularization of the slip using Laplacian smoothing or roughness constraints, as in, e.g., Diao et al. (2016), Vasyura-Bathke et al. (2020), Yang et al. (2023), and Zhang et al. (2014) is not required in the case of the PDR. The slip distributions from the PDR are smooth by nature of the boundary value solutions. For instance,

I have shown in Chapter 2.1 for the 2016 Kumamoto and the 2015 Illapel earthquakes, that steps within the stress distribution result in a smooth slip distribution due to self-stressing effects within the fracture.

The PDR implemented in *Pyrocko* assumes a linear scaling between shear wave and rupture velocity. This allows to reproduce heterogeneities in the rupture propagation as a result of non-isotropic media, if present in the shear wave speeds of the given underground model. Thereby, the PDR can resolve further details compared to simple constant rupture velocity models as by Haskell (1964) and Heimann (2011). The linear scaling and the current dependency on 1D velocity structures prevents the PDR from capturing more complex rupture front propagation patterns with 3D variations, though. Here, more sophisticated kinematic models as the IDS source (Diao et al., 2016; Zhang et al., 2014) or from BEAT (Vasyura-Bathke et al., 2020) can be better suited.

5.2 Insights into complex ruptures

I have provided examples for the application of the PDR within seismic and geodetic inversions in Chapters 3 and 4 as well as Petersen et al. (2023) capturing features of several complex earthquakes: the 2021 South Sandwich earthquake, the 01 July 2022 triplet in SE Iran and the 2023 Türkiye earthquakes.

The PDR inversion is versatile, as it allows to invert for the location, mechanism, fault orientation and slip of large ($M_w > 8.0$), slow rupturing subduction zone earthquakes, but also of $M_w \sim 6.0$ shallow events including parameter uncertainties. Retrieved static features of the rupture as the moment magnitude, the centroid or the location of the dominant slip patch are in agreement with known studies or agency results for South Sandwich (Chap. 3 and Jia et al., 2022), for the 2022 Iran triplet (Chap. 4 and Yang et al., 2023) and for the 2023 Türkiye earthquakes (e.g., Abdelmeguid et al., 2023; Goldberg et al., 2023; Mai et al., 2023; Meng & Ji, 2023; Okuwaki et al., 2023; Petersen et al., 2023).

Our applications do also show, that less prominent rupture processes as smaller slip patches are only resolved in the case of clear seismic signals as for the deeper subevents bounding the large, shallow 2021 South Sandwich earthquake (Chap. 3). A complex rupture propagation along multiple branches with a complex seismic signal is harder to resolve, even with a multiple source setup (Petersen et al., 2023).

Using the results from PDR inversion for tsunami wave height modeling has not reproduced the details of the recorded tsunamis due to the limited resolution of slip heterogeneities (Sec. 2.2.2 and 5.1). The approach showed good first order estimates of the wave amplitudes (Chap. 3), though. More detailed source studies and combined inversions of tsunami and either seismic or geodetic data could increase both the resolution on the fault slip, and also the tsunami fit (e.g., Gusman et al., 2015; Ho et al., 2021; Ulrich, Vater, et al., 2019).

Tsunami forward modeling aided in cross-validating the results from PDR inversions for the 2021 South Sandwich earthquake. The use of other techniques as the low-frequent moment tensor inversion (Chap. 3 and 4), array-based back-projection (Chap. 3 and Petersen et al., 2023) or

aftershock clustering or relocation (Chap. 3 and 4) has also helped to confirm and interpret PDR inversion results as the rupture propagation direction and speed.

The joint analysis of results of multiple independent techniques is crucial for a profound understanding of the rupture processes, especially when studying curved or multi-modal ruptures with superposed seismic or ground deformation signals (Chap. 3 and 4). There, the increased number of free parameters may result in larger uncertainties or unwanted inversion effects (Chap. 4).

In this regard it is always crucial to invert not only for the PDR but also the MT point source. We have shown strong centroid depth differences between solutions from multiple PDR and multiple DC inversions for the 2022 Iran sequence in Chapter 4. The joint interpretation of both triple DC and triple PDR results allowed to attribute them to effects of the large number of free parameters within the triple PDR estimate.

5.3 Gains and limits of the PDR in its current implementation

The PDR has been implemented into *Pyrocko* (Heimann et al., 2017) and *Grond* (Heimann et al., 2019). The incorporation of the model into these wideley-used open-source toolboxes allows for simple use within the scientific community. Thereby, not only my results can be reproduced, but also new analysis on other earthquakes are easy to perform.

Through the implementation of the PDR into *Pyrocko* and *Grond*, features of the PDR were updated or enhanced (Chap. 2.2 and Fig. 1.2). The simplicity of the PDR gives also the possibility for an easy extension or further developments following on the already presented steps. Within the Chapters 3 and 4, I have shown two possible and rather simple ways of extending the single plane PDR model to a double or triple source model (check also Sec. 2.2.2). Certain dynamic features, as the stress transfer between the multiple source planes are not considered, though, and should be taken into account in future applications.

Kinematic models, widely used within inversions (e.g., Jia et al., 2022; Steinberg et al., 2020), yield only a constant slip (e.g., Haskell, 1964; Heimann, 2011). The PDR inversion within *Grond* with constant tractions and a peak slip provides smooth, self-similar slip distributions instead. Together with the use of Okada (1992) for coefficient calculation, the PDR can even resolve the effect of the free surface (Chap. 2.1). Thereby, the PDR is able to enhance Bayesian finite fault inversions to estimate physics-based slip patterns. As mentioned before, the constant traction assumption forces the PDR inversion to focus on the dominant slip patch of a rupture. Important features as the rupture initiation on a splay fault of the East-Anatolian Fault Zone in case of the 2023 Türkiye earthquake, are therefore missed within the PDR inversion (Petersen et al., 2023).

Chapters 3 and 4 have revealed larger uncertainties for the width and the relative downdip nucleation point coordinate (`nucleation_y`) of the inverted PDR fault planes. This could be attributed to a decreased depth resolution resulting from using long-periodic waveforms, which is often observed in seismic inversions. Another reason could be the relative origin coordinates. As the origin location relative to the fault top edge is controlled by a combination of width

and `nucleation_y`, larger width and smaller `nucleation_y` may result in the same location as a smaller width combined with a larger `nucleation_y`. This fact could prevent the width and `nucleation_y` from convergence within an inversion.

The resolution of the PDR slip distribution depends on the number of sub-faults. The more sub-faults, the better is the fit between the slip distribution of the PDR and known analytical equations (Metz, 2019). High numbers of sub-faults result also in increased forward modeling computation times (see Sec. 2.2.2). Our applications for the 2021 South Sandwich earthquake, the 2022 SE Iran sequence, and the 2023 Türkiye earthquakes have shown that $8x5$ sub-faults are the maximum limit to obtain PDR solutions within a reasonable time (up to 1 week) using the optimal number of 4 cores. More effective inversion strategies may help to extent this limit in the future. Another possibility to reduce the computation time may be reached by using neural networks as waveform storage (Lehmann, Metz, et al., 2023).

The current implementation in *Pyrocko* and *Grond* allows for manifold and simple usage of the PDR by the scientific community. The available documentation on the *Pyrocko* web page (https://pyrocko.org/docs/current/topics/pseudo-dynamic-rupture.html) allows for simple waveform and ground deformation forward modeling of complex ruptures with the PDR. Although implementation is still ongoing, the PDR is already included into *Grond* . This gives the opportunity to invert for complex earthquakes.

6 | Conclusions and outlook

6.1 Conclusions

Extended seismic source models are the key for a better understanding of the rupture process of larger earthquakes. My dissertation has shown the methodological development, the numerical implementation and two applications of a new extended seismic source model, the pseudo-dynamic rupture model (PDR). I highlighted its capability to resolve information on stress-drops, complex ruptures and also secondary effects like tsunamis.

PDR forward modeling (Chap. 2.1) revealed a high coherency between PDR results and both analytical equations and published results on the investigated earthquakes. We have also provided new explanations for the rupture of unstressed fault patches and apparent supershear.

Inversions of single and muliple plane PDR (Chap. 3 and 4) have proven to shed light onto two complex seismic unrests in different tectonic settings. I showed how PDR results help to gain a deeper understanding of crustal rupture processes. Cross-validating outcomes from the PDR with other commonly used techniques as back-projection, the inversion of moment tensors or even tsunami wave height forward modeling provided the base of a profound tectonic interpretation.

Throughout this dissertation, I have shown and discussed numerical features of the PDR in its current implementation within *Pyrocko* and *Grond*. Together with the shown applications, I emphasized the advantages of the simple PDR model, and discussed the resulting limits like the focus on dominant slip patches within a PDR inversion.

By implementing the PDR for forward modeling and inversion in open-source Python software, I hope to provide helpful tools that facilitate future studies on complex or large earthquakes.

6.2 Outlook

Based on applications of the PDR discussed within this dissertation, I identified different options for future enhancements of the PDR implementation within the open-source toolbox *Pyrocko*. I want to introduce them briefly within the following paragraphs.

Global stress models (e.g., Heidbach et al., 2016; Heidbach et al., 2018) provide a rather good understanding of regionally acting stress regimes. In future, these might be used to restrict the stress drop on the pseudo-dynamic rupture plane. Thereby, the stress drop distribution along the fault plane could be modeled with higher accuracy and, hence, better slip modeling results

could be obtained.

The current parametrization of the PDR with the trade-off between the rupture width and the relative down-dip nucleation point `nucleation_y` decreases the resolution of both parameters. Here, new absolute rupture origin parameters could help.

The inversion could be also enhanced by introducing models with a higher complexity. This could include heterogeneous tractions along the fault plane allowing for more complex slip distributions. It would be interesting to test the double or triple PDR model assuming a stress transfer from one fault plane to the next. Currently, each fault plane is uncoupled from the others.

At the moment, the PDR is not capable to perform in (near-)real-time applications due to the rather long computation time for calculating the coefficient matrix and the forward modeling of the waveforms. In future, this might change with the use of neural networks as a waveform storage. Assessing a trained neural network to retrieve synthetic waveforms based on the PDR and the underground model in the case of an earthquake might reduce the computation time significantly (Lehmann, Metz, et al., 2023).

The application of the PDR inversion in real-time source estimates could make use of mapped faults or a priori information on past seismicity (Fig. 6.1). Thereby, a priori probability density functions for fault orientations can be included based on the known seismicity and faults. Samples within the inversions are then drawn from this posterior function. I have tested this concept for a simple point source inversion appraoch in the scope of the EWRICA project (see Sec. 1.2). The results are rather promising and show a faster convergence towards the true earthquake mechanism in the case of the M_w 6.5 2016 Norcia, Italy, and the M_w 7.0 2020 Samos, Greece, earthquakes. Adopting this scheme for the PDR could enhance its use for real-time purposes.

Currently, the PDR is defined as a rectangular fault plane for *Grond* inversions (Sec. 2.2.2). Although simpler and less computationally expensive, the current implementation does not allow for curved rupture plane edges and does also not take a known centroid into account. In this regard, it would be interesting to test the two-step inversion similar to the suggestions in Chapter 2.1 (or, e.g., Vasyura-Bathke et al., 2020). Then, a low-frequent inversion would resolve the centroid first. The extent of the rupture and also its kinematic parameters as rupture origin or rupture to shear-wave velocity ratio would be determined within then second independent step, thereafter.

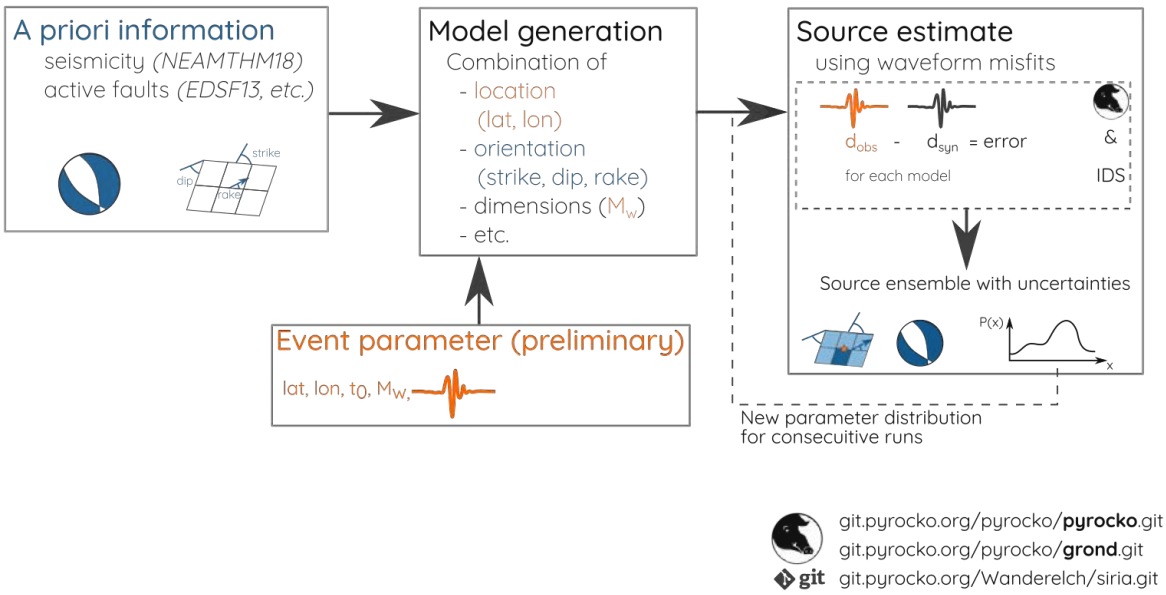

Figure 6.1: Schematic overview of the fast inversion scheme as proposed within the EWRICA project. It was tested for point source models and is available as an open-source Python tool box. The inversion scheme uses a priori information (left) available at the location of an earthquake (bottom) to generate the models (middle) tested within the inversion (right). This inversion procedure is iterative with later runs using the probability density functions of earlier runs to restrict the searched model space.

Bibliography

Abdelmeguid, M., Zhao, C., Yalcinkaya, E., Gazetas, G., Elbanna, A., & Rosakis, A. (2023). Revealing The Dynamics of the Feb 6th 2023 M7.8 Kahramanmaras/-Pazarcik Earthquake: near-field records and dynamic rupture modeling. *EarthArXiv*. https://doi.org/10.31223/X5066R

Aki, K. (1979). Characterization of barriers on an earthquake fault. *Journal of Geophysical Research: Solid Earth*, *84*(B11), 6140–6148. https://doi.org/https://doi.org/10.1029/JB084iB11p06140

Bai, K., & Ampuero, J.-P. (2017). Effect of seismogenic depth and background stress on physical limits of earthquake rupture across fault step overs. *Journal of Geophysical Research: Solid Earth*, *122*(12), 10, 280–10, 298. https://doi.org/https://doi.org/10.1002/2017JB014848

Barka, A. A., & Kadinsky-Cade, K. (1988). Strike-slip fault geometry in turkey and its influence on earthquake activity. *Tectonics*, *7*(3), 663–684. https://doi.org/https://doi.org/10.1029/TC007i003p00663

Beeler, N. M., Tullis, T. E., & Goldsby, D. L. (2008). Constitutive relationships and physical basis of fault strength due to flash heating. *Journal of Geophysical Research: Solid Earth*, *113*(B1). https://doi.org/https://doi.org/10.1029/2007JB004988

Beresnev, I. A. (2003). Uncertainties in finite-fault slip inversions: To what extent to believe? (A critical review). *Bulletin of the Seismological Society of America*, *93*(6), 2445–2458. https://doi.org/10.1785/0120020225

Biasi, G. P., & Wesnousky, S. G. (2016). Steps and Gaps in Ground Ruptures: Empirical Bounds on Rupture Propagation. *Bulletin of the Seismological Society of America*, *106*(3), 1110–1124. https://doi.org/10.1785/0120150175

Brune, J. N. (1970). Tectonic Stress and the Spectra, of Seismic Shear Waves from Earthquakes. *Journal of Geophysical Research*, *75*(26), 4997–5009. https://doi.org/10.1029/JB075i026p04997

Brune, J. N. (1971). Correction to: Tectonic Stress and the Spectra, of Seismic Shear Waves from Earthquakes. *Journal of Geophysical Research*, *76*(20), 1971.

Carrillo Ponce, A., Dahm, T., & Cesca, S. (2023). Joint single-force problem applied to seismic signals generated by landslides. *in preparation*.

Carrillo Ponce, A., Dahm, T., Cesca, S., Tilmann, F., Babeyko, A., & Heimann, S. (2021). Bayesian multiple rupture plane inversion to assess rupture complexity: application to the 2018 Mw 7.9 Alaska earthquake. *EGU General Assembly 2021, Online, 19–30 Apr 2021*, (EGU2021-1583). https://doi.org/10.5194/egusphere-egu21-1583

Cesca, S., Metz, M., Büyükakpınar, P., & Dahm, T. (2023). He energetic 2022 seismic unrest related to magma intrusion at the north mid-atlantic ridge. *submitted to Geophysical Research Letters*.

Cesca, S., Heimann, S., Stammler, K., & Dahm, T. (2010). Automated procedure for point and kinematic source inversion at regional distances. *Journal of Geophysical Research: Solid Earth*, *115*(6), 1–24. https://doi.org/10.1029/2009JB006450

Cook, K. L., Rekapalli, R., Dietze, M., Pilz, M., Cesca, S., Rao, N. P., Srinagesh, D., Paul, H., Metz, M., Mandal, P., Suresh, G., Cotton, F., Tiwari, V. M., & Hovius, N. (2021). Detection and potential early warning of catastrophic flow events with regional seismic networks. *Science*, *374*(6563), 87–92. https://doi.org/10.1126/science.abj1227

Daout, S., Steinberg, A., Isken, M. P., Heimann, S., & Sudhaus, H. (2020). Illuminating the spatio-temporal evolution of the 2008–2009 qaidam earthquake sequence with the joint use of insar time series and teleseismic data. *Remote Sensing*, *12*(17), 1–23. https://doi.org/10.3390/rs12172850

Delouis, B., Giardini, D., Lundgren, P., & Salichon, J. (2002). Joint inversion of InSAR, GPS, teleseismic, and strong-motion data for the spatial and temporal distribution of earthquake slip: Application to the 1999 İzmit mainshock. *Bulletin of the Seismological Society of America*, *92*(1), 278–299. https://doi.org/10.1785/0120000806

Delouis, B., Lundgren, P., Salichon, J., & Giardini, D. (2000). Joint inversion of InSAR and teleseismic data for the slip history of the 1999 Izmit (Turkey) earthquake. *Geophysical Research Letters*, *27*(20), 3389–3392. https://doi.org/10.1029/2000GL011511

Di Toro, G., Goldsby, D. L., & Tullis, T. E. (2004). Friction falls towards zero in quartz rock as slip velocity approaches seismic rates. *Nature*, *427*(6973), 436–439.

Diao, F., Wang, R., Aochi, H., Walter, T. R., Zhang, Y., Zheng, Y., & Xiong, X. (2016). Rapid kinematic finite-fault inversion for an Mw 7+ scenario earthquake in the Marmara Sea: An uncertainty study. *Geophysical Journal International*, *204*(2), 813–824. https://doi.org/10.1093/gji/ggv459

Dreger, D. S., Gee, L., Lombard, P., Murray, M. H., & Romanowicz, B. (2005). Rapid finite-source analysis and near-fault strong ground motions: Application to the 2003 Mw 6.5 San Simeon and 2004 Mw 6.0 Parkfield earthquakes. *Seismological Research Letters*, *76*(1), 40–48. https://doi.org/10.1785/gssrl.76.1.40

Dumbser, M., & Käser, M. (2006). An arbitrary high-order discontinuous Galerkin method for elastic waves on unstructured meshes — II. The three-dimensional isotropic

case. *Geophysical Journal International*, *167*(1), 319–336. https://doi.org/10.1111/j.1365-246X.2006.03120.x

Dunham, E. M., Belanger, D., Cong, L., & Kozdon, J. E. (2011a). Earthquake ruptures with strongly rate-weakening friction and off-fault plasticity, part 1: Planar faults. *Bulletin of the Seismological Society of America*, *101*(5), 2296–2307. https://doi.org/10.1785/0120100075

Dunham, E. M., Belanger, D., Cong, L., & Kozdon, J. E. (2011b). Earthquake ruptures with strongly rate-weakening friction and off-fault plasticity, part 2: Nonplanar faults. *Bulletin of the Seismological Society of America*, *101*(5), 2308–2322. https://doi.org/10.1785/0120100076

Dziewoński, A. M., Chou, T.-A., & Woodhouse, J. H. (1981). Determination of earthquake source parameters from waveform data for studies of global and regional seismicity. *Journal of Geophysical Research*, *86*(B4), 2825–2852.

Ekström, G., Nettles, M., & Dziewoński, A. M. (2012). The global CMT project 2004-2010: Centroid-moment tensors for 13,017 earthquakes. *Physics of the Earth and Planetary Interiors*, *200-201*, 1–9. https://doi.org/10.1016/j.pepi.2012.04.002

Fang, Z., & Dunham, E. M. (2013). Additional shear resistance from fault roughness and stress levels on geometrically complex faults. *Journal of Geophysical Research: Solid Earth*, *118*(7), 3642–3654. https://doi.org/10.1002/jgrb.50262

Feigl, K. L., Sarti, F., Vadon, H., McClusky, S., Ergintav, S., Durand, P., Bürgmann, R., Rigo, A., Massonnet, D., & Reilinger, R. (2002). Estimating slip distribution for the İzmit mainshock from coseismic GPS, ERS-1, RADARSAT, and SPOT measurements. *Bulletin of the Seismological Society of America*, *92*(1), 138–160. https://doi.org/10.1785/0120000830

Fukuda, J., & Johnson, K. M. (2008). A Fully Bayesian Inversion for Spatial Distribution of Fault Slip with Objective Smoothing. *Bulletin of the Seismological Society of America*, *98*(3), 1128–1146. https://doi.org/10.1785/0120070194

Gabriel, A. A., Ampuero, J. P., Dalguer, L. A., & Mai, P. M. (2013). Source properties of dynamic rupture pulses with off-fault plasticity. *Journal of Geophysical Research: Solid Earth*, *118*(8), 4117–4126. https://doi.org/10.1002/jgrb.50213

Gilbert, F. (1970). Excitation of the Normal Modes. *Geophysical Journal of the Royal Astronomical Society*, *22*, 223–226.

Goldberg, D. E., Koch, P., Melgar, D., Riquelme, S., & Yeck, W. L. (2022). Beyond the teleseism: Introducing regional seismic and geodetic data into routine usgs finite-fault modeling. *Seismological Society of America*, *93*(6), 3308–3323.

Goldberg, D. E., Taymaz, T., Reitman, N. G., Hatem, A. E., Yolsal-, S., Barnhart, W. D., Irmak, T. S., Wald, D. J., Öcalan, T., Yeck, W. L., Özkan, B., Jobe, J. A. T., Shelly, D. R., Thompson, E. M., Duross, C. B., Earle, P. S., Briggs, R. W., Benz, H., Erman, C., ... Altunta, C. (2023). Rapid Characterization of the February

2023 Kahramanmaraş, Türkiye, Earthquake Sequence. *The Seismic Record*, *3*(2), 156–167. https://doi.org/10.1785/0320230009

Grandin, R., Vallée, M., & Lacassin, R. (2017). Rupture process of the Mw 5.8 Pawnee, Oklahoma, Earthquake from Sentinel-1 InSAR and Seismological Data. *Seismological Research Letters*, *88*(4), 994–1004. https://doi.org/10.1785/0220160226

Grandin, R., Vallée, M., Satriano, C., Lacassin, R., Klinger, Y., Simoes, M., & Bollinger, L. (2015). Rupture process of the Mw = 7.9 2015 Gorkha earthquake (Nepal): Insights into Himalayan megathrust segmentation. *Geophysical Research Letters*, *42*(20), 8373–8382. https://doi.org/10.1002/2015GL066044

Gusman, A. R., Murotani, S., Satake, K., Heidarzadeh, M., Gunawan, E., Watada, S., & Schurr, B. (2015). Fault slip distribution of the 2014 Iquique, Chile, earthquake estimated from ocean-wide tsunami waveforms and GPS data. *Geophysical Research Letters*, *42*(4), 1053–1060. https://doi.org/10.1002/2014GL062604

Hanks, T. C., & Kanamori, H. (1979). A moment magnitude scale. *Journal of Geophysical Research: Solid Earth*, *84*(B5), 2348–2350. https://doi.org/10.1029/JB084iB05p02348

Hartzell, S. H., & Heaton, T. H. (1983). Waveform Data for the Fault Rupture History of the 1979 Imperial Valley, California, Earthquake. *Bulletin of the Seismological Society of America*, *73*(6), 1553–1583.

Haskell, N. A. (1964). Total energy and energy spectral density of elastic wave radiation from propagating faults. *Bull. Seismol. Soc. Am.*, *54*(6), 1811–1841.

Haskell, N. A. (1969). Elastic displacements in the near-field of a propagating fault. *Bull. Seismol. Soc. Am.*, *59*(2), 865–908.

Heidbach, O., Rajabi, M., Reiter, K., Ziegler, M., & Team, W. (2016). World Stress Map Database Release 2016. V. 1.1. https://doi.org/10.5880/WSM.2016.001

Heidbach, O., Rajabi, M., Cui, X., Fuchs, K., Müller, B., Reinecker, J., Reiter, K., Tingay, M., Wenzel, F., Xie, F., Ziegler, M. O., Zoback, M.-L., & Zoback, M. (2018). The world stress map database release 2016: Crustal stress pattern across scales. *Tectonophysics*, *744*, 484–498. https://doi.org/https://doi.org/10.1016/j.tecto.2018.07.007

Heimann, S. (2011). *A Robust Method To Estimate Kinematic Earthquake Source Parameters* (Doctoral dissertation). Universität Hamburg. https://doi.org/10.1016/j.jnoncrysol.2017.11.034

Heimann, S., Isken, M., Kühn, D., Sudhaus, H., Steinberg, A., Vasyura-Bathke, H., Daout, S., Cesca, S., & Dahm, T. (2018). Grond - A probabilistic earthquake source inversion framework. https://doi.org/10.5880/GFZ.2.1.2018.003

Heimann, S., Kriegerowski, M., Isken, M., Cesca, S., Daout, S., Grigoli, F., Juretzek, C., Megies, T., Nooshiri, N., Steinberg, A., Sudhaus, H., Vasyura-Bathke, H., Willey, T., & Dahm, T. (2017). Pyrocko - An open-source seismology toolbox and library. https://doi.org/10.5880/GFZ.2.1.2017.001

Heimann, S., Vasyura-Bathke, H., Sudhaus, H., Paul Isken, M., Kriegerowski, M., Steinberg, A., & Dahm, T. (2019). A Python framework for efficient use of pre-computed Green's functions in seismological and other physical forward and inverse source problems. *Solid Earth*, *10*(6), 1921–1935. https://doi.org/10.5194/se-10-1921-2019

Hernandez, B., Cotton, F., & Campillo, M. (1999). Contribution of radar interferometry to a two-step inversion of the kinematic process of the 1992 Landers earthquake. *Journal of Geophysical Research*, *104*(B6), 13083–13099. https://doi.org/10.1029/1999JB900078

Hicks, S. P., Rietbrock, A., Haberland, C. A., Ryder, I. M. A., Simons, M., & Tassara, A. (2012). The 2010 mw 8.8 maule, chile earthquake: Nucleation and rupture propagation controlled by a subducted topographic high. *Geophysical Research Letters*, *39*(19). https://doi.org/https://doi.org/10.1029/2012GL053184

Hirose, T., & Shimamoto, T. (2005). Slip-Weakening Distance of Faults during Frictional Melting as Inferred from Experimental and Natural Pseudotachylytes. *Bulletin of the Seismological Society of America*, *95*(5), 1666–1673. https://doi.org/10.1785/0120040131

Ho, T. C., Satake, K., Watada, S., Hsieh, M. C., Chuang, R. Y., Aoki, Y., Mulia, I. E., Gusman, A. R., & Lu, C. H. (2021). Tsunami Induced by the Strike-Slip Fault of the 2018 Palu Earthquake (Mw = 7.5), Sulawesi Island, Indonesia. *Earth and Space Science*, *8*(6), 1–19. https://doi.org/10.1029/2020EA001400

Hoechner, A., Babeyko, A. Y., & Sobolev, S. V. (2008). Enhanced GPS inversion technique applied to the 2004 Sumatra earthquake and tsunami. *Geophysical Research Letters*, *35*(8), 10–14. https://doi.org/10.1029/2007GL033133

Ji, C., Wald, D. ., & Helmberger, D. V. (2002). Source description of the 1999 Hector Mine, California, earthquake, part I: Wavelet domain inversion theory and resolution analysis. *Bulletin of the Seismological Society of America*, *92*(4), 1192–1207. https://doi.org/10.1785/0120000916

Jia, Z., Shen, Z., Zhan, Z., Li, C., Peng, Z., & Gurnis, M. (2020). The 2018 fiji mw 8.2 and 7.9 deep earthquakes: One doublet in two slabs. *Earth and Planetary Science Letters*, *531*, 115997. https://doi.org/https://doi.org/10.1016/j.epsl.2019.115997

Jia, Z., Wang, X., & Zhan, Z. (2020). Multifault models of the 2019 ridgecrest sequence highlight complementary slip and fault junction instability. *Geophysical Research Letters*, *47*(17). https://doi.org/https://doi.org/10.1029/2020GL089802

Jia, Z., Zhan, Z., & Kanamori, H. (2022). The 2021 South Sandwich Island Mw 8.2 earthquake: a slow event sandwiched between regular ruptures. *Geophys. Res. Lett.*, *49*, 1–8. https://doi.org/10.1029/2021GL097104

Jónsson, S., Zebker, H., Segall, P., & Amelung, F. (2002). Fault slip distribution of the 1999 Mw 7.1 Hector Mine, California, earthquake, estimated from satellite radar and GPS measurements. *Bulletin of the Seismological Society of America*, *92*(4), 1377–1389. https://doi.org/10.1785/0120000922

Kanamori, H. (1994). Mechanics of Earthquakes. *Annual Review of Earth and Planetary Sciences*, *22*(1), 207–237. https://doi.org/10.1146/annurev.earth.22.1.207

Kanamori, H., & Anderson, D. L. (1975). Theoretical basis of some empirical relations in seismology. *Bull. Seismol. Soc. Am.*, *65*(5), 1073–1095.

Koch, P., Bravo, F., Riquelme, S., & Crempien, J. G. (2019). Near-real-time finite-fault inversions for large earthquakes in chile using strong-motion data. *Seismological Research Letters*, *90*(5), 1971–1986.

Kuge, K., & Lay, T. (1994). Systematic non-double-couple components of earthquake mechanisms: the role of fault zone irregularity. *Journal of Geophysical Research*, *99*(B8), 15457–15467. https://doi.org/10.1029/94jb00140

Lehmann, L., Metz, M., Ohrnberger, M., & Heimann, S. (2023). Accelerating the synthetic waveform generation via neural networks - showcasing the possibility to train a neural network for synthetic waveform prediction. *in preparation*.

Lehmann, L., Ohrnberger, M., Metz, M., & Heimann, S. (2023). Ccelerating low-frequency ground motion simulation for finite fault sources using neural networks. *accepted at Geophysical Journal International*.

Mai, P. M., Aspiotis, T., Aquib, T. A., Cano, E. V., & Castro-, D. (2023). The Destructive Earthquake Doublet of 6 February 2023 in South-Central Türkiye and Northwestern Syria : Initial Observations and Analyses. (February). https://doi.org/10.1785/0320230007

Mai, P. M., Schorlemmer, D., Page, M., Ampuero, J. P., Asano, K., Causse, M., Custodio, S., Fan, W., Festa, G., Galis, M., Gallovic, F., Imperatori, W., Käser, M., Malytskyy, D., Okuwaki, R., Pollitz, F., Passone, L., Razafindrakoto, H. N., Sekiguchi, H., ... Zielke, O. (2016). The earthquake-source inversion Validation (SIV) project. *Seismological Research Letters*, *87*(3), 690–708. https://doi.org/10.1785/0220150231

Meng, L., & Ji, C. (2023). Earthquake : A Multi-segment Rupture in A Millennium Supercycle. https://doi.org/10.21203/rs.3.rs-2747911/v1

Metz, M. (2019). *A quasi-dynamic and self-consistent rupture model to simulate earthquake ruptures* (Master's thesis). University Potsdam.

Müller, G. (1973). Seismic moment and long-period radiation of underground nuclear explosions. *Bulletin of the Seismological Society of America*, *63*(3), 847–857. https://doi.org/10.1785/bssa0630030847

Noda, H., Dunham, E. M., & Rice, J. R. (2009). Earthquake ruptures with thermal weakening and the operation of major faults at low overall stress levels. *Journal of Geophysical Research: Solid Earth*, *114*(B7). https://doi.org/https://doi.org/10.1029/2008JB006143

Okada, Y. (1992). Gravity and potential changes due to shear and tensile faults in a half-space. *Journal of Geophysical Research*, *82*(2), 1018–1040. https://doi.org/10.1029/92JB00178

Okuwaki, R., Yagi, Y., Taymaz, T., & Hicks, S. P. (2023). Multi-scale rupture growth with alternating directions in a complex fault network during the 2023 south-eastern Türkiye and Syria earthquake doublet. *Geophysical Research Letters*.

Pedersen, R., Jónsson, S., Árnadóttir, T., Sigmundsson, F., & Feigl, K. L. (2003). Fault slip distribution of two June 2000 MW6.5 earthquakes in South Iceland estimated from joint inversion of InSAR and GPS measurements. *Earth and Planetary Science Letters*, *213*(3-4), 487–502. https://doi.org/10.1016/S0012-821X(03)00302-9

Pelties, C., Gabriel, A.-A., & Ampuero, J.-P. (2014). Verification of an ader-dg method for complex dynamic rupture problems. *Geoscientific Model Development*, *7*(3), 847–866. https://doi.org/10.5194/gmd-7-847-2014

Perfettini, H., & Ampuero, J. P. (2008). Dynamics of a velocity strengthening fault region: Implications for slow earthquakes and postseismic slip. *Journal of Geophysical Research: Solid Earth*, *113*(9), 1–22. https://doi.org/10.1029/2007JB005398

Petersen, G. M., Büyükakpinar, P., Orlando, F., Sanhueza, V., Metz, M., Cesca, S., Akbayram, K., Saul, J., & Dahm, T. (2023). The 2023 Southeast Türkiye Seismic Sequence : Rupture of a Complex Fault Network. *The Seismic Record*, *3*(2), 134–143. https://doi.org/10.1785/0320230008

Ruiz, S., & Madariaga, R. (2011). Determination of the friction law parameters of the Mw 6.7 Michilla earthquake in northern Chile by dynamic inversion. *Geophysical Research Letters*, *38*(9), 2–7. https://doi.org/10.1029/2011GL047147

Sato, T., & Hirasawa, T. (1973). Body Wave Spectra from Propagating Shear Cracks. *J. Phys. Earth*, *21*, 415–431.

Segall, P., & Pollard, D. D. (1980). Mechanics of discontinuous faults. *Journal of Geophysical Research: Solid Earth*, *85*(B8), 4337–4350. https://doi.org/https://doi.org/10.1029/JB085iB08p04337

Shimizu, K., Yagi, Y., Okuwaki, R., & Fukahata, Y. (2020). Development of an inversion method to extract information on fault geometry from teleseismic data. *Geophysical Journal International*, *220*(2), 1055–1065. https://doi.org/10.1093/gji/ggz496

Steinberg, A., Sudhaus, H., Heimann, S., & Krüger, F. (2020). Sensitivity of InSAR and teleseismic observations to earthquake rupture segmentation. *Geophysical Journal International*, *223*(2), 875–907. https://doi.org/10.1093/gji/ggaa351

Steinberg, A., Sudhaus, H., & Krüger, F. (2022). Using teleseismic backprojection and InSAR to obtain segmentation information for large earthquakes: a case study of the 2016 Mw 6.6 Muji earthquake. *Geophysical Journal International*.

Sudhaus, H., & Jónsson, S. (2009). Improved source modelling through combined use of InSAR and GPS under consideration of correlated data errors: Application to the June 2000 Kleifarvatn earthquake, Iceland. *Geophysical Journal International*, *176*(2), 389–404. https://doi.org/10.1111/j.1365-246X.2008.03989.x

Tinti, E., Fukuyama, E., Piatanesi, A., & Cocco, M. (2005). A kinematic source-time function compatible with earthquake dynamics. *Bulletin of the Seismological Society of America*, *95*(4), 1211–1223. https://doi.org/10.1785/0120040177

Trugman, D. T., Chamberlain, C. J., Savvaidis, A., & Lomax, A. (2023). GrowClust3D.jl: A Julia Package for the Relative Relocation of Earthquake Hypocenters Using 3D Velocity Models. *Seismological Research Letters*, *94*(1), 443–456. https://doi.org/10.1785/0220220193

Trugman, D. T., & Shearer, P. M. (2017). GrowClust: A Hierarchical clustering algorithm for relative earthquake relocation, with application to the Spanish Springs and Sheldon, Nevada, earthquake sequences. *Seismological Research Letters*, *88*(2), 379–391. https://doi.org/10.1785/0220160188

Tsutsumi, A., & Shimamoto, T. (1997). High-velocity frictional properties of gabbro. *Geophysical Research Letters*, *24*(6), 699–702. https://doi.org/https://doi.org/10.1029/97GL00503

Tullis, T. E., & Goldsby, D. L. (2003). Flash Melting of Crustal Rocks at Almost Seismic Slip Rates. *AGU Fall Meeting Abstracts*, *2003*, Article S51B-05, S51B–05.

Tullis, T., & Goldsby, D. (2003). Laboratory experiments on fault shear resistance relevant to coseismic earthquake slip. *SCEC Ann. Prog. Rep., Southern California Earthquake Center*.

Ulrich, T., Vater, S., Madden, E. H., Behrens, J., van Dinther, Y., van Zelst, I., Fielding, E. J., Liang, C., & Gabriel, A. A. (2019). Coupled, Physics-Based Modeling Reveals Earthquake Displacements are Critical to the 2018 Palu, Sulawesi Tsunami. *Pure and Applied Geophysics*, *176*(10), 4069–4109. https://doi.org/10.1007/s00024-019-02290-5

Ulrich, T., Gabriel, A. A., Ampuero, J. P., & Xu, W. (2019). Dynamic viability of the 2016 Mw 7.8 Kaikōura earthquake cascade on weak crustal faults. *Nature Communications*, *10*(1). https://doi.org/10.1038/s41467-019-09125-w

Uphoff, C., Rettenberger, S., Bader, M., Madden, E. H., Ulrich, T., Wollherr, S., & Gabriel, A.-A. (2017). Extreme scale multi-physics simulations of the tsunamigenic 2004 sumatra megathrust earthquake. *Proceedings of the International Conference for High Performance Computing, Networking, Storage and Analysis*. https://doi.org/10.1145/3126908.3126948

Vallée, M., Nocquet, J. M., Battaglia, J., Font, Y., Segovia, M., Régnier, M., Mothes, P., Jarrin, P., Cisneros, D., Vaca, S., Yepes, H., Martin, X., Béthoux, N., & Chlieh, M. (2013). Intense interface seismicity triggered by a shallow slow slip event in the Central Ecuador subduction zone. *Journal of Geophysical Research: Solid Earth*, *118*(6), 2965–2981. https://doi.org/10.1002/jgrb.50216

Vasyura-Bathke, H., Dettmer, J., Steinberg, A., Heimann, S., Isken, M. P., Zielke, O., Mai, P. M., Sudhaus, H., & Jónsson, S. (2020). The bayesian earthquake analysis

tool. *Seismological Research Letters*, *91*(2), 1003–1018. https://doi.org/10.1785/0220190075

Weng, H., & Ampuero, J. (2022). Integrated rupture mechanics for slow slip events and earthquakes. *Nat Commun*, *13*(7327). https://doi.org/https://doi.org/10.1038/s41467-022-34927-w

Wesnousky, S. (2006). Predicting the endpoints of earthquake ruptures. *Nature*, *444*, 358–360. https://doi.org/https://doi.org/10.1038/nature05275

Yang, Y.-h., Li, X., Hu, J.-c., Song, J., Zhao, J., & Yassaghi, A. (2023). The 2022 Hormozgan Doublet Earthquake : Two Blind Thrusts-Related Folding in Zagros Fold-And-Thrust Belt , Southeast Iran. *Geophysical Research Letters*, *50*. https://doi.org/10.1029/2022GL101902

Yu, Z., Zhao, D., Li, J., Huang, Z., Nishizono, Y., & Inakura, H. (2019). Stress field in the 2016 kumamoto earthquake (m 7.3) area. *Journal of Geophysical Research: Solid Earth*, *124*(3), 2638–2652. https://doi.org/https://doi.org/10.1029/2018JB017079

Zhan, Z., Kanamori, H., Tsai, V. C., Helmberger, D. V., & Wei, S. (2014). Rupture complexity of the 1994 bolivia and 2013 sea of okhotsk deep earthquakes. *Earth and Planetary Science Letters*, *385*, 89–96. https://doi.org/https://doi.org/10.1016/j.epsl.2013.10.028

Zhang, Y., Wang, R., Zschau, J., Chen, Y.-t., Parolai, S., Dahm, T., & Tsai, V. C. (2014). Automatic imaging of earthquake rupture processes by iterative deconvolution and stacking of high-rate GPS and strong motion seismograms. *Journal of Geophysical Research: Solid Earth*, *119*, 5633–5650. https://doi.org/10.1002/2014JB011180

Zhao, D., & Negishi, H. (1998). The 1995 kobe earthquake: Seismic image of the source zone and its implications for the rupture nucleation. *Journal of Geophysical Research: Solid Earth*, *103*(B5), 9967–9986. https://doi.org/https://doi.org/10.1029/97JB03670

Zheng, X., Zhang, Y., Wang, R., Zhao, L., Li, W., & Huang, Q. (2020). Automatic Inversions of Strong-Motion Records for Finite-Fault Models of Significant Earthquakes in and Around Japan. *Journal of Geophysical Research: Solid Earth*, *125*(9), 1–19. https://doi.org/10.1029/2020JB019992

Acknowledgments

First of all, I want to thank my supervisors Torsten Dahm, and Frank Küger for their continuous support, their feedback on and their interest in my research through the course of my doctoral studies.

I also want to thank Simone Cesca and Matthias Ohrnberger for the help with different aspects of my work and fruitful discussions along with filter coffee or espresso.

The PDR development and implementation into *Pyrocko* and *Grond* would not have been successful without Sebastian Heimann and Marius Isken. Thanks to both of you for sharing your expertise with me, great hackdays and your patiance with my messy code.

Jens Tronicke has helped me a lot with the (self)organization through the doctoral project. Thanks for your help!

My doctoral study was, although disturbed by Corona, dominated by good chats on geophysics and other things in the garden, the seminar room or the office. Thanks for that, Philipp, Henning, René, Gesa, Peter, Lukas, Pınar, Angela, Pouria, Juliane, Carla, ... And thanks, Gesa, for your very thorough proofreading which has significantly reduced misplaced commas and improved this work.

I also want to thank the whole GFZ sections 2.1 and 2.6 as well as the seismology and applied geophysics working group of the University of Potsdam for three and a bit years of exchange, discussions and fun lunch breaks.

Zum Schluss danke an dich, Maja. Du hast spätestens in der zweiten Hälfte meines Doktorierens für eine sehr ausgewogene Work-Life Balance gesorgt und es trotz so mancher zehrender Nacht immer wieder geschafft, mir ein Lächeln aufs Gesicht zu zaubern. Ein dickes Danke auch dir, Rosi, dafür, dass du es mit einem manchmal verpeilten, abends müden, und mitunter arbeitswütigen Doktoranden ausgehalten und nebenbei auch noch Maja betüdelt hast. Die letzten Jahre wären ohne dich nicht möglich gewesen!